Risk Assessment and Optimal Response Strategies for Resilience of Electric Power Infrastructure to Extreme Weather

by

Hao-yu Derek Chang

B.S., M.S., Massachusetts Institute of Technology (2015)

Submitted to the Department of Civil and Environmental Engineering
in partial fulfillment of the requirements for the degree of

Doctor of Philosophy in Civil Engineering and Computation

at the

MASSACHUSETTS INSTITUTE OF TECHNOLOGY

June 2021

© Massachusetts Institute of Technology 2021. All rights reserved.

Author .....
Department of Civil and Environmental Engineering
April 5, 2021

Certified by .....
Saurabh Amin
Associate Professor of Civil and Environmental Engineering
Thesis Supervisor

Accepted by .....
Nicolas Hadjiconstantinou
Professor of Mechanical Engineering
Co-Director, Center for Computational Science and Engineering

Accepted by .....
Colette Heald
Professor of Civil and Environmental Engineering
Chair, Graduate Program Committee

Risk Assessment and Optimal Response Strategies for Resilience of Electric Power Infrastructure to Extreme Weather

by

Hao-yu Derek Chang

Submitted to the Department of Civil and Environmental Engineering
on April 5, 2021, in partial fulfillment of the
requirements for the degree of
Doctor of Philosophy in Civil Engineering and Computation

Abstract

Extreme weather is an increasingly critical threat to infrastructure systems. This thesis develops a stochastic modeling and decision-making framework for proactive resource allocation and response strategies to improve the resilience of electric power infrastructure in the wake of severe weather events. The framework is based on a physically-based, probabilistic risk assessment approach to estimating the weather-induced damage, and accounts for power flow constraints in designing response actions within electricity distribution networks.

Firstly, we formulate an asymmetric hurricane wind field model that is applicable to forecasting and large-scale ensemble simulation. The hurricane wind field model incorporates low-wavenumber asymmetries, and its parameters are estimated using a Constrained Nonlinear Least Squares problem. Inclusion of asymmetries in the model improves the accuracy of wind risk assessment in the hurricane eye wall, where wind velocities are maximized.

Secondly, the wind field forecasts are used as inputs to a probabilistic model for damage estimation in infrastructure systems. The novelty of this damage model is that it accounts for the spatial variability in damage estimates resulting from the hurricane wind field and forecast uncertainty in the hurricane's temporal evolution. We demonstrate that our model is capable of accurately predicting outage rates resulting from damage to the electrical grid following Hurricane Michael.

Thirdly, we develop a computational approach for optimal resource allocation and multi-step response operations. Using a two-stage stochastic mixed-integer formulation, we model the strategic deployment of distributed energy resources (DERs) ahead of a storm's landing, and the joint operation of islanded microgrids and repair of damaged components in the post-storm stage. The failure scenarios in this formulation are drawn from our physically-based damage model. The key challenge here is that the size of the optimization problem increases super-linearly with the network size. To address this computational bottleneck, we develop three solution approaches

based on L-shaped Benders decomposition. These approaches incorporate the network structure and power flow constraints to derive more effective Benders cuts. We evaluate the scalability of these approaches on benchmark networks, and show that they are useful in evaluating the resiliency improvements due to optimal DER allocation and response strategies under various resource constraints.

Thesis Supervisor: Saurabh Amin
Title: Associate Professor of Civil and Environmental Engineering

Acknowledgments

First, I would like to express my sincerest gratitude for my PhD advisor, Saurabh Amin. He has provided me with unconditional support throughout my graduate years, fostered my analytical abilities, and helped me fulfill my intellectual goals as a young researcher. I would also like to thank Prof. Kerry Emanuel for his long-standing guidance as my MS advisor, PhD committee member, and research collaborator on two of my main contributions to this thesis. Additionally, I would like to thank Prof. Dara Entekhabi for his support throughout my career, as my undergraduate advisor at MIT and PhD committee chair; and Prof. Ozlem Ergun for her invaluable advice on my work, from the point-of-view of disaster management and network resilience. This thesis would not be possible without the supervision and guidance of my outstanding and supportive committee.

Next, I wish to thank the Resilient Infrastructure Networks Lab (RESIL) for being my "home away from home" during my PhD studies. I owe a special thanks to Dr. Devendra Shelar for being a great collaborator in my research projects on power systems. I also wish to thank my current labmates (Manxi, Samarth, Rene, Sohil, and Gauthier), my former labmates (including Li, Jeff, Mathieu, Andrew, Zaid, and Abhishek), and my "labmates" at EAPS (Jonathan, Raphael, Rohini, and Sydney) for their emotional support and camaraderie. In particular, I would like to thank Jonathan Lin for his help with Forecasts of Hurricanes using Large-Ensemble Outputs (FHLO) in my work on probabilistic damage modeling. In addition, I appreciate the support from the staff at MIT Civil & Environmental Engineering (CEE) and the Center for Computational Science & Engineering (CCSE) for facilitating my progress through the program.

The completion of my PhD would not be possible without the support of my network of friends. A big thank you is in order for Tom and David H., who provided me unparalleled support in the final months of my PhD. I would further like to thank my friends whom I met at MIT (including Andy, Maria, and Fabian); through Tufts and BKB (including Fabio, Biplab, Terence, Lisa, and Olga); and elsewhere in this

world (including Alice, Jay, and David C.). I would like to give thanks to MIT Kickboxing and MIT Kung Fu Taichi Club, who provided a special community for self-growth during my graduate years. I am also grateful for Dr. Maria Khotimsky, my MIT Russian language instructor.

Last, but not least, I would like to thank my parents and my sister Ava for their unparalleled love, support, and sacrifices. Even in a lifetime, I would not be able to repay their dedication to my growth in this inspiring but chaotic world.

The work in this thesis was supported in part by the National Science Foundation Graduate Research Fellowship Program (NSF GRFP) and the MIT Martin Family Society of Fellows for Sustainability.

Contents

List of Figures

List of Tables

Chapter 1

Introduction

Extreme weather is becoming an increasingly critical threat to electrical grids [77]. Weather-induced disruptions, which contribute to about 44% of outage events in the U.S. power grid and cost between $20 and $55 billion annually [11], are becoming more challenging to handle due to the increasing frequency of stronger hurricanes induced by global warming [31]. According to recent findings in a November 2018 *Nature* article, climate simulations of hurricanes indicate that if little is done to curb greenhouse gas emissions and the world warms by 3-4°C this century, then hurricane rainfall will increase up to a third while wind speed will be boosted by as much as 25 knots [69, 79]. The increasingly destructive potential of hurricanes was highlighted in 2017 when the U.S. struggled to handle the aftermath of Hurricanes Harvey, Irma, and Maria. For instance, Hurricane Irma disrupted power supply for 7 million households and businesses in Florida as the storm plowed through the state [22]. Hurricane Maria left more than 1 million residents without power in Puerto Rico, many suffering from prolonged month-long delays in restoration of power [94].

Hurricanes are not the only weather-related threat to the reliable operation of electrical grids. In 2021, only days after the writing of this thesis had commenced, a series of severe winter storms significantly derailed the operation of the electric grid in Texas. Because extremely cold weather is rare in Texas (temperatures dropped as low as -2°F / -19°C at Dallas-Fort Worth International Airport), the local power equipment is not properly reinforced to survive extended periods of low temperatures

[21, 28]. Both natural gas power generation facilities and wind turbines suffered from equipment malfunctions, leading to widespread outages. By February 17, the third day of outages, over 2 million Texan power customers were without power [109, 49]. This catastrophe is a reminder that power grids' aging or inadequate infrastructure is an enormous vulnerability to extreme weather events, which are expected to become more frequent as a result of climate change.[1]

Meanwhile, the rapid evolution of the power grid into a "smart grid" provides government agencies and utilities increased flexibility in pre-storm and real-time decision-making to minimize grid damage induced by hurricanes. Unlike a traditional centralized grid, the smart grid incorporates distributed energy resources (DERs) in the form of portable microgrids, localized renewable energy, storage devices, and electric vehicles. DERs permit portions of electricity distribution networks (DNs) to obtain power even if DNs are disconnected from bulk generators due to weather-induced damages [19, 1, 41]. In particular, DERs are useful for supplying power to critical loads (e.g. police stations, hospitals) during disasters. Furthermore, smart grid technologies introduce flexibility by permitting multi-directional power flows (unlike single-direction flows in traditional grids) and information flows provided by sensing and control infrastructure, such that the power grid can quickly respond to component failures and appropriately re-route power in real time [87]. Overall, smart grids are crucial in achieving a more reliable, secure, and sustainable supply of energy, including enabling the deployment of clean energy technologies.

Despite these advancements, the current smart grids are not sufficiently hurricane-resilient. For example, Florida Power & Light (FPL), the largest electricity provider in the state, invested $3 billion in smart technologies such as sophisticated sensors and automated switches in 2013 [99]. FLP was able to mitigate many outages during Hurricanes Matthew and Hermine in 2016. However, Hurricane Irma in 2017 left as many as 15 million people in the state without electricity and the FPL with "a very, very lengthy restoration, arguably the longest and most complex in U.S. his-

[1]Furthermore, the winter storm lead not only to power shortages, but also to days-long water shortages.

tory" [81]. Restoration of Puerto Rico's grid following Hurricane Maria took even longer, with many residents suffering from prolonged months-long delays in power restoration [94]. Why does it take so long? Smart grid technologies for sensing and control enable faster localization of damage, but crews still need to travel to damage sites for inspection and repair, a process that frequently takes multiple days. The repair process is further delayed if we lack sufficient tools to forecast hurricane winds, which affect flooding and debris-induced damage. A rich body of literature relates to power network repair optimization [103, 93]. However, the difficulties in power restoration following these recent storms point to the importance of alternative generation resources while centralized power supplies are unavailable and the grid is under repair.

In this thesis, we develop an integrated decisions-based modeling framework for optimizing resilience of electricity networks to extreme weather events. Resilience enhancement strategies for infrastructural systems can be broadly classifed in two main categories: (i) long-term planning for infrastructural adaptability; and (ii) days or weeks-ahead and post-disaster operational planning [78]. In the context of electric power infrastructure, infrastructural upgrades and hardening include enforcing distribution lines; building protective enclosures for equipment such as substations; installing underground distribution lines that will be less affected by adverse weather; and vegetation management. However, in this thesis, we focus on proactive and post-disaster operational planning for electric power infrastructure. Such strategies include establishing an inventory of emergency resources; strategically allocating distributed energy resources (DERs) in distribution networks; damage localization; crew dispatch; and repair of damaged infrastructural assets.

The rest of this section is partitioned as follows. In Section 1.1, we discuss electric power infrastructure, smart microgrids, and existing approaches for response and repair pertaining to power grids in the literature. In Section 1.2, we discuss hurricane wind risk assessment, including modeling of wind-induced damage. In Section 1.3, we introduce the concepts of risk and resilience, and describe how they relate to our defined research objectives. In Section 1.4, we discuss how the models and

decision-based tools developed in this thesis contribute towards addressing our research objectives. Finally, in Section 1.5, we provide an outline of the subsequent chapters.

1.1 Optimal Response in Electric Power Grids

1.1.1 Components of Electric Power Infrastructure

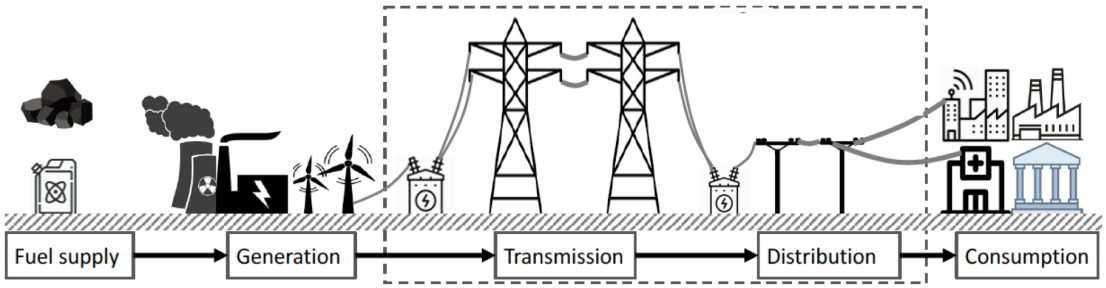

Figure 1-1: Major parts of power system. Figure shows (from left to right) conventional sources of energy, bulk power plants, transmission towers, distribution poles, and electricity consumers (smart buildings, industries, hospitals, universities).

The operation of the power grid consists of five major parts: fuel supply, power generation, transmission, distribution and consumption. Fuel supply may be provided by fossil fuels (i.e., coal, oil, natural gas), uranium, or renewable sources (i.e., hydroelectric, wind, solar). Power generation is typically provided by bulk power plants, and the power is dispatched to the high-voltage transmission system. Energy is transitioned from the high-voltage transmission system to the low-voltage distribution system via a substation. The distribution system provides power to the end users, which include households and businesses.

All parts of the power grid are susceptible to damage resulting from hurricane-related threats. For example, the prolonged outages in Puerto Rico resulting from Hurricane Maria (2017) were primarily due to damaged transmission lines and utility poles [23, 38]. In contrast, the 2021 Texas power crisis primarily resulted from disruptions to natural gas pipelines and power plants [21, 80], i.e., fuel supply and power

generation. Although each of these major parts need to be operationally resilient for the grid to function effectively, we limit the scope of our research to the resiliency assessment of the distribution networks; about 90% of outages occur in electricity distribution networks (DNs) [11].

Electricity network components can be adversely affected by security failures, which are carried out by malicious adversaries (i.e., cyber-hackers); or reliability failures, which are the result of adverse natural conditions such as disruptive weather (i.e., hurricanes, heat waves, wildfires, and snowstorms). This thesis focuses on quantifying the resilience of electric power infrastructure to hurricane wind fields. We note that other hurricane-induced threats, such as storm surge or rainfall, can also be disruptive to infrastructure systems [62].

1.1.2 DERs and Microgrids

Integration of Distributed Energy Resources or DERs (see 1-2) into microgrids within DNs can be particularly useful in improving post-hurricane grid resilience.

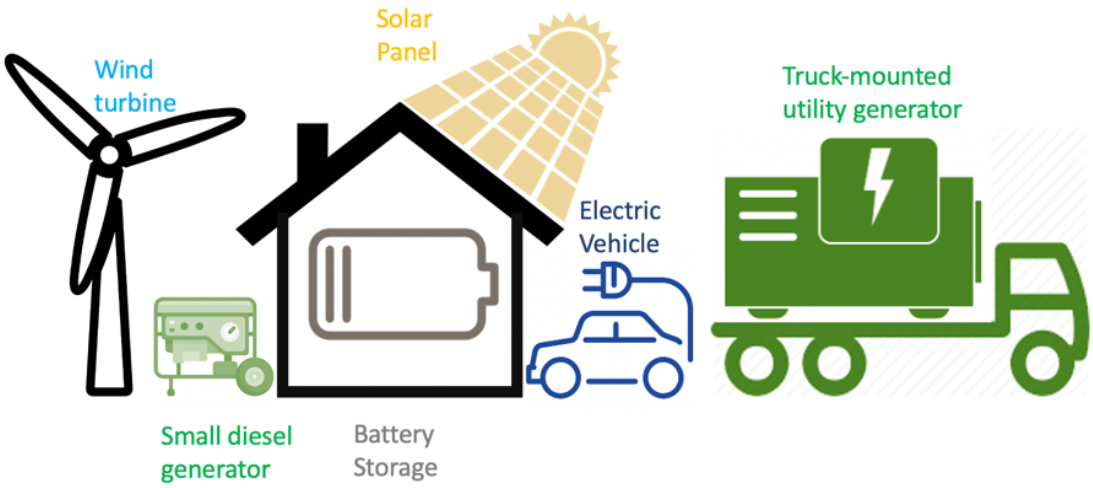

Figure 1-2: Examples of Distributed Energy Resources.

Figure 1-2 provides a few examples of relevant DERs. They include synchronous generators that are powered by diesel or natural gas, which have ratings that vary from 1 kilowatt to several megawatts [24]; a typical energy content for such generators

is ∼70 MWh. Energy may also be generated by small-scale wind turbines or solar panels that are installed on top of the buildings of homes or local businesses. Electric vehicles may provide energy due their energy storage capability and bidirectional charging flexibility [41]. In addition, truck-mounted utility generators are useful in providing mobile sources of power, and are particularly useful when applied to repairs or public works. These generators have smaller capacities, typically up to 15 kilowatts [7].

The inclusion of DERs in the power grid, including local generators and storage devices, permits the operation of microgrids. A microgrid is an aggregation of a number of technologies that, together, enable the partial, occasional or complete independent generation, regulation and supply of electricity within a relatively small geographic area. The microgrid can either operate connected to the bulk grid or as an island. Islands frequently form in electric power infrastructure as a result of hurricane-induced asset failures; allocation of DERs within an island results in a microgrid island. Once repairs commence, the islands increase in size over time and eventually merge. Over the course of this process, the system operator needs to make decisions regarding the operation of the DERs. A "smart microgrid" is predominantly powered by renewable energy sources [97].

By placing DERs in DNs, sources of power are closer to the demand nodes, which results in lower transmission and distribution losses [95]. In addition, they can also be used as contingency reserves which can be dispatched during contingencies [104].

1.1.3 Proactive Response and Repair in DNs

The idea of DER allocation in microgrids has received attention in recent literature [20, 59, 86, 41]. Chen et al. [20] considered remote control of DER-powered microgrids, using a distributed multiagent coordination scheme. Lei et. al. [59, 60] studied the allocation, routing, and scheduling of mobile power sources using a two-stage optimization framework. Gao et al. discussed a stochastic program for the allocation of diesel oil, batteries, and electric buses as generation resources [41]. Sedzro et al. [86] formulated a problem for allocation of mobile and fixed distributed generators,

in order to form microgrids in radial and/or meshed topologies. Kim and Dvorkin [50] considered allocation and routing of electrochemical energy storage units. However, these previous approaches do not consider resource allocation in the context of damage uncertainty and dynamic repair of damaged network components. This limitation can result in suboptimal utilization of DER resources. Furthermore, to fully exploit the potential of DER-enabled microgrids during and after hurricanes, the system operator needs to jointly optimize their efforts in resource allocation and response (network repair) actions to reduce prolonged outages and economic losses.

One way to account for pre- and post-storm decisions, while incorporating damage uncertainty, is to formulate two-stage stochastic optimization problems [88]. Accounting for damage uncertainty in resource allocation can significantly increase the computational complexity of the associated optimization problems. If we consider damage scenarios as vectors of binary variables, which indicate whether or not each infrastructure asset has failed, then the number of possible damage scenarios increases exponentially with the number of assets. Solution approaches to solve the two-stage programs include Benders decomposition [4], column-and-constraint generation [60], and progressive hedging [50].

As a brief summary, an effective DER allocation scheme should consider (i) the effect of post-storm network restoration on the cost due to loss-of-service (outages) and (ii) the effect of damage uncertainties. However, inclusion of uncertainties poses a computational challenge in two-stage optimization. In this thesis, we aim to address the abovementioned modeling challenges, as well as formulate solution approaches that remedy the issue of computational feasibility. Furthermore, adequate modeling of damage uncertainties requires the formulation of an appropriate hurricane wind risk assessment framework.

1.2 Hurricane Risk Assessment

Models of hurricanes for risk assessment should capture the hurricane track and wind velocities (intensity or wind field), as well as quantify the uncertainty in the forecasts.

Hurricane risk assessment approaches may be used for the purpose of (i) forecasting or nowcasting and (ii) long-term risk assessment. For both purposes, simulation of an "ensemble" of hurricanes is desirable. In forecasting or nowcasting, one considers an incoming hurricane that is expected to make landfall in 1-3 days. Under this scenario, the objective is to predict the hurricane wind field velocities over the course of these days, using a large ensemble of hurricane track and intensity forecasts as well as a suitable wind field model. Ensemble-based approaches can account for the highly non-deterministic nature of the hurricane track's temporal evolution. In long-term risk assessment, large-scale ensemble simulation is used to generate an ensemble of synthetic hurricane tracks, and then to predict the time-varying wind field at points along the track. Ensemble simulation can assume an embedded large-scale atmospheric environment, and is thus suitable to analyzing how hurricane activity is dependent on changes in climate.

1.2.1 Hurricane Track and Intensity:

Well-known synthetic track generation models combine both physical and statistical modeling approaches [13, 106, 34] and use historical hurricane 'best track' data as input. In the forecasting or nowcasting setting, hurricane track forecasts are typically provided by the National Hurricane Center (NHC) hour/days ahead of the hurricane's forecasted landfall (see Figure 1-3a). Forecasts provide estimated future locations of the hurricane eye (center) at discrete time steps (3-6 hour intervals are typical). The NHC forecast also includes strictly climatological track uncertainty estimates in the form of a "cone of uncertainty", which surrounds the forecasted track and represents the probable trajectories that the hurricane may take.[2] In recent history, the realized hurricane track fell within the cone about 60-70% of the time [14]. This suggests that the temporal evolution of the hurricane track is highly uncertain. However, ensemble prediction systems have the potential to significantly improve probabilistic forecasts

[2]To form the cone of uncertainty, one estimates the uncertainty in the forecasted track location at each discrete time step. The uncertainty at a time step is represented by a circle that surrounds the forecasted track location associated with this time. The union of the circles is the cone of uncertainty, and the cone shape reflects increasing uncertainty with time.

of hurricanes by accounting for real-time uncertainties [67, 43, 61] (see Figure 1-3b).

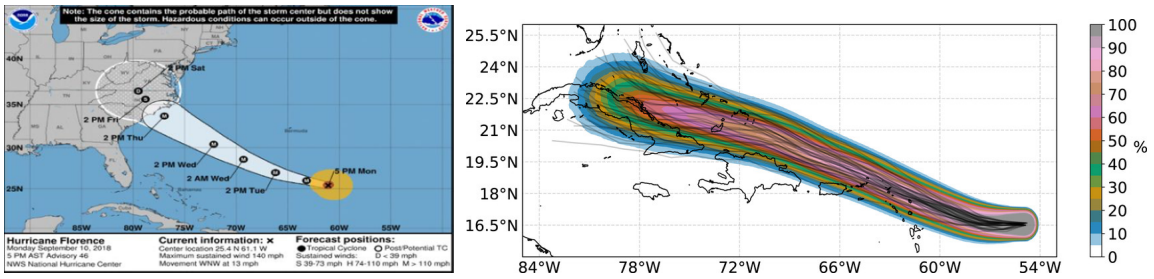

(a) (b)

Figure 1-3: *(a)* – Example of a National Hurricane Center (NHC) track forecast for Hurricane Sandy (adapted from [14]), with the "cone of uncertainty". *(b)* – Example of an ensemble track forecast given by Forecasts of Hurricanes using Large-Ensemble Outputs [61]. The colors indicate the "strike probability", or the likelihood that the hurricane track would fall in the denoted spatial location.

Maximum wind intensity estimates along the tracks are provided by models such as the Coupled Hurricane Intensity Prediction System (CHIPS) [33] or FAST intensity simulator [32].

1.2.2 Hurricane Wind Field:

Given a hurricane track and intensity, one can deduce wind velocities at arbitrary locations that may be affected by the storm, as given by a surface wind field.[3] Wind field models typically account for two sources of variability in wind velocities: (i) radial variability, i.e., with respect to distance from the storm center; and (ii) azimuthal variability, i.e., with respect to angle (azimuth) measured from a defined reference direction (typically the storm translation direction).

Axisymmetric ("mean field") models account only for radial variability in wind velocities [105, 30, 107, 113, 47, 48, 18]; see Figure 1-4. These models typical contain the following parameters: maximum intensity V_m; radius of maximum winds R_m, which determines the radial distance at which velocity is maximized; and a set of shape parameters that determine the rate of wind velocity decay with respect to radial distance.

[3]Most wind field models estimate 1- or 10-minute sustained winds.

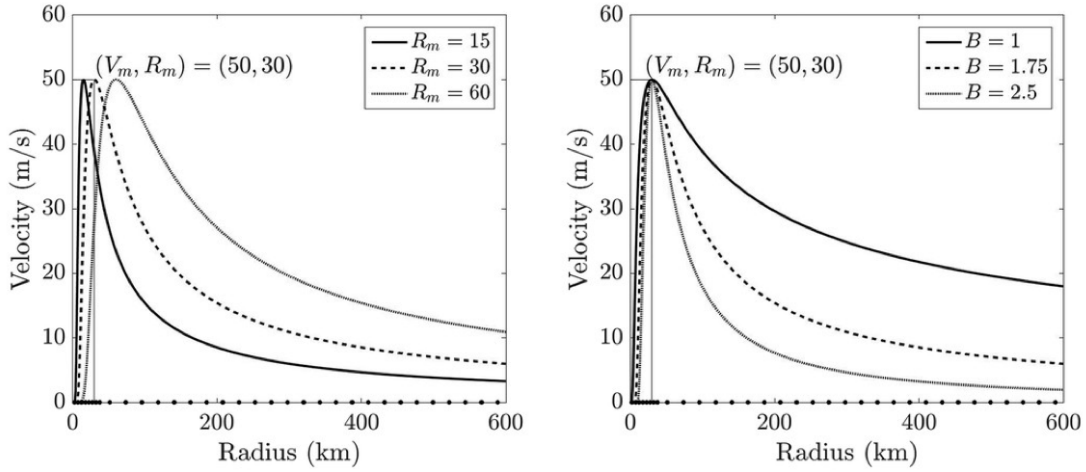

Figure 1-4: Demonstration of radial variability in the hurricane wind field. The radial wind profile is given by the parametric Holland 1980 model [47] under various values of the radius of maximum winds R_m (*left*) or of the shape parameter B (*right*). $(V_m,\ R_m) = (50\ \text{m/s},\ 30\ \text{km})$ for the dashed curve on the left plot and for all curves on the right plot.

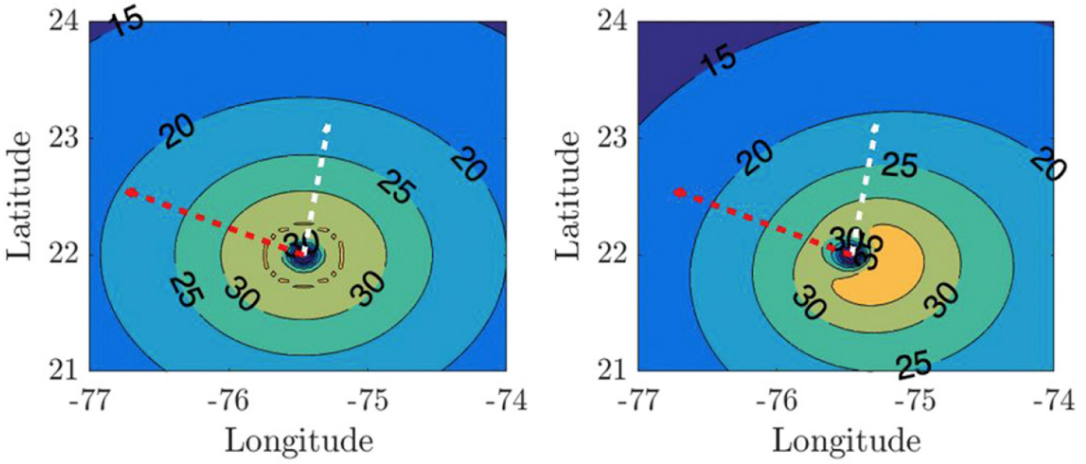

Figure 1-5: Demonstration of azimuthal variability in the hurricane wind field. *Left*: Example of an axisymmetric wind field (radial variability). *Right*: Example of an asymmetric wind field (radial and azimuthal variability). Note that the velocity contours form perfect circles in the axisymmetric wind field, but not in the asymmetric wind field.

In reality, however, hurricane wind fields tend to be asymmetric (include significant azimuthal variability). Not accounting for this inherent asymmetry can negatively affect hurricane risk assessment of aboveground infrastructure components such as electric distribution lines, whose failure probabilities depend on local surface wind intensities [118, 3]; see Figure 1-5. In fact, the difference between the highest and lowest velocities around the radius of maximum winds can readily be around 10 m/s [100]. The relationships of asymmetries to environmental inputs were studied in [115], [100], [108], and [53]. While asymmetric wind field models exist in the literature [115, 15], most are not directly applicable forecasting and ensemble simulation, as opposed to only hindcasting.

In this thesis, we will frequently apply Forecasts of Hurricanes using Large-Ensemble Outputs (FHLO), which quantifies the forecast uncertainty of a hurricane by generating probabilistic forecasts with a three-component framework: 1) a track model that generates synthetic tracks from the hurricane tracks of an ensemble numerical weather prediction (NWP) model, 2) an intensity model that predicts the intensity along each synthetic track, and 3) a hurricane wind field model that estimates the time-varying two-dimensional surface wind field [61]. The resulting forecast is represented by an ensemble of $O(10^3)$ randomly-generated hurricanes. We employ FHLO because it is computationally inexpensive, while still reliable and accurate in its probabilistic wind forecasts.

1.2.3 Probabilistic Damage Modeling

Given forecasts or estimates of a hurricane's temporally-evolving wind field, one can then predict or estimate the damage, loss-of-service, and/or cost due to the wind velocities. Hurricane winds result in infrastructural damage, which in turn result in loss-of-service (outages) within the power grid. Total cost can be calculated using the loss-of-service measurements (see Section 1.3).

The Federal Emergency Management Agency's Hazus Program provides standardized tools and data for estimating risk from earthquakes, floods, tsunamis, and hurricanes. Hazus models, which are packaged in software distributed as a GIS-based

desktop application, combine expertise from many disciplines to create actionable risk information that increases community resilience. The Hazus Hurricane model [70] specifically addresses hurricane winds, rainfall rates, and storm surge, and is aimed at primarily estimating debris-based structural damage and financial losses. With regards to hurricane wind modeling, Hazus incorporates a model of surface roughness to account for the effect of land topology on the hurricane winds, in order to consider how landfall impacts the wind field. In addition, Hazus considers the effect of hurricanes on tree blowdown, which can in turn damage buildings.

The Hazus models do not directly address damage to electric power infrastructural assets. Failures of overhead infrastructural assets are dependent on hurricane wind characteristics such as local wind speed, direction, and duration, which are functions of the hurricane track and intensity. About 90% of outages occur in electricity distribution networks (DNs) [11], particularly due to the toppling of electricity distribution lines and poles. Indeed, previous works model the wind-induced failure of distribution lines using Poisson process models [8, 3, 116, 55]. These studies suggest that the failure rate is a quadratic or exponential function of the wind velocity. However, these studies did not evaluate the spatial variability in estimated Poisson failure rates due to the physical structure of the hurricane wind field, even though hurricane wind velocities vary significantly with space and time. Furthermore, they do not consider the considerable temporal uncertainty that typically characterizes hurricane track forecasts.

While the Hazus models for windborne debris and structural damage might be indirectly useful in our study, they are not applicable to estimating loss-of-service (outages) in electric power infrastructure. This is because the level of service depends on the network topology, which is subject to physical laws and managed by system operators. Thus damage in itself is not a direct predictor of loss-of-service. Regarding effects of network topology, damage to a critical component (i.e., substation) might result in longer and more widespread outages than damage to a downstream overhead distribution line. Regarding effects of physical laws, damage of infrastructural assets will alter the power flows in the network, leading to potential violations of voltage

bounds that would result in further outages.

Generalized linear or additive regression models are commonly used to predict outages [63, 64, 45] in electric power infrastructure, as a function of inputs related to the hurricane's physical structure and the local environment. These inputs include not only the hurricane wind velocities, but also soil moisture anomalies, precipitation, land cover, and other considerations. Data regarding the power system – such as the number of transformers, poles, overhead lines, underground lines, and customers – are also included as inputs. However, these models do not predict locations of damage as a function of the hurricane winds and environmental inputs. Thus, they provide limited insight on the physical effect of the hurricane on the infrastructural assets. This in turn impedes damage localization and repair operations [58]. Furthermore, faster recovery requires effective pre-storm resource allocation, warehouse selection, and vehicle fleet routing, which benefit significantly from accurate damage predictions [103]. Slow damage localization and system repair result in an increased time duration during which the infrastructure fails to adequately provide service to end-users.

At this point, we have discussed the existing work in strategic, operational decision-making and hurricane risk assessment. Next, we more precisely define risk. We also introduce a modeling and decisions framework pertaining to risk quantification and minimization, which motivates our research contributions.

1.3 Defining Risk and Infrastructural Resilience

1.3.1 Risk and Resilience

Our research objective is to develop a framework for strategic operational decision-making (proactive resource allocation and network response) to minimize risk in electric power infrastructure. The risk (expected cost) in response to an adverse event is defined as follows:

$$\textbf{Risk (expected cost)} \;=\; \sum_{s \in \mathcal{S}'} \mathbb{P}(s) \times \mathrm{C}(s), \tag{1.1}$$

where $\mathcal{S}'$ is the set of possible infrastructural damage scenarios that may result due to the adverse event (hurricane wind field), $\mathbb{P}(s)$ is the probability of a scenario s, and $\mathrm{C}(s)$ is the cost associated with scenario s. To estimate the damage probabilities $\mathbb{P}(s)$, one needs to understand how the hurricane wind field physically impacts assets in electric power infrastructure. Furthermore, one should be able to quantify the uncertainty in the wind field, as well as the uncertainty in how the wind field impacts the infrastructure. The costs $\mathrm{C}(s)$ should be dependent on not only the damage scenario s, but also the network properties such as topology and physical constraints.

Now, we define the key research questions that will be addressed in the thesis:

1. How does one obtain probabilistic estimates of damage, given by $\mathbb{P}(s),\ \forall s \in \mathcal{S}'$?
2. How does one quantify the cost associated with hurricane-induced damage, given by $\mathrm{C}(s),\ \forall s \in \mathcal{S}'$?
3. How does one make decisions pre- and post-hurricane, in order to minimize risk?

Next, we more specifically discuss the concept of resilience, and how it relates to risk. Generally speaking, the resilience of a system is defined as "its ability to prepare and plan for, absorb, recover from, and more successfully adapt to adverse events" [102].

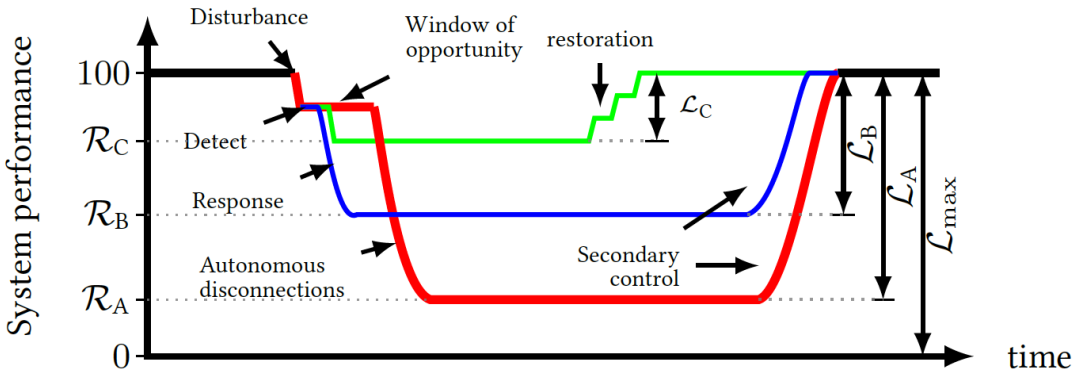

Figure 1-6: System performance under various infrastructural response capabilities.

In this context, we can define the resilience of a system to an adverse event using the time-varying system performance (see Figure 1-6). The nominal system perfor-

mance is 100% (i.e., the system is fully able to meet service its associated demand). After an adverse event, the system performance likely degrades due to disturbances or infrastructural damage. Then the system performance increases over time due to network recovery and repair. Eventually, the full network functionality is restored and the system performance returns to its nominal value of 100%. Note that if an adverse event is sufficiently disruptive and the network is inadequately prepared, the damage could be so severe such that the system performance never returns to its nominal value.

The degree of post-disaster system performance degradation, as well as the rate of recovery of the system performance, depend on conditions such as: efficacy of pre-disaster planning and resource allocation; efficiency of damage localization; and efficiency of network repair. Decisions that affect these conditions are dependent on the accuracy of probabilistic hurricane damage estimates, which in turn depend on the hurricane forecast. The potential variability in system performance is illustrated by the green, blue, and red curves in Figure 1-6.

The system's resilience in response to an adverse event can be defined as the system performance integrated over time. By selecting decisions that minimize the risk (expected cost), we also maximize the expected resilience of the system to the adverse event.

1.3.2 Generalized Modeling and Decisions Framework

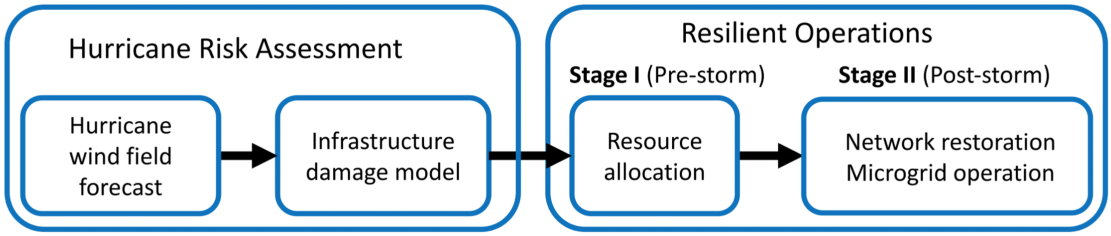

Figure 1-7: Framework of models and decisions addressed in the thesis.

Figure 1-7 provides an overview of the modeling and decisions framework that we formulate in this thesis. The hurricane model and infrastructural damage model are

used to estimate the damage probabilities $\mathbb{P}(s)$. The cost function $\mathrm{C}(s)$ is dependent on the damage scenario s, the network properties, pre-storm decisions regarding resource allocation, and post-storm decisions regarding network restoration and microgrid operation. Our objective is to select pre- and post-storm decisions which minimize the risk (expected cost) due to the hurricane event.

Hurricane Risk Assessment:

Hurricane wind field forecast:

A suitable risk assessment approach should capture the stochastic nature of hurricane arrival, landfall location, and intensity. More specifically, typical approaches to hurricane wind risk assessment rely on capturing two aspects of hurricane structure: (1) *track*, or trajectory of the storm from its formation over the ocean to dissipation over land; and (2) *wind velocities* at various points along the track, modeled by either a single intensity measurement (e.g., maximum sustained 10 m wind speed) or a surface wind field. The hurricane wind velocity is frequently estimated using the maximum intensity measurement or rating on the Saffir-Simpson hurricane wind scale (SSHWS). However for risk assessment of large-scale infrastructure systems, the impact of spatially heterogeneous wind velocities must be suitably captured. Thus, a reliable model of the whole surface wind field is desirable. The surface wind field at a given time is represented by wind velocities at a set of geographical locations. We are interested in how the wind field evolves with time over the course of the hurricane's lifetime. Furthermore, uncertainties in hurricane track forecasts can be accounted for using ensemble forecasting techniques.

Infrastructure damage model and cost function:

We are interested in probabilistic, spatially-varying estimates of damage in the infrastructure system. The damage estimate at a given location in the infrastructure system is dependent on the local time history of the hurricane wind velocity, which is given by the hurricane wind field forecast.[4] Given a damage estimate, one then quantifies the infrastructure system's *loss-of-service* induced by the damage. In the

[4]Other considerations such as soil cover and tree density have also been shown to be relevant to modeling of infrastructural damage, but here we consider the isolated effect of winds.

specific case of electric power infrastructure, loss-of-service can be defined by outages. The outages depend not only on the locations of damage, but also on the network topology, physical constraints, and operational constraints which determine the network's restoration rate. The cost $\mathrm{C}(s)$ due to damage scenario s can then be defined as the total network loss-of-service integrated over time. Alternatively, one can define the cost as the incurred financial cost resulting from the network's loss-of-service, using an appropriate financial loss model. The relationship between damage, loss-of-service, and financial loss is illustrated in Figure 1-8.

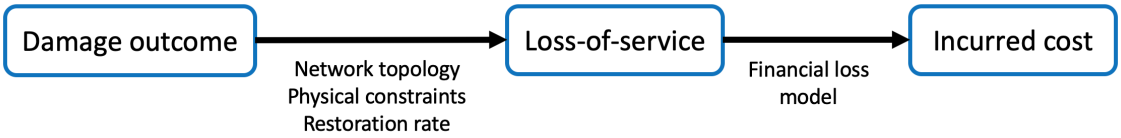

Figure 1-8: Framework for modeling the cost function $\mathrm{C}(s)$ as a function of damage given by s.

Resilient Operations: Effective operational decision-making can decrease the loss-of-service resulting from hurricane-induced damage. We consider both Stage I (pre-storm) decisions as well as Stage II (post-storm decisions).

Stage I (pre-storm) decisions: A subset of these decisions can relate to days- or weeks-ahead pre-storm resource allocation and planning, which include resource stockpiling, distributed energy resources (DER) allocation, and crew allocation. These decisions should depend on the expected incurred cost resulting from infrastructural damage or loss-of-service (see Eq. 1.1). Computing the expected cost depends on the uncertainties in the damage estimates, specifically the probabilities of various damage scenarios given by $\mathbb{P}(s)$ and the associated costs $\mathrm{C}(s)$. The cost $\mathrm{C}(s)$ depends on the Stage II (post-storm) decisions taken, and ideally should be minimized by optimal selection of the Stage II decisions. In this work, we primarily focus on resource allocation decisions in Stage I.

Stage II (post-storm) decisions: Given a realized damage scenario and set of pre-storm decisions, one then selects post-storm decisions related to network restoration which minimize the cost. Network restoration consists of localizing infrastructural

damage, repairing damaged assets, and re-allocation of resources that have been placed in the network prior to the disaster. The pre-storm placement of DERs permits operation of microgrid islands in portions of the electric power infrastructure. As the network is gradually restored, the topology of the islands changes due to their growth and eventual merging. With each period of restoration, the optimal power flows in the microgrid islands need to be re-computed.

1.4 Our Contributions

In this thesis, we develop a decisions-based modeling framework for optimizing resilience of electricity networks to extreme weather events. Our contributions lie at the nexus of two primary areas of research (see Figure 1-9): strategic and operational decision-making (discussed in Section 1.1) and hurricane risk assessment (discussed in Section 1.2). Regarding hurricane risk assessment, we formulate a probabilistic, physically-based modeling approach for estimating risk (expected damage) in infrastructure systems due to hurricanes. Regarding decision-making, we devise a modeling and solution approach based on two-stage stochastic optimization, for resource allocation and repair in electricity networks that are disrupted by hurricanes. As such, this work is among the first to study optimal resource allocation and proactive response pertaining to post-hurricane repair and operation of microgrids, informed by physically-based hurricane risk assessment.

Our approach for damage estimation in infrastructure systems consists of two components: (i) hurricane wind field modeling for forecasting and ensemble simulation applications and (ii) probabilistic estimation of spatially-varying damage using wind field inputs. We devise a wind field model that incorporates low-wavenumber asymmetries to model azimuthal variability in wind velocities. Using a constrained nonlinear least squares (CNLS) approach to estimate model parameters, we demonstrate that our model performs better than a standard benchmark in the literature. Then, we devise a probabilistic modeling approach for damage estimates. The approach incorporates uncertainty in wind velocities with "Forecasts for Hurricanes usi-

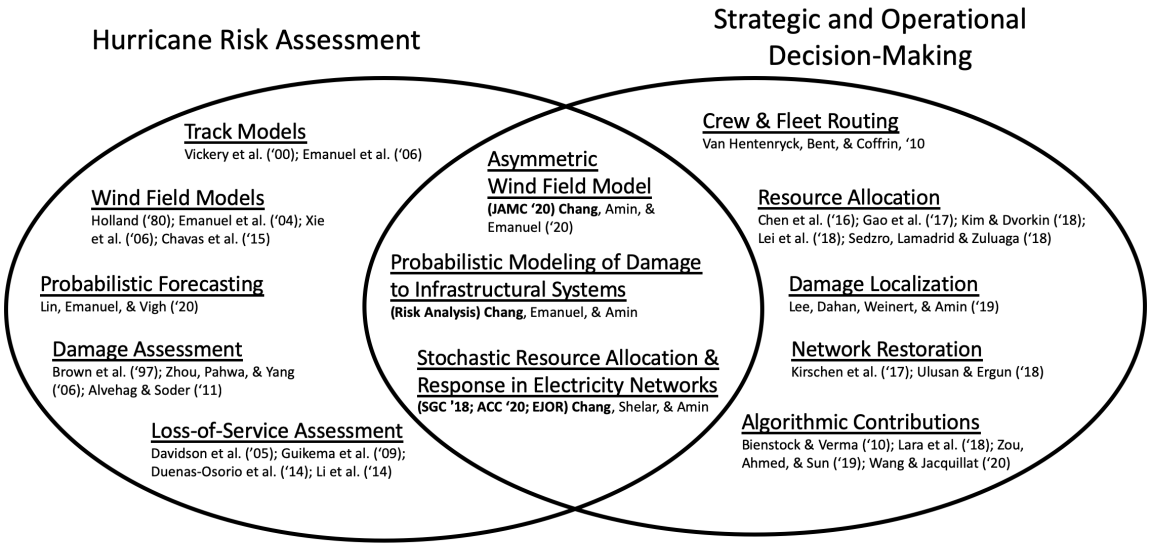

Figure 1-9: Venn diagram of research contributions in hurricane risk assessment as well as strategic and operational decision-making. Our contributions integrate both areas of research.

ing large Ensemble Outputs" (FHLO) [61], and spatial variability of damage estimates using a Nonhomogeneous Poisson Process (NHPP) model. We apply our approach to prediction of outage rates in historical hurricanes.

Our approach for resource allocation and repair in electricity networks considers pre-storm (Stage I) resource allocation decisions and post-storm (Stage II) decisions regarding network restoration and multi-master microgrid operation over a multi-period timeframe. We formulate a two-stage stochastic mixed integer linear program (SMIP2) in order to optimally select decisions. Importantly, the Stage II decisions are dependent on uncertainties in locations of infrastructural damage, which can be estimated using our NHPP damage model. This approach is novel in that it incorporates uncertainties based on the hurricane's physical structure, but this model feature poses a computational scalability challenge. To handle this issue, we develop algorithmic solution approaches based on L-shaped Benders decomposition (LBD), to ensure that resource allocation problems can be solved for distribution networks of a realistic size. We compare the three approaches (LBD-Greedy, LBD-DIC, and NBD) in the thesis.

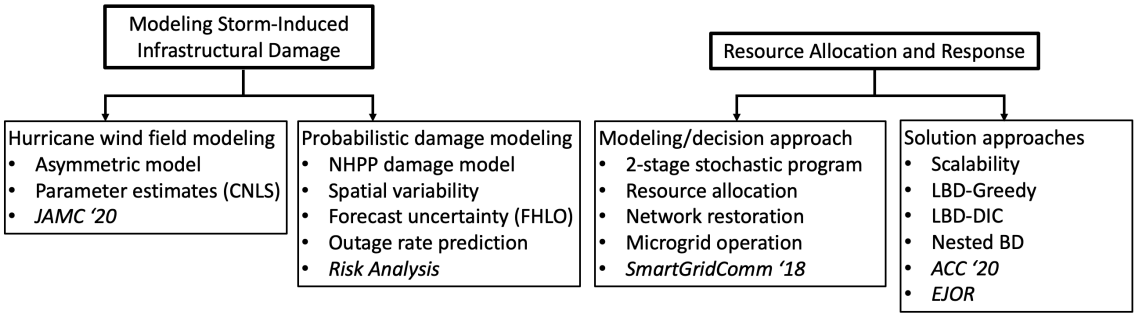

Figure 1-10: Summary of the contributions.

1.4.1 Modeling Storm-Induced Infrastructural Damage

Modeling of Asymmetric Hurricane Wind Fields:

For hurricane risk assessment of large-scale infrastructure systems, we construct a physically-informed hurricane wind field model, in order to suitably capture the impact of spatially heterogeneous wind velocities. The model's velocity outputs may be used to produce probabilistic estimates of infrastructural damage. In particular, we formulate a model of the hurricane gradient wind field; one can then use a boundary layer model for the gradient-to-surface wind conversion. The proposed approach captures the wind field for the purpose of (i) forecasting or nowcasting and (ii) large-scale ensemble simulation. In this thesis, we include brief remarks on how our estimated wind field model can be applied for simulating wind fields in a statistically generated ensemble.

Some previous works have also introduced asymmetries into an existing mean field model by considering that the mean field parameter(s) vary with azimuth. In particular, [115] introduce a real-time nowcasting asymmetric model, but that model cannot be readily used to simulate a wind field ensemble. [100] and [108] quantify asymmetries in storms using the semispectral approach, but their focus is on hindcasting and they do not explicitly parameterize asymmetries in wind field models.

Wind Field Model: We formulate an asymmetric wind field that is an extension of the mean field model of Holland 2010 [48]. The wind field model extends the previous work [115, 100, 108, 53] by modeling wind field asymmetries as a function

of environmental inputs, specifically by parametric incorporation of asymmetries into established models for mean field estimation.

To account for radial variability in the wind field (which we denote as the "mean field"), our model includes the following parameters: maximum intensity; radius of maximum winds, or the radial distance at which velocity is maximized; and a set of shape parameters that determines the decay of wind velocities with radial distance. To account for azimuthal variability (asymmetries) in the wind field, the model's maximum intensity parameter is set to be a harmonic function of the azimuthal angle. The azimuthal variability is given by two wavenumber-1 asymmetries, which correspond to the environmental inputs of storm translation and environmental shear. Each wavenumber-1 asymmetry is quantified in terms of an amplitude and phase, which are affine functions of the corresponding environmental input.

Parameter Estimation: The parameters that model the amplitudes and phases in the asymmetry correction are estimated by solving a constrained, nonlinear least squares (CNLS) problem. Solving this problem entails minimizing the sum of squared errors between velocity estimates and historical storm data for the region between the storm center and a pre-decided 'cutoff' radius in the storm's outer region. The method can jointly estimate the amplitude and phase parameters while accounting for the nonlinearity of the asymmetric wind field model and parameter constraints. While we consider the Holland mean field model here due to its relative simplicity, the proposed CNLS formulation can be adapted to other mean field models such as [30] and [18].

Model Estimation and Evaluation: For the purposes of model estimation and evaluation, we use two sources of wind field data [82, 112]. We consider several wind field models which differ in terms of the asymmetries included in the wind field, and estimate the parameters using the CNLS procedure for each model. For the purpose of evaluating the models, we consider three metrics: cross-validation error, Bayesian Information Criterion (to penalize overfitting), and mean squared error on held-out test data.

A typical state-of-the-art means of modeling hurricane asymmetry (azimuthal vari-

ability) is to add the storm translation vector to the wind field. We demonstrate that our wind field model incorporating low-wavenumber asymmetries performs better than the benchmark wind field with storm translation vector, using the evaluation metrics that we select. Adding the storm translation vector to our asymmetric wind field model further improves the model's estimation performance. In addition, inclusion of the wavenumber-1 asymmetry resulting from translation results in a greater decrease in modeling error than does inclusion of the wavenumber-1 shear-induced asymmetry. Overall, the CNLS estimation method can handle the inherently nonlinear wind field model in a flexible manner; thus, it is well suited to capture the radial variability in the hurricane wind field's asymmetry.

Probabilistic Modeling of Infrastructural Damage:

We formulate a probabilistic modeling approach for obtaining spatially-varying estimates of damage in infrastructure systems. More specifically, our approach is applicable to the estimation of probabilities of damage scenarios given by $\mathbb{P}(s)$, for all possible scenarios $s \in \mathcal{S}'$. We are interested in obtaining a probabilistic damage estimate in each defined spatial location $g \in \mathcal{G}$, where $\mathcal{G}$ denotes the set of spatial locations of interest. Then, a scenario is defined as $s = \{s_g\}_{g \in \mathcal{G}}$ where s_g is the number of failures in location g.

Using damage estimates, one can predict the loss-of-service in the infrastructure system (i.e., outages in electric power infrastructure). For networked infrastructure systems, the loss-of-service depends on the network topology as well as the locations of damage. Then, given certain assumptions regarding the rate of damage localization and repair within the system, one can calculate the incurred cost (i.e., financial cost) as a function of the loss-of-service.

Modeling Approach: Our modeling approach for probabilistic damage estimation is used to estimate a probability distribution over the number of damaged infrastructural assets in each location $g \in \mathcal{G}$. The probability of s_g asset failures in location g is denoted by $\Pr(s_g)$. Then, the probability of a scenario $s = \{s_g\}_{g \in \mathcal{G}}$ is given by:

$$\mathbb{P}(s) \;=\; \prod_{g \in \mathcal{G}} \Pr(s_g). \tag{1.2}$$

The approach accounts for both hurricane forecast uncertainty and spatial variability of wind velocities. To represent the impact of uncertainty in the hurricane track's temporal evolution, we employ "Forecasts of Hurricanes using Large-Ensemble Outputs" (FHLO), which produces 1000-member forecast track and intensity ensembles [61]. It is particularly suitable for our approach because its ensemble members are computationally inexpensive to produce, in comparison to using typical ensemble numerical weather prediction (NWP) systems [96, 71]. In addition, FHLO is designed to readily scale with advancements in the physics, resolution, and size of ensemble numerical weather prediction models, which have the ability to improve hurricane intensity forecasts.

Using the probabilistic wind forecast given by FHLO as input, we employ a physically-based Nonhomogeneous Poisson Process (NHPP) model [8, 118, 3, 116] that outputs spatially-varying probability distributions of the extent of damage (number of asset failures). The distribution is parameterized by a failure rate (expected number of failed assets), which varies spatially to reflect the radial and azimuthal variations in hurricane wind velocities. The failure rate at a given location is dependent on the local time history of the hurricane wind velocity. More specifically, we consider that the failure rate per unit time is small and constant below a defined critical velocity threshold, which governs the wind velocity threshold above which hurricane winds are sufficiently intense to impact the infrastructure assets. Above this critical threshold, the failure rate per unit time increases quadratically with wind velocity.

Analysis: We analyze how NHPP-estimated spatial extent and variability of damage depend on hurricane intensity and size, as well as the inclusion of wind field asymmetries. To analyze the spatial extent of damage, we introduce the so-called "critical zone", the geographical region that suffers from hurricane wind-induced damage. One way to define the boundaries of the critical zone is to use the critical velocity parameter in the NHPP model, whose value is dependent on the physical properties of the assets. Furthermore, we analyze variations in failure rates within the critical zone, which are significant and would not be captured by a model that does not account for spatial variability in damage estimates.

Next, we study how incorporating the forecast uncertainty as given by FHLO affects the NHPP model damage estimates in the cases of Hurricanes Hermine (2016) and Michael (2018). In particular, we show that not incorporating forecast uncertainty can result in underestimated failure rates and spatial extent of damage (i.e., critical zone). This in turn can lead to ineffective damage localization and inaccurate estimates of cost due to system loss-of-service. Furthermore, we show that utilizing FHLO results in higher estimated probabilities for scenarios associated with a large number of damaged assets (i.e., longer tails in the probability distributions). Our results highlight the limitations of using deterministic damage estimates, which do not account for uncertainties in hurricane track forecasts, to quantify the severity and spatial extent of damage.

Application to Outage Prediction: We apply our modeling approach to the prediction of outages (i.e., loss-of-service) in electric power infrastructure due to Hurricane Michael. We consider the electric power grid, because North American power grids typically contain a large number of overhead assets (i.e., poles, distribution lines). Using our approach, we demonstrate a statistically significant relationship between outages and damage estimates by considering county-wide outage statistics in Northern Florida. In addition, we show in the case of Hurricane Michael that the relationship between outages and hurricane velocities is well-represented by an S-shaped curve. This result suggests that outage prediction could be improved using physically-based and uncertainty-aware damage estimation.

The application of our modeling approach to outage prediction is a step forward in quantifying the cost $\mathrm{C}(s)$ associated with loss-of-service resulting from damage scenario s. Future work on loss-of-service modeling could also account for network topology, operational constraints, and repair strategies, following our discussion in Section 1.3.2.

Finally, we provide brief insights into how hurricane intensity and size impact total damage and resulting financial losses.

1.4.2 Resource Allocation and Repair in Networks

Our objective is to develop a modeling framework that (i) accounts for the likely locations of infrastructural asset failures for damage assessment; and (ii) enables the design of pre-storm resource allocation strategies as well as post-storm repair operations. To address these challenges, we formulate a two-stage stochastic optimization problem. The problem involves selecting decisions in Stage I (pre-storm) and Stage II (post-storm) which minimize the expected cost incurred by the system operator due to the hurricane-induced damage.

In this work, we focus on decision-making for electricity distribution networks (DNs), where about 90% of outages occur [11] and Distributed Energy Resources (DERs) can be allocated to permit power supply to loads even when the bulk supply from central generation is disrupted.

Modeling Approach:

In our optimization problem formulation, we consider strategic placement of DERs at a subset of DN nodes in the pre-storm stage, given the uncertainty in locations of infrastructural asset failures and the resulting outages and lost load for a particular storm. These DERs can then be used to sustain microgrids in the post-storm stage (Stage II), when the asset repair operations are being completed and the connection to bulk supply is being restored. A key aspect of our formulation is that we allow for the partial DN operation in situations when the bulk power supply is no longer available, and it is beneficial to operationalize microgrids during the recovery period.

More specifically, our two-stage stochastic mixed-integer problem considers the DER placement decisions in Stage I (pre-storm), and a multi-period repair problem with DER dispatch within each microgrid in Stage II (post-storm). The objective is to minimize the sum of the cost incurred in DER allocation and the expected cost of unmet demand during the time period of repair and recovery operations. Figure 1-11 summarizes the order of events and decisions in our formulation.

For a given DER allocation (placement) and a realization of DN component disruptions, Stage II is a multi-period problem in which asset repair schedules and dispatch

within each microgrid are jointly determined. From a practical viewpoint, each period can be viewed as one work shift of the repair crews and the number of repairs per period is constrained. In the 0th period, the subnetworks formed as a result of disruptions start to operate as microgrids using the available DER supply. In the subsequent time periods, damaged lines are repaired, permitting connections between smaller microgrids to progressively form larger microgrids. In the last time period, the DN is connected back to the main grid, and normal operation is restored. We also allow for the flexibility of DER re-allocation in the post-storm stage, as the network repair progresses, to serve loads without access to power.

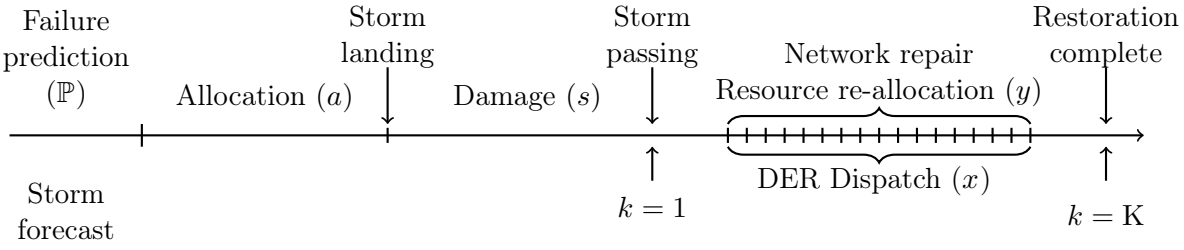

Figure 1-11: Timeline of events and operator decisions. $\mathbb{P}$ denotes the probability distribution over failure scenarios; a the DER allocation decisions taken before the storm hits; s a specific realization of the uncertainty; r^s the network restoration schedule; x^s the aggregated network state variables. The line repair and dispatch decisions are made over periods $k = 0, 1, \cdots, \mathrm{K}$.

The total cost incurred due to the hurricane-induced damage, as a function of DER allocation a and damage scenario s, can be written as:

$$\mathrm{C}\,(a, s) \;=\; \mathrm{J}^{\mathrm{I}}(a) + \mathrm{J}^{\mathrm{II}}\,(a, s)\,, \tag{1.3}$$

where $\mathrm{J}^{\mathrm{I}}(a)$ is the Stage I (pre-storm) cost of DER allocation and $\mathrm{J}^{\mathrm{II}}\,(a, s)$ is the Stage II (post-storm) cost of loss-of-service (i.e., lost demand due to outages). Then, the expected cost under a DER allocation a is:

$$\begin{aligned} g(a) \;&=\; \sum_{s \in \mathcal{S}'} \mathbb{P}(s)\ \mathrm{C}\,(a, s) \\ &=\; \mathrm{J}^{\mathrm{I}}(a) + \sum_{s \in \mathcal{S}'} \mathbb{P}(s)\ \mathrm{J}^{\mathrm{II}}\,(a, s) \\ &=\; \mathrm{J}^{\mathrm{I}}(a) + \mathbb{E}_{s \sim \mathcal{P}}[\mathrm{J}^{\mathrm{II}}\,(a, s)] \end{aligned} \tag{1.4}$$

We formulate the problem of pre-storm resource allocation under uncertainty and post-storm network restoration as a two-stage stochastic mixed-integer program (SMIP2). By solving (SMIP2), we aim to obtain a DER allocation a which minimizes the expected cost $g(a)$, under resource, operational, and physical constraints. SMIP2 can be rewritten in a Deterministic Equivalent Formulation (DEF) which is a mixed-integer program (MIP) with copies of Stage II variables for each scenario.

Resource Allocation Model (Stage I): In the pre-storm stage (Stage I), two sets of decisions are considered: (i) which DN nodes should be developed as DN sites and (ii) to which DN nodes should available DERs be allocated. A subset of nodes are considered suitable for site development. Before a DER can be allocated to a DN node, the operator needs to develop a site at that node to ensure a safe and reliable integration with the DN. After developing the sites, the operator allocates the DERs (i.e., synchronous or photovoltaic generators) amongst the available developed sets. It is important to note that the DER resource constraint (number of available DERs) significantly affects the post-damage system performance of the DN. Furthermore, a subset of DERs are mobile, which suggests that they can be re-allocated after the hurricane passes as needed.

DN Restoration Model (Stage II): After the hurricane has passed, the system operator makes decisions regarding DN restoration over a multi-period horizon given by $k = 1, \cdots, \mathrm{K}$. Crucially, the Stage II problem relies on an estimate of the total number of time periods needed for full recovery, which we discuss in our modeling formulation. The first set of restoration decisions pertain to repairs of damaged infrastructural assets in the DN. For the purposes of this work, we focus on damaged distribution lines, which connect the various nodes in the DN. The second set of restoration decisions pertain to re-allocation of movable DERs in the DN, in order to more optimally supply loads when line repairs permit increased connectivity between the loads and available DERs. The system operator can also develop new sites as necessary, to which the movable DERs can be re-allocated.

Microgrid Model with Multi-Master DER Operation (Stage II): At each period, the system operator must decide how to optimally supply power within the islanded mi-

crogrids that form as a result of hurricane damage, DER placement, and period-wise repairs. We formulate a microgrid model that permits multi-master DER operation, in which multiple simultaneously share the responsibility of providing voltage and/or frequency regulation in a single microgrid. This model considers DER dispatch, load disconnection due to violation of physical constraints (i.e., voltage bounds), and power flow. In particular, we also utilize a novel model of linear power flow (*LinDistFlow*) for a microgrid island with parallel operation of multiple DER inverters [90].

Solution Approach and Algorithms:

The two-stage stochastic mixed-integer program (SMIP2) is computationally challenging to solve, because the problem size increases at a superlinear rate with respect to the network size and resource constraints. Firstly, the number of possible damage scenarios increases exponentially with the network size, which renders simple enumeration of scenarios infeasible when the network size is sufficiently large. To handle this issue, we use the sample average approximation (SAA) method [2] to solve (SMIP2).

Secondly, the number of feasible DER allocations increases exponentially with the number of available DERs. Hence it is inefficient to solve (SMIP2) by calculating the total cost under every feasible allocation. In our work, we propose more efficient approaches based on L-shaped Benders decomposition (LBD), which is widely applied to solve two-stage stochastic programs. LBD typically alternates between a master problem and sub-problem(s) at each iteration. More specifically, at a given iteration, the master problem outputs a feasible DER allocation that is then used as input to solve the sub-problem(s). The sub-problem solution(s) at each iteration would be used to generate optimality (Benders) cut(s) that are added back to the master problem. The algorithm converges when a defined convergence criterion is met or the master problem is rendered infeasible by the cuts (i.e., all DER allocations have been eliminated from the feasible set).

In the formulation of LBD-based solution approaches, we identified three main challenges related to implementation and scalability. First, LBD is typically applicable when the recourse (Stage II) problem is convex, but the Stage II mixed-integer

linear programs in (SMIP2) are discontinuous and non-convex. Second, the number of integer variables in the Stage II problems increases quadratically with the network size, which poses a scalability challenge. These two challenges complicate the process of efficiently solving the Stage II problems. Third, LBD convergence could be slow (as measured by number of iterations).

We now proceed to discuss contributions related to our three formulated approaches: LBD-Greedy, LBD-DIC, and NBD. In our discussion, we focus on the LBD challenges identified above.

L-shaped Benders Decomposition with Greedy Approach (LBD-Greedy): The first feature of this method, which motivates the method's name, is the "greedy approach" we employ to solve the Stage II recourse problems. In the greedy approach, we obtain a greedy solution to the recourse problem using a period-wise decomposition. This greedy solution is used to decrease the computational time needed to solve the recourse problem by serving as a warm start. The second feature is a two-step process to obtain the Benders cut at each iteration. More specifically, for each recourse problem, we solve the MILP and then fix the integer variables in order to solve the resultant linear program. The algorithm terminates when the Benders cuts render the master problem infeasible. We demonstrate that LBD-Greedy is more efficient in solving (SMIP2) than simple enumeration of all feasible DER allocations. However, despite our usage of the greedy approach, the recourse problems are MILPs and still expensive to solve when we increase the network size.

L-shaped Benders Decomposition with Dual Integer Cuts (LBD-DIC): This method involves solving linear program (LP) relaxations to the Stage II recourse problems, in order to form the Benders cuts at each iteration. Because we do not solve the full Stage II MILPs, there is gap in the estimated recourse objectives given by the LP relaxation and the full MILP. To address this limitation, we formulate a "dual integer cut", an optimality cut formed by leveraging values of Stage II integer variables that estimated using the properties in our model formulation. The algorithm terminates when the difference between the lower bound (estimated using solutions to the master problem) and a defined "relaxation" upper bound is sufficiently small. While solving

LP relaxations to the Stage II MILPs is more efficient than solving the full MILPs, the convergence of LBD-DIC can still be slow when the number of available DERs is large.

Nested Benders Decomposition (NBD) is similar to LBD-DIC, with the exception that a "nested" approach is employed to solve the Stage II recourse problems. In the nested approach, we decompose the recourse problem by period. We obtain a feasible solution to the recourse problem by solving the period-wise problems from first to last period ("forward pass"). Then, we solve the period-wise problems from last to first period ("backward pass"). The solutions to the backward pass are used to form the Benders cuts in the master problem. Importantly, the backward pass solutions provide cost-to-go approximations, which are lower bound estimates of the costs associated with each scenario-wise Stage II recourse problem. We demonstrate that the cost-to-go approximations strengthen the Benders cuts and typically ensure faster algorithm convergence, as compared to LBD-DIC.

1.5 Thesis Outline

The rest of the thesis is organized as follows. Chapter 2 introduces the asymmetric wind field model and associated parameter estimation method, which are applicable to forecasting and ensemble simulation. Chapter 3 introduces our modeling approach for probabilistic damage estimation in infrastructure systems. Importantly, we analyze the effect of forecast uncertainty and spatial variability on the damage estimates, and apply the approach to outage estimation in electric power infrastructure. In Chapter 4, we formulate the two-stage stochastic optimization problem (SMIP2) for resource allocation in electricity distribution networks, to minimize the cost of hurricane-induced damage. Chapter 5 discusses solution approaches based on L-shaped Benders decomposition to efficiently solve (SMIP2). In Chapter 6, we conclude the thesis by summarizing the contributions and introducing several future directions.

Chapter 2

Modeling of Asymmetric Hurricane Surface Wind Fields

Hurricane risk assessment typically involves modeling of storm tracks, wind fields, and occurrence frequency [111]. A common approach to risk assessment is to simulate an ensemble of storms, in order to capture the stochastic nature of hurricane arrival, landfall location, and intensity. This simulation-based approach relies on capturing two aspects of hurricane structure: (1) *track*, or trajectory of the storm from its formation over the ocean to dissipation over land; and (2) *wind velocities* at various points along the track, modeled by either a single intensity measurement (e.g., maximum sustained 10 m wind speed) or a surface wind field. For risk assessment of large-scale infrastructure systems, the impact of spatially heterogeneous wind velocities must be suitably captured. Thus, a reliable model of the whole surface wind field is desirable.

This section focuses on constructing a physically-informed model of the hurricane gradient wind field; one can then use a boundary layer model for the gradient-to-surface wind conversion. Well-known gradient wind field models are estimated from deterministic axisymmetric models, which we refer to as mean field (MF) models. In reality, however, hurricane wind fields tend to be asymmetric. Not accounting for this inherent asymmetry can negatively affect hurricane risk assessment of aboveground infrastructure components such as electric distribution lines, whose failure probabil-

ities depend on local surface wind intensities [118, 3]. We formulate an asymmetric wind field model that is an extension of the mean field model of Holland et al., 2010 [48] in that the model's maximum intensity parameter is set to be a harmonic function of the azimuthal angle.

The work detailed in this chapter has been published in [15]. In Section 2.1, we provide a full model description. In Section 2.2, we discuss our model parameter estimation approach based on a Constrained Nonlinear Least Squares (CNLS) formulation. In Section 2.3, we present the setup for estimation and evaluation of the asymmetric wind field model, using multiple sources of hurricane wind data. In Section 2.4, we discuss the performance of this model, and highlight some observations about the relationship between asymmetries and environmental inputs. In Section 2.5, we briefly discuss how the model can be useful in wind field simulation along tracks in a statistically-generated ensemble. Section 2.6 summarizes the results and proposes future directions of study.

2.1 Hurricane Wind Field Model

2.1.1 Mean field model

Given a simulated track produced from a track generation model, the Holland et al., 2010 model [48] can be used to estimate the mean tangential wind at points along the track:

$$v(r) = \mathrm{V_m}\left(\left(\frac{\mathrm{R_m}}{r}\right)^{\mathrm{B}} \exp\left(1 - \left(\frac{\mathrm{R_m}}{r}\right)^{\mathrm{B}}\right)\right)^{\mathrm{S}(r)} \tag{2.1}$$

where

$$\mathrm{S}(r) = \begin{cases} 0.5, & r \leq \mathrm{R_m} \\ 0.5 + (r - \mathrm{R_m})\frac{\mathrm{S}_n - 0.5}{r_n - \mathrm{R_m}}, & r > \mathrm{R_m}. \end{cases} \tag{2.2}$$

The model relates the gradient wind velocity v (m s^{-1}) to the radial distance from the storm center r (km). Model parameters are: maximum velocity $\mathrm{V_m}$, radius of maximum wind $\mathrm{R_m}$, shape parameter B governing wind decay rate from the storm center, and scaling parameter S to adjust the profile shape. The parameter S is fixed

to 0.5 at radius $r \leq \mathrm{R_m}$ and varies linearly with r for $r > \mathrm{R_m}$. In the function for radius $r > \mathrm{R_m}$, S_n is taken to be the value of S at which the estimated Holland velocity $v(r)$ is equal to a wind velocity observation in the storm periphery at radius r_n.

The Holland et al., 2010 model reduces to the original Holland 1980 model [47], when S is fixed as 0.5 at all values of radius r. The original model tends to overestimate the wind's decay with radial distance; thus, it underestimates the wind velocities in the storm's outer regions [114]. The revised 2010 model uses the radially-varying scaling parameter S in order to partially rectify these limitations.

For the purpose of modeling asymmetry in the wind field, we empirically estimate the mean field parameters for each snapshot. A snapshot is a depiction of the hurricane wind field at a point in time. We estimate the maximum wind intensity $\mathrm{V_m}$ by averaging the velocity data points in the vicinity of the radius of maximum winds $\mathrm{R_m}$ (i.e., $0.9\mathrm{R_m}$-$1.2\mathrm{R_m}$). Consequently, $\mathrm{V_m}$ is effectively the azimuthally-averaged maximum intensity. The parameter $\mathrm{R_m}$ for each snapshot is taken to be the value of radius r at which the maximum velocity in the snapshot occurs. Then, the remaining parameters B and S in Eq. 2.1 are chosen for each snapshot to best fit the data. In particular, we search over discrete values of B in the range 0.5-4; for each value of B, we take r_n to be the maximum r in the snapshot, and obtain S as a function of r using Equation 2.2. The B and S that minimize the absolute difference between the snapshot wind data and the Holland model estimates are chosen as the empirical model parameters for that snapshot. We note that while [47] suggests that B be selected from the range of 1-2.5, we consider a wider range of B to ensure that the estimated mean field best fits the data. Hereafter, the empirically-estimated maximum intensity parameter for the mean field is referred to as $\bar{\mathrm{V}}_\mathrm{m}$, whereas $\mathrm{V_m}$ refers to the maximum intensity as a function of azimuth, i.e., the asymmetry model discussed in Section 2.1.2.

2.1.2 Asymmetry model

Before presenting our asymmetry model based on the Holland mean field model, we first summarize some of the previous approaches to model asymmetry in wind fields.

One way to account for the asymmetry is by setting R_m in the Holland model to be a polynomial function of the azimuthal angle [115]. This approach is shown to produce more accurate real-time forecasts than mean field models. Estimation of the function parameters requires forecasted values of storm wind velocities (radial extent of 34-, 50-, and 64-knot winds), which can be obtained from the National Hurricane Center (NHC) tropical cyclone forecasts. However, such detailed information on wind velocities is not available as input in simulation applications; thus the approach by [115] is not applicable for simulation of a representative wind field ensemble. A more closely-related work is by [100] – hereafter referred to as U14 – who model asymmetry by representing V_m as an azimuthally-varying harmonic function. Specifically in U14, V_m is parameterized by the wavenumber-0 mean field maximum velocity, and the wavenumber-1 asymmetric amplitude and phase. Then, the linear relationships between the wavenumber-1 parameters (amplitude and phase) and environmental inputs (storm translation speed and wind shear) at R_m are estimated. It is well-recognized that the main environmental inputs contributing to asymmetry are storm translation and wind shear [89].

We represent V_m as a harmonic function in which the amplitude(s) and phase(s) are parameterized by storm translation V_{tr} and shear V_{sh}, which are available, time-dependent inputs. Hereafter, we add subscripts *tr* for translation and *sh* for wind shear to azimuth λ, amplitude A, and phase ϕ. Specifically, λ_{tr} (resp. λ_{sh}) is the azimuth defined clockwise from the translation (resp. shear) direction, while A_{tr}, ϕ_{tr} (resp. A_{sh}, ϕ_{sh}) define the asymmetry induced by translation (resp. shear). We model the maximum intensity V_m as the following harmonic function:

$$\begin{aligned} V_m(\lambda_{tr}, \lambda_{sh};\ \bar{V}_m, V_{tr}, V_{sh}) = \bar{V}_m &+ A_{tr}(V_{tr}) \cos[\lambda_{tr} - \phi_{tr}(V_{tr})] \\ &+ A_{sh}(V_{sh}) \cos[\lambda_{sh} - \phi_{sh}(V_{sh})], \end{aligned} \tag{2.3}$$

to express the maximum intensity as a function of the variables (azimuths λ_{tr} and λ_{sh}) and model inputs ($\bar{\text{V}}_{\text{m}}$, V_{tr}, and V_{sh}). The parameter $\bar{\text{V}}_{\text{m}}$, which is the estimated maximum intensity in the mean field model, is the wavenumber-0 component in the formulation.

In Eq. 2.3, the amplitudes and phases of the asymmetries are modeled as affine functions of translation and shear:

$$\text{A}_{\text{tr}}(\text{V}_{\text{tr}}) = x^{(0)}_{\text{tr,A}} + x^{(1)}_{\text{tr,A}}\text{V}_{\text{tr}} \tag{2.4a}$$

$$\phi_{\text{tr}}(\text{V}_{\text{tr}}) = x^{(0)}_{\text{tr},\phi} + x^{(1)}_{\text{tr},\phi}\text{V}_{\text{tr}} \tag{2.4b}$$

$$\text{A}_{\text{sh}}(\text{V}_{\text{sh}}) = x^{(0)}_{\text{sh,A}} + x^{(1)}_{\text{sh,A}}\text{V}_{\text{sh}} \tag{2.4c}$$

$$\phi_{\text{sh}}(\text{V}_{\text{sh}}) = x^{(0)}_{\text{sh},\phi} + x^{(1)}_{\text{sh},\phi}\text{V}_{\text{sh.}} \tag{2.4d}$$

The values of the estimated amplitudes are constrained to be strictly non-negative:

$$\text{A}_{\text{tr}}(\text{V}_{\text{tr}}) \geq 0;\ \text{A}_{\text{sh}}(\text{V}_{\text{sh}}) \geq 0, \tag{2.5}$$

where $\text{A}_{\text{tr}}(\text{V}_{\text{tr}})$ and $\text{A}_{\text{sh}}(\text{V}_{\text{sh}})$ are given by Eq. 2.4a (resp. Eq. 2.4c). Furthermore, the values of the estimated phases are constrained to be within a range that spans 2π:

$$\text{b}_{\phi,\text{tr}} \leq \phi_{\text{tr}}(\text{V}_{\text{tr}}) \leq \text{b}_{\phi,\text{tr}} + 2\pi; \quad \text{b}_{\phi,\text{sh}} \leq \phi_{\text{sh}}(\text{V}_{\text{sh}}) \leq \text{b}_{\phi,\text{sh}} + 2\pi, \tag{2.6}$$

where $\phi_{\text{tr}}(\text{V}_{\text{tr}})$ and $\phi_{\text{sh}}(\text{V}_{\text{sh}})$ are given by Eq. 2.4b (resp. Eq. 2.4d). The parameters $\text{b}_{\phi,\text{tr}}$ and $\text{b}_{\phi,\text{sh}}$ are the lower bounds of the ranges for translation (resp. shear); thus the respective ranges for the phases are $[\text{b}_{\phi,\text{tr}}, \text{b}_{\phi,\text{tr}} + 2\pi]$ and $[\text{b}_{\phi,\text{sh}}, \text{b}_{\phi,\text{sh}} + 2\pi]$.

In summary, the complete wind field model is defined by the mean field model (Eq. 2.1-2.2), the asymmetry model (Eq. 2.3-2.4), and the constraints (Eq. 2.5-2.6). The asymmetry model involves a total of 8 unknowns (parameters) – 4 to capture translation effects and 4 to capture shear effects.

Another way to account for the effect of translation would be to add the storm translation vector to the wind field [85, 107]. The maximum velocity under equal radius when the storm translation vector is added to the mean field occurs at exactly 90°

clockwise of the translation direction, where the storm motion and cyclostrophic wind direction are aligned. However, U14 found that if the translation-induced asymmetry is modeled as a wavenumber-1 component, the azimuth corresponding to the maximum velocity (i.e., phase ϕ_{tr}) varies linearly with translation speed. To ensure that the model-estimated and observationally-based asymmetries are aligned, we model the asymmetry owing to translation as a wavenumber-1 component with tunable parameters $\mathbf{x}_{\text{tr}}$. In Section 2.1.3, we discuss how our asymmetry model is extended to include the translation vector in addition to wavenumber-1 asymmetries.

2.1.3 Combined wind field model

To present the combined mean field and asymmetry model, we denote the 8 unknowns (parameters) in Section 2.1.2 as $\mathbf{x}_{\text{tr}} = (x^{(0)}_{\text{tr,A}}, x^{(1)}_{\text{tr,A}}, x^{(0)}_{\text{tr},\phi}, x^{(1)}_{\text{tr},\phi})$ and $\mathbf{x}_{\text{sh}} = (x^{(0)}_{\text{sh,A}}, x^{(1)}_{\text{sh,A}}, x^{(0)}_{\text{sh},\phi}, x^{(1)}_{\text{sh},\phi})$. The full vector of unknowns is denoted as $\mathbf{x} = (\mathbf{x}_{\text{tr}}, \mathbf{x}_{\text{sh}})$.

We can re-write the combined wind field model as a function of the unknowns $\mathbf{x}$, variables (radial distance r as well as azimuthal angles λ_{tr} and λ_{sh}), and input parameters to the mean field and asymmetry models. In the mean field model, velocity v was expressed as a function of the radius r (Eq. 2.1-2.2) and parameterized by empirically-estimated Holland parameters $\bar{\text{V}}_{\text{m}}$, R_{m}, B, and $\text{S}(r)$. Furthermore, in the asymmetry model, the maximum intensity parameter V_{m} in Eq. 2.1 was expressed as a function of azimuths λ_{tr} and λ_{sh}, and parameterized by translation V_{tr}, wind shear V_{sh}, and the input parameter $\bar{\text{V}}_{\text{m}}$ (Eq. 2.3-2.4). To summarize, the mean field is affected by the radius r and Holland parameters $\mathbf{S}(r) = (\text{R}_{\text{m}}, \text{B}, \text{S}(r))$; and the asymmetry model is affected by the azimuthal angles $\boldsymbol{\lambda} = (\lambda_{\text{tr}}, \lambda_{\text{sh}})$, Holland parameter $\bar{\text{V}}_{\text{m}}$, and environmental inputs $\mathbf{u} = (\text{V}_{\text{tr}}, \text{V}_{\text{sh}})$.

With a slight abuse of notation, we use $v(r, \boldsymbol{\lambda};\ \mathbf{S}(r), \bar{\text{V}}_{\text{m}}, \mathbf{u};\ \mathbf{x})$ to refer to the velocity function. We use this notation to emphasize that the velocity is a function of variables r and $\boldsymbol{\lambda}$; model inputs $\mathbf{S}(r)$, $\bar{\text{V}}_{\text{m}}$, and $\mathbf{u}$; and unknown parameters $\mathbf{x}$. Then, we can write:

$$v(r, \boldsymbol{\lambda};\ \mathbf{S}(r), \bar{\text{V}}_{\text{m}}, \mathbf{u};\ \mathbf{x}) \ = \ \text{V}_{\text{m}}(\boldsymbol{\lambda};\ \bar{\text{V}}_{\text{m}}, \mathbf{u};\ \mathbf{x})\ \text{Y}(r;\ \mathbf{S}(r)) \tag{2.7}$$

where

$$\begin{aligned} \mathrm{V_m}(\boldsymbol{\lambda};\ \bar{\mathrm{V}}_\mathrm{m}, \mathbf{u};\ \mathbf{x}) \ =\ \bar{\mathrm{V}}_\mathrm{m} \ +\ \mathrm{A_{tr}}(\mathrm{V_{tr}};\ \mathbf{x}_{\mathrm{tr,A}})\ \cos[\lambda_\mathrm{tr} - \phi_\mathrm{tr}(\mathrm{V_{tr}};\ \mathbf{x}_{\mathrm{tr},\phi})] + \\ \mathrm{A_{sh}}(\mathrm{V_{sh}};\ \mathbf{x}_{\mathrm{sh,A}})\ \cos[\lambda_\mathrm{sh} - \phi_\mathrm{sh}(\mathrm{V_{sh}};\ \mathbf{x}_{\mathrm{sh},\phi})], \end{aligned} \tag{2.8a}$$

$$\mathrm{Y}(r;\ \mathbf{S}(r)) \ =\ \left(\left(\frac{\mathrm{R_m}}{r}\right)^{\mathrm{B}} \exp\left(1 - \left(\frac{\mathrm{R_m}}{r}\right)^{\mathrm{B}}\right)\right)^{\mathrm{S}(r)}. \tag{2.8b}$$

Here, $\mathbf{x}_{\mathrm{tr,A}} = (x^{(0)}_{\mathrm{tr,A}}, x^{(1)}_{\mathrm{tr,A}})$, $\mathbf{x}_{\mathrm{tr},\phi} = (x^{(0)}_{\mathrm{tr},\phi}, x^{(1)}_{\mathrm{tr},\phi})$, $\mathbf{x}_{\mathrm{sh,A}} = (x^{(0)}_{\mathrm{sh,A}}, x^{(1)}_{\mathrm{sh,A}})$, and $\mathbf{x}_{\mathrm{sh},\phi} = (x^{(0)}_{\mathrm{sh},\phi}, x^{(1)}_{\mathrm{sh},\phi})$. Equation 2.7 can be rewritten as follows, to express the wind field model as the sum of the mean field winds and the asymmetries owing to translation and shear:

$$\begin{aligned} v(r,\boldsymbol{\lambda};\ \mathbf{S}(r), \bar{\mathrm{V}}_\mathrm{m}, \mathbf{u};\ \mathbf{x}) \ =\ \mathrm{V_{MF}} + \mathrm{V_{m,tr}}(\lambda_\mathrm{tr};\ \mathrm{V_{tr}};\ \mathbf{x}_\mathrm{tr})\ \mathrm{Y}(r;\ \mathbf{S}(r)) \\ + \mathrm{V_{m,sh}}(\lambda_\mathrm{sh};\ \mathrm{V_{sh}};\ \mathbf{x}_\mathrm{sh})\ \mathrm{Y}(r;\ \mathbf{S}(r)) \end{aligned} \tag{2.9}$$

where

$$\mathrm{V_{MF}} \ =\ \bar{\mathrm{V}}_\mathrm{m}\ \mathrm{Y}(r;\ \mathbf{S}(r)) \tag{2.10a}$$

$$\mathrm{V_{m,tr}}(\lambda_\mathrm{tr};\ \mathrm{V_{tr}};\ \mathbf{x}_\mathrm{tr}) \ =\ \mathrm{A_{tr}}(\mathrm{V_{tr}};\ \mathbf{x}_{\mathrm{tr,A}})\ \cos[\lambda_\mathrm{tr} - \phi_\mathrm{tr}(\mathrm{V_{tr}};\ \mathbf{x}_{\mathrm{tr},\phi})] \tag{2.10b}$$

$$\mathrm{V_{m,sh}}(\lambda_\mathrm{sh};\ \mathrm{V_{sh}};\ \mathbf{x}_\mathrm{sh}) \ =\ \mathrm{A_{sh}}(\mathrm{V_{sh}};\ \mathbf{x}_{\mathrm{sh,A}})\ \cos[\lambda_\mathrm{sh} - \phi_\mathrm{sh}(\mathrm{V_{sh}};\ \mathbf{x}_{\mathrm{sh},\phi})]. \tag{2.10c}$$

Here, $\mathrm{V_{MF}}$ denotes the mean field, $\mathrm{V_{m,tr}}(\lambda_\mathrm{tr};\ \mathrm{V_{tr}};\ \mathbf{x}_\mathrm{tr})$ the asymmetry owing to translation, and $\mathrm{V_{m,sh}}(\lambda_\mathrm{sh};\ \mathrm{V_{sh}};\ \mathbf{x}_\mathrm{sh})$ the asymmetry owing to shear. The estimated wind field velocities are one-minute sustained winds.

To obtain a simpler wind field model that considers only asymmetry owing to the translation vector, one can just perform vector addition of the mean field and translation vector. The resultant asymmetric winds are referred to as $\mathrm{V_{MF+TV}}$.[1] To obtain a model that considers both the translation vector and wavenumber-1 asymmetries, the terms $\mathrm{V_{m,tr}}(\lambda_\mathrm{tr};\ \mathrm{V_{tr}};\ \mathbf{x}_\mathrm{tr})\mathrm{Y}(r;\ \mathbf{S}(r))$ and $\mathrm{V_{m,sh}}(\lambda_\mathrm{sh};\ \mathrm{V_{sh}};\ \mathbf{x}_\mathrm{sh})\mathrm{Y}(r;\ \mathbf{S}(r))$ are added to $\mathrm{V_{MF+TV}}$. In Section 2.4, we evaluate the effects of wavenumber-1 asymmetries and

[1]The velocities $\mathrm{V_{MF+TV}}$ are dependent on the storm translation magnitude $\mathrm{V_{tr}}$ and direction θ_{tr}, in addition to $\bar{\mathrm{V}}_\mathrm{m}$, r, $\mathbf{S}(r)$, and the azimuthal angle.

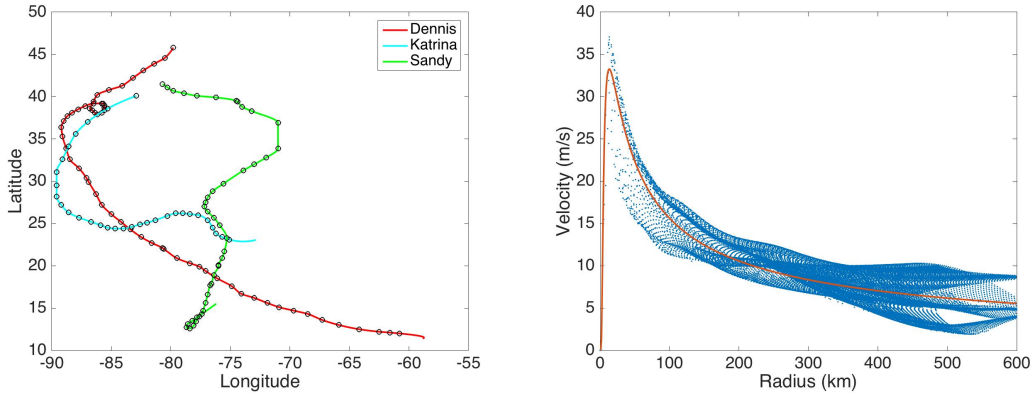

Figure 2-1: Examples of hurricane tracks, interpolated using HURDAT data (*left*). An example of HWind velocity data (blue) from one snapshot and a best-fit Holland mean field estimate (red) as a function of radius.

the translation vector on the model performance.

2.1.4 Data

We use data on hurricane tracks and wind field snapshots for parameter estimation (see Figure 2-1 for plots of example tracks and snapshots). The National Hurricane Centers HURricane DATabases (HURDAT-2) is used for track locations of past storms [56], which provide data every six hours on the storm's location and maximum sustained wind speed. The wind field data include: (1) the Hurricane Research Division HWind radial structure database [82]; and (2) output from the Pennsylvania State University (PSU) Weather Research and Forecasting model (WRF)-based ensemble Kalman filter (EnKF) data assimilation system [112]. These data sets contain surface ($\sim$10m) wind velocity estimates obtained by processing direct observations through statistical models, data assimilation, and objective analyses. Although we use surface wind field data to estimate parameters of a gradient wind field model, [84] showed that the speed of surface winds is the same as that of the gradient wind in an axisymmetric, steady-state storm over the sea.

A subset of the wind field data is used for estimation of the asymmetric wind field model parameters, and the resulting model is evaluated by comparing to the remaining data. Only HWind snapshots were used for estimating model parameters. HWind

snapshots are one-minute sustained winds, derived by assimilation and processing of in-situ and remotely-sensed observations. The snapshots are given at a typical interval of 3 hours and horizontal grid spacing of 6 km. Naturally, one would expect that the estimated parameters and asymmetry model are affected by the HWind data's inherent biases and variability. Total variability among observations at a particular radius ranges from 7% near the eyewall to about 15% in storm outer regions. There is a roughly 10% positive bias in wind speeds around the eyewall, and this bias decreases with r [27].

Both HWind and WRF data are used for evaluation of the estimated wind field model, mainly because WRF data are only available for two of the storms studied here (Katrina and Sandy) and thus not sufficient for parameter estimation. The WRF snapshots are instantaneous wind estimates produced by assimilating observations (e.g., airborne Doppler radar velocity data) into the convection-permitting WRF EnKF analysis. These snapshots are more fine-grained than HWind snapshots, occur at an interval of 30 minutes (Sandy) or 1 hour (Katrina), and have horizontal grid spacing of around 3 km over an approximately 1700×1700 km region (Katrina) or 900×900 km region (Sandy). The intensity of simulated WRF storms is sensitive to the model's air-sea surface flux parameterization scheme [42]. In addition, WRF data for an ensemble of storms display large forecast track divergence due to uncertainties in environmental flow [73]. These sensitivities affect the comparative model performance of WRF and HWind data, which is reported in Section 5c. We converted the WRF data to one-minute sustained winds following Equation 1 from [54].

2.2 Parameter Estimation

This section details the constrained nonlinear least squares (CNLS) optimization problem for parameter estimation of the asymmetric wind field model. The goal of a standard CNLS problem is to select unknown parameters $\mathbf{x}$ that minimize an objective function $f(\mathbf{x})$ while also satisfying predefined constraints that capture allowable bounds on the parameters. Specifically, $f(\mathbf{x}) = \frac{1}{2}\sum_{i=1}^{\mathrm{N}} e_i^2(\mathbf{x})$ for N data points, where

$e_i(\mathbf{x})$ is the residual at data point i. Commonly-used optimization solvers rely on the gradient and Hessian of the objective function to iteratively obtain estimates of the parameters until the objective function is minimized or the number of iterations is exceeded. The objective, gradient, and Hessian for a CNLS problem with unknown vector $\mathbf{x}$ of length M are expressed as:

$$\begin{aligned} f(\mathbf{x}) &= \frac{1}{2}\sum_{i=1}^{\mathrm{N}} e_i^2(\mathbf{x}) \\ \nabla f(\mathbf{x}) &= J(\mathbf{x})^\top e(\mathbf{x}) \\ \nabla^2 f(\mathbf{x}) &= J(\mathbf{x})^\top J(\mathbf{x}) + \sum_{i=1}^{\mathrm{N}} e_i(\mathbf{x})\nabla^2 e_i(\mathbf{x}) \end{aligned} \tag{2.11}$$

where the N × M matrix $J(\mathbf{x})$ is the Jacobian, whose terms are derivatives of the residuals with respect to $\mathbf{x}$. In general, one can express the equality and inequality constraints as follows:

$$\begin{aligned} g_k(\mathbf{x}) &= c_k, \quad k = \{1, ..., K\} \\ h_l(\mathbf{x}) &\geq d_l, \quad l = \{1, ..., L\}, \end{aligned} \tag{2.12}$$

where $g_k(\cdot)$ and $h_l(\cdot)$ are linear functions of $\mathbf{x}$, while c_k and d_l are constants.

We now specify the objective of the CNLS problem for the purpose of estimating the wind field model introduced in Section 2.1. Recall that the unknowns in CNLS are the 8 parameters in Eq. 2.3-2.4. The objective is to minimize the sum of squared residuals. For the i-th data point, the residual between the observed velocity v_i and model-estimated velocity $\hat{v}_i$ is $e_i(\mathbf{x}) = v_i - \hat{v}_i$, in which $\hat{v}_i$ is assigned the value of the velocity function (Eq. 2.7 or 2.9) evaluated for the i-th data point. Note that we replace v_{MF} with $v_{\mathrm{MF+TV}}$ if the translation vector is included in the model. Henceforth, t denotes a snapshot and $t(i)$ the snapshot index corresponding to data point i. Consider that there are T snapshots and N_t velocity measurements per snapshot t. Thus, the total number of data points N is given by $\sum_t \mathrm{N}_t$. The CNLS

problem for estimating the optimal parameter vector is written as:

$$\underset{\mathbf{x}}{\text{Minimize}}\ f(\mathbf{x}) = \frac{1}{2}\sum_{i=1}^{\mathrm{N}} e_i^2(\mathbf{x}) = \frac{1}{2}\sum_{i=1}^{\mathrm{N}} \Big(v_i - \hat{v}_i(r_i, \boldsymbol{\lambda}_i;\ \mathbf{S}_i(r_i), \bar{\mathrm{V}}_{\mathrm{m},t(i)}, \mathbf{u}_{t(i)};\ \mathbf{x})\Big)^2, \tag{2.13}$$

subject to the constraints given by Eq. 2.5-2.6 for each snapshot t, which restrict the range of allowable values that the unknown parameters $\mathbf{x}$ may take. The indices of data points are dropped hereafter for notational simplicity. While we consider the Holland mean field model here due to its relative simplicity, the proposed CNLS formulation can be adapted to other mean field models.

Parameter estimates are obtained using the MATLAB interior point constrained nonlinear solver, which takes an initial parameter vector $\mathbf{x}$ and iteratively updates it to minimize the objective. We use the following `fmincon` options: interior-point algorithm, user-supplied gradient and Hessian, and maximum number of iterations set to 100.[2] See Section 2.7 (Appendix A) for the gradient and Hessian derivations that are supplied to the solver.

2.3 Experimental Design

This section covers data preparation, CNLS parameter estimation, and model evaluation.

2.3.1 Preparation of data

Storm track and wind field data are required for estimation of the wind field model (see Section 22.1.4). This study uses HURDAT tracks from Hurricanes Andrew (1992), Isabel (2003), Dennis (2005), Katrina (2005), Wilma (2005), Irene (2011), Isaac (2012), Sandy (2012), and Ingrid (2013). HWind data are obtained for all storms and WRF data for Katrina and Sandy, to represent the wind field. The Sandy WRF data used here are 10 members of the 60-member ensemble forecast [73]. All 10 ensemble members had relatively accurate landfall locations (track error of 233.8 km averaged over

[2]Further details regarding the interior point algorithm can be found in [75].

a time window of 6 hours before and after landing). The Katrina WRF data used are from a single ensemble member [42], as other WRF simulations of Katrina were run on different air-sea flux parameterization schemes. In total, two Katrina 'storms' (one HWind and one WRF) and 11 Sandy 'storms' (one HWind and 10 WRF) are used in this study. As a proxy for excluding times at which storms have undergone extratropical transition, snapshots at a latitude greater than 35°N are not included in the data set.

The wind shear for all snapshots is calculated using Global Forecast System (GFS) operational analyses, which are given at $\sim 1^\circ$ resolution. The first step in calculating the wind shear is to subtract an estimate of the hurricane vortex streamfunction [40] from the GFS wind field, in order to isolate the environmental winds. Then, the mean environmental winds at heights of 850 and 250 hPa are calculated by averaging over a 200 km radius around the storm center, and the 850-250-hPa-wind shear vector (magnitude V_{sh} and direction θ_{sh}) is obtained by vector subtraction of the two means. We use the GFS analyses because these data provide a more fine-grained estimation of the wind shear. However, for comparison purposes, we discuss model performance using wind shear from both the GFS analyses and Statistical Hurricane Intensity Prediction Scheme (SHIPS) database [26] in Section 2.4.

Next, we interpolate the HURDAT track positions to half-hour intervals using a Piecewise Cubic Hermite Interpolating Polynomial (PCHIP) [18]. The storm translation vector (magnitude V_{tr} and direction θ_{tr}) is calculated using the interpolated storm center positions. Then, the wind shear vector is interpolated to half-hour intervals using PCHIP. The interpolated V_{tr} and V_{sh} are used as inputs to the CNLS problem.

Then, velocity data are locally averaged, because there are more data points at larger values of radius r in both HWind and WRF snapshots. To prepare for local averaging, the azimuths λ_{tr} and λ_{sh} are calculated for all data points as angles clockwise from θ_{tr} and θ_{sh}, respectively. Then, velocity data from each snapshot are binned in $r - \lambda_{tr}$ space, and the velocity data in each bin are averaged. These locally-averaged velocities v ($\sim$800-900 per snapshot), as well as the radii r and azimuths λ_{tr} and λ_{sh}

corresponding to the bins, are used as inputs to CNLS. As a result of local averaging, the velocity inputs to CNLS are equally distributed across the entire range of r. The final step is to estimate the Holland parameters $\mathbf{S}(r)$ and $\bar{\mathrm{V}}_{\mathrm{m}}$.

A remaining issue to address is that the asymmetry varies radially, but the amplitudes and phases in Equation 2.3 are not parameterized by radius r. It is difficult to model amplitudes and phases as a function of r using simple parametric forms. Instead, we only use velocities corresponding to radii less than a cut-off radius $\mathrm{R}_{\mathrm{cut}}$ as input for parameter estimation and evaluation, removing the need to parameterize asymmetry as a function of r. The radius $\mathrm{R}_{\mathrm{cut}}$ is defined as $\max(\min(r_{15}, 300), \min(r_{0.75\bar{\mathrm{V}}_{\mathrm{m}}}, 300))$ where r_{15} denotes the radius at which the mean field velocity is 15 m s^{-1} and $r_{0.75\bar{\mathrm{V}}_{\mathrm{m}}}$ denotes the radius at which the mean field velocity is $0.75\bar{\mathrm{V}}_{\mathrm{m}}$. The radius r_{15} is a conservative practical cut-off for hurricane risk analysis of above-ground infrastructure components, such as overhead electricity lines and poles.[3] However, for snapshots with low maximum intensity parameter $\bar{\mathrm{V}}_{\mathrm{m}}$, a cut-off of r_{15} would omit most of the data points in the snapshot. Thus, we also ensure that radial regions of the storm with mean field velocity greater than $0.75\bar{\mathrm{V}}_{\mathrm{m}}$ are included, regardless of whether or not $r_{0.75\bar{\mathrm{V}}_{\mathrm{m}}}$ is greater than r_{15}. Finally, $\mathrm{R}_{\mathrm{cut}}$ is less than 300 km to ensure that peripheral storm regions are not included.

2.3.2 Parameter estimation

Four CNLS-estimated asymmetric models with wavenumber-1 asymmetries are estimated. These asymmetric models are compared to the two benchmark models: mean field and mean field plus translation vector (see Table 2.1 for the complete list of six models considered).

Parameter initializations for solving the CNLS problem are obtained following a two-step approach. First, we empirically estimate the translation- and shear-relative

[3]Specifically, according to a model estimated using historical storm data that includes wind data from hurricanes, tropical depressions, and tropical storms [116], electricity distribution lines are expected to fail at a frequency that increases quadratically with wind speed above 20 m s^{-1} and much less likely to fail below 20 m s^{-1}. Another cut-off value might be appropriate in other contexts, such as thunderstorms or storm surge.

Table 2.1: List of six wind field models evaluated. The asymmetric models are classified as V_{tr} models (consider only translation) or $V_{tr} + V_{sh}$ models (consider both translation and shear). Furthermore, the model names containing the terms 'TV' denote the inclusion of the translation vector and 'WVN-1' the wavenumber-1 component(s) owing to translation and/or shear. The mean field and V_{tr} (TV) models serve as benchmark models; all other models have unknown parameters to be estimated using the CNLS method.

Model	***Translation effects***	***Shear effects***
Mean field	—	—
V_{tr} *models*		
V_{tr} (TV)	Translation vector	—
V_{tr} (WVN-1)	WVN-1	—
V_{tr} (TV+WVN-1)	Trans. vector, WVN-1	—
$V_{tr} + V_{sh}$ *models*		
V_{tr} (TV) + V_{sh} (WVN-1)	Translation vector	WVN-1
V_{tr} (TV+WVN-1) + V_{sh} (WVN-1)	Trans. vector, WVN-1	WVN-1

wavenumber-1 amplitude and phase at the radius of maximum winds for each snapshot. Then we simply use the unconstrained least squares method to estimate $\mathbf{x}$, in which the estimated amplitudes and phases are the inputs. The resulting value of $\mathbf{x}$ is taken as the initial parameter vector for the CNLS problem.

Snapshots from Hurricanes Andrew, Dennis, Ingrid, Isaac, Sandy and Wilma (all HWind data) are used to train the models. In addition, a few storms are set aside as held-out test data for evaluation of the models: Irene (HWind), Isabel (HWind), Katrina (HWind, WRF), and Sandy (HWind, WRF). The training-test split of the data is made (Table 2.2) so that the selected training storms are heterogeneous in: geographical track coverage (including land coverage), time of occurrence (month and year), and maximum intensity.[4]

[4]Note that HWind snapshots of Hurricane Sandy have been split across the training and test sets. The radial extent of Sandy (HWind) is unusually large at northerly latitudes compared to the other HWind storms studied here, so HWind snapshots of Sandy are split among training and testing data to account for this feature of storm structure in parameter estimation.

Table 2.2: Key characteristics of storms used for training and testing. The latitude range is the range covered by the snapshots, not the actual range traveled by the storm. Maximum intensity metrics are obtained from HURDAT data and given in knots. All storms use HWind, except for two test storms labeled as WRF.

Training Set	Max. intensity	Latitude range (°N)	Time	No. snapshots
Andrew	150	25.38, 25.64	Aug '92	4
Dennis	130	15.77, 31.15	Jul '05	28
Ingrid	75	19.11, 23.79	Sept '13	12
Isaac	70	14.70, 29.91	Aug-Sept '12	41
Sandy	100	13.58, 39.76	Oct-Nov '12	21
Wilma	160	15.68, 28.51	Oct '05	30
Test Set				
Irene	105	15.08, 41.80	Aug '11	27
Isabel	145	21.30, 33.95	Sept '03	27
Katrina	175	24.30, 25.99	Aug '05	16
Katrina (WRF)	175	24.40, 38.34	Aug '05	120
Sandy	100	13.58, 37.02	Oct-Nov '12	20
Sandy (WRF)	100	24.66, 41.86	Oct-Nov '12	256

2.3.3 Evaluation of model performance

We report three performance metrics as a measure of model performance: cross-validation error (CVE), Bayesian Information Criterion (BIC), and mean squared error (MSE) on the test data.

The cross-validation error is obtained from a k-fold cross-validation procedure. To perform k-fold cross-validation, we partition the set of training snapshots into $k = 5$ subsets (folds). Then, five sets of data are formed, in which each set consists of the training data with one fold of snapshots omitted. For each set of data, we obtain the mean squared error on the omitted fold using the model estimated with the entire training set. The cross-validation error of a model is equal to the mean squared error averaged over the five folds. This process of parameter estimation followed by evaluation on the held-out fold is conducted for each of the six models.

The Bayesian Information Criterion is a metric that rewards a model's goodness of fit, but also includes an overfitting penalty that is an increasing function of the

number of parameters [10] - see Section 2.3.3 (Appendix B) for further details. One can assess the relative likelihoods of two models by using their BIC. Then, the models' MSEs evaluated on the held-out test data are intended to validate the expected model performance suggested by the CVE and BIC.

2.4 Results

This section discusses the CNLS-estimated parameters of the asymmetric wind field models, then compares the performance of the models. See Tables 2.3-2.4 for the CNLS parameter estimates.

Table 2.3: Parameter estimates of the CNLS-estimated models for the wavenumber-1 asymmetry owing to storm translation. The parameters in boldface indicate statistical significance. For models including the effects of shear, parameters are given for GFS ('G') and SHIPS ('S').

Model		$\hat{x}^{(0)}_{\mathrm{tr,A}}$	$\hat{x}^{(1)}_{\mathrm{tr,A}}$	$\hat{x}^{(0)}_{\mathrm{tr},\phi}$	$\hat{x}^{(1)}_{\mathrm{tr},\phi}$
V_{tr} (WVN-1)		$\mathbf{1.17 \pm 0.25}$	$\mathbf{0.40 \pm 0.04}$	$\mathbf{123.9 \pm 4.3}$	$\mathbf{-1.7 \pm 0.5}$
V_{tr} (TV+WVN-1)		$\mathbf{-0.58 \pm 0.23}$	$\mathbf{0.82 \pm 0.03}$	$\mathbf{-126.8 \pm 3.2}$	$\mathbf{2.6 \pm 0.4}$
V_{tr} (TV)	G	—	—	—	—
$+ V_{sh}$ (WVN-1)	S	—	—	—	—
V_{tr} (TV+WVN-1)	G	$\mathbf{-0.59 \pm 0.23}$	$\mathbf{0.82 \pm 0.04}$	$\mathbf{-127.1 \pm 3.2}$	$\mathbf{2.7 \pm 0.4}$
$+ V_{sh}$ (WVN-1)	S	$\mathbf{-0.55 \pm 0.21}$	$\mathbf{0.77 \pm 0.04}$	$\mathbf{-150.8 \pm 4.7}$	$\mathbf{5.8 \pm 0.6}$

2.4.1 Parameter estimates of V_{tr} models

Here, we discuss the parameter estimates of two CNLS-estimated models that incorporate asymmetry owing to translation: V_{tr} (WVN-1) model – asymmetry modeled as the wavenumber-1 (WVN-1) component; and V_{tr} (TV+WVN-1) model – asymmetry modeled as the translation vector (TV) and the wavenumber-1 component. We compare these models to the V_{tr} (TV) benchmark model – asymmetry modeled as only the translation vector added to the mean field.

Table 2.4: Parameter estimates of the CNLS-estimated models for the wavenumber-1 asymmetry owing to wind shear. The parameters in boldface indicate statistical significance. For models including the effects of shear, parameters are given for GFS ('G') and SHIPS ('S').

Model		$\hat{x}^{(j,0)}_{\text{sh,A}}$	$\hat{x}^{(j,1)}_{\text{sh,A}}$	$\hat{x}^{(j,0)}_{\text{sh},\phi}$	$\hat{x}^{(j,1)}_{\text{sh},\phi}$
V_{tr} (WVN-1)		—	—	—	—
V_{tr} (TV+WVN-1)		—	—	—	—
V_{tr} (TV)	G	$\mathbf{1.32 \pm 0.20}$	0.00±0.02	$\mathbf{-148.9 \pm 8.5}$	$\mathbf{10.9 \pm 0.8}$
+ V_{sh} (WVN-1)	S	$\mathbf{1.01 \pm 0.19}$	$\mathbf{-0.03 \pm 0.02}$	-2.3±13.6	$\mathbf{-8.9 \pm 1.9}$
V_{tr} (TV+WVN-1)	G	-0.01±0.18	$\mathbf{0.08 \pm 0.02}$	6.1±22.0	$\mathbf{-9.9 \pm 1.6}$
+ V_{sh} (WVN-1)	S	-0.01±0.17	$\mathbf{0.11 \pm 0.02}$	6.1±12.7	$\mathbf{-8.7 \pm 1.0}$

The parameters $\hat{\mathbf{x}}_{\text{tr}}$ of the V_{tr} (WVN-1) model demonstrate a statistically significant (> 95% confidence) linear relationship between translation speed V_{tr} and both amplitude A_{tr} and phase ϕ_{tr}. The key difference between the V_{tr} (TV) model and the V_{tr} (WVN-1) model is the azimuth corresponding to the maximum intensity. In the V_{tr} (TV) model, the maximum velocity under equal radius occurs at 90° clockwise of the translation direction, as was discussed in Section 2.1. In the V_{tr} (WVN-1 model), the maximum velocity under equal radius occurs slightly clockwise of 90°, because of the hurricane inflow component.

The key difference between our result and U14's result is that we find a significant downwind storm-motion-relative phase rotation with increasing translation speed (i.e., the slope parameter $\hat{x}^{(1)}_{\text{tr},\phi} < 0$). In contrast, U14 find an upwind phase rotation ($\hat{x}^{(1)}_{\text{tr},\phi} > 0$). This discrepancy can be attributed to different parameter estimation methods. U14 use unconstrained least squares to estimate $\mathbf{x}_{\text{tr}}$, in which the inputs are empirically-estimated wavenumber-1 amplitudes and phases at the radius of maximum winds. In contrast, the inputs for CNLS are observed velocities that lie within the cutoff radius R_{cut}. Indeed, we find a significant upwind storm-motion-relative phase rotation with translation speed ($\hat{x}^{(1)}_{\text{tr},\phi} = 3.4°$) when applying U14's procedure.

The parameters of the V_{tr} (TV+WVN-1) model also demonstrate a significant

relationship between translation speed and both amplitude and phase. In this model, the wavenumber-1 parameters $\hat{\mathbf{x}}_{\mathrm{tr}}$ estimate the residual asymmetry owing to translation that remains after the translation vector has been added to the mean field. The phase associated with this residual asymmetry is more than 90° counterclockwise from the translation direction ($\hat{x}^{(0)}_{\mathrm{tr},\phi} = -126.8°$) and rotates upwind with increasing translation speed ($\hat{x}^{(1)}_{\mathrm{tr},\phi} > 0$).

2.4.2 Parameter estimates of $\mathrm{V_{tr}} + \mathrm{V_{sh}}$ models

Two CNLS-estimated models with translation- and shear-induced asymmetries ('$\mathrm{V_{tr}}$+ $\mathrm{V_{sh}}$ models') are discussed here: $\mathrm{V_{tr}}$ (TV) + $\mathrm{V_{sh}}$ (WVN-1) model – asymmetry modeled as the translation vector (TV) and wavenumber-1 component owing to shear; and $\mathrm{V_{tr}}$ (TV+WVN-1) + $\mathrm{V_{sh}}$ (WVN-1) model – asymmetry modeled as the translation vector and wavenumber-1 component owing to both translation and shear. The parameters $\hat{\mathbf{x}}_{\mathrm{sh}}$ of both models demonstrate a significant linear relationship between shear magnitude and both amplitude $\mathrm{A_{sh}}$ and phase ϕ_{sh}.

The phase parameters $\hat{\mathbf{x}}_{\mathrm{sh},\phi}$ estimated using SHIPS data demonstrate that the phase rotates downwind from downshear to left of shear with increasing shear magnitude ($\hat{x}^{(1)}_{\mathrm{sh},\phi} < 0$ for both models). This result is in agreement with that of U14, who also used SHIPS data. However, in contrast to our approach, U14 subtract only the estimated wavenumber-1 asymmetry owing to translation from the storm winds, before estimating the wavenumber-1 asymmetry owing to shear. They did not consider the translation vector because the wind data they used did not provide the wind direction.

The parameters of the $\mathrm{V_{tr}}$ (TV+WVN-1) + $\mathrm{V_{sh}}$ (WVN-1) model using GFS also indicate a downwind rotation of the phase from downshear to left of shear. However, the parameters of the $\mathrm{V_{tr}}$ (TV) + $\mathrm{V_{sh}}$ (WVN-1) model instead indicate that the phase rotates upwind ($\hat{x}^{(1)}_{\mathrm{sh},\phi} > 0$), from upshear left ($-180° < \phi^{(j)}_{\mathrm{sh}} < -90°$) to downshear left ($-90° < \phi^{(j)}_{\mathrm{sh}} < 0°$). A previous study also found that the asymmetry owing to shear tends to be downshear left or upshear left, but they used SHIPS data rather than GFS data [53].

The final key observation is that the wavenumber-1 asymmetry owing to shear is smaller in the V_{tr} (TV+WVN-1) + V_{sh} (WVN-1) model than in the V_{tr} (TV) + V_{sh} (WVN-1) model. In particular, in the V_{tr} (TV+WVN-1) + V_{sh} (WVN-1) model, the intercept term $\hat{x}^{(0)}_{sh,A}$ is not statistically significant and the slope term $\hat{x}^{(1)}_{sh,A} < 0.2$. This result indicates that when both the wavenumber-1 component and translation vector are used to model asymmetry owing to translation, the resultant wavenumber-1 asymmetry owing to shear becomes smaller.

2.4.3 Model performance and selection

Now, we compare the performance of the wind field models listed in Table 2.1. The first performance metric discussed is the cross-validation error (CVE) of the models (see Table 2.5). The models ordered from lowest to highest cross-validation error are: V_{tr} (TV+WVN-1) + V_{sh} (WVN-1), V_{tr} (TV+WVN-1), V_{tr} (TV) + V_{sh} (WVN-1), V_{tr} (TV), V_{tr} (WVN-1), and mean field. Thus, the model with the lowest CVE is the V_{tr} (TV+WVN-1) + V_{sh} (WVN-1) model – asymmetry modeled as the translation vector and wavenumber-1 asymmetries owing to both translation and shear.

Three key observations are evident from the cross-validation results. First, addition of wavenumber-1 asymmetries to the wind field model predictably lowers the cross-validation error by decreasing the variance of the residuals. Second, the benchmark V_{tr} (TV) model has a lower cross-validation error than the V_{tr} (WVN-1) model. The main reason why the V_{tr} (TV) model is better-performing is that its mean residual is 0.9 lower than that of the mean field (indicating a smaller model bias). Third, for the GFS data, the difference in cross-validation error is small when comparing the V_{tr} (TV) + V_{sh} (WVN-1) model to the V_{tr} (TV) model, or the V_{tr} (TV+WVN-1) + V_{sh} (WVN-1) model to the V_{tr} (TV+WVN-1) model. Thus, adding shear-induced asymmetry only marginally decreases the cross-validation error when using the GFS data.

The second metric discussed is the Bayesian information criterion (BIC). A lower BIC indicates a better model. The V_{tr} (TV+WVN-1) + V_{sh} (WVN-1) model has the lowest BIC, followed by the V_{tr} (TV+WVN-1) model. Wind field models with more

Table 2.5: Performance of models measured in terms of cross-validation error (CVE) and mean squared error (MSE) on test storms. The CVE and MSE of models including asymmetry owing to shear are given for GFS ('G') and SHIPS ('S'). The best-performing model under each metric is in boldface. MSE results for Sandy WRF are given as averaged MSE across 10 ensemble members. 'Ir' is Irene, 'Is' is Isabel, 'K' is Katrina, 'S' is Sandy.

Model		CVE	MSE (Test Storms)					
			HWind				WRF	
			Ir	Is	K	S	K	S
Mean field		33.2	33.6	32.9	**8.9**	31.4	**64.7**	65.4
V_{tr} (WVN-1)		29.5	24.0	29.4	10.8	28.7	74.3	**54.2**
V_{tr} (TV)		25.9	23.7	28.4	16.7	32.9	75.3	126.9
V_{tr} (TV+WVN-1)		20.0	25.7	26.2	11.6	25.3	72.1	77.7
V_{tr} (TV)	G	25.7	**23.6**	28.0	18.5	33.2	77.4	124.0
+ V_{sh} (WVN-1)	S	21.4	**15.7**	28.9	17.1	23.6	95.2	92.2
V_{tr} (TV+WVN-1)	G	**19.9**	26.2	**26.1**	11.6	**24.9**	71.0	77.4
+ V_{sh} (WVN-1)	S	**17.2**	16.7	**25.9**	11.4	**16.8**	95.2	90.7

parameters have lower BIC values: as the number of parameters increases, the penalty term for overfitting in the BIC grows at a slower rate compared to the decrease in the objective. The penalty term grows relatively slowly because the number of velocity data points N is much larger than the number of parameters M in our model.[5]

Next, we discuss the performance of the models on the HWind test data as measured by mean squared error (see Table 2.5). The models with the lowest mean squared error under both GFS and SHIPS are: V_{tr} (TV) + V_{sh} (WVN-1) for Irene, V_{tr} (TV+WVN-1) + V_{sh} (WVN-1) for Isabel and Sandy, and the mean field for Katrina. Thus, the best-performing models on all storms except Katrina include asymmetry owing to both translation and shear. Specifically, the V_{tr} (TV+WVN-1) + V_{sh} (WVN-1) model has the lowest mean squared error averaged over the four HWind test storms. Figures 2-2 – 2-3 demonstrate how the mean squared error varies

[5]The wind field estimation error among physically-neighboring locations may be correlated, which results in the 'effective' number of data points being smaller than N.

over time for each storm.

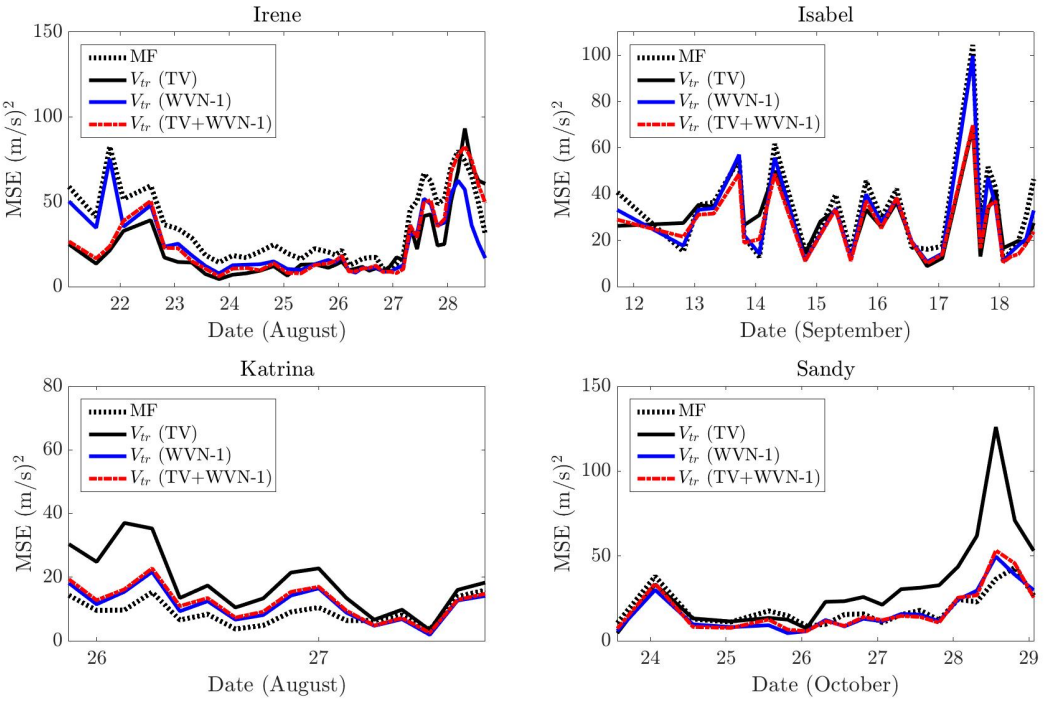

Figure 2-2: Performance of the mean field and V_{tr} models on HWind testing storms, in terms of mean squared error (MSE).

Figures 2-4 – 2-7 compare the CNLS- and empirically-estimated amplitudes and phases at the radius of maximum winds. The figures demonstrate that the mean field is the best for Katrina, because the estimated relationships between the phases and environmental inputs did not accurately estimate the phases of the Katrina snapshots. In addition, the CNLS-estimated amplitudes tend to be smaller than the empirical amplitudes. This is because wavenumber-1 asymmetries at the radius of maximum winds and other radii can differ; thus CNLS-estimated amplitudes are smaller in order to decrease inaccuracies in velocity estimates introduced by radial variations in asymmetry.

Finally, we discuss the mean squared error of the models on the WRF test data. Because the wind field models are trained using HWind data, test performance on WRF storms is worse than on HWind storms. Models estimated using HWind velocity data are not able to capture the greater azimuthal variability in wind velocities present

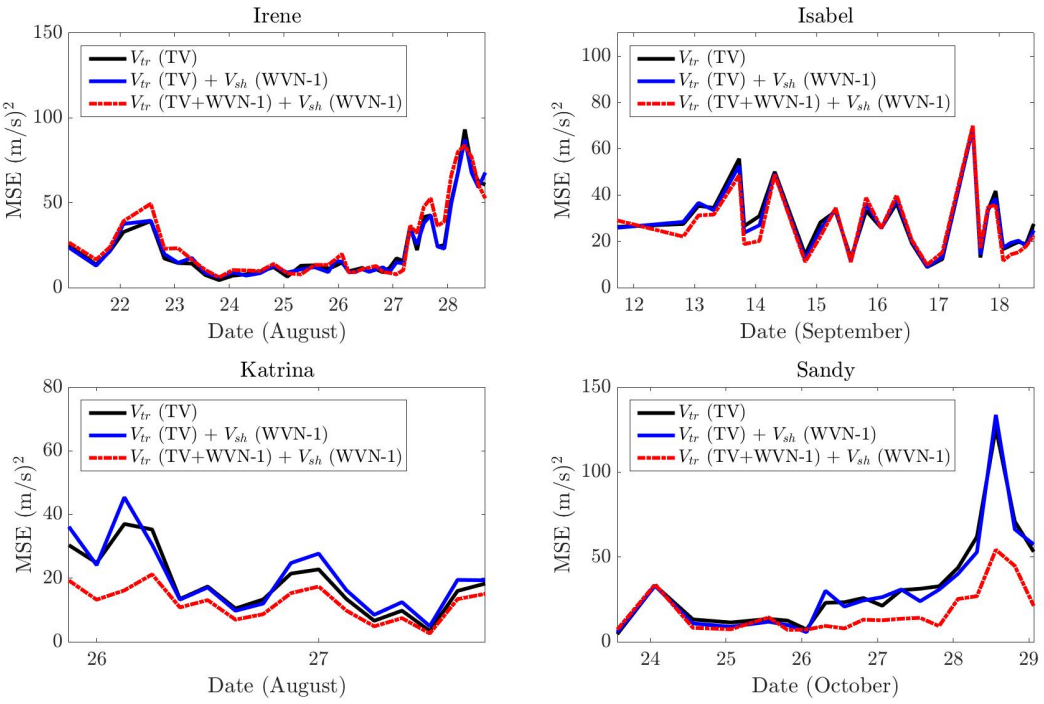

Figure 2-3: Performance of the V_{tr} (TV) model and V_{tr} + V_{sh} models on HWind testing storms and using GFS data for shear, in terms of mean squared error (MSE).

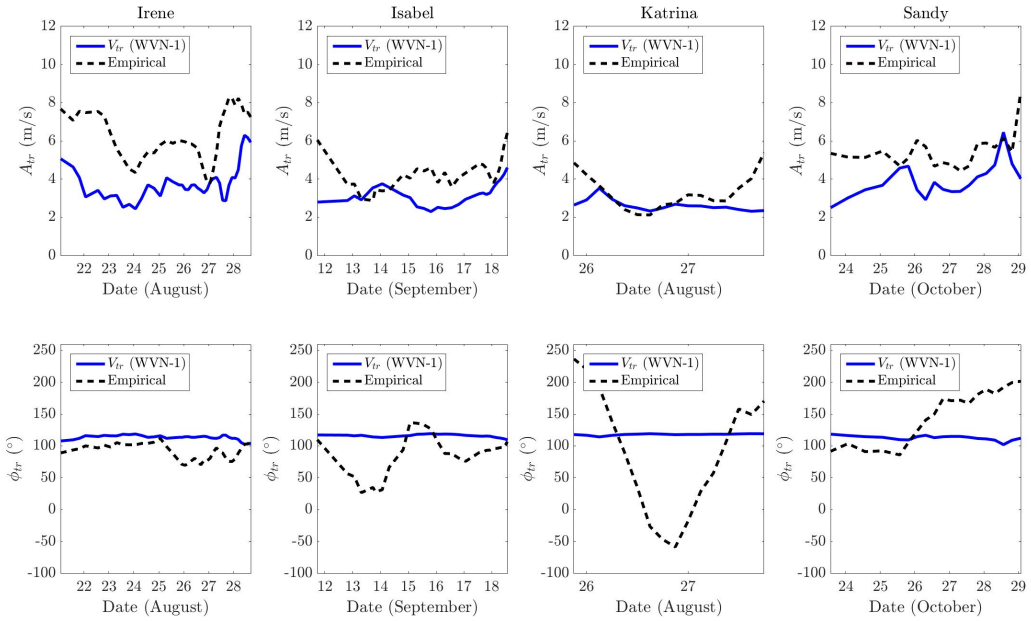

Figure 2-4: Wavenumber-1 amplitudes and phases owing to translation (A_{tr} and ϕ_{tr}, respectively) for HWind testing storms, as estimated by the V_{tr} (WVN-1) model. Empirically-estimated amplitudes and phases at the radius of maximum winds are also plotted for comparison purposes.

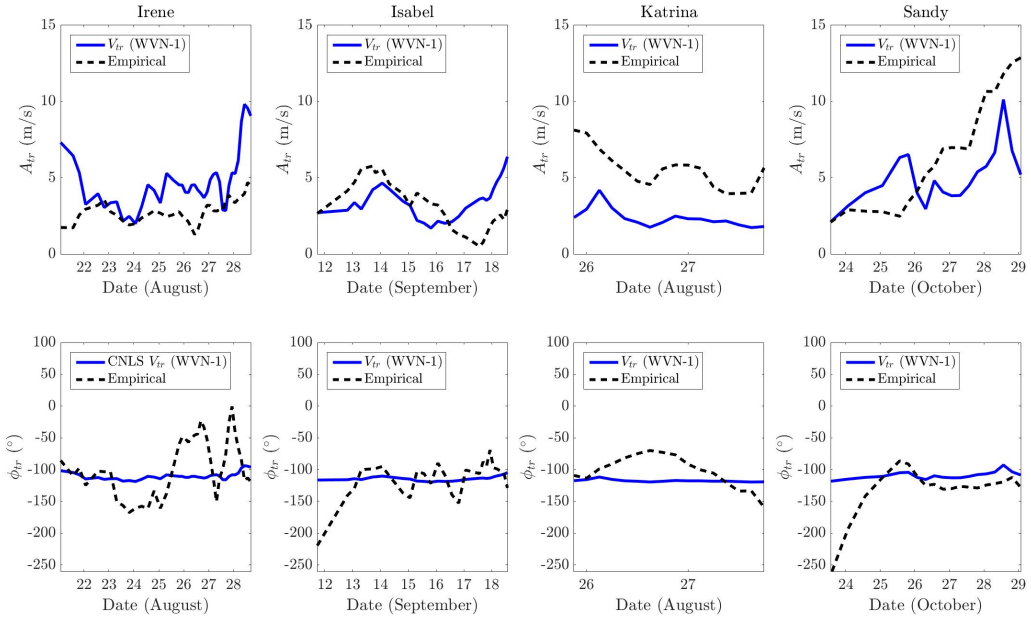

Figure 2-5: As in Figure 2-4, but as estimated by the V_{tr} (TV+WVN-1) model.

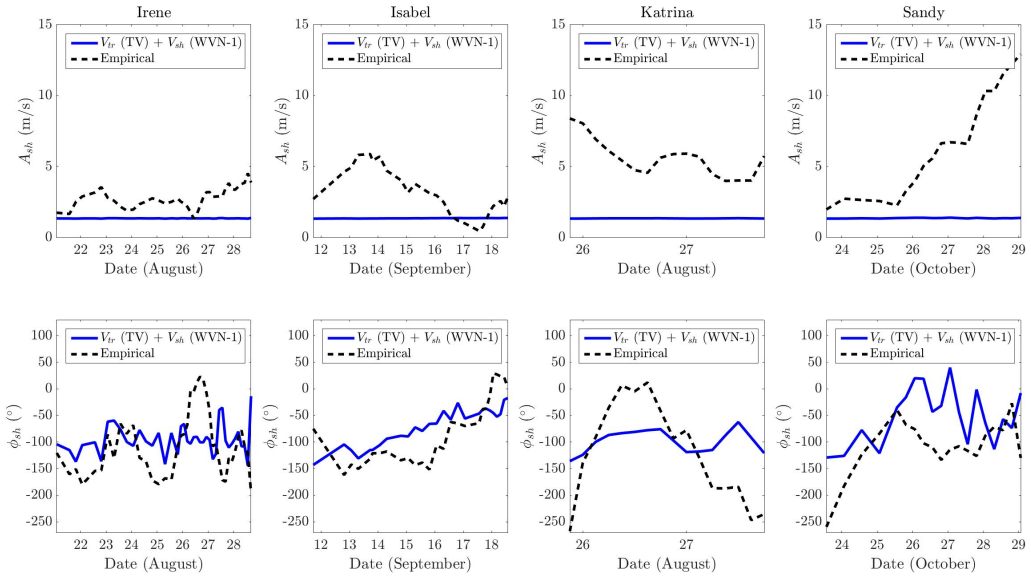

Figure 2-6: Wavenumber-1 amplitudes and phases owing to shear (A_{sh} and ϕ_{sh}, respectively) for HWind testing storms and GFS data, as estimated by the V_{tr} (TV) + V_{sh} (WVN-1) model. Empirically-estimated amplitudes and phases at the radius of maximum winds are also plotted for comparison purposes.

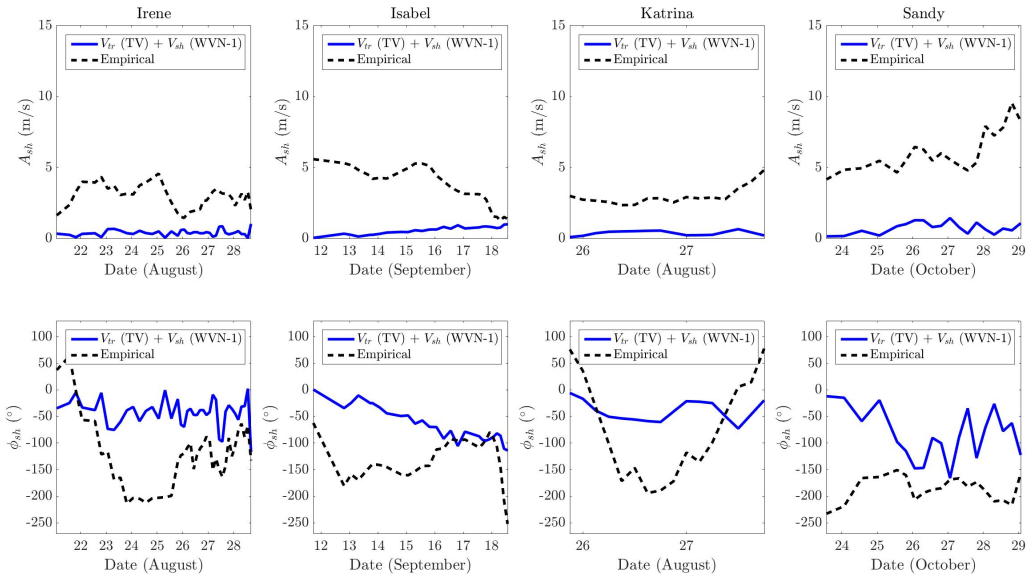

Figure 2-7: As in Figure 2-6, but as estimated by the V_{tr} (TV+WVN-1) + V_{sh} (WVN-1) model.

in the WRF data. Converting the WRF data to one-minute sustained winds, as was discussed in Section 2.1.4, did not noticeably change the velocities. The azimuthal variability is reflected in the empirical asymmetric amplitudes A_{tr} and A_{sh} estimated at the radius of maximum winds. The HWind amplitudes for Katrina (resp. Sandy) using GFS data are: A_{tr} = 3.13 (4.20) and A_{sh} = 2.65 (2.12). In contrast, the WRF amplitudes for Katrina (resp. Sandy) using GFS data are: A_{tr} = 7.08 (5.10) and A_{sh} = 4.44 (10.73).

The results suggest that the best model is the V_{tr} (TV+WVN-1) + V_{sh} (WVN-1) model. However, the CVEs of the models including wavenumber-1 owing to shear are only marginally better than those of models that do not include shear. For this reason, we perform one-way analysis of variance (ANOVA) as a measure of whether the differences in performance between two models are significant.[6] According to the one-way ANOVA, there is not a significant difference in performance between the V_{tr} (TV+WVN-1) + V_{sh} (WVN-1) and V_{tr} (TV+WVN-1) models, which is evident in the very similar wind fields estimated by these two models in Figure 2-8. Similarly, there

[6]Here, the one-way ANOVA tests whether there is a statistically significant difference between the mean residuals of two different models.

is not a significant performance difference between the V_{tr} (TV) + V_{sh} (WVN-1) and V_{tr} (TV) models. Parameter estimation using a larger training set and/or evaluating the parameters on more test storms would permit a more definitive conclusion on the effect of shear on asymmetry.

2.5 Application of Model to Wind Field Simulation

Given an ensemble consisting of a large number (typically $> 10^3$) of synthetic storm tracks, the asymmetric surface wind field can be simulated at points along each track using the model proposed in this paper. Storm tracks can be generated using the method proposed in [34]. After gradient wind fields are simulated along the tracks using our model, a suitable boundary layer model such as the model proposed by [107] may be used to convert the gradient winds to surface winds.

To simulate the mean field winds along each track would require estimation of the Holland parameters. The parameters $\bar{V}_m$ and R_m can be estimated using coupled intensity models [33, 32]. The parameter B can be estimated as a function of the central pressure difference and V_m, as suggested by [48]. The parameter $S(r)$ can be estimated as a function of r_0, the outer radius at which wind velocity is zero. Finally, a lognormal distribution is recommended for drawing the radius r_0 [35, 25].

To simulate the asymmetries in the wind field along the track, one can use the estimated V_{tr} (TV+WVN-1) + V_{sh} (WVN-1) model in Table 2.3-2.4.[7] Then, the asymmetries can be simulated provided that the storm translation and wind shear inputs are available. To further improve estimation of asymmetries, one can set the amplitudes and phases to be a function of the asymmetries at a previous time step, as well as the shear and translation at the current time. Our model can be suitably extended to account for the dependence of asymmetry on the wind field at previous times.

[7] This is the best-performing model, as discussed in Section 2.4.3. We elect to use the model estimated using GFS because the wind shear obtained using GFS analyses with vortex inversion is a more accurate estimate than using SHIPS.

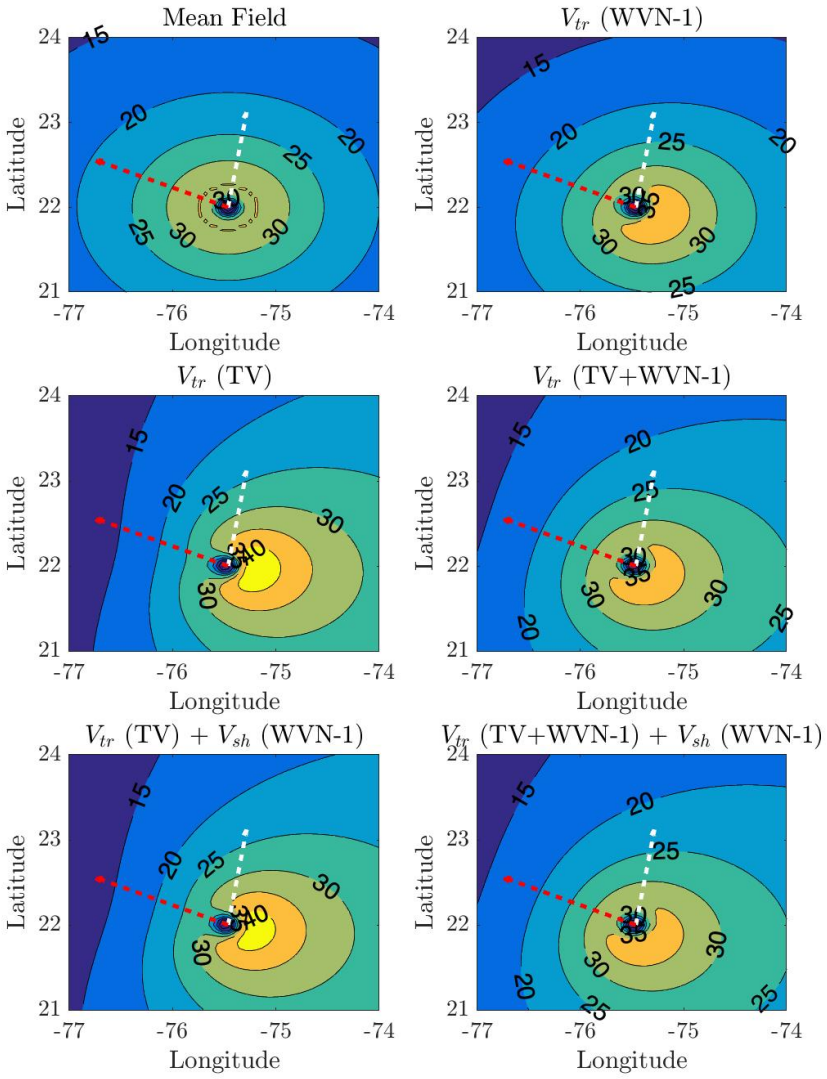

Figure 2-8: Visualization of 2D gradient wind field estimation. The plots show the estimated wind field of Hurricane Sandy on October 25 at 16:30 using the following models: mean field (upper left), V_{tr} (WVN-1) model (upper right), V_{tr} (TV) model (middle left), V_{tr} (TV+WVN-1) model (middle right), V_{tr} (TV) + V_{sh} (WVN-1) model (lower left), and V_{tr} (TV+WVN-1) + V_{sh} (WVN-1) model (lower right). The plots show the translation vector (white) and shear vector (red), with the length of the vectors indicating their relative magnitudes.

2.6 Summary

We proposed an asymmetric wind field model for the purpose of wind field estimation along hurricane tracks. Our model incorporates wavenumber-1 asymmetries as a function of storm translation speed and wind shear, modulating maximum intensity V_m in the Holland equation. To obtain parameter estimates for our model, we formulate a constrained, nonlinear least-squares (CNLS) optimization problem in which the objective function is the sum of squared errors between model-estimated and observationally-based velocity values.

The main contribution of our work is a systematic approach to asymmetric hurricane wind field estimation for the purpose of simulating the wind field along statistically-generated tracks in an ensemble. We fit a parametric model to past hurricane velocity wind fields and use environmental variables to estimate asymmetry. Specifically, our asymmetry model captures the wavenumber-1 asymmetric structure with or without incluson of the translation vector in the model. Below we summarize our key findings:

- Inclusion of the translation vector in the wind field affects the wavenumber-1 asymmetry owing to translation. If the translation vector is not added to the winds, the wavenumber-1 phase occurs slightly more than 90° clockwise of the translation direction and rotates downwind with increasing translation speed. If the translation vector is added, the wavenumber-1 component estimates the residual asymmetry that remains in the wind field. The phase of this residual asymmetry occurs slightly more than 90° counterclockwise of the translation direction and rotates upwind with increasing translation speed.

- When using SHIPS data, the wavenumber-1 shear-relative phase rotates downwind from downshear to left of shear with increasing shear magnitude. When using GFS data, the phase rotates from downshear to left of shear with increasing shear magnitude if the wavenumber-1 component owing to translation is included, but rotates upwind from upshear left to downshear left with increasing shear magnitude otherwise. The asymmetry owing to shear is substantially smaller when the wavenumber-1 asymmetry owing to translation is included.

- To determine the best model, we evaluate models using the cross-validation error, Bayesian information criterion, and mean squared error on test storms as metrics. The procedure suggests that the best-performing model is the V_{tr} (TV+WVN-1) + V_{sh} (WVN-1) model, which accounts for the translation vector as well as wavenumber-1 asymmetries owing to translation and shear. However, omission of the wavenumber-1 component owing to shear from this model only marginally decreases the model performance. Additional data for estimation would permit us to generate more conclusive results on asymmetry owing to shear.

- Model performance is relatively weak on WRF data, because all the models are trained using HWind data. Since WRF velocity data are instantaneous winds, WRF snapshots have greater azimuthal variability that is not captured by models estimated using HWind data. Additional WRF storms would allow us to draw more decisive conclusions on the effect of using HWind vs. WRF snapshots in parameter estimation.

2.7 Appendix A: Objective Function – Jacobian and Hessian

Recall in Section 2.2 that to minimize the CNLS objective $f(\mathbf{x})$, we supply the gradient $\nabla f(\mathbf{x})$ and Hessian $\nabla^2 f(\mathbf{x})$ to the solver (see Equation 2.11). These derivatives require the residual vector $e(\mathbf{x})$, Jacobian $J(\mathbf{x})$, and second derivative of the residuals $\nabla^2 e(\mathbf{x})$. The residual vector $e(\mathbf{x})$ was defined for the wind field model in Section 2.2. The Jacobian for velocity data point i, $\nabla e_i(\mathbf{x})$, is one row of $J(\mathbf{x})$ and given as $(J_i(\mathbf{x}_{\text{tr}})^\top,\ J_i(\mathbf{x}_{\text{sh}})^\top)^\top$, where $J_i(\mathbf{x}_{\text{tr}}) = (J_i(\mathbf{x}_{\text{tr,A}})^\top,\ J_i(\mathbf{x}_{\text{tr},\phi})^\top)^\top$ and

$J_i(\mathbf{x}_{\text{sh}}) = (J_i(\mathbf{x}_{\text{sh,A}})^\top,\ J_i(\mathbf{x}_{\text{sh},\phi})^\top)^\top$. Furthermore:

$$\begin{aligned}
J_i(\mathbf{x}_{\text{tr,A}}) &= -\,\mathrm{Y}_i \cdot \cos[\lambda_{\text{tr},i} - \phi_{\text{tr}}(\mathrm{V}_{\text{tr},t(i)};\ \mathbf{x}_{\text{tr},\phi})] \cdot d_{tr,t(i)} \\
J_i(\mathbf{x}_{\text{tr},\phi}) &= -\,\mathrm{Y}_i \cdot \mathrm{A}_{\text{tr}}(\mathrm{V}_{\text{tr},t(i)};\ \mathbf{x}_{\text{tr,A}}) \cdot \sin[\lambda_{\text{tr},i} - \phi_{\text{tr}}(\mathrm{V}_{\text{tr},t(i)};\ \mathbf{x}_{\text{tr},\phi})] \cdot d_{tr,t(i)} \\
J_i(\mathbf{x}_{\text{sh,A}}) &= -\,\mathrm{Y}_i \cdot \cos[\lambda_{\text{sh},i} - \phi_{\text{sh}}(\mathrm{V}_{\text{sh},t(i)};\ \mathbf{x}_{\text{sh},\phi})] \cdot d_{sh,t(i)} \\
J_i(\mathbf{x}_{\text{sh},\phi}) &= -\,\mathrm{Y}_i \cdot \mathrm{A}_{\text{sh}}(\mathrm{V}_{\text{sh},t(i)};\ \mathbf{x}_{\text{sh,A}}) \cdot \sin[\lambda_{\text{sh},i} - \phi_{\text{sh}}(\mathrm{V}_{\text{sh},t(i)};\ \mathbf{x}_{\text{sh},\phi})] \cdot d_{sh,t(i)}
\end{aligned} \tag{2.14}$$

where $d_{tr,t(i)} = (1,\ \mathrm{V}_{\text{tr},t(i)})^\top$, $d_{sh,t(i)} = (1,\ \mathrm{V}_{\text{sh},t(i)})^\top$ and Y_i is used to denote $\mathrm{Y}_i(r_i, \mathbf{S}_i(r_i))$, or the mean field component for data point i. The second-derivatives of the residuals are given as:

$$\nabla^2 e_i(\mathbf{x}) = \begin{pmatrix} \frac{\partial^2 e_i(\mathbf{x})}{\partial \mathbf{x}_{tr}^2} & \mathbf{0} \\ \mathbf{0} & \frac{\partial^2 e_i(\mathbf{x})}{\partial \mathbf{x}_{\text{sh}}^2} \end{pmatrix} \tag{2.15}$$

where

$$\frac{\partial^2 e_i(\mathbf{x})}{\partial \mathbf{x}_{tr}^2} = \begin{pmatrix} \mathbf{0} & \frac{\partial^2 e_i(\mathbf{x})}{\partial \mathbf{x}_{\text{tr,A}} \partial \mathbf{x}_{\text{tr},\phi}} \\ \left(\frac{\partial^2 e_i(\mathbf{x})}{\partial \mathbf{x}_{\text{tr,A}} \partial \mathbf{x}_{\text{tr},\phi}}\right)^\top & \frac{\partial^2 e_i(\mathbf{x})}{\partial \mathbf{x}_{tr,\phi}^2} \end{pmatrix}, \tag{2.16}$$

and

$$\frac{\partial^2 e_i(\mathbf{x})}{\partial \mathbf{x}_{\text{sh}}^2} = \begin{pmatrix} \mathbf{0} & \frac{\partial^2 e_i(\mathbf{x})}{\partial \mathbf{x}_{\text{sh,A}} \partial \mathbf{x}_{\text{sh},\phi}} \\ \left(\frac{\partial^2 e_i(\mathbf{x})}{\partial \mathbf{x}_{\text{sh,A}} \partial \mathbf{x}_{\text{sh},\phi}}\right)^\top & \frac{\partial^2 e_i(\mathbf{x})}{\partial \mathbf{x}_{\text{sh},\phi}^2} \end{pmatrix}. \tag{2.17}$$

Furthermore:

$$\begin{aligned}
\frac{\partial^2 e_i(\mathbf{x})}{\partial \mathbf{x}_{\text{tr,A}} \partial \mathbf{x}_{\text{tr},\phi}} &= -\,\mathrm{Y}_i \cdot \sin[\lambda_{\text{tr},i} - \phi_{\text{tr}}(\mathrm{V}_{\text{tr},t(i)};\ \mathbf{x}_{\text{tr},\phi})] \cdot \left(d_{tr,t(i)}\right)^\top \left(d_{tr,t(i)}\right) \\
\frac{\partial^2 e_i(\mathbf{x})}{\partial \mathbf{x}_{\text{tr},\phi}^2} &= \mathrm{Y}_i \cdot \mathrm{A}_{\text{tr}}(\mathrm{V}_{\text{tr},t(i)};\ \mathbf{x}_{\text{tr,A}}) \\
&\quad \cdot \cos[\lambda_{\text{tr},i} - \phi_{\text{tr}}(\mathrm{V}_{\text{tr},t(i)};\ \mathbf{x}_{\text{tr},\phi})] \cdot \left(d_{tr,t(i)}\right)^\top \left(d_{tr,t(i)}\right),
\end{aligned} \tag{2.18}$$

and

$$\begin{aligned}
\frac{\partial^2 e_i(\mathbf{x})}{\partial \mathbf{x}_{\mathrm{sh,A}} \partial \mathbf{x}_{\mathrm{sh},\phi}} &= -\mathrm{Y}_i \cdot \sin[\lambda_{\mathrm{sh},i} - \phi_{\mathrm{sh}}(\mathrm{V}_{\mathrm{sh},t(i)};\ \mathbf{x}_{\mathrm{sh},\phi})] \cdot \left(d_{sh,t(i)}\right)^{\top} \left(d_{sh,t(i)}\right) \\
\frac{\partial^2 e_i(\mathbf{x})}{\partial \mathbf{x}^2_{\mathrm{sh},\phi}} &= \mathrm{Y}_i \cdot \mathrm{A}_{\mathrm{sh}}(\mathrm{V}_{\mathrm{sh},t(i)};\ \mathbf{x}_{\mathrm{sh,A}}) \cdot \cos[\lambda_{\mathrm{sh},i} - \phi_{\mathrm{sh}}(\mathrm{V}_{\mathrm{sh},t(i)};\ \mathbf{x}_{\mathrm{sh},\phi})] \\
&\quad \cdot \left(d_{sh,t(i)}\right)^{\top} \left(d_{sh,t(i)}\right).
\end{aligned} \tag{2.19}$$

2.8 Appendix B: Bayesian Information Criterion

The Bayesian Information Criterion (BIC) is defined as:

$$\mathrm{BIC} = -2\ln(\hat{L}) + \ln(\mathrm{N})\mathrm{M} \tag{2.20}$$

where $\hat{L}$ is the maximum likelihood of the model, N is the number of data points, and M is the number of model parameters. A lower value of the BIC corresponds to a higher-quality model.

The sum of squared residuals is the metric minimized using the CNLS method (Equation 2.11), but computing the BIC requires the model's maximum likelihood. Thus we estimate $\ln(\hat{L})$ to be the maximum log-likelihood of a Gaussian model, for which the estimation error at each data point i is independently distributed with mean $e_i(\mathbf{x})$ and variance $\hat{\sigma}^2$:

$$\ln(\hat{L}) = -\frac{\mathrm{N}}{2}\ln(2\pi\hat{\sigma}^2) - \frac{1}{2\hat{\sigma}^2}\sum_{i=1}^{\mathrm{N}} e_i^2(\hat{\mathbf{x}}). \tag{2.21}$$

The parameter $\hat{\sigma}$ is the empirical standard deviation of the residuals. The BIC is computed for each model and the minimum BIC is denoted as $\overline{\mathrm{BIC}}$. Then, the final metric reported is the probability of each model m divided by the probability of the best-performing model, given by $\exp(-0.5(\mathrm{BIC}_m - \overline{\mathrm{BIC}}))$. See [10] for further details.

Chapter 3

Probabilistic Modeling of Storm-Induced Damage in Infrastructure Systems

In this section, we develop a modeling approach for probabilistic estimation of hurricane wind-induced damage to overhead infrastructural assets. Our approach aims to bridge a gap that exists between hurricane models and forecasting methods [67, 43, 61, 105, 30, 107, 47, 18, 115, 15, 33, 32] on one hand, and probabilistic models for prediction of damages or outages [63, 64, 45, 8, 118, 3, 116] on the other. In particular, our modeling approach captures real-time hurricane forecast uncertainties as well as the inherent spatial variability of hurricane wind velocities.

To represent the impact of uncertainty in the forecasted hurricane track's temporal evolution, we employ "Forecasts of Hurricanes using Large-Ensemble Outputs" (FHLO), which produces 1000-member forecast track and intensity ensembles [61]. FHLO is particularly suitable for our approach because its ensemble members are computationally inexpensive to produce, in comparison to using typical ensemble numerical weather prediction (NWP) systems [96, 71]. Using the probabilistic wind forecast given by FHLO as input, we employ a physically-based Nonhomogeneous Poisson Process (NHPP) model [8, 118, 3, 116] that outputs spatially-varying probability distributions of the extent of damage (number of asset failures). The distri-

bution is parameterized by a failure rate (expected number of failed assets), which varies spatially to reflect the radial and azimuthal variations in hurricane wind velocities. The failure rate at a given location is dependent on the local time history of the hurricane wind velocity.

The contributions in this section are detailed in our recent submission to *Risk Analysis*. In Section 3.1, we discuss our modeling approach for probabilistic damage estimation. In Section 3.2, we analyze how NHPP-estimated spatial extent and variability of damage depend on hurricane intensity and size, as well as the inclusion of wind field asymmetries. In Section 3.3, we study how incorporating the forecast uncertainty as given by FHLO affects the NHPP model damage estimates in the cases of Hurricanes Hermine (2016) and Michael (2018). Section 3.4 applies our modeling approach to the prediction of outages (i.e., loss-of-service) in electric power infrastructure due to Hurricane Michael. In Section 3.5, we provide brief insights into how hurricane intensity and size impact total damage and resulting financial losses. Finally, we provide concluding remarks in Section 3.6.

3.1 Modeling Approach

In this section, we develop a probabilistic model for estimating spatially-varying damage to overhead assets in infrastructure systems. To evaluate damage due to hurricane winds, we estimate a probability distribution over the number of failed assets in each defined two-dimensional spatial region $g \in \mathcal{G}$. In our approach, the location-specific probability distribution is dependent on the hurricane surface wind field velocities, which are forecasted at each location $g \in \mathcal{G}$ and time $t \in \mathcal{T}$. The set of times $\mathcal{T}$ encompasses discrete time steps between the initial forecast time t_0 and final forecast time t_f, where forecast duration $\mathrm{T} = t_\mathrm{f} - t_0$. The times are equally spaced and separated by a time interval of Δt.

We use $\mathbf{H} = \{v_{g,t}\}_{g\in\mathcal{G},t\in\mathcal{T}}$ to denote the hurricane wind field as a random field, where $v_{g,t}$ defines the velocity at location g and time t. Furthermore, $\mathbf{H}_g = \{v_{g,t}\}_{t\in\mathcal{T}}$ denotes the velocities corresponding to location g, and $\mathbf{H}_t = \{v_{g,t}\}_{g\in\mathcal{G}}$ the velocities

corresponding to time t. Henceforth, we will use the notation $\tilde{\mathbf{H}}$ to denote a specific instance of a hurricane wind field, which can be appropriately subscripted using g and t.

The probabilistic hurricane surface wind field forecast is given by Forecasts of Hurricanes using Large-Ensemble Outputs (FHLO), which we discuss in Section 3.1.1. Using a surface wind field forecast (FHLO) as input, we estimate probability distributions of damage (number of failed assets) within the infrastructure system by employing the nonhomogeneous Poisson Process (NHPP) model (Section 3.1.2). We discuss an NHPP model for hurricane wind-induced failures of overhead assets in electricity infrastructure (see Section 3.1.3), which we use in the remainder of this article. Finally, we discuss how the NHPP model outlined in Section 3.1.3 can be integrated with FHLO, in order to account for forecast uncertainties in damage estimates (see Section 3.1.4).

3.1.1 Forecasts of Hurricanes using Large-Ensemble Outputs (FHLO)

Forecasts of Hurricanes using Large-Ensemble Outputs (FHLO) is a physically-based model framework developed by Lin, Emanuel, and Vigh [61], which generates probabilistic forecasts of the hurricane wind field. Specifically, FHLO is used to produce probability distributions of wind velocity at fixed locations in space, using a three-component framework: 1) a track model that bootstraps 1,000 synthetic tracks from the much smaller number of forecast hurricane tracks from an ensemble numerical weather prediction model; 2) an intensity model that predicts the maximum wind speed along each synthetic track; and 3) a parametric wind field model that estimates the time-varying two-dimensional surface wind field along each synthetic track given the position and intensity of the storm. We use $\mathcal{H} = \{\tilde{\mathbf{H}}^{(i)}\}_{\forall i \in \{1,\ldots,\mathrm{H}\}}$ to refer to a hurricane ensemble obtained from FHLO: the ensemble consists of $\mathrm{H} = 1,000$ ensemble members, where each member is indexed by i and denoted by $\tilde{\mathbf{H}}^{(i)} = \{v_{g,t}^{(i)}\}_{g \in \mathcal{G}, t \in \mathcal{T}}$. The empirical probability of the wind field $\tilde{\mathbf{H}}^{(i)}$ is $1/\mathrm{H}$.

FHLO assumes an initialization time at which the forecast begins, typically 1-3 days before the hurricane is projected to make landfall. Randomness in hurricane tracks and wind velocities stems from forecast uncertainty in the hurricane track evolution, dynamic and thermodynamic environments, and initial conditions. The probabilistic intensity forecasts given by FHLO are comparable in accuracy to those of HWRF, an advanced numerical weather prediction model, but also far less computationally intensive to produce.

3.1.2 Nonhomogeneous Poisson Process (NHPP) Model

We now focus on generating probabilistic, spatially-varying estimates of damage, using a hurricane wind field $\tilde{\mathbf{H}}$ as input. For each spatial location $g \in \mathcal{G}$, we aim to compute a probability distribution over the number of damaged assets in g accumulated over the set of times $t \in \mathcal{T}$.

To compute the probability distributions, we employ a Nonhomogeneous Poisson Process (NHPP) model. The Poisson process is appropriate not only because it models a countable response variable (number of asset failures), but also because its resulting probability distribution is right-skewed. Occurrences of a large number of infrastructural asset failures in a day are atypical, and usually only occur as a result of severe disruptions such as high-intensity hurricanes [118]. This is appropriately modeled by a right-skewed distribution, in which the probability of large numbers of failures is small. A Poisson process is *nonhomogeneous* if the rate of failures is time-dependent. We choose a nonhomogeneous Poisson process model because in our model, infrastructural asset failures are dependent on the time-varying hurricane wind velocities. On the other hand, a *homogeneous* Poisson process assumes an asset failure rate that is constant with time.

Here, the NHPP model is used to estimate the Poisson intensities $\lambda_{g,t}$ for locations $g \in \mathcal{G}$ and at times $t \in \mathcal{T}$. The Poisson intensity is the expected number of failures per unit time, normalized by the asset density. For instance, if we are modeling failure of overhead electricity distribution lines, then the asset density is given by the length (km) of lines. More broadly, asset density could also be represented as an area or

volume, depending on the asset in question.

We model the Poisson intensity $\lambda_{g,t}$ to be a function of the velocity $v_{g,t}$; the parametric form of the function depends on the infrastructure system and asset type in question. The Poisson intensities $\lambda_{g,t}v_{g,t}$) for $t \in \mathcal{T}$ can be used to compute the failure rate Λ_g, the expected number of failures in g accumulated over the hurricane's lifetime and normalized by the asset density:

$$\Lambda_g(\mathbf{H}_g) \;=\; \sum_{t\in\mathcal{T}} \lambda_{g,t}(v_{g,t})\;\Delta t, \tag{3.1}$$

where Δt is the time spacing between each time $t \in \mathcal{T}$. A typical measure of Δt is one hour.

Both the Poisson intensity and failure rate are measures of expected damage when the number of assets per location can be treated as a large number (infinite). Under this assumption, the probability that there are s_g failures in location g, normalized by asset density, is given by the Poisson distribution:

$$\Pr(s_g \mid \Lambda_g) \;=\; \frac{\Lambda_g^{s_g}}{s_g!}\exp(-\Lambda_g), \tag{3.2}$$

where Λ_g, the failure rate, is also referred to as the Poisson parameter.

If the asset density l_g in g is known, then the corresponding "total" failure rate is $l_g\Lambda_g$. If we wish to obtain the distribution over the total number of failures (rather than normalized failures) in a location g, we use $l_g\Lambda_g$ as the Poisson parameter in place of Λ_g. In the example of electricity distribution lines, Λ_g would be the expected number of failures per kilometer of distribution lines and l_g is the length of distribution lines in kilometers within location g.

In reality, the number of assets per location is finite and varies across locations. If there are a finite number of assets $\bar{S}_g$ in a location g, then the distribution over the total number of failed assets must be modified accordingly:

$$\Pr(s_g \mid l_g\Lambda_g) \;=\; \left\{\begin{array}{ll} \frac{(l_g\Lambda_g)^{s_g}}{s_g!}\exp(-l_g\Lambda_g), & \text{for } s_g < \bar{S}_g \\ 1-\exp(-l_g\Lambda_g)\sum_{x=0}^{\bar{S}_g-1}\frac{(l_g\Lambda_g)^x}{x!}, & \text{for } s_g = \bar{S}_g \end{array}\right\} \tag{3.3}$$

Hereafter, we refer to the distribution given by Eq. 3.3 as incorporating "saturation" in the number of failures. Under this distribution, the expected number of failures $\mathbb{E}[s_g]$ normalized by asset density is not given by $\bar{S}_g\Lambda_g$, but rather by:

$$\begin{aligned}
\mathbb{E}[s_g] &= \sum_{x=0}^{\bar{S}_g} x \Pr(s_g = x) \\
&= \sum_{x=0}^{\bar{S}_g-1} x \frac{(l_g\Lambda_g)^x}{x!} \exp(-l_g\Lambda_g) \\
&\quad + \bar{S}_g \left[1 - \exp(-l_g\Lambda_g) \sum_{x=0}^{\bar{S}_g-1} \frac{(l_g\Lambda_g)^x}{x!}\right] \\
&= l_g\Lambda_g \exp(-l_g\Lambda_g) \sum_{x=1}^{\bar{S}_g-1} \frac{(l_g\Lambda_g)^{x-1}}{(x-1)!} \\
&\quad + \bar{S}_g \left[1 - \exp(-l_g\Lambda_g) \sum_{x=0}^{\bar{S}_g-1} \frac{(l_g\Lambda_g)^x}{x!}\right],
\end{aligned} \tag{3.4}$$

where $\Pr(s_g = x)$ is the probability of x events as given by the Poisson distribution in Eq. 3.3. Fig. 3-1 demonstrates how incorporating saturation affects the expected number of failures $\mathbb{E}[s_g]$ in a location g, following Eq. 3.4. Notice that $\mathbb{E}[s_g]$ asymptotically approaches $\bar{S}$, the total number of assets in g. In this case we consider a location with $\bar{S}_g = 30$ distribution lines (3 kilometers of lines in the location, where each line has a length of 100 meters).

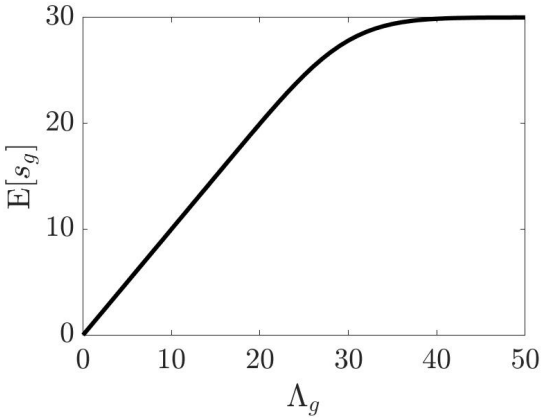

Figure 3-1: Expected number of failures $\mathbb{E}[s_g]$ given by Eq. 3.4 vs. failure rate Λ_g.

3.1.3 NHPP Model for Failure of Overhead Power Infrastructure Assets

In the remainder of this work, we focus on an application of the NHPP model to hurricane wind-induced failures of overhead infrastructure assets in electricity distribution systems. In particular, failures of electricity distribution lines are a frequent cause of outages in electricity power systems [11]. Line failures typical result from downing of supporting poles or toppling by nearby trees. A standard means of modeling the Poisson intensity is to use a quadratic function [8, 3, 116], which reflects the fact that the pressure exerted on trees and poles is a function of the wind velocity squared. On the other hand, a previous study suggests that the number of outages as a function of wind velocity is best described by an exponential relationship [55]. Both quadratic and exponential models suggest that the Poisson intensity increases at a superlinear rate with respect to the wind velocity.[1]

For this work, we focus on a quadratic model for Poisson intensity $\lambda_{g,t}$, the expected number of failures per hour and kilometer of assets (i.e., distribution lines):

$$\lambda_{g,t}(v_{g,t}) = \begin{cases} \left(1 + \alpha\Big(\left(\frac{v_{g,t}}{\mathrm{V_{crit}}}\right)^2 - 1\Big)\right)\lambda_{\mathrm{norm}}, & \text{if } v_{g,t} \geq \mathrm{V_{crit}} \\ \lambda_{\mathrm{norm}}, & \text{if } v_{g,t} < \mathrm{V_{crit}}. \end{cases} \tag{3.5}$$

The model's key physically-based feature is the quadratic relationship between $\lambda_{g,t}$ and $v_{g,t}$ when $v_{g,t}$ is greater than the so-called critical velocity $\mathrm{V_{crit}}$. For velocities below $\mathrm{V_{crit}}$, the infrastructure system only suffers from a fixed nominal failure rate of λ_{norm}.[2] The parameter α is a scaling parameter that controls for the increase in failure rate with velocities above $\mathrm{V_{crit}}$. All three model parameters ($\mathrm{V_{crit}}$, λ_{norm}, and α) are dependent on the asset type and properties (i.e., height, age, material composition).

[1] Other considerations such as precipitation and soil cover have also been shown to be relevant to modeling of failures and outages, but we focus solely on the variability of Poisson intensities due to the hurricane wind velocities.

[2] Literature has suggested that $\mathrm{V_{crit}}$ is 8 m/s, when using historical Swedish weather data in which velocities did not exceed 20 m/s [3], In contrast, $\mathrm{V_{crit}}$ was estimated to be 20.6 m/s when using velocities from historical hurricanes up to Category 2 intensity on the Saffir-Simpson scale [116].

For the remainder of this article, we use the following parameter values (adapted from [116]): $\mathrm{V}_{\mathrm{crit}} = 20.6$ m/s, $\alpha = 4175.6$, and $\lambda_{\mathrm{norm}} = 3.5 \times 10^{-5}$ failures/hr/km.

The equation can be rewritten accordingly, to separate the constant term and velocity-dependent term:

$$\lambda_{g,t}(v_{g,t}) \;=\; \lambda_{\mathrm{norm}}(1-\alpha) \;+\; \lambda_{\mathrm{norm}}\alpha f^2(v_{g,t}), \tag{3.6}$$

where

$$f(v_{g,t}) \;=\; \frac{\max(\mathrm{V}_{\mathrm{crit}}, v_{g,t})}{\mathrm{V}_{\mathrm{crit}}}. \tag{3.7}$$

Using Eq. 3.1, the failure rate Λ_g for all $g \in \mathcal{G}$ is given by:

$$\Lambda_g(\mathbf{H}_g) \;=\; \lambda_{\mathrm{norm}}\mathrm{T}(1-\alpha) \;+\; \lambda_{\mathrm{norm}}\alpha\Delta t \sum_{t\in\mathcal{T}} f^2(v_{g,t}). \tag{3.8}$$

Previous applications of the presented quadratic model [118, 3, 116] did not evaluate the spatial variability in estimated Poisson failure rates due to the physical structure of the hurricane wind field, even though hurricane wind velocities vary significantly with space and time. In contrast, our approach incorporates spatiotemporal variabilities in winds to estimate the Poisson failure rates. We are also readily able to replace the quadratic model with an exponential model for the Poisson intensity within the modeling approach. Furthermore, it is worth noting that our estimated failure rates use wind velocity inputs at one-hour intervals, as opposed to intervals of 3+ hours in the abovementioned applications of the quadratic model. In Section 3.2, we study the dependence of failure rates on variations in the hurricane wind field velocities.

3.1.4 Integrating FHLO and NHPP Model

We discuss how to incorporate hurricane forecast uncertainty, as given by FHLO, in estimating the failure rates and failure distributions using the quadratic NHPP model in Section 3.1.3. In contrast, previous works [118, 3, 116] did not incorporate hurricane forecast uncertainties in failure rate estimation, in addition to not analyzing

how failure rates are affected by wind velocity variability.

Consider a hurricane ensemble $\mathcal{H}$ obtained from FHLO. We define the expected velocity $\bar{v}_{g,t}$ in location g at time t:

$$\bar{v}_{g,t} \;=\; \mathbb{E}[v_{g,t}] \;=\; \frac{1}{\mathrm{H}}\sum_{i=1}^{\mathrm{H}} v_{g,t}^{(i)}, \tag{3.9}$$

in which $v_{g,t}^{(i)}$ is the velocity in grid g at time t, for ensemble member i. For notational convenience, we use $\mathbb{E}[\mathbf{H}_g]$ to denote $\{\bar{v}_{g,t}\}_{t\in\mathcal{T}}$ and $\mathbb{E}[\mathbf{H}]$ to denote $\{\bar{v}_{g,t}\}_{g\in\mathcal{G},t\in\mathcal{T}}$.

One can consider two ways to incorporate FHLO in estimating failure rates:

- **Failure Rate 1 (FR-1)**: the failure rate as a function of the ensemble-averaged wind velocities, denoted by $\Lambda_g(\mathbb{E}[\mathbf{H}_g])$. Using Eq. 3.1, FR-1 for a location g can be written as:

  $$\Lambda_g(\mathbb{E}[\mathbf{H}_g]) \;=\; \sum_{t\in\mathcal{T}} \lambda_{g,t}(\bar{v}_{g,t})\Delta t. \tag{3.10}$$

  Then, using Eq. 3.8, FR-1 under the quadratic NHPP model can be written as:

  $$\Lambda_g(\mathbb{E}[\mathbf{H}_g]) \;=\; \lambda_{\mathrm{norm}}\mathrm{T}(1-\alpha) \;+\; \lambda_{\mathrm{norm}}\alpha\Delta t\sum_{t\in\mathcal{T}} f^2(\bar{v}_{g,t}). \tag{3.11}$$

- **Failure Rate 2 (FR-2)**: the ensemble-averaged failure rate, denoted by $\mathbb{E}[\Lambda_g(\mathbf{H}_g)]$. Using Eq. 3.1, FR-2 for a location g can be written as:

  $$\begin{aligned}\mathbb{E}[\Lambda_g(\mathbf{H}_g)] \;&=\; \frac{1}{\mathrm{H}}\sum_{i=1}^{\mathrm{H}} \Lambda_g(\tilde{\mathbf{H}}_g^{(i)}) \\ &=\; \frac{1}{\mathrm{H}}\sum_{i=1}^{\mathrm{H}}\sum_{t\in\mathcal{T}} \lambda_{g,t}(v_{g,t}^{(i)})\Delta t.\end{aligned} \tag{3.12}$$

Then, using Eq. 3.8, FR-2 under the quadratic NHPP model can be written as:

$$\begin{aligned}
\mathbb{E}[\Lambda_g(\mathbf{H}_g)] &= \lambda_{\text{norm}}\mathrm{T}(1-\alpha) + \lambda_{\text{norm}}\alpha\Delta t\frac{1}{\mathrm{H}}\sum_{i=1}^{\mathrm{H}}\sum_{t\in\mathcal{T}} f^2(v_{g,t}^{(i)}) \\
&= \lambda_{\text{norm}}\mathrm{T}(1-\alpha) + \lambda_{\text{norm}}\alpha\Delta t\sum_{t\in\mathcal{T}}\frac{1}{\mathrm{H}}\sum_{i=1}^{\mathrm{H}} f^2(v_{g,t}^{(i)}), \\
&= \lambda_{\text{norm}}\mathrm{T}(1-\alpha) + \lambda_{\text{norm}}\alpha\Delta t\sum_{t\in\mathcal{T}}\mathbb{E}[f^2(v_{g,t})].
\end{aligned} \tag{3.13}$$

Obtaining FR-2 requires computing the failure rate for each ensemble member. Thus FR-2 more completely incorporates the uncertainty in the hurricane wind field represented by the ensemble members, in comparison to FR-1. In this article, we compute both FR-1 and FR-2, to demonstrate how more exhaustive incorporation of uncertainty from FHLO in the case of FR-2 affects the failure rate estimates. More specifically, we prove that FR-2 is greater than or equal to FR-1:

Proposition 3.1.1. *For a location g and wind velocities $\mathbf{H}_g$, the following holds for the failure rate Λ_g:*

$$\mathbb{E}[\Lambda_g(\mathbf{H}_g)] \geq \Lambda_g(\mathbb{E}[\mathbf{H}_g]) \tag{3.14}$$

Proof. First, we show that the following inequality holds:

$$\mathbb{E}[f^2(v_{g,t})] \geq f^2(\bar{v}_{g,t}). \tag{3.15}$$

To do so, we restate the term $f^2(\bar{v}_{g,t})$ following Eq. 3.6:

$$f^2(\bar{v}_{g,t}) = \left\{ \begin{array}{ll} 1, & \text{for } \bar{v}_{g,t} < \mathrm{V}_{\text{crit}} \\ \left(\frac{\bar{v}_{g,t}}{\mathrm{V}_{\text{crit}}}\right)^2, & \text{for } \bar{v}_{g,t} \geq \mathrm{V}_{\text{crit}} \end{array} \right\} \tag{3.16}$$

We can note from Eq. 3.16 that:

$$\frac{\bar{v}_{g,t}^2}{\mathrm{V}_{\text{crit}}^2} \geq f^2(\bar{v}_{g,t}). \tag{3.17}$$

Because $f(v_{g,t}) = \max(\mathrm{V}_{\text{crit}},\ v_{g,t})/\mathrm{V}_{\text{crit}}$, it follows that $f(v_{g,t}) \geq v_{g,t}/\mathrm{V}_{\text{crit}}$ and

$f(v_{g,t}) \geq 1$. Then, we obtain the following:

$$\mathbb{E}[f^2(v_{g,t})] \geq \frac{\mathbb{E}[v_{g,t}^2]}{\mathrm{V}_{\mathrm{crit}}^2} \geq \frac{\bar{v}_{g,t}^2}{\mathrm{V}_{\mathrm{crit}}^2} \tag{3.18}$$

The right-hand inequality in Eq. 3.18 is a consequence of Jensen's inequality, noting that $v_{g,t}^2$ is a quadratic function and therefore convex.

From Eq. 3.17-3.18, we conclude that Eq. 3.15 holds. Using Eq. 3.11 and 3.13, we arrive at Eq. 3.14. □

In 3.3.1, we estimate FR-1 and FR-2 for historical hurricanes, and discuss the implications of Proposition 3.1.1 on the failure rate estimates.

Next we define two estimates of the failure distribution in a location g, which incorporate FHLO. In defining the distribution estimates, we assume a very large (infinite) number of assets, in order to focus on the relationship between wind velocities and the failure distributions rather than the effect of infrastructure-specific characteristics (i.e., number of assets).

Let $\Pr(s_g \mid x)$ refer to the Poisson distribution given by 3.2, which determines the number of failures s_g in location g under Poisson parameter x. Then, the distribution estimates are given as follows:

- **Failure Distribution A (FD-A)** is given by $\Pr(s_g \mid \mathbb{E}[\Lambda_g(\mathbf{H}_g)])$, i.e., the Poisson distribution with the ensemble-averaged failure rate (FR-2) as the distribution's Poisson parameter.

- **Failure Distribution B (FD-B)** is an ensemble-averaged distribution obtained as follows: First, for each ensemble member i, we obtain a Poisson distribution which uses $\Lambda_g^{(i)} = \Lambda_g(\tilde{\mathbf{H}}_g^{(i)})$ as the Poisson parameter. Then, the probability that there are s_g failures in grid g is given by:

$$\Pr(s_g) \;=\; \frac{1}{\mathrm{H}} \sum_{i=1}^{\mathrm{H}} \Pr(s_g \mid \Lambda_g^{(i)}) \tag{3.19}$$

  i.e., we consider that the distribution given by parameter $\Lambda_g^{(i)}$ for ensemble member i occurs with probability 1/H. This is a valid probability distribution

because the probability mass owing to each ensemble member is 1/H and there are H ensemble members.

By definition, the expected number of failures under both models is equivalent. However, FD-B more completely incorporates the uncertainty in the wind field represented by the ensemble members, because it is calculated by using the ensemble member-specific Poisson distributions. In 3.3.2, we compare FD-A vs. FD-B when computed using historical hurricane wind fields, in order to demonstrate how the more complete incorporation of uncertainty in FD-B affects the probabilities of high-failure scenarios.

3.2 Analyzing Spatial Variability of Damage

As we have discussed in the previous section, our probabilistic modeling approach accounts for spatial variability and forecast uncertainty in the damage estimates. In this section, we analyze how spatial variability in NHPP-estimated failure rates is dependent on key hurricane wind field parameters such as hurricane intensity, size, and asymmetries. We assume a deterministic hurricane track (i.e., no uncertainty in the hurricane's track evolution). This permits us to isolate the dependency of damage on the hurricane wind field's physical structure. In Section 3.3, we assess how forecast uncertainty given by FHLO affects the computed failure rates and failure distributions.

For our analysis in this section, we consider a simple axisymmetric hurricane (see Section 3.2.1). We quantify the spatial extent of damage, as measured by what we define as the 'critical zone' (see Section 3.2.2), the geographical region in which failure rates exceed a defined threshold. Finally, we analyze how varying hurricane parameters including asymmetries affect the critical zone area and asset density-normalized failure rates (see Sections 3.2.3 – 3.2.4).

3.2.1 Simple hurricane

We consider a simple, stylized axisymmetric model in which the hurricane track deterministically moves in a straight line from a defined initial (genesis) point $\mathrm{x}_0^{\mathrm{h}}$ to final (lysis) point $\mathrm{x}_{\mathrm{f}}^{\mathrm{h}}$. In addition, the hurricane (or more specifically, the hurricane center/eye) travels at a constant rate given by V_{tr}, the hurricane translation speed. For a time duration t after hurricane genesis, the hurricane track location is $\mathrm{x}_t^{\mathrm{h}} = \mathrm{x}_0^{\mathrm{h}} + \mathrm{V}_{\mathrm{tr}} t$. The parameters $\mathrm{x}_0^{\mathrm{h}}$, $\mathrm{x}_{\mathrm{f}}^{\mathrm{h}}$, and V_{tr} are length-2 vectors, to separately model the hurricane's north-south and east-west movement.

Given the hurricane track, we estimate the wind field $\tilde{\mathbf{H}} = \{v_{g,t}\}_{g\in\mathcal{G},t\in\mathcal{T}}$, which consists of velocities defined at grids $g \in \mathcal{G}$ and times $t \in \mathcal{T}$. Here, $\mathcal{T} = \{t_0, ..., t_{\mathrm{f}}\}$, where hurricane genesis occurs at time t_0 in location $\mathrm{x}_0^{\mathrm{h}}$ and dissipates at time t_{f} in location $\mathrm{x}_{\mathrm{f}}^{\mathrm{h}}$. We assume that the wind field at a time t, defined as $\tilde{\mathbf{H}}_t = \{v_{g,t}\}_{g\in\mathcal{G}}$, is given by the Holland 1980 model [47]:

$$v_{g,t}(r_{g,t}) \;=\; \mathrm{V}_{\mathrm{m}}\Big(\frac{\mathrm{R}_{\mathrm{m}}}{r_{g,t}}\Big)^{\mathrm{B}/2} \exp\left(\frac{1}{2}\Big(1 - \Big(\frac{\mathrm{R}_{\mathrm{m}}}{r_{g,t}}\Big)^{\mathrm{B}}\Big)\right), \tag{3.20}$$

where $r_{g,t} = \left\|\mathrm{x}_g - \mathrm{x}_t^{\mathrm{h}}\right\|_2$ (L2 norm) and x_g denotes the centre-point of grid g. For the purposes of this section, we assume that the Holland parameters remain constant for the duration of the storm and $\mathrm{B} = 1$.[3]

3.2.2 Effect of hurricane parameters on critical zone

We now define the so-called hurricane "critical zone", which is a measure of the spatial extent of hurricane-induced damage:

Definition 3.2.1. *Consider a hurricane wind field $\tilde{\mathbf{H}}_t$ at time t for which the maximum intensity $\mathrm{V}_{\mathrm{m}}(t) \geq \mathrm{V}_{\mathrm{thres}}$, where $\mathrm{V}_{\mathrm{thres}}$ is a defined threshold velocity. Then the **critical zone** of $\tilde{\mathbf{H}}_t$ consists of all spatial locations $g \in \mathcal{G}$ for which (1) radius $r_{g,t} < \mathrm{R}_{\mathrm{m}}(t)$; or (2) $r_{g,t} \geq \mathrm{R}_{\mathrm{m}}(t)$ and $v_{g,t} \geq \mathrm{V}_{\mathrm{thres}}$, where $\mathrm{R}_{\mathrm{m}}(t)$ is the radius of maximum winds at time t. Furthermore, the **critical zone** of the entire wind field $\tilde{\mathbf{H}}$ consists of the union of the critical zones for the time-specific wind fields $\tilde{\mathbf{H}}_t$, $\forall t \in \mathcal{T}$.*

[3] Typically B is between 1 and 2.5.

If the maximum intensity $\mathrm{V_m}(t) < \mathrm{V_{thres}}$ *at time* t*, then the wind field* $\tilde{\mathbf{H}}_t$ *does not have a critical zone.*

If a wind field $\tilde{\mathbf{H}}_t$ at time t is axisymmetric, then the wind velocity $v_{g,t}$ is only dependent on radial distance $r_{g,t}$ and we can define a so-called "critical radius":

Definition 3.2.2. *Assume that for an axisymmetric hurricane wind field* $\tilde{\mathbf{H}}_t$ *at time* t*,* $\mathrm{V_m}(t) \geq \mathrm{V_{thres}}$*. Then, the* ***critical radius*** $\mathrm{R_{crit}}(\mathrm{V_{thres}}, t)$ *is defined as a radius* $r \geq \mathrm{R_m}$ *at which the velocity* $v = \mathrm{V_{thres}}$*. The wind field does not have a critical radius if* $\mathrm{V_m}(t) < \mathrm{V_{thres}}$*.*

According to Definitions 3.2.1-3.2.2, the **critical zone** of an axisymmetric wind field $\tilde{\mathbf{H}}_t$ consists of all spatial locations g for which the radius $r_{g,t}$ is less than the defined critical radius $\mathrm{R_{crit}}(\mathrm{V_{thres}}, t)$. We now present a simple result, under the restriction that we consider the simple, stylized axisymmetric hurricane model:

Lemma 3.2.3. *Assume that a hurricane has a straight-line track and constant translation speed* $\mathrm{V_{tr}}$*. Furthermore, the hurricane has a Holland wind field given by Eq. 3.20 with constant Holland parameters, maximum intensity* $\mathrm{V_m} \geq \mathrm{V_{thres}}$*, and a defined critical radius* $\mathrm{R_{crit}}(\mathrm{V_{thres}})$ *(with a slight abuse of notation,* $\mathrm{V_m}$ *and* $\mathrm{R_{crit}}$ *are constant with time and thus not a function of* t*). Then, the critical zone of a hurricane wind field* $\tilde{\mathbf{H}}$ *forms an obround with area* $\mathrm{A_{crit}}$ *given by:*

$$\mathrm{A_{crit}} \;=\; 2\mathrm{R_{crit}}(\mathrm{V_{thres}})\mathrm{T}\left\|\mathrm{V_{tr}}\right\|_2 + \pi[\mathrm{R_{crit}}(\mathrm{V_{thres}})]^2, \tag{3.21}$$

where T *is the hurricane lifetime, the obround's rectangle length* $\mathrm{T}\left\|\mathrm{V_{tr}}\right\|_2$ *is the distance covered by the hurricane track, and the rectangle width is given by two times the critical radius* $\mathrm{R_{crit}}(\mathrm{V_{thres}})$*. The first half-circle at one end of the obround corresponds to one-half of the critical zone area for the hurricane at genesis. The second half-circle at the other end corresponds to one-half of the critical zone area for the hurricane at lysis.*

For the remainder of the paper, we will focus on the quadratic NHPP model and set $\mathrm{V_{thres}} = \mathrm{V_{crit}}$, where $\mathrm{V_{crit}}$ is the model's critical velocity parameter. This case

is particularly important, because the Poisson intensity is equal to λ_{norm} when the hurricane velocity is below V_{crit}. Under this specific model, we present a further result:

Proposition 3.2.4. *For the quadratic NHPP model given by Eq. 3.5 and the parameter* $\text{V}_{\text{thres}} = \text{V}_{\text{crit}}$*, the failure rate* $\Lambda_g > \lambda_{norm}\text{T}$ *if and only if a spatial location* g *falls in the critical zone of an axisymmetric hurricane* $\tilde{\mathbf{H}}$ *with duration* T*.*

Proof. If location g is not in the critical zone of $\tilde{\mathbf{H}}$, then the Poisson intensity $\lambda_{g,t} = \lambda_{\text{norm}}$ at all times $t \in \mathcal{T}$ and thus $\Lambda_g = \lambda_{\text{norm}}\text{T}$. If g is in the critical zone of $\tilde{\mathbf{H}}$, then the velocity $v_{g,t} > \text{V}_{\text{crit}}$ for at least one time $t \in \mathcal{T}$ (following Definitions 3.2.1-3.2.2). Since velocity $v_{g,t}$ exceeds V_{crit}, we have $\lambda_{g,t} > \lambda_{\text{norm}}$ and from Eq. 3.8, we conclude that $\Lambda_g > \lambda_{\text{norm}}\text{T}$. □

3.2.3 Effect of hurricane parameters on critical zone

Now we demonstrate how the critical radius R_{crit} and critical zone area A_{crit} vary with the hurricane parameters V_{m} and R_{m}, using the simple hurricane outlined in Section 3.2.1. Because of the Holland model's inherent nonlinearity, it is difficult to analytically determine R_{crit} as a function of the Holland parameters. However, we can obtain an approximate estimate of R_{crit} by first defining the 'normalized' critical radius $r^{\star}_{\text{norm}}$:

$$r^{\star}_{\text{norm}} = \frac{\text{R}_{\text{crit}}}{\text{R}_{\text{m}}}. \tag{3.22}$$

Because Eq. 3.22 suggests that R_{crit} varies linearly with R_{m}, we consider a function of the following form for R_{crit}:

$$\text{R}_{\text{crit}}(\text{V}_{\text{m}},\ \text{R}_{\text{m}}) \ = \ \begin{cases} 0 & \text{V}_{\text{m}} < \text{V}_{\text{crit}} \quad \text{(3.23a)} \\ a_1 \text{R}_{\text{m}} \Big(\dfrac{\text{V}_{\text{m}}}{\text{V}_{\text{crit}}} \Big)^{a_2} & \text{V}_{\text{m}} \geq \text{V}_{\text{crit}}. \quad \text{(3.23b)} \end{cases}$$

We obtain Eq. 3.23a by noting that $\text{R}_{\text{crit}}/\text{R}_{\text{m}} = 0$ when $\text{V}_{\text{m}} < \text{V}_{\text{crit}}$. We obtain Eq. 3.23b by observing that $\text{R}_{\text{crit}}/\text{R}_{\text{m}} = 1$ for $\text{V}_{\text{m}} = \text{V}_{\text{crit}}$ and increases with V_{m} for $\text{V}_{\text{m}} > \text{V}_{\text{crit}}$.

Using Lemma 3.2.3, we arrive at an equation for the critical zone area A_{crit} as a function of R_m and V_m, when $V_m \geq V_{crit}$:

$$\begin{aligned} A_{crit}(V_m, R_m) &= 2R_{crit}T\left\|V_{tr}\right\|_2 + \pi {R_{crit}}^2 \\ &= 2T\left\|V_{tr}\right\|_2 a_1 R_m \left(\frac{V_m}{V_{crit}}\right)^{a_2} + \pi a_1^2 R_m^2 \left(\frac{V_m}{V_{crit}}\right)^{2a_2} \\ &= b_1 R_m \left(\frac{V_m}{V_{crit}}\right)^{a_2} + b_2 R_m^2 \left(\frac{V_m}{V_{crit}}\right)^{2a_2}, \end{aligned} \tag{3.24}$$

where $b_1 = 2T\left\|V_{tr}\right\|_2 a_1$ and $b_2 = \pi a_1^2$. The complete defined parametric function for A_{crit} is as follows:

$$A_{crit}(V_m, R_m) = \begin{cases} 0 & V_m < V_{crit} \quad (3.25a) \\ b_1 R_m \left(\frac{V_m}{V_{crit}}\right)^{a_2} + b_2 R_m^2 \left(\frac{V_m}{V_{crit}}\right)^{2a_2} & V_m \geq V_{crit}. \quad (3.25b) \end{cases}$$

For purposes of estimating the parameters a_1 and a_2, we calculate the critical radius numerically for hurricanes with values of R_m between 20 and 50 km (step size of 1 km) and V_m between 21 and 80 m/s (step size of 1 m/s). These hurricanes have a straight-line track moving northward with a lifetime $T = 121$ and translation speed $\left\|V_{tr}\right\|_2 = 3$ m s^{-1}. Then, we take the logarithm of Eq. 3.23b and use the least-squares method to estimate the parameters relating V_m and R_m to the critical radius. The resulting parameters, $a_1 = 1.84$ and $a_2 = 2.32$, are statistically significant with 95% confidence (see Figure 3-2).

Figure 3-3 illustrates how the critical zone area, as well as failure rates within the critical zone, depend on the hurricane's maximum intensity V_m. The critical zone areas for the hurricanes in Figure 3-3 are: 2.27×10^5 km^2 (Tropical Storm), 7.31×10^5 km^2 (Category 1), and 1.36×10^6 km^2 (Category 2). Moreover, the failure rates vary more significantly with radial distance within the critical zone if the maximum intensity is higher. The maximum asset density-normalized failure rate achieved in the critical zone is the following for each storm: 0.6 failures/km (Tropical Storm), 5.7 failures/km (Category 1), and 12.9 failures/km (Category 2). As a benchmark, the

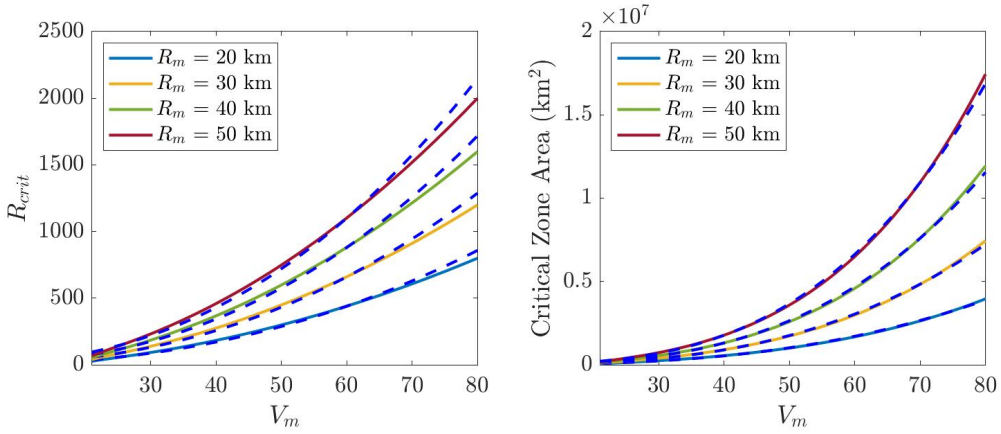

Figure 3-2: Numerically-computed critical radius R_{crit} (*left*) and critical zone area A_{crit} (*right*), as a function of V_m for fixed values of R_m. Best-fit polynomial functions are included for each curve in both plots, given by the dotted blue lines.

failure rate threshold for a location g belonging in the critical zone, $\lambda_{norm}T$, is equal to 0.0042 failures/km. The average asset density-normalized failure rate in the critical zone is given by the following for each storm: 0.3 failures/km (Tropical Storm), 2.2 failures/km (Category 1), and 4.3 failures/km (Category 2).

Figure 3-4 illustrates the dependency of the critical zone and failure rates on the hurricane's radius of maximum winds R_m, a conventional indicator of hurricane size. The critical zone areas for the hurricanes in Figure 3-4 are: 4.50×10^5 km^2 (R_m = 20 km), 7.31×10^5 km^2 (R_m = 30 km), and 1.05×10^6 km^2 (R_m = 40 km). Both the critical zone area and maximum failure rate achieved increase at a slower rate with respect to R_m, in comparison to V_m. The maximum asset density-normalized failure rate achieved in the critical zone is the following for each storm: 3.8 failures/km (R_m = 20 km), 5.7 failures/km (R_m = 30 km), and 7.6 failures/km (R_m = 40 km). The average asset density-normalized failure rate in the critical zone is given by the following for each storm: 1.5 failures/km (R_m = 20 km), 2.2 failures/km (R_m = 30 km), and 2.9 failures/km (R_m = 40 km).

The results in Figures 3-2 – 3-4 are applicable under a straight-line hurricane track and an axisymmetric Holland wind field with time-constant Holland parameters. Once these conditions are relaxed, the critical zone area and variability in failure rates would differ. For instance, hurricane maximum intensity V_m is time-varying, and

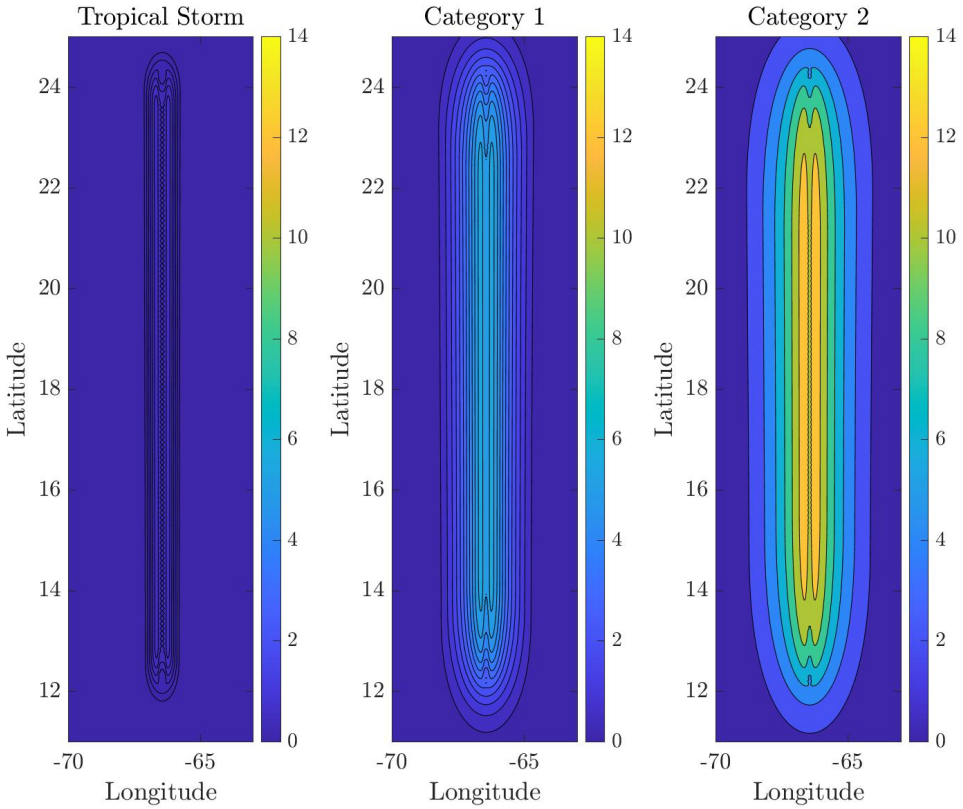

Figure 3-3: Spatially-varying failure rates as a function of a hurricane wind field, under different maximum intensities V_m. An axisymmetric Holland wind field with time-constant Holland parameters is used (see Section 3.2.1). Parameters are: $V_{tr} \approx 3$ m s^{-1}, $R_m = 30$ km, $B = 1$. The choices of V_m are 25 m s^{-1} (*left*), 37 m s^{-1} (*center*), and 46 m s^{-1} (*right*), corresponding respectively to tropical storm, Category I, and Category II on the Saffir-Simpson scale. The obround in each subfigure indicates the critical zone, and failure rates are given as failures per kilometer of infrastructure assets.

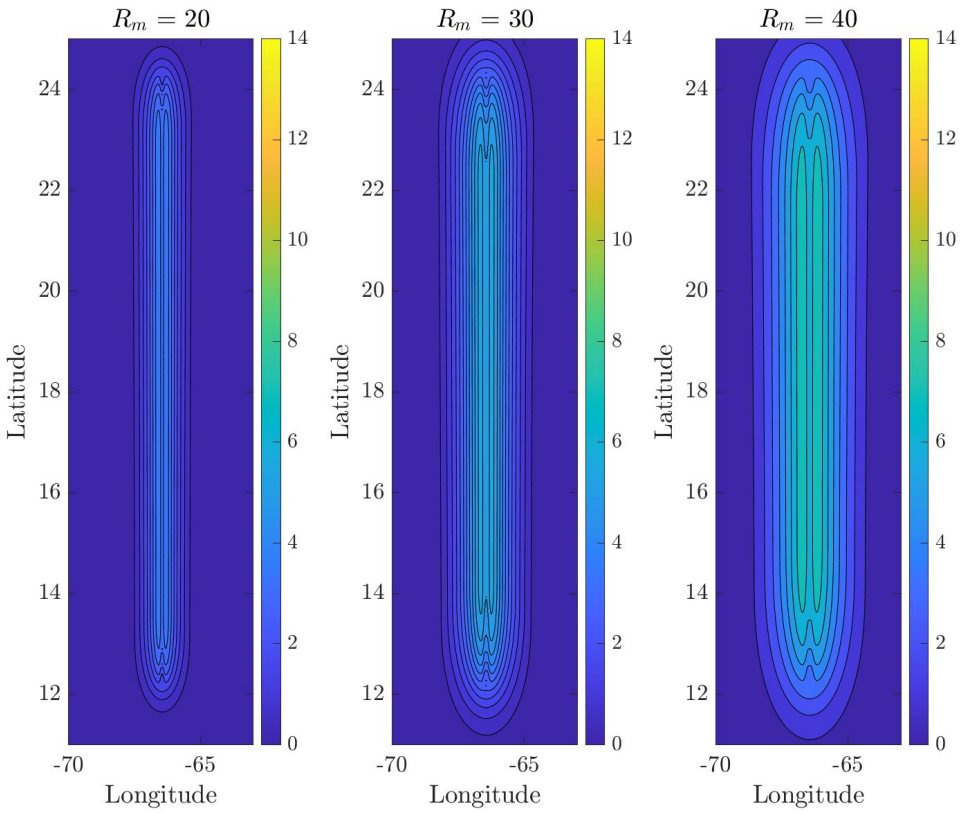

Figure 3-4: As in Figure 3-3, but for different values of the radius of maximum winds R_m, with V_m fixed to 37 m s^{-1}.

usually lower at the beginning and end of the hurricane's lifetime. Furthermore, the Holland wind field considered here only includes one shape parameter, but additional shape parameters would affect the decay in wind velocities with radial distance; the updated Holland 2010 model [48] includes more shape parameters. The Holland model also does not account for wind field asymmetries, which we will consider in the following subsection.

3.2.4 Effect of hurricane asymmetries

So far we considered axisymmetric wind fields, in which the hurricane velocities are equivalent at equiradial distances from the storm center. Now we discuss how introducing asymmetries to the wind field would alter the critical zone and failure rates. Asymmetries refer to variability in velocities with respect to the azimuthal angle, which is measured as degrees clockwise from a defined reference direction (typically the storm translation direction) [100, 15]. Figure 3-5 demonstrates how an axisymmetric wind field (i.e., without asymmetries) differs from an asymmetric wind field.

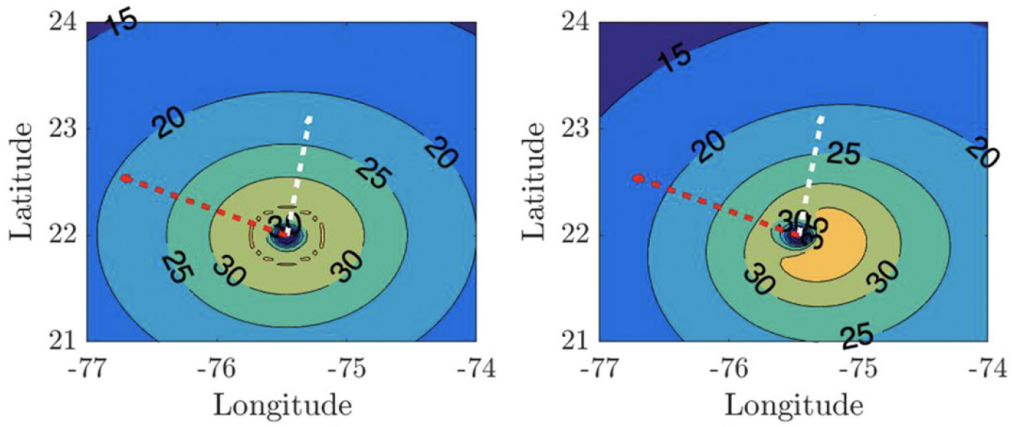

Figure 3-5: Example of an estimated axisymmetric wind field (*left*) and asymmetric wind field (*right*), adapted from [15]. The plots show the storm translation vector (white) and wind shear vector (red), with the length of the vectors indicating their relative magnitudes.

To analyze the effect of asymmetries on the damage estimates, we introduce an asymmetry to the Holland wind field by adding the storm-translation vector to the winds. Figure 3-6 demonstrates how the critical zone and failure rates are altered

when the storm-translation vector is added to the axisymmetric wind field. The maximum velocity under equal radius occurs at exactly 90° clockwise of the translation direction, where the storm motion and cyclostrophic wind direction are aligned. This is reflected in Figure 3-6, where the storm is translating northward and the maximum failure rates occur in a wall east of the storm track. The critical zones no longer display the obround shapes suggested by Eq. 3.21.

The critical zone area differs when comparing axisymmetric and asymmetric hurricanes. For the hurricanes that include asymmetry due to the storm-translation vector in Figure 3-6, the corresponding critical zone areas are: 2.47×10^5 km^2 (Tropical Storm), 7.89×10^5 km^2 (Category 1), and 1.18×10^6 km^2 (Category 2). Adding the storm-translation vector results in a greater critical zone area for the Tropical Storm and Category 1 hurricane, but not for the Category 2 hurricane. However, the sum of the failure rates is greater under the asymmetric hurricanes regardless of the hurricane intensity. The average asset density-normalized failure rate in the critical zone is given by the following for each storm: 0.5 failures/km (Tropical Storm), 2.3 failures/km (Category 1), and 5.4 failures/km (Category 2).

Compared to axisymmetric hurricanes, the critical zones in Figure 3-6 have higher maximum failure rates because of the high wind velocities occurring east of the storm track. The maximum failure rates corresponding to Figure 3-6 are: 1.2 failures/km (Tropical Storm), 6.7 failures/km (Category 1), and 14.4 failures/km (Category 2). When comparing these statistics to the maximum failure rates for the axisymmetric hurricanes in Figure 3-3, it is evident that the discrepancy in maximum failure rate between the axisymmetric and asymmetric hurricanes increases with maximum intensity V_m. This suggests that not accounting for asymmetries in hurricane wind field forecasts can lead to significant underestimation of failure rates due to high-intensity hurricanes.

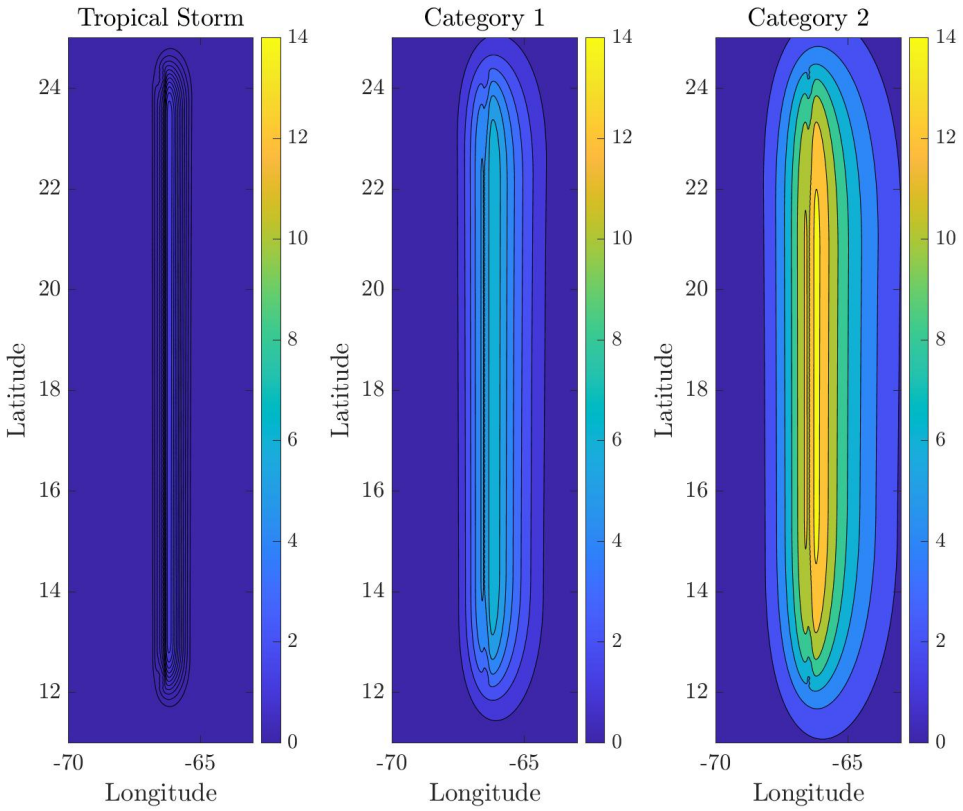

Figure 3-6: As in Figure 3-3, but under inclusion of asymmetry due to the storm-translation vector.

3.3 Analyzing Effect of Forecast Uncertainty on Damage

In this section, we assess how forecast uncertainty affects the probabilistic estimates of infrastructure damage, using wind field forecasts given by FHLO for Hurricanes Hermine and Michael. We analyze the effect of forecast uncertainty on estimated failure rates (FR-1 vs. FR-2) in Section 3.3.1. Then we analyze the effect of forecast uncertainty on probability distributions over the number of failures (FD-A vs. FD-B) in Section 3.3.2.

For computation of both FR-1 and FR-2 in this section, we obtain the asset density-normalized failure rate for each grid, then multiple it by the asset density. Specifically, we assume that each spatial grid has an asset density of $l_g = 7.08$ km of overhead infrastructure assets.[4]

3.3.1 Effect of forecast uncertainty on failure rates

Recall that in Section 3.1.4, we proved FR-2 is greater than or equal to FR-1 when using the quadratic NHPP model to estimate failure rates. We discuss implications of this result on the failure rates for Hermine (2016) and Michael (2018), hurricanes which made landfall in northwestern Florida. These two hurricanes are considered because they have different intensities: Hermine is Category 1, whereas Michael is Category 5. The differences between FR-1 and FR-2 could vary depending on the hurricane intensity.

Analysis for Hurricane Hermine: Figure 3-7 plots Hermine's wind field $\tilde{\mathbf{H}}$ and corresponding Poisson intensities $\lambda_{g,t}$ at six designated times t, for a single ensemble member. Note the hurricane's northeasterly movement, which is consistent with the hurricane's historical track. We calculate failure rates (FR-1 and FR-2) for a geographical region consisting of $0.1^\circ \times 0.1^\circ$ grids within the latitude range 29.70°N

[4]We considered The City of Tallahassee Utilities. They have 1,800 km of distribution lines over 255 km^2, averaging to 7.08 km of line/km^2 area [74]. We assume each location g has an area of 1 km^2.

to 30.69°N and longitude range 83.21°W to 85.20°W. This region has as approximate north-south length of 110 km and east-west length of 192 km.

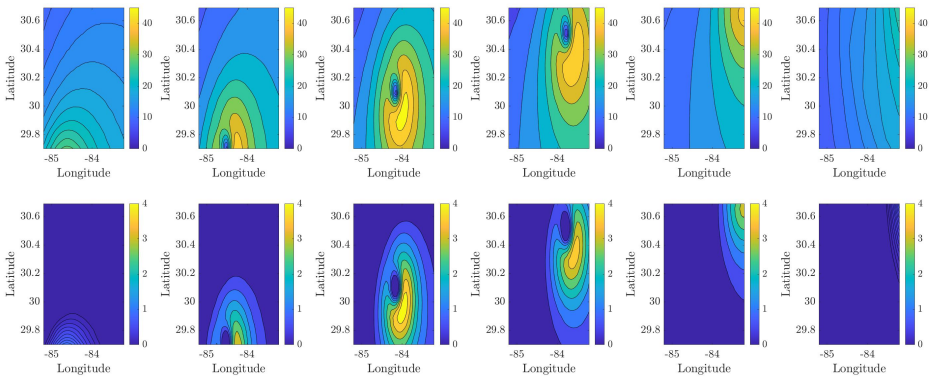

Figure 3-7: Plot of Hurricane Hermine wind velocities (*top row*) and corresponding Poisson intensities (*bottom row*) for a single ensemble member. Each of the six columns corresponds to a specific time, given in Coordinated Universal Time (UTC).

Figure 3-8 plots Hurricane Hermine's ensemble-averaged wind field given by $\mathbb{E}[\mathbf{H}] = \{\bar{v}_{g,t}\}_{g\in\mathcal{G},t\in\mathcal{T}}$. The velocity contours are much smoother after averaging, and the majority of the geographical region does not contain significant velocity exceedances above the critical velocity parameter V_{crit}. More specifically, critical velocity exceedances within $\mathbb{E}[\mathbf{H}]$ occur for only six out of the 121 times for which the wind field forecast is available. We will discuss how the 'smoothing' of velocity contours in the ensemble-averaged wind field affect failure rate estimates given by FR-1.

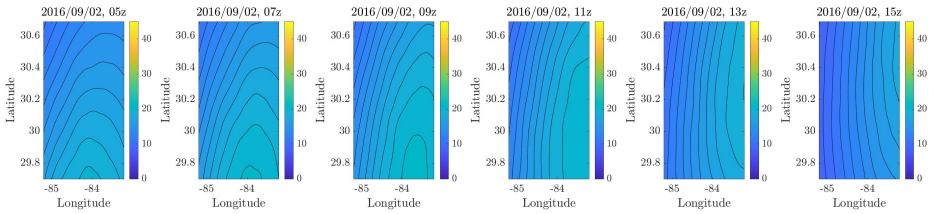

Figure 3-8: Plot of Hurricane Hermine's velocities averaged across all ensemble members.

Figure 3-9 demonstrates how the spatially-varying failure rates are dependent on the choice of failure rate estimate (FR-1 or FR-2). When using FR-1 as the failure rate estimate, only 20.9% of the considered geographical region (4,414 km^2) falls within the critical zone. In contrast, 100% of the considered geographical region falls within

the critical zone when using FR-2. Furthermore, the region-averaged failure rate is 0.12 failures/kilometer of assets for FR-1 and 3.34 for FR-2. This suggests that failure rates are, on average, more than 28 times higher under FR-2. The main reason for this discrepancy is that supercritical velocities are averaged out if FR-1 is used. The same would be expected for other Tropical Storms or Category 1 hurricanes in which the maximum intensity is not significantly higher than the critical threshold V_{crit}. On the other hand, FR-2 considers the individual ensemble member wind fields in failure rate estimation. In this sense, FR-2 is more realistic, as the supercritical velocities in the ensemble member wind fields are accounted for in failure rate estimation.

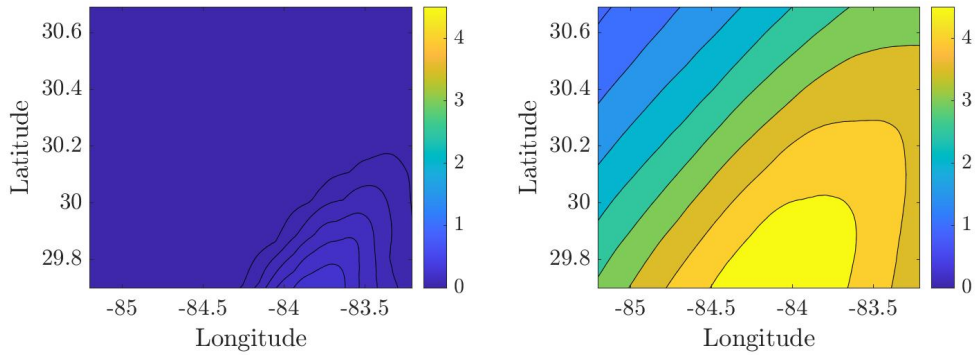

Figure 3-9: Plot of failure rates given by FR-1 (*left*) and FR-2 (*right*) for Hurricane Hermine.

Analysis for Hurricane Michael: Figures 3-10 – 3-12 demonstrate how the failure rates given by FR-1 and FR-2 differ for Hurricane Michael (2018). We calculate failure rates (FR-1 and FR-2) for a geographical region consisting of $0.1° \times 0.1°$ grids within the latitude range 29.60°N to 32.20°N and longitude range 83.40°W to 86.50°W. This region has as approximate north-south length of 289 km and east-west length of 300 km.

Similar to Hermine, Michael made landfall in northwestern Florida. However, Michael was a more intense, Category 5 hurricane that reached peak maximum intensities of around 70 m/s. This is reflected in the higher velocities and estimated Poisson intensities in Figure 3-10. Critical velocity exceedances in the ensemble-averaged wind field $\mathbb{E}[\mathbf{H}]$ occur at 26 out of the 121 times for which the wind field

forecast from FHLO is available (Figure 3-11). This indicates that the ensemble-averaged wind field contains more frequent and significant exceedances of the critical velocity, in comparison to Hermine. Estimates of FR-1 are consequently much higher than for Hermine, as demonstrated in the left-hand plot of Figure 3-12.

When using FR-1 as the failure rate estimate, 60.3% of the considered geographical region (52,303 km^2) falls within the critical zone. For FR-2, 96.3% of the region (83,492 km^2) falls within the critical zone. The region-averaged failure rate is 2.69 failures/kilometer of assets for FR-1 and 4.48 for FR-2, which implies that the average failure rate is 1.67 times higher under FR-2. The difference between FR-1 and FR-2 is less pronounced than for Hermine, because Michael is a high-intensity hurricane and hence a more significant portion of the geographical region falls in the critical zone under FR-1.

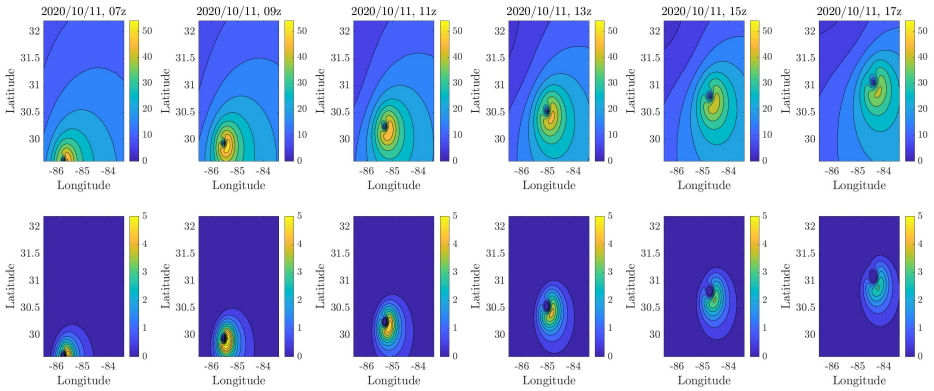

Figure 3-10: Plot of Hurricane Michael wind velocities (*top row*) and corresponding Poisson intensities (*bottom row*) for a single ensemble member. Each of the six columns corresponds to a specific time, given in Coordinated Universal Time (UTC).

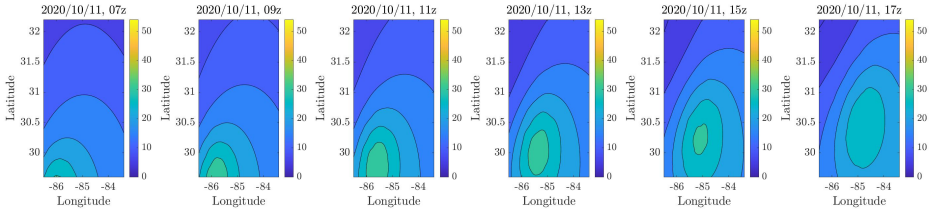

Figure 3-11: Plot of Hurricane Michael's velocities averaged across all ensemble members.

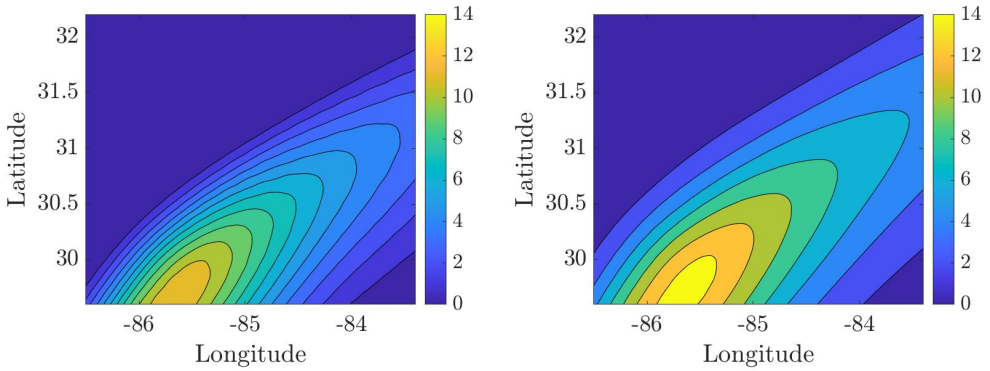

Figure 3-12: Plot of failure rates given by FR-1 (*left*) and FR-2 (*right*) for Hurricane Michael.

3.3.2 Effect of forecast uncertainty on failure distributions

In this subsection, we analyze how the spatially-varying probability distribution over the number of failures differs depending on the distribution of choice (FD-A vs. FD-B). We will show that FD-A tends to underestimate the probabilities of high-failure scenarios, in comparison to FD-B, using wind field data from FHLO for Hermine and Michael. Specifically for both hurricanes, the probabilities of high-failure scenarios are many times higher when using FD-B in place of FD-A. This insight has significant implications for risk estimation, particularly in the case of high-intensity hurricanes such as Michael.

Analysis for Hurricane Hermine: Figure 3-13 demonstrates how FD-A and FD-B differ for Hurricane Hermine at a few select locations. These locations are selected because they differ in terms of minimum radial distance to the storm center achieved during the hurricane's lifetime. Because Hermine is a Category 1 hurricane, there are relatively few exceedances of the critical velocity, and thus the probabilities peak at 1-2 failures in the case of FD-A. As is typical for the Poisson distribution, FD-A is right-skewed. However, FD-B is even more right-skewed: the probability is maximum at zero failures and decreases with increasing number of failures. Furthermore, FD-B has a more pronounced tail than FD-A. Specifically, the 95% percentiles for number of failures under FD-A are given as follows (for the locations from left to right in Figure 3-13): 4, 6, 7, 7. In contrast, the 95% percentiles under FD-B are:

12, 12, 13, 15. Amongst the four locations, it is anywhere between 4.6 and 80 times more likely to have nine or more failures when using FD-B in place of FD-A. The difference in the probability of 9+ failures, as given by FD-A vs. FD-B, is greater for locations that are farther from the storm track. This suggests that FD-A particularly underestimates the probabilities of high-damage outcomes for locations in the storm periphery.

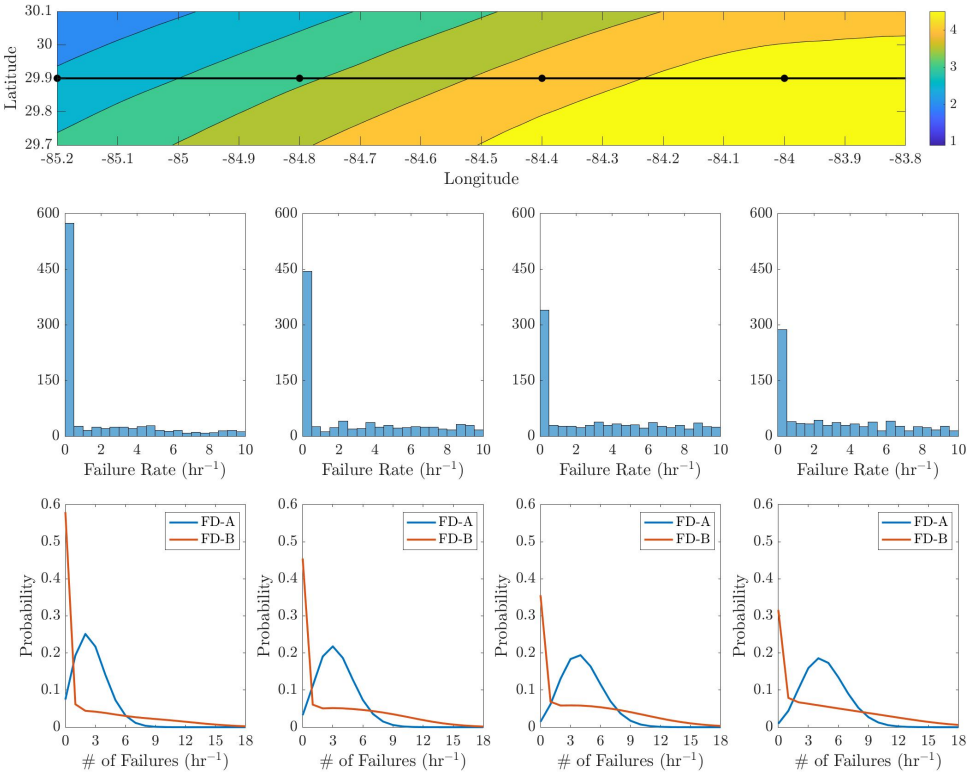

Figure 3-13: Illustration of how the probability distribution over number of failures depends on the selected failure distribution (FD-A vs. FD-B) for Hurricane Hermine. *Top row*: contour plot of spatially-varying failure rates given by FR-2 or $\mathbb{E}[\Lambda_g(\mathbf{H}_g)]$, with four locations g for analysis marked by the black dots. *Middle row*: Histogram of ensemble member failure rates $\Lambda_g^{(i)}$ at the four identified locations. *Bottom row*: Corresponding probability distributions over number of failures.

Analysis for Hurricane Michael: Figure 3-14 demonstrates how FD-A and FD-B differ for Hurricane Michael. Because Michael is significantly more intense than Hermine, the distributions have more pronounced tails, particularly at locations closer to the hurricane eye (towards the right in Figure 3-14). Both the failure histograms and probability distributions for locations closer to the hurricane eye display smaller

right-skewedness, reflecting an increased likelihood of high-damage scenarios as a result of the hurricane intensity.

As in the case of Hermine, FD-B has a more pronounced tail than FD-A.The 95% percentiles for number of failures under FD-A are given as follows (for the locations from left to right in Figure 3-14): 7, 15, 20, 18. In contrast, the 95% percentiles under FD-B are: 16, 23, 25, 24.

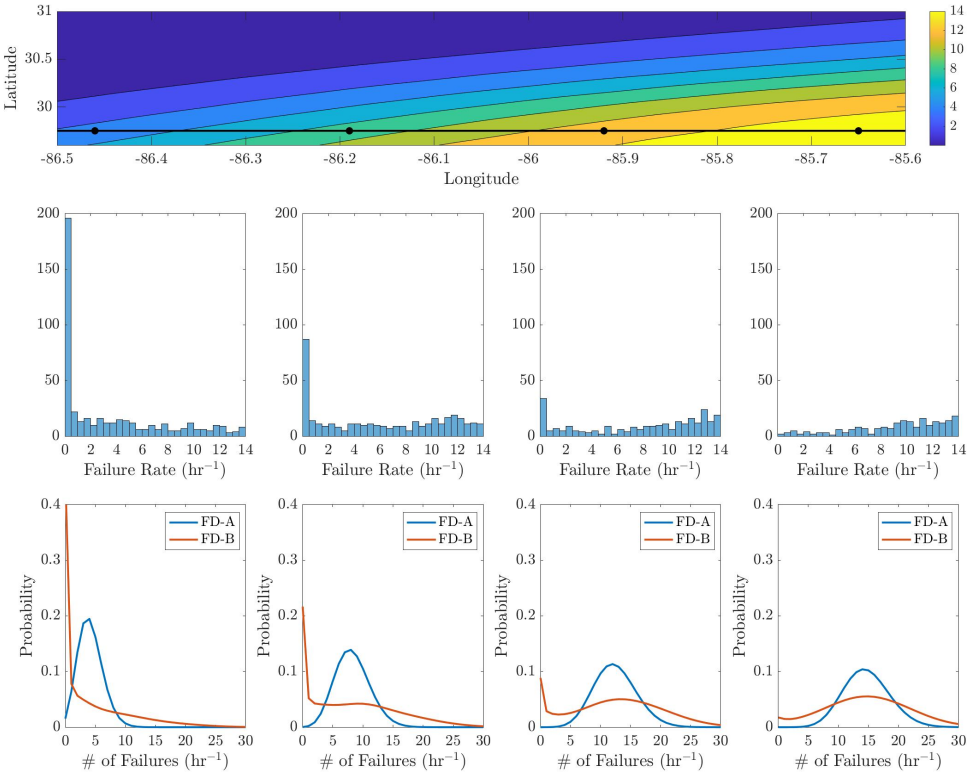

Figure 3-14: As in Figure 3-13, but for Hurricane Michael.

3.4 Predicting Outages in Historical Hurricanes

A lack of accurate damage predictions can impede estimates of loss-of-service within infrastructure systems. Improved estimation of loss-of-service is desirable in estimating hurricane-induced risk on the infrastructure system, as well as in informing proactive strategies to maintain post-disaster infrastructural functionality. In Sections 3.2-3.3, we focused on the spatial variability in NHPP estimates of probabilistic damage and effects of forecast uncertainty given by FHLO. In this section, we con-

sider the relationship between damage and loss-of-service. Specifically, we analyze the accuracy of estimated NHPP failure rates in predicting loss-of-service within electric power infrastructure resulting from Hurricane Michael. For electricity networks, we consider that loss-of-service is given by outages, or loss of electrical power network supply to customers. The failure rates (FR-2) are estimated using wind field forecasts given by FHLO as input (see Section 3.1.4).

We discuss the computational setup in Section 3.4.1: the application of FHLO and NHPP, the selected geographical region of interest, and the outage data employed. Our analysis focuses on the northwestern Florida region (including the Tallahassee urban area), where Hurricane Michael made landfall. In Section 3.4.2, we analyze the accuracy of estimated failure rates in predicting outages. In Section 3.4.3, we formulate regression models to predict outages, and demonstrate that a statistically significant relationship exists between the estimated failure rates and outage rates.

3.4.1 Computational Setup

The probabilistic wind field forecast for Michael is given by a 1,000-member ensemble forecast using FHLO. For each ensemble member, the velocity is forecasted at locations within the latitude range 29.3°N to 32.2°N and longitude range 82.6°W to 88.7°W, with $0.1° \times 0.1°$ grid spacing. The forecast is initialized on October 9, 2018 at 12Z (Coordinated Universal Time). This time corresponds with around 7:00am Central Daylight Time (CDT), which is about 1.5 days before Michael made landfall near Mexico Beach, Florida.

We obtain outage data from the Florida Division of Emergency Management [83]. Our analysis focuses on October 10-12, the days during and immediately after Michael's landfall in Florida. On these three days, outage data is available at six different times given in Central Daylight Time (CDT): October 10, 15:40; October 10, 16:35; October 10, 19:50; October 11, 19:40; October 11, 22:00; and October 12, 23:05. At each time, the outages are measured by number of households without power in each county. The total number of households and geographical area associated with each county are also included in the data. Using this data, one can compute the total

number of outages per county, the percentage of households experiencing outages, as well as percentage or number of households with outages normalized by area. We focus on outages in the counties of Northern Florida (particularly the Tallahassee area).

To compare outages to failure rates (FR-2), we first estimate the failure rates in each county on an hourly basis using the quadratic NHPP model (Section 3.1.3). This requires computing the Poisson intensity $\lambda_{g,t}^{(i)}$ using Eq. 3.5 in each $0.1^\circ \times 0.1^\circ$ grid g, at each hour t, and for each ensemble member i. For a grid g, the ensemble-averaged failure rate $\Lambda_g(t')$ at a given time $t' \leq t_\mathrm{f}$ (where t_f corresponds to Oct. 14 at 12Z, the last time for which FHLO is available) is given by:

$$\Lambda_g(t') \;=\; \frac{1}{\mathrm{H}} \sum_{i=1}^{\mathrm{H}} \sum_{t=t_0}^{t'} \lambda_{g,t}^{(i)}. \tag{3.26}$$

This summation is similar to Eq. 3.1, except that the summation is taken over $t \in \{t_0, ..., t'\}$ rather than $t \in \mathcal{T}$ where $\mathcal{T} = \{t_0, ..., t_\mathrm{f}\}$. These failure rates are expected to be increasing with time t', reflecting accumulated exposure of the electric power infrastructure to hurricane winds over time. Then, we map the grid-wise failure rates to county-wise failure rates. To do so, we assign a grid to a county, if the majority of the grid's spatial area is occupied by said county. We obtain the county-wise failure rate by averaging the grid-wise failure rates corresponding to the county.

We also define the ensemble-averaged "cumulative velocity" at a time t' and for grid g as follows:

$$\mathcal{V}_g(t') \;=\; \frac{1}{\mathrm{H}} \sum_{i=1}^{\mathrm{H}} \sum_{t=t_0}^{t'} v_{g,t}^{(i)}, \tag{3.27}$$

i.e., it is the ensemble-averaged sum of the grid-specific velocities over all measurement times from t_0 to t'. We will use the cumulative velocity as a predictor of the outage rate in Section 3.4.3. Next we compute county-wise cumulative velocities, using the same procedure that we applied to the failure rates. After obtaining the county-wise failure rates and cumulative velocities in Northern Florida, we can analyze the strength of these inputs as predictors of the outage data.

3.4.2 Outage and Failure Rates due to Hurricane Michael

In Figure 3-15, we plot the outage rates (number of outages per 100 households) and asset density-normalized failure rates (FR-2) in Northern Florida at four different times. Failure rates are calculated using Figure 3.26. Figure 3-15a plots the outages and failure rates about three hours after Hurricane Michael made landfall in Florida. In contrast, Figure 3-15d shows the results nearly 33 hours after landfall. Generally speaking, high failure rates correspond to high outage rates (and vice versa). More specifically, the highest outage and failure rates mostly occur in the geographical region between Panama City and Tallahassee. The counties with high outages rates mostly fall in the critical zone of the hurricane, which corresponds to the counties where the failure rates are higher (denoted by light blue, green, orange or yellow colors), as opposed to sub-critical regions corresponding to dark blue.

In Figure 3-15c – 3-15d, which correspond to October 11, nearly 100% of households suffer from outages in a few of the counties (mostly between Panama City and Tallahassee). However, failure rates differ noticeably across these counties. This illustrates 'saturation' of the outage rate at 100% when the failure rate is sufficiently high, due to a finite number of assets in the infrastructure system, which we accounted for in the probability distribution given by Eq. 3.3 in Section 3.1.2. The variability in failure rates within this region may also result due to the network topology of distribution feeders in the power infrastructure. For example, if a substation within a distribution feeder is disrupted, then power supply to all downstream loads will be interrupted. As another example, failure of a critical asset in the power infrastructure can cause multiple outages, whereas failure of non-critical assets may not cause any outage if the network is able to survive in the presence of these failures.

One would expect higher correlation between failure rate and outage rate if FHLO for Hurricane Michael were more accurate in forecasting landfall location. Because FHLO was initialized over a day before landfall, discrepancy between the forecasted and observed landfall location is expected. This is reflected in the estimated failure rates using FHLO. The highest estimated failure rates occur in Gulf County, whereas

Hurricane Michael made landfall in Bay County, which is directly to the west of Gulf County. The discrepancy between forecasted and observed landfall location is expected to decrease if FHLO is initialized closer to the observed landfall time.[5]

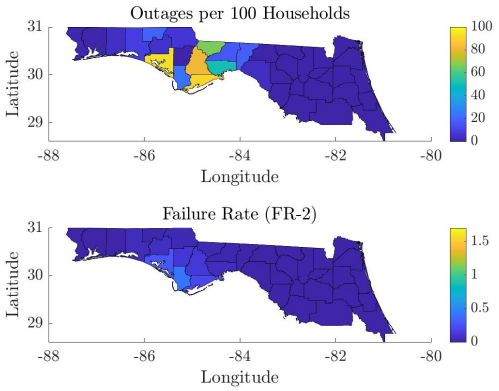

(a) October 10, 16:35

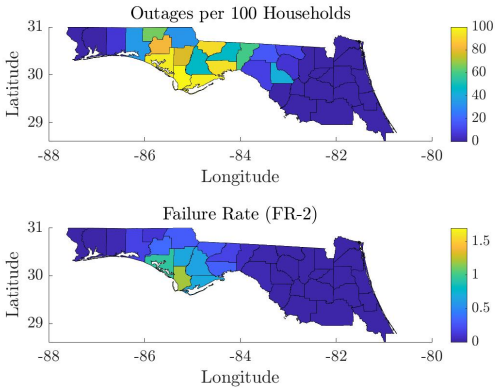

(b) October 10, 19:50

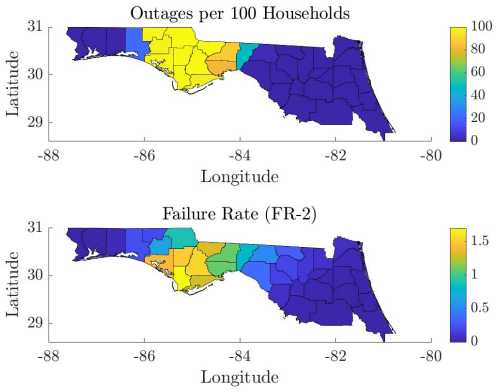

(c) October 11, 19:40

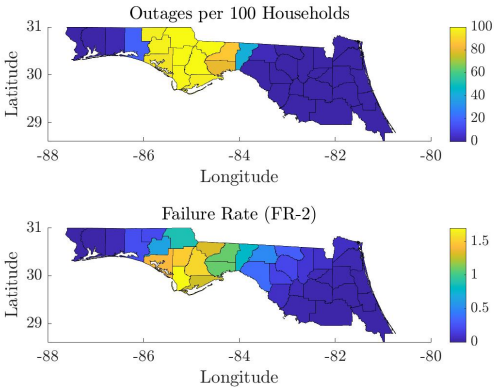

(d) October 11, 22:00

Figure 3-15: Comparison of outage rates and failure rates (FR-2) in Northern Florida for Hurricane Michael, at four different times after landfall. The outage rate for each county is given by outages per 100 households. The failure rate in each county at a given time is obtained by accumulating Poisson intensities estimated using FHLO from 10/9/2018 at 12Z (7:00am in Florida) to the time in question.

[5]On another note, the post-landfall hurricane maximum intensity forecast given by FHLO was lower than the observed intensity.

3.4.3 Outage Prediction via Regression Models

We estimate regression models that relate outage rate (outages per 100 households) to one of two inputs: failure rate (FR-2, Eq. 3.26) or cumulative velocity (Eq. 3.27). The cumulative velocity is employed in order to analyze the extent to which the critical velocity V_{crit} affects the outage prediction. According to the quadratic model, Poisson intensities are small and constant for velocities below V_{crit}. Thus we hypothesize that failure rates remain insignificant below a certain cumulative velocity threshold, which translates to near-zero outage rates. Our goal is to evaluate this hypothesis using the empirical observations of outages.

To assess the strength of cumulative velocities and failure rates as predictors of outage rates, we estimate binomial regression models (BRMs), a specific type of generalized linear model (GLM). In particular, the BRM gives the probability over number of successes out of a set of Bernoulli trials. In our case, a "success" is an outage and the number of "trials" is given by the number of households in a given county. We estimate a BRM for each input (cumulative velocity or failure rate) and at each time for which outage data is available. Figure 3-16 (resp. 3-17) plots the outage rate vs. cumulative velocity (resp. failure rate) at four different times; estimated binomial regression models are included in the plots. For more details regarding implementation of the BRM, please see Section 3.7 (Appendix A).

We find that cumulative velocity is a statistically significant predictor (p-value less than 0.05) at all considered times except October 12, 23:05 (about 58 hours after landfall), and failure rate is a statistically significant predictor at all times. The cumulative velocity-outage rate relationship is not statistically significant on October 12, 23:05, because it has been over two days since Hurricane Michael made landfall in Northern Florida. Over the course of this time, Michael traveled northward; there was ample time for utilities to repair damage and restore electricity service. This suggests that cumulative velocity alone would not be a sufficient predictor of outages at this time, because spatially-varying repair rates become increasingly important with time.

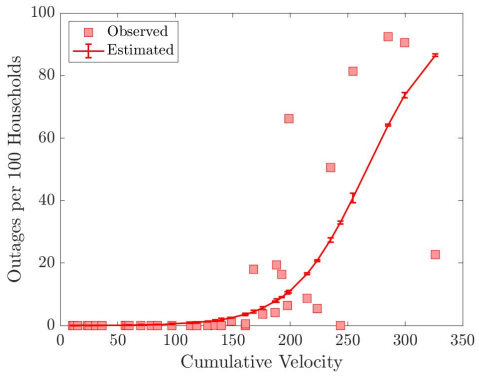

(a) October 10, 16:35

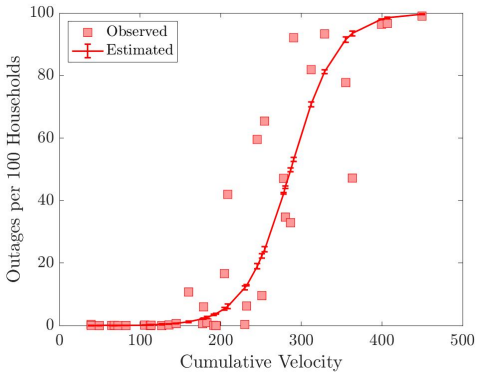

(b) October 10, 19:50

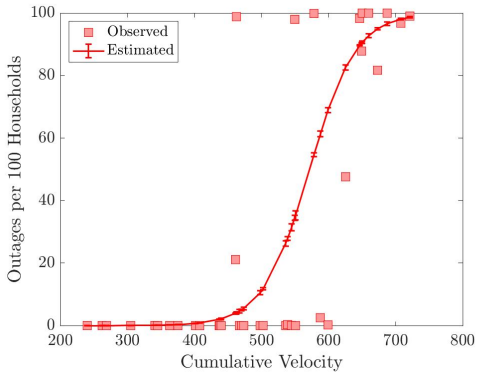

(c) October 11, 19:40

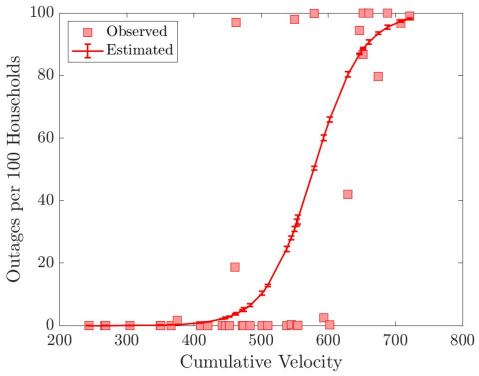

(d) October 11, 22:00

Figure 3-16: Scatterplots of outages vs. cumulative velocity in Northern Florida for Hurricane Michael, at four different times, accompanied by corresponding estimated binomial regression models. Outages are measured by households without power. The cumulative velocity in a county at a given time is obtained by accumulating velocities estimated using FHLO from 12Z (7:00 in Florida) to the time in question, and then taking the cumulative velocity averaged across all $0.01° \times 0.01°$ grids in the county.

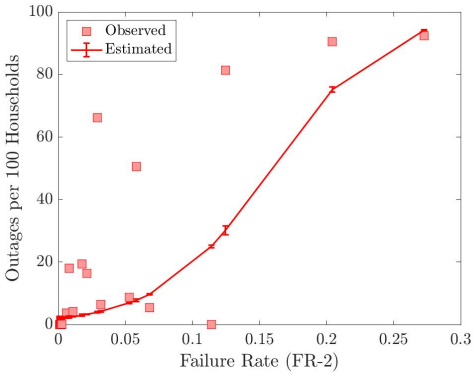

(a) October 10, 16:35

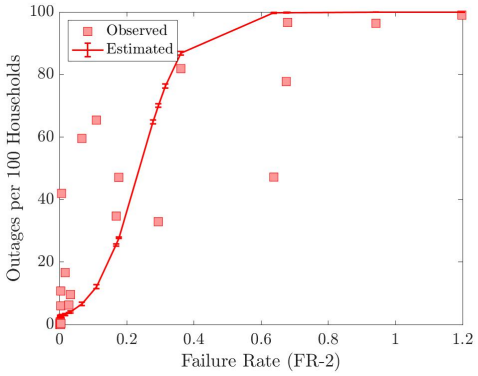

(b) October 10, 19:50

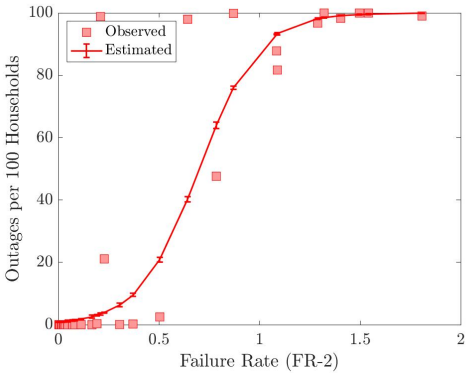

(c) October 11, 19:40

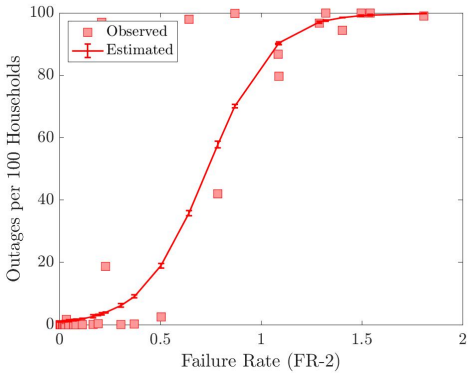

(d) October 11, 22:00

Figure 3-17: As in Figure 17, but for outages vs. failure rates.

We observe from the figures that the relationship between outage rate and cumulative velocity could be approximately represented by an S-shaped curve. The outage rate is near-zero and roughly constant for cumulative velocities below a certain threshold. Once this cumulative velocity threshold is passed, we observe a rapid increase in the outage rate with cumulative velocity, because of the quadratic relationship between Poisson intensity and velocity above V_{crit}. Then once the cumulative velocity becomes sufficiently high, the outage rate approaches 100%, i.e., saturation has occurred. The lower end of the S-shaped curve suggests that empirical observations regarding outages are consistent with the inclusion of the critical velocity parameter in the NHPP model. In summary, the binomial regression model is able to account for the impact of the critical velocity on the outage rates, as well as the saturation of outage rates at 100%.

In the plots of outage rate vs. failure rate, a large number of counties have low failure rates and thus are bunched in the left-hand side of the plots. This results in a shortening of the lower end of the "S", and thus the S-shaped curve is not as apparent in the plots of the outage rate vs. failure rate. These counties with low failure rates may exhibit significant variability in cumulative velocity, but they have few exceedances above V_{crit} and thus the variations in velocities are not reflected in the failure rates.

Not surprisingly, there are some outliers in Figures 17-18. For example, the point in the upper left hand corner of Figures 3-17c – 3-17d corresponds to Holmes county. This county has the smallest area of all 37 counties we considered in this study as well as a low population density (ranks in the bottom quartile among Florida counties) [9], which can explain why it had a particularly high percentage of outages.

3.5 Modeling Damage and Financial Losses

In this section, we estimate parametric models that relate total hurricane-induced damage and financial losses in an infrastructure system to key storm parameters.

In particular, we consider the storm intensity parameter V_m and size parameter

R_m (see Section 3.2.1). The parametric models are estimated using the quadratic nonhomogeneous Poisson process (NHPP) model detailed in Section 3.1.3, to demonstrate simple power law relationships between damage, financial losses, and hurricane parameters. In Section 3.5.1, we discuss the estimated model that relates total infrastructural damage to V_m and R_m; in Section 3.5.2, we do the same for financial losses. Further details related to the parametric models are included in Sections 3.8-3.9 (Appendix B-C).

We note that in order to isolate the relationship between damage, financial losses, and hurricane parameters, we do not employ FHLO in this section. To use FHLO for estimating parametric models of total damage and losses, we would need to obtain wind field ensembles from a large number of historical hurricanes. Naturally, the computational expense of calculating failure rates from all the ensembles would be high. Furthermore, hurricane intensity and size will vary temporally in FHLO, which would make estimating the parametric functions less straightforward. However it would also be possible to repeat the exercise we conduct in this section using FHLO.

For the purpose of estimating the parametric models, we assume that hurricanes have the same characteristics as were defined in Section 3.2.1; that is, we assume the hurricane moves in a straight line at a constant translation speed; the hurricane wind field is given by the Holland model; and the Holland parameters (V_m, R_m, B) stay constant during the hurricane lifetime.

3.5.1 Damage Dependency on Hurricane Intensity and Size

We now estimate a parametric function that relates the total expected damage Λ_{total} to the hurricane intensity V_m and size R_m. The total expected damage (per unit length of assets) is measured by the sum of the failure rates over all grids, i.e., $\Lambda_{\text{total}} = \sum_g \Lambda_g$. Using Eq. 3.8 to calculate Λ_g, the total expected damage is given by:

$$\Lambda_{\text{total}} \;=\; |\mathcal{G}|\lambda_{\text{norm}}\mathrm{T} + \lambda_{\text{norm}}\alpha \sum_{g\in\mathcal{G}_c}\sum_{t\in\mathcal{T}_{c,g}} \Big(f^2(v_{g,t}) - 1\Big)\Delta t, \tag{3.28}$$

where $\mathcal{G}_c$ denotes the set of grids inside the critical zone and $\mathcal{T}_{c,g}$ denotes the set of times for which $v_{g,t} \geq \mathrm{V_{crit}}$. The first term in Eq. 3.28 denotes the value of Λ_{total} under nominal conditions; the second term denotes the increase in Λ_{total} due to hurricane winds exceeding the critical velocity $\mathrm{V_{crit}}$. The full derivation of Eq. 3.28 is given in Section 3.8.1 (Appendix B).

Due to the highly nonlinear nature of the Holland model, it is not convenient to use Eq. 3.28 for relating total expected damage Λ_{total} to $\mathrm{V_m}$ and $\mathrm{R_m}$. Instead we formulate a parametric function for Λ_{total} which accounts for two important considerations. First, the total expected damage depends on the area of the critical zone $\mathrm{A_{crit}}$, which is represented by $\mathcal{G}_c$ in Eq. 3.28 and can be estimated using Eq. 3.25a in Section 3.2.2. Second, we account for the critical velocity $\mathrm{V_{crit}}$, because damage in regions with subcritical winds corresponds to nominal (no-hurricane) damage and is independent of hurricane velocities in the quadratic NHPP model. We define a new function to incorporate this consideration:

$$g(\mathrm{V_m}) = \frac{\max(\mathrm{V_{crit}}, \mathrm{V_m}) - \mathrm{V_{crit}}}{\mathrm{V_{crit}}} \tag{3.29}$$

The function $g(\mathrm{V_m}) = 0$ if $\mathrm{V_m} \leq \mathrm{V_{crit}}$, and increases linearly with $\mathrm{V_m}$ otherwise.

Using the critical zone area calculated following Eq. 3.25a, we formulate a parametric function that relates total expected damage to $\mathrm{R_m}$ and $g(\mathrm{V_m})$. We find that the total expected damage is roughly proportional to $\mathrm{R_m^2}$ and $[g(\mathrm{V_m})]^{2.3}$, as opposed to the quadratic relationship between location-specific failure rate and velocity in Eq. 3.5. When $\mathrm{V_m} \geq \mathrm{V_{crit}}$, this power law relationship can be expressed as:

$$\Lambda_{\mathrm{total}}(\mathrm{V_m}, \mathrm{R_m}) \ \sim \ \mathrm{O}\big(\mathrm{R_m^2}(\mathrm{V_m} - \mathrm{V_{crit}})^{2.3}\big). \tag{3.30}$$

This relationship is suggested by the estimated parametric function for $\Lambda_{\mathrm{total}}(\mathrm{V_m}, \mathrm{R_m})$:

$$\Lambda_{\mathrm{total}}(\mathrm{V_m}, \mathrm{R_m}) \ = \ c_1 + c_2 \mathrm{R_m}[g(\mathrm{V_m})]^{1.1} + c_3 \mathrm{R_m^2}[g(\mathrm{V_m})]^{2.3} - c_4 \mathrm{R_m} g(\mathrm{V_m}). \tag{3.31}$$

The parametric function and its parameter values are discussed in further detail in

Section 3.8.2 (Appendix B). Note that Eq. 3.31 does not account for finiteness in the total number of assets, and thus the total expected damage Λ_{total} continues to increase even when V_m reaches very high values.

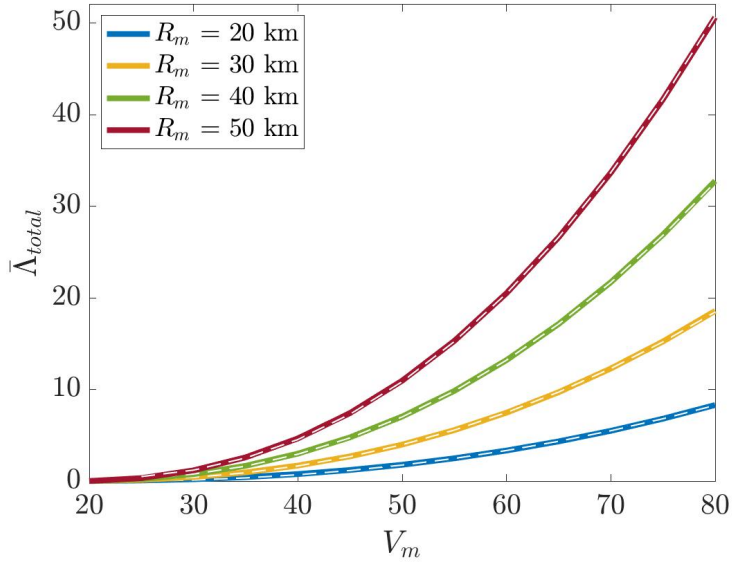

Figure 3-18: Normalized expected damage $\bar{\Lambda}_{\text{total}}$ as a function of V_m for fixed values of R_m. The estimated parametric function using Eq. 3.31 is denoted by the white dotted lines. The numerically-computed values of $\bar{\Lambda}_{\text{total}}$ are given by the dark-colored lines (see Section 3.8.2 in Appendix B for details).

In Figure 3-18, we plot the expected normalized damage $\bar{\Lambda}_{\text{total}} = \Lambda_{\text{total}}/|\mathcal{G}|$ vs. maximum intensity V_m, which is accompanied by parametric fits given by Eq. 3.31.

Now we compute expected normalized damage $\bar{\Lambda}_{\text{total}}$ under the assumption of finiteness in the number of assets. Figure 3-19 illustrates the expected normalized damage in a typical rural area that has about $\bar{S}_g = 6.5$ distribution lines in each spatial location $g \in \mathcal{G}$.[6] The plots of $\bar{\Lambda}_{\text{total}}$ vs. V_m in the left-hand figure feature an S-shaped curve that is similar to what we observed in Figure 17, under R_m = 30, 40, or 50 km. For R_m = 20 km, the S shape is less pronounced, but the expected normalized damage still asymptotically approaches $\bar{S} = 6.5$ with sufficiently high V_m. In the right-hand plot of damage vs. R_m and V_m, a large portion of the contour plot

[6]We considered Talquin Electric Cooperative in Northwestern Florida. They have about 4,400 km of distribution lines, which provide coverage for about 6700 km^2, averaging to 0.65 km of line/km^2 area [92]. Under the assumption that a distribution line is on average 100 meters in length, this averages to 6.5 lines/km^2 area. We assume that each spatial location g has an area of 1 km^2.

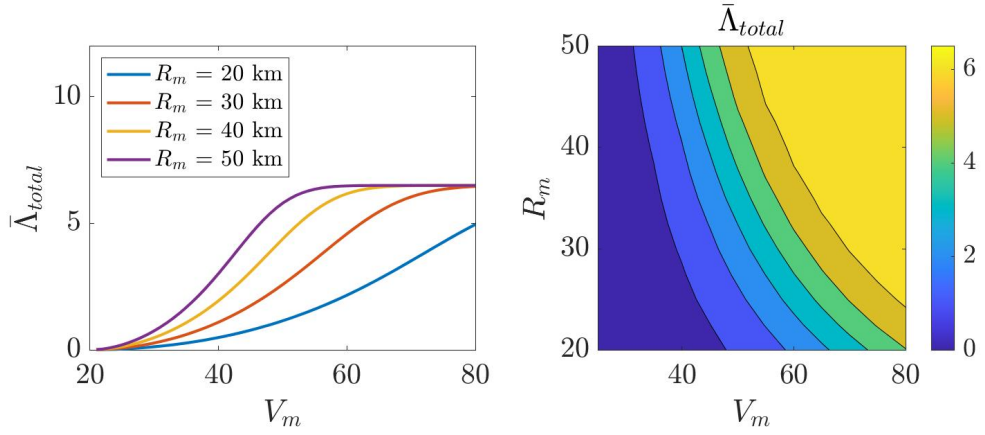

Figure 3-19: Expected normalized damage $\bar{\Lambda}_{\text{total}}$ in a typical rural area, under the saturation model. *Left*: $\bar{\Lambda}_{\text{total}}$ vs. V_m, under four different values of R_m. *Right*: $\bar{\Lambda}_{\text{total}}$ as a function of both V_m and R_m.

has a value of 6.5, indicating the saturation.

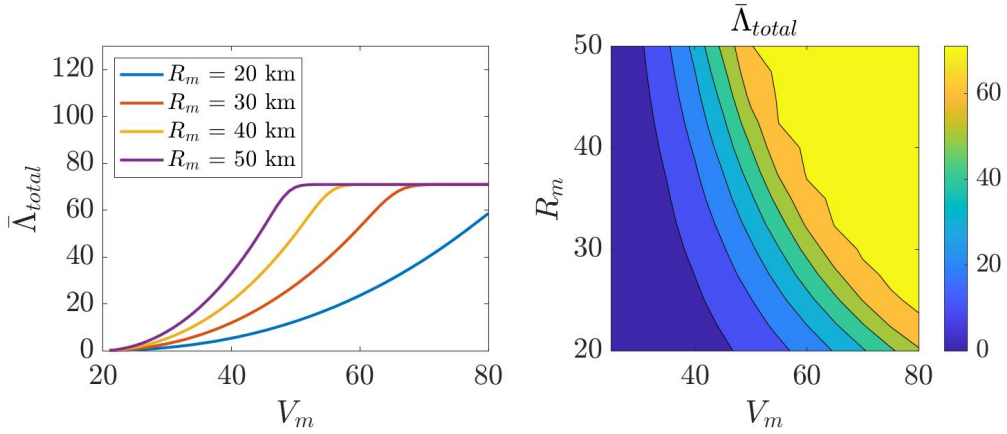

Figure 3-20: As in Figure 3-19, but for a typical urban area.

In Figure 3-20, we plot $\bar{\Lambda}_{\text{total}}$ in a typical urban area that has about 71 lines per km^2 of area.[7] Once again, we see S-shaped curves as we did in the rural area, as well as large regions of saturation in the right-hand plot.

[7]We considered The City of Tallahassee Utilities. They have 1,800 km of distribution lines over 255 km^2, averaging to 7.08 km of line/km^2 area [74]. This averages to about 71 distribution lines per grid.

3.5.2 Financial Loss Dependency on Hurricane Intensity and Size

Finally, we formulate a parametric function that relates the total expected financial losses $\mathrm{L_{total}}$ to the hurricane parameters $\mathrm{R_m}$ and $g(\mathrm{V_m})$. We can write the total expected financial losses as:

$$\mathrm{L_{total}} \;=\; \sum_{g\in\mathcal{G}} \mathrm{L}_g(s_g), \tag{3.32}$$

where $\mathrm{L}_g(s_g)$ is the loss in location g as a function of the number of failures s_g.

To determine the relationship between L_g and s_g, we assume that we have an estimate of the financial loss per failed asset per unit time, and that the estimate is constant with time and for all assets. This estimate permits us to compute the financial loss $\mathrm{L}_{g,k}$ in each location g at a given time k after repairs have commenced. Then we estimate L_g by integrating $\mathrm{L}_{g,k}$ over time up to a defined time horizon, at which repairs are assumed to be complete. Because the damaged assets in an infrastructure system are repaired over an extended period of time, certain assets may not be repaired for awhile and thus L_g is expected to be a nonlinear function of damage s_g. Under a repair schedule dictated by the network repair model detailed in Section 3.9.1 (Appendix C), $\mathrm{L}_{g,k}$ (resp. L_g) scales linearly (resp. quadratically) with the number of failures s_g.

We use the network repair model to derive an analytical model of total expected financial losses:

$$\begin{aligned}\mathrm{L_{total}} \;=\; \frac{1}{2}\frac{\mathrm{L}_f}{\mathrm{Y}}\Bigg(|\mathcal{G}|(\lambda_{\mathrm{norm}}\mathrm{T})^2 \;+\; 2\lambda_{\mathrm{norm}}^2\alpha\mathrm{T}\sum_{g\in\mathcal{G}_u}\sum_{t\in\mathcal{T}_{c,g}}\big(f^2(v_{g,t})-1\big)\Delta t \\ +\; (\lambda_{\mathrm{norm}}\alpha)^2\sum_{g\in\mathcal{G}_u}\Bigg(\sum_{t\in\mathcal{T}_{c,g}}\big(f^2(v_{g,t})-1\big)\Delta t\Bigg)^2\Bigg)\end{aligned} \tag{3.33}$$

Follow Eq. 3.33, the total financial loss under nominal (no-hurricane) conditions is given by

$$\mathrm{L_{total,nom}} \;=\; \frac{1}{2}\frac{\mathrm{L}_f}{\mathrm{Y}}|\mathcal{G}|(\lambda_{\mathrm{norm}}\mathrm{T})^2. \tag{3.34}$$

The remaining terms in Eq. 3.33 denote the increase in $\mathrm{L}_{\mathrm{total}}$ due to hurricane winds exceeding the critical velocity. In particular, the term $(\lambda_{\mathrm{norm}}\alpha)^2 \sum_{g\in\mathcal{G}_u} \big(\sum_{t\in\mathcal{T}_{c,g}} \big(f^2(v_{g,t}) - 1\big)\Delta t\big)^2$ indicates that the location-specific financial loss scales with the wind velocity to the 4^{th} power within the critical zone. The derivation of Eq. 3.33 is detailed in Section 3.9.2 of Appendix C.

In order to formulate a parametric model that relates total expected financial loss to R_{m} and $g(\mathrm{V}_{\mathrm{m}})$, we consider the parametric model for damage in Section 3.5.1 and the network repair model in Section 3.9.1 of Appendix C. Because of the quadratic relationship between location-specific financial loss and number of damages, we expect that the polynomial orders associated with R_{m} and $g(\mathrm{V}_{\mathrm{m}})$ for $\mathrm{L}_{\mathrm{total}}$ are greater than those for expected damage Λ_{total}. Specifically, when $\mathrm{V}_{\mathrm{m}} \geq \mathrm{V}_{\mathrm{crit}}$, we find that the relationship between total expected financial loss $\mathrm{L}_{\mathrm{total}}$ and hurricane parameters can be expressed as:

$$\mathrm{L}_{\mathrm{total}}(\mathrm{V}_{\mathrm{m}}, \mathrm{R}_{\mathrm{m}}) \;\sim\; \mathrm{O}\big(\mathrm{R}_{\mathrm{m}}^3(\mathrm{V}_{\mathrm{m}} - \mathrm{V}_{\mathrm{crit}})^{4.8}\big). \tag{3.35}$$

This relationship is suggested by the estimated parametric function for $\mathrm{L}_{\mathrm{total}}$:

$$\begin{aligned}\mathrm{L}_{\mathrm{total}}(\mathrm{V}_{\mathrm{m}}, \mathrm{R}_{\mathrm{m}}) \;&= d_1\mathrm{R}_{\mathrm{m}}[g(\mathrm{V}_{\mathrm{m}})]^{1.6} + d_2\mathrm{R}_{\mathrm{m}}^2[g(\mathrm{V}_{\mathrm{m}})]^{3.2} + d_3\mathrm{R}_{\mathrm{m}}^3[g(\mathrm{V}_{\mathrm{m}})]^{4.8} \\ &\quad + d_4\mathrm{R}_{\mathrm{m}}^2[g(\mathrm{V}_{\mathrm{m}})]^{1.8} + d_5\mathrm{R}_{\mathrm{m}}^3[g(\mathrm{V}_{\mathrm{m}})]^{1.8} + d_6\mathrm{R}_{\mathrm{m}}^3[g(\mathrm{V}_{\mathrm{m}})]^{3.5}\end{aligned} \tag{3.36}$$

The parametric function and its parameter values are discussed in further detail in Section 3.9.3 of Appendix C. As was the case for total expected damage, we assume that the total number of assets is infinite.

In Figure 3-21, we plot the expected normalized financial losses $\bar{\mathrm{L}}_{\mathrm{total}} = \mathrm{L}_{\mathrm{total}}/|\mathcal{G}|$ versus maximum intensity V_{m}, which is accompanied by parametric fits given by Eq. 3.36.

Previous work by William D. Nordhaus [76] has suggested that total hurricane-induced financial losses are roughly a function of V_{m} to the 8-th power. In contrast, we estimate the relationship between total financial losses and $g(\mathrm{V}_{\mathrm{m}})$, rather than V_{m}. This accounts for our expectation of insignificant damage below the critical velocity $\mathrm{V}_{\mathrm{crit}}$, which we showed is in agreement with empirical observations in Section 3.4. By using $g(\mathrm{V}_{\mathrm{m}})$ as a predictor, we estimate that total losses are roughly proportional to

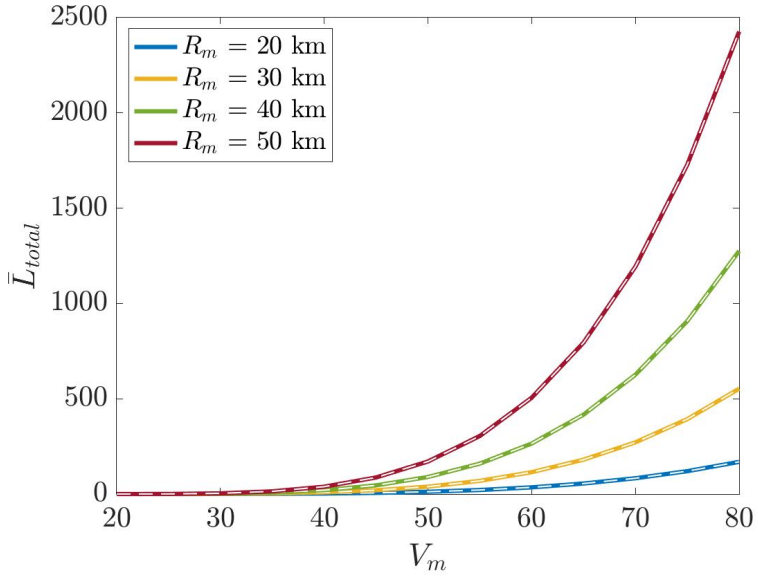

Figure 3-21: Normalized expected loss as a function of V_m for fixed values of R_m. The estimated parametric function using Eq. 3.36 is denoted by the white dotted lines. The numerically-computed values of $\bar{L}_{total}$ are given by the dark-colored lines.

$V_m - V_{crit}$ to the 4.8-th power, when $V_m \geq V_{crit}$. In contrast, when we used V_m as a predictor, we found that losses were proportional to V_m to the 7.8-th power.

Unlike Nordhaus, we can also incorporate 'saturation' into the damage and financial loss estimation. This would entail using Eq. 3.4 for the purpose of numerically computing the total expected damage. Then, we could estimate sigmoid functions that relate total damage and financial losses to the storm parameters V_m and R_m.

3.6 Concluding remarks

In this section, we introduced a modeling approach for probabilistic estimation of hurricane wind-induced damage to infrastructural assets. Our approach uses a Non-homogeneous Poisson Process (NHPP) model to estimate spatially-varying probability distributions of damage as a function of the hurricane wind field velocities. The NHPP model is applied to failures of overhead assets in electricity distribution systems, and features a quadratic relationship between the Poisson intensity and wind velocity above a defined critical velocity threshold. In order to incorporate hurricane

forecast uncertainty in estimation of the damage distributions, we use wind field ensembles given by Forecasts of Hurricanes using Large-Ensemble Outputs (FHLO) as inputs into the NHPP model.

The NHPP model's critical velocity parameter motivates us to define the "critical zone", a measure of the spatial extent of hurricane-induced damage. Using a simple, stylized model of the hurricane that incorporates the axisymmetric Holland wind field model, we demonstrate how the critical zone and failure rates are dependent on hurricane intensity, size, and asymmetries. Furthermore, we show that not incorporating hurricane forecast uncertainty given by FHLO results in underestimation of failure rates, and assess the degree of underestimation under two hurricanes of different intensities (Hermine and Michael). In addition, we empirically demonstrate that improperly estimating probability distributions of damage results in underestimation of high-damage scenarios. These findings suggest that forecast uncertainty plays a critical role in estimation of hurricane-induced damage.

Our modeling approach is able to accurately predict outages resulting from Hurricane Michael. By fitting binomial regression models (BRMs), we demonstrate that failure rate and cumulative velocity are statistically significant predictors of the outage rate. The fitted BRMs also demonstrate that empirical observations are reflective of the critical velocity parameter in the NHPP model, and that the outage rates saturate at 100% once failure rates are sufficiently high. Finally, we fit simple parametric models that relate total damage and financial losses to key hurricane parameters (intensity and size). Under a simple, stylized hurricane model, we show that total damage is proportional to intensity (resp. size) to the 2.3-th (resp. 2-th) power, and that total financial losses is proportional to intensity (resp. size) to the 4.8-th (resp. 3-rd) power.

Future work on this topic will focus on the joint effects of damage and network topology on infrastructure system loss-of-service. Network topology determines connectivity between the service producers and end-users, as well as the criticality of various infrastructure assets, such that damage of more critical assets results in an especially significant loss-of-service. It is also worth noting that this work focuses

on hurricane winds, rather than other relevant physically-based threats induced by hurricanes. These threats, such as storm surge and rainfall, can also cause substantial damage to infrastructure systems.

A second avenue of future work is to apply improved damage and loss-of-service estimates to the design of proactive (pre-storm) strategies that minimize hurricane wind-induced risk on infrastructure systems. Accurate estimation of spatially-varying damage minimizes risk by not only improving the optimality of proactive strategies, but also by increasing the efficiency of damage localization and repair. For instance, a plethora of works address optimal proactive allocation of distributed energy resources (DERs) [41, 86, 16, 17] in distribution feeders of electric power infrastructure; our work is readily applicable to the proposed methods in these works.

3.7 Appendix A: Binomial Regression Model

The binomial regression model (BRM) is a specific type of generalized linear model (GLM), which is a generalization of ordinary linear regression models that allows for response variables to have non-Gaussian error distribution models. In the BRM, model inputs are used to estimate the probability associated with a Bernoulli trial. Then, this probability estimate is used as a parameter in the binomial distribution, which provides probabilities over the number of outages given a specified number of Bernoulli trials (number of households). The model inputs we consider are the cumulative velocity $\mathcal{V}$ or failure rate Λ.

The binomial distribution is stated as follows for our problem:

$$\Pr(o_{c,t} \mid \mathbf{x}_{c,t}) \;=\; \binom{nh_c}{o_{c,t}} (\pi_{c,t})^{o_{c,t}} (1-\pi_{c,t})^{nh_c - o_{c,t}} \tag{3.37}$$

which predicts the probability that $o_{c,t}$ households suffer from outages at time t and county c, given the input $\mathbf{x}_{c,t}$, single-household outage probability $\pi_{c,t}$, and number of households nh_c. The probability $\pi_{c,t}$ is determined using a generalized linear model

(GLM) equation:

$$g(\pi_{c,t} \mid \mathbf{x}_{c,t}) \;=\; \beta_0^{(\mathbf{x},t)} + \beta_1^{(\mathbf{x},t)} \mathbf{x}_{c,t}, \tag{3.38}$$

where $\mathbf{x}_{c,t}$ is given by the failure rate $\Lambda_{c,t}$ or cumulative velocity $\mathcal{V}_{c,t}$ calculated at time t, and $g(\cdot)$ is given by the logistic (logit) linking function:

$$g(\pi_{c,t}) \;=\; \ln\Big(\frac{\pi_{c,t}}{1-\pi_{c,t}}\Big). \tag{3.39}$$

Our goal is to estimate the coefficients of the GLM equation, $\beta_0^{(\mathbf{x},t)}$ and $\beta_1^{(\mathbf{x},t)}$, under each choice of input $\mathbf{x}$ (failure rate or cumulative velocity) and at each time t. In order to estimate the coefficients, we use the MATLAB function `glmfit`.

3.8 Appendix B: Parametric Damage Models

3.8.1 Analytical Solution for Total Damage

For the purpose of formulating an equation for total expected damage, let $\mathcal{G}_c$ denote the set of grids that lie inside the critical zone and $\mathcal{G}_u = \mathcal{G} \setminus \mathcal{G}_c$ the set of grids outside the critical zone. Furthermore, we assume that velocities are measured at a discrete set of times $\mathcal{T}$. For a grid g, $\mathcal{T}_{c,g}$ is the set of times for which $v_{g,t} \geq \mathrm{V_{crit}}$ and $\mathcal{T}_{u,g} = \mathcal{T} \setminus \mathcal{T}_{c,g}$ is the set of times for which $v_{g,t} < \mathrm{V_{crit}}$. We define $\mathrm{T}_{c,g}$ to be the total duration of time during which $v_{g,t} \geq \mathrm{V_{crit}}$ and $\mathrm{T}_{u,g} = \mathrm{T} - \mathrm{T}_{c,g}$ to be the total duration of time during which $v_{g,t} < \mathrm{V_{crit}}$.

Then the expected damage in a region (per unit of length of assets) is given by Λ_{total}:

$$
\begin{aligned}
\Lambda_{\text{total}} &= \sum_{g\in\mathcal{G}} \Lambda_g \\
&= \sum_{g\in\mathcal{G}} \Big[\lambda_{\text{norm}} \mathrm{T}(1-\alpha) \;+\; \lambda_{\text{norm}}\alpha\Delta t \sum_{t\in\mathcal{T}} f^2(v_{g,t})\Big] \\
&= |\mathcal{G}|\lambda_{\text{norm}}\mathrm{T}(1-\alpha) + \lambda_{\text{norm}}\alpha\Delta t \sum_{g\in\mathcal{G}}\sum_{t\in\mathcal{T}} f^2(v_{g,t}) \\
&= |\mathcal{G}|\lambda_{\text{norm}}\mathrm{T}(1-\alpha) + \lambda_{\text{norm}}\alpha \sum_{g\in\mathcal{G}} \left(\mathrm{T}_{u,g} + \sum_{t\in\mathcal{T}_{c,g}} \Delta t f^2(v_{g,t})\right) \\
&= |\mathcal{G}|\lambda_{\text{norm}}\mathrm{T}(1-\alpha) + \lambda_{\text{norm}}\alpha \sum_{g\in\mathcal{G}} \left(\mathrm{T} + \sum_{t\in\mathcal{T}_{c,g}} \Big(f^2(v_{g,t}) - 1\Big)\Delta t\right) \\
&= |\mathcal{G}|\lambda_{\text{norm}}\mathrm{T} + \lambda_{\text{norm}}\alpha \sum_{g\in\mathcal{G}_c}\sum_{t\in\mathcal{T}_{c,g}} \Big(f^2(v_{g,t}) - 1\Big)\Delta t.
\end{aligned}
\tag{3.40}
$$

3.8.2 Formulation of Parametric Model for Total Damage

To formulate a parametric model for damage, we need to account for the critical velocity V_{crit} and critical zone area, as discussed in Section 3.5.1. Regarding the critical zone area, we note that velocity increases with radius r for $r \leq \mathrm{R_m}$, and then decreases with r for $r > \mathrm{R_m}$. Consequently, the region of the hurricane surrounding the hurricane center (eye) contains subcritical velocities. However, this region is part of the critical zone as defined in Section 3.2.2, and thus we need to form a parametric model that corrects for this. Let us consider the following parametric damage function:

$$
\bar{\Lambda}_{\text{total}}(\mathrm{V_m}, \mathrm{R_m}) \;=\; \Lambda_{\text{total,nom}} + \Lambda_{\text{total,crit}}(\mathrm{V_m}, \mathrm{R_m}) - \Lambda_{\text{total,inner}}(\mathrm{V_m}, \mathrm{R_m}), \tag{3.41}
$$

where expected normalized damage $\bar{\Lambda}_{\text{total}} = \Lambda_{\text{total}}/|\mathcal{G}|$ refers to the expected number of failures per grid per unit length of assets, and:

$$
\begin{aligned}
\Lambda_{\text{total,nom}} &= c_1 \\
\Lambda_{\text{total,crit}}(\mathrm{V_m}, \mathrm{R_m}) &= c_2 \mathrm{R_m}[g(\mathrm{V_m})]^{p_1} + c_3 \mathrm{R_m^2}[g(\mathrm{V_m})]^{2p_1} \\
\Lambda_{\text{total,inner}}(\mathrm{V_m}, \mathrm{R_m}) &= c_4 \mathrm{R_m}[g(\mathrm{V_m})]^{p_2} + c_5 \mathrm{R_m^2}[g(\mathrm{V_m})]^{2p_2},
\end{aligned}
\tag{3.42}
$$

where $\Lambda_{\text{total,nom}} = c_1$ is the intercept term; $\Lambda_{\text{total,crit}}(\text{V}_\text{m}, \text{R}_\text{m})$ is an estimate of damage due to velocity exceedances in the critical zone; and $\Lambda_{\text{total,inner}}(\text{V}_\text{m}, \text{R}_\text{m})$ corrects for the inner hurricane region with subcritical velocities. $\Lambda_{\text{total,crit}}(\text{V}_\text{m}, \text{R}_\text{m})$ contains two terms – the first term is a linear function of R_m and the second is a quadratic function of R_m, which is reflective of Eq. 3.24. Likewise, the first and second terms of $\Lambda_{\text{total,crit}}(\text{V}_\text{m}, \text{R}_\text{m})$ are respectively functions of $[g(\text{V}_\text{m})]^{p_1}$ and $[g(\text{V}_\text{m})]^{2p_1}$. The term $\Lambda_{\text{total,inner}}(\text{V}_\text{m}, \text{R}_\text{m})$ has the same structure as $\Lambda_{\text{total,crit}}(\text{V}_\text{m}, \text{R}_\text{m})$. If we wish to obtain the total expected damage Λ_{total}, we simply multiply all estimated coefficients (c_1, c_2, c_3, c_4, c_5) by $|\mathcal{G}|$.

For purposes of estimating Eq. 3.41, we numerically compute expected damage to overhead assets in electricity infrastructure systems, using the NHPP model with the following parameters: $\lambda_{\text{norm}} = 3.5 \times 10^{-5}$ failures/hr/km, $\alpha = 4175.6$, and $\text{V}_{\text{crit}} = 20.6$ m/s [116]. We assume a hurricane of duration T = 24 hr and consider a geographical region consisting of $|\mathcal{G}| = 1,000$ grids. The expected damage is calculated under values of R_m between 20 and 50 km (step size of 1 km) and V_m between 21 and 80 m/s (step size of 1 m/s). Then to estimate Eq. 3.41, we consider values of p_1 between 1 and 1.5, and values of p_2 between -0.5 and 0.5. For each combination of p_1 and p_2, we estimate the parameters c_1, c_2, c_3, c_4, and c_5 using the least squares method. The best-fitting polynomials are $p_1 = 1.13$ and $p_2 = 0.00$, i.e., no dependency of $\Lambda_{\text{total,inner}}(\text{V}_\text{m}, \text{R}_\text{m})$ on $g(\text{V}_\text{m})$. All coefficients except c_5 are statistically significant, so we omit the second term of $\Lambda_{\text{total,inner}}(\text{V}_\text{m}, \text{R}_\text{m})$ from the final parametric equation. The accompanying best-fitting coefficients are: $c_1 = -0.265$, $c_2 = 0.007$, $c_3 = 0.002$, $c_4 = -0.009$.

Based on the estimated parameters, $\bar{\Lambda}_{\text{total}}$ is roughly proportional to $g(\text{V}_\text{m})$ to the 2.26-th power.

3.9 Appendix C: Parametric Loss Models

3.9.1 Network Repair Model

We assume that the financial loss $\mathrm{L}_{g,k}$ in a location (grid) g at a given time k scales linearly with the number of failures:

$$\mathrm{L}_{g,k} = \mathrm{L}_f kl_{g,k}, \tag{3.43}$$

where L_f is the estimated financial loss per failed asset per unit time and $kl_{g,k}$ is the number of failures remaining in grid g at time k. There are s_g failures at time $k = 0$ (after the passing of the hurricane), i.e., we assume all failures have occurred by the time the hurricane passes. Due to repairs, $kl_{g,k} \leq s_g$ at all times $k > 0$.

In addition, we assume that each grid g has a constant repair rate Y (i.e., Y assets are repaired per unit time). Thus the number of failures remaining to be repaired decreases linearly with time by the rate Y, such that the amount of time needed to repair all failures in a grid is given by $\mathrm{K}_g = s_g/\mathrm{Y}$:

$$kl_{g,k} = \begin{cases} s_g - \mathrm{Y}k & \text{for } 0 \leq k \leq \mathrm{K}_g \\ 0 & \text{for } k > \mathrm{K}_g. \end{cases} \tag{3.44}$$

Under this model, the total loss accrued in grid g is given by:

$$\begin{aligned} \mathrm{L}_g &= \int_{k=0}^{\mathrm{K}_g} \mathrm{L}_f kl_{g,k} dk \\ &= \mathrm{L}_f \int_{k=0}^{k=\mathrm{K}_g} (s_g - \mathrm{Y}k) dk \\ &= \frac{1}{2} \frac{\mathrm{L}_f}{\mathrm{Y}} s_g^2, \end{aligned} \tag{3.45}$$

which indicates that the total loss L_g scales quadratically with number of failures s_g.

The model we employ here does not consider the effect of network topology on financial losses (in the case of a networked infrastructure system). A more sophisticated model would consider that financial loss incurred at a given time depends

more specifically on the loss-of-service in the infrastructure system, rather than the number of damages. The loss-of-service depends on the locations of the damage, as well as the topological properties if the infrastructure system is networked. A relevant example would be an electricity distribution network. After a hurricane passes, some distribution lines that connect bulk power supplies to end users are damaged, and thus a subset of the end users cannot receive electricity. The distribution lines are then repaired, with the repair rate constrained by the available resources and repair crew capacity. At each time period, a financial loss is incurred, which corresponds to the cost of repair and the cost of electricity demand not met. Generally speaking, we expect that this financial loss will decrease with each set of repairs, after which more end users receive electricity due to reconnection of loads to bulk power supplies.

3.9.2 Formulation of Analytical Model for Total Financial Losses

The total expected financial loss (per unit of length of assets) is given by:

$$
\begin{aligned}
\mathrm{L_{total}} &= \frac{1}{2}\frac{\mathrm{L}_f}{\mathrm{Y}}\sum_{g\in\mathcal{G}} s_g^2 \\
&= \frac{1}{2}\frac{\mathrm{L}_f}{\mathrm{Y}}\sum_{g\in\mathcal{G}} \Lambda_g^2 \\
&= \frac{1}{2}\frac{\mathrm{L}_f}{\mathrm{Y}}\sum_{g\in\mathcal{G}} \left[\lambda_{\mathrm{norm}}\mathrm{T}(1-\alpha) + \lambda_{\mathrm{norm}}\alpha\left(\mathrm{T}_{u,g} + \sum_{t\in\mathcal{T}_{c,g}} f^2(v_{g,t})\Delta t\right)\right]^2 \\
&= \frac{1}{2}\frac{\mathrm{L}_f}{\mathrm{Y}}\sum_{g\in\mathcal{G}} \left[\lambda_{\mathrm{norm}}\mathrm{T}(1-\alpha) + \lambda_{\mathrm{norm}}\alpha\left(\mathrm{T} + \sum_{t\in\mathcal{T}_{c,g}} \big(f^2(v_{g,t})-1\big)\Delta t\right)\right]^2 \\
&= \frac{1}{2}\frac{\mathrm{L}_f}{\mathrm{Y}}\sum_{g\in\mathcal{G}} \left[\lambda_{\mathrm{norm}}\mathrm{T} + \lambda_{\mathrm{norm}}\alpha \sum_{t\in\mathcal{T}_{c,g}} \big(f^2(v_{g,t})-1\big)\Delta t\right]^2 \\
&= \frac{1}{2}\frac{\mathrm{L}_f}{\mathrm{Y}}|\mathcal{G}_u|(\lambda_{\mathrm{norm}}\mathrm{T})^2 + \frac{1}{2}\frac{\mathrm{L}_f}{\mathrm{Y}}\sum_{g\in\mathcal{G}_u} \left[\lambda_{\mathrm{norm}}\mathrm{T} + \lambda_{\mathrm{norm}}\alpha \sum_{t\in\mathcal{T}_{c,g}} \big(f^2(v_{g,t})-1\big)\Delta t\right]^2 \\
&= \frac{1}{2}\frac{\mathrm{L}_f}{\mathrm{Y}}\Bigg(|\mathcal{G}|(\lambda_{\mathrm{norm}}\mathrm{T})^2 + \sum_{g\in\mathcal{G}_u}\Bigg[2\lambda_{\mathrm{norm}}^2\alpha\mathrm{T}\sum_{t\in\mathcal{T}_{c,g}} \big(f^2(v_{g,t})-1\big)\Delta t + \\
&\qquad (\lambda_{\mathrm{norm}}\alpha)^2\Bigg(\sum_{t\in\mathcal{T}_{c,g}} \big(f^2(v_{g,t})-1\big)\Delta t\Bigg)^2\Bigg]\Bigg) \\
&= \frac{1}{2}\frac{\mathrm{L}_f}{\mathrm{Y}}\Bigg(|\mathcal{G}|(\lambda_{\mathrm{norm}}\mathrm{T})^2 + 2\lambda_{\mathrm{norm}}^2\alpha\mathrm{T}\sum_{g\in\mathcal{G}_u}\sum_{t\in\mathcal{T}_{c,g}} \big(f^2(v_{g,t})-1\big)\Delta t + \\
&\qquad (\lambda_{\mathrm{norm}}\alpha)^2\sum_{g\in\mathcal{G}_u}\Bigg(\sum_{t\in\mathcal{T}_{c,g}} \big(f^2(v_{g,t})-1\big)\Delta t\Bigg)^2\Bigg)
\end{aligned}
\tag{3.46}
$$

3.9.3 Formulation of Parametric Model for Total Financial Losses

In order to formulate a parametric model for total financial loss given by $\mathrm{L_{total}}$, we consider the parametric model for damage given by Eq. 3.41 and the network repair model in Section 3.9.1. Specifically, Eq. 3.41 states that total damage $\Lambda_{\mathrm{total}} \sim$

$O(R_m^2 g(V_m)^{2c})$ where c is an arbitrary constant, and Section 3.9.1 suggests that financial loss is a quadratic function of damage.

Then, let's consider the following parametric financial loss function:

$$\begin{aligned}\bar{L}_{total}(V_m, R_m) = d_1 &+ d_2 R_m [g(V_m)]^{q_1} + d_3 R_m^2 [g(V_m)]^{2q_1} + d_4 R_m^3 [g(V_m)]^{3q_1} \\ &+ d_5 R_m^4 [g(V_m)]^{4q_1} + d_6 R_m^2 [g(V_m)]^{q_2} + d_7 R_m^3 [g(V_m)]^{q_2} \\ &+ d_8 R_m^3 [g(V_m)]^{2q_2} + d_9 R_m^4 [g(V_m)]^{2q_2} \\ &+ d_{10} R_m + d_{11} R_m^2 + d_{12} R_m^3 + d_{13} R_m^4\end{aligned} \tag{3.47}$$

where total expected normalized financial loss $\bar{L}_{total} = L_{total}/|\mathcal{G}|$ refers to the expected financial loss per grid per unit length of assets. We obtain Eq. 3.47 by taking the square of the function for total expected normalized damage given by Eq. 3.41 and summing like terms in the resultant expression.

For purposes of estimating Eq. 3.47, we numerically compute expected financial loss using the NHPP parameters, hurricane duration parameters, and geographical region size given in Section 3.8.2. The expected financial loss is calculated under values of R_m between 20 and 50 km (step size of 1 km) and V_m between 21 and 80 m/s (step size of 1 m/s). Then to estimate Eq. 3.47, we consider values of q_1 between 1.2 and 1.4 and q_2 between 0 and 2. For each considered set of values q_1 and q_2, we estimate the parameters d_1 – d_{13} using the least squares method. The best-fitting polynomial degrees are $q_1 = 1.59$ and $q_2 = 1.77$. For these polynomial degrees, the statistically significant coefficients are: $d_2 = 0.021$, $d_3 = 1.91 \times 10^{-4}$, $d_4 = 4.71 \times 10^{-5}$, $d_6 = -0.001$, $d_7 = 5.01 \times 10^{-5}$, $d_8 = 3.34 \times 10^{-4}$. With a slight abuse of notation, the parameters d_2, d_3, d_4, d_6, d_7, d_8 respectively correspond to parameters d_1, d_2, d_3, d_4, d_5, d_6 in Section 3.5.2.

Based on the estimated parameters, $\bar{L}_{total}$ is roughly proportional to $g(V_m)$ to the 4.77-th power.

Chapter 4

Resource Allocation and Response in Electricity Distribution Networks

Operational, days-ahead strategies for enhancing electric power infrastructure resilience in the face of extreme weather are imperative. In particular, strategic pre-storm planning and efficient response are crucial in order to prevent prolonged delays in restoring power supply following high-intensity hurricane events. Distributed energy resources (DERs) have the potential utility to maintain power supply to critical consumers following hurricanes, while damage is being localized and repaired. However, effective pre-storm DER allocation is dependent on (i) a model that enables consideration of pre-storm resource allocation strategies as well as post-storm repair operations; and (ii) accurate forecasts of the locations of damage, which increase the efficiency of damage localization and repair.

In this section, we summarize an integrated modeling approach for improving resilience in DNs against hurricanes (or more broadly, tropical storms). We consider both proactive pre-storm planning decisions (DER allocation), and post-storm response actions such as microgrid formation, component repairs, and DER dispatch. Importantly, the pre-storm DER allocation decisions are dependent on uncertainties in component failures. In our model, we allow for the flexibility of DER re-allocation in the post-storm stage, as the network repair progresses, to serve loads without access to power. We formulate the problem of pre-storm resource allocation under uncer-

tainty and post-storm network restoration as a two-stage stochastic mixed-integer program (SMIP2). SMIP2 can be rewritten in a Deterministic Equivalent Formulation (DEF) which is a mixed-integer program (MIP) with copies of Stage II variables for each scenario.

We provide a generic formulation of the two-stage stochastic mixed-integer program (SMIP2) regarding decisions for network resilience to hurricane-induced damage in Section 4.1. In Section 4.2, we formulate physically-based models for resource allocation, network restoration, and multi-master operation of islanded microgrids. In Section 4.3, we discuss a few stylized network examples that illustrate the novel features of our modeling approach. In Section 4.4, we provide a few computational experiments that illustrate the effect of model constraints and parameters on network system performance. Finally, we conclude our discussion in Section 4.5.

4.1 Stochastic Programming Formulation

We consider a radial DN facing risk of storm-induced disruptions. The DN is denoted as $\mathcal{G} = (\mathcal{N} \cup \{0\}, \mathcal{E})$, where 0 is the substation node, $\mathcal{N}$ the set of nodes, and $\mathcal{E}$ the set of edges. In our model, the operator anticipates that the storm events can cause the failure of DN components (lines), and proactively plans for a set of pre-defined line failure scenarios.[1] We assume that after the storm passes, the uncertainty in line failures is fully realized, and the nominal connectivity of loads with the bulk power source is disrupted. Then, the restoration phase commences, during which the DERs are activated to support power supply to loads within the resulting microgrids formed due to failures.

Ahead of a storm, the operator is given a subset of DN nodes $\mathcal{U} \subseteq \mathcal{N}$ where DERs can be potentially allocated. The operator selects nodes in $\mathcal{U}$ to be developed into sites, at which DERs can be installed and integrated with the DN. We primarily focus on natural gas and diesel generators with capacity between 10 kW to 5 MW with a total energy content of up to 72 MWh [24, 37]. We denote by $\mathcal{D}$ the set of

[1] In general, failed components can also include DN nodes or other DN equipment.

DERs available to the operator. We also consider that a subset $\mathcal{D}_{\mathrm{m}} \subseteq \mathcal{D}$ are mobile DERs (i.e. they can be reallocated to DER sites during the post-storm restoration phase). The set of remaining DERs denoted by $\mathcal{D}_{\mathrm{f}} = \mathcal{D} \backslash \mathcal{D}_{\mathrm{m}}$ consist of fixed DERs (i.e., once allocated in Stage I, these DERs cannot be reallocated to a different site during restoration).

In the restoration phase, the operator implements a line repair schedule. Additionally, she can also choose to develop additional DER sites, and is able to reallocate mobile DERs among the developed sites. As the line repairs progress, the DERs can support the formation of larger microgrids by allowing more loads to be energized. Naturally, in our two-stage decision framework, these post-storm scenario-specific restoration actions are accounted for in the pre-storm planning.

In this section, we first present a generic Deterministic Equivalent Formulation (DEF) of our two-stage stochastic program (Section 4.1.1), with multi-period restoration in the second stage (Section 4.1.2). Then, we discuss the details of our distribution network component failure model (Section 4.1.3), which is based on the modeling approach detailed in 3. We conclude with a description of how we select scenarios, which represent realizations of component failures, to use in implementing the two-stage stochastic program (Section 4.1.4).

4.1.1 Two-Stage Mixed-Integer Program (SMIP2)

We formulate the two-stage mixed-integer program (SMIP2) as:

$$\begin{aligned} \min_{a} \quad & g(a) \coloneqq \mathrm{J}^{\mathrm{I}}(a) + \mathbb{E}_{s\sim\mathcal{P}}[\mathrm{J}^{\mathrm{II}}(a,s)], \\ \text{s.t.} \quad & \mathrm{A}_1 a \geq b, \\ & a \in \{0,1\}^{N_1} \end{aligned} \tag{SMIP2}$$

where a is an N_1-dimensional binary vector that denotes the Stage I resource allocation strategy, and $\mathrm{A}_1 a \geq b$ denotes linear constraints that strategy a must satisfy. The set $\mathcal{A} \coloneqq \{a \in \{0,1\}^{N_1} \mid \mathrm{A}_1 a \geq b\}$ denotes the set of feasible Stage I strategies. Additionally, $\mathrm{J}^{\mathrm{I}}(a) \coloneqq c_1^{\top} a$ denotes the Stage I cost; $\mathcal{S}'$ the set of component failure

scenarios; $s \in \mathcal{S}'$ a specific scenario represented by a length-$|\mathcal{E}|$ vector, in which $s_e = 1$ if edge e is failed and 0 otherwise; and $\mathcal{P}$ the distribution from which s is drawn. For a fixed allocation-scenario pair $(a, s) \in \mathcal{A} \times \mathcal{S}'$, we denote by $\mathrm{J}^{\mathrm{II}}(a, s)$ the optimal value of the Stage II recourse problem. Here, $\mathbb{E}_{s\sim\mathcal{P}}[\mathrm{J}^{\mathrm{II}}(a, s)]$ denotes the expected Stage II cost under allocation a.

The deterministic equivalent formulation (DEF) [17] of (SMIP2) can be stated as follows:

$$\begin{aligned} \min_{a} \quad & g(a, \mathcal{S}') \coloneqq \mathrm{J}^{\mathrm{I}}(a) + \sum_{s\in\mathcal{S}'} \mathbb{P}(s)\ \mathrm{J}^{\mathrm{II}}(a, s)\,, \\ \text{s.t.} \quad & \mathrm{A}_1 a \geq b, \\ & a \in \{0,1\}^{N_1} \end{aligned} \tag{DEF}$$

where the probability of scenario s is denoted by $\mathbb{P}(s)$, and thus $\sum_{s\in\mathcal{S}'} \mathbb{P}(s)\ \mathrm{J}^{\mathrm{II}}(a, s)$ denotes the expected Stage II cost under allocation a.

4.1.2 Stage II recourse problem

Next, we discuss formulation of the Stage II recourse problems, which provide the optimal objective values corresponding to $\mathrm{J}^{\mathrm{II}}(a, s)$ in (SMIP2) and (DEF). Consider a multi-period horizon $\mathcal{K} = \{1, \cdots, \mathrm{K}\}$. Here, each period can be viewed as a work shift of the repair crew. The decision variables in each period involve repairing damaged lines, developing new DER sites, reallocating DERs, and restoring power supply to loads. We formulate the Stage II problem as a multi-period mixed-binary linear program (MILP):

$$
\begin{aligned}
\text{REC}(a,s): \ \mathrm{J}^{\mathrm{II}}(a,s) = \min_{x^s, r^s} \quad & \sum_{k\in\mathcal{K}} \left(\mathrm{J}^{\mathrm{II}}_{\mathrm{R}}(\rho^{ks}) + \mathrm{J}^{\mathrm{II}}_{\mathrm{L}}(\chi^{ks}) \right) \\
\text{s.t.} \quad & \mathrm{B}_2 r^s + \mathrm{B}_3 x^s \geq \mathrm{h} - \mathrm{F}a \\
& \rho^{ks} \in \{0,1\}^{N_2} && \forall\ k \in \mathcal{K} \\
& \chi^{ks} \in \mathbb{R}^{N_3} && \forall\ k \in \mathcal{K} \\
& \chi^{ks}_i \in \{0,1\} && \forall\ i \in \mathcal{I}_3, k \in \mathcal{K}
\end{aligned}
\tag{S2}
$$

where $\rho^{ks} \in \{0,1\}^{N_2}$ denote DN restoration actions (line repairs, site development, and DER reallocation); $\chi^{ks} \in \mathbb{R}^{N_3}$ the mixed-binary network state variables; $\mathcal{I}_3 \subseteq \{1, 2, \cdots, N_3\}$ the set of indices corresponding to the binary network state variables; $r^s = [\rho^{ks}]_{k\in\mathcal{K}}$ the scenario-specific restoration strategy; $x^s = [\chi^{ks}]_{k\in\mathcal{K}}$ the network state variables for the multiple periods; $\mathrm{J}^{\mathrm{II}}_{\mathrm{R}}(\rho^{ks})$ the cost of network restoration ρ^{ks}; $\mathrm{J}^{\mathrm{II}}_{\mathrm{L}}(\chi^{ks})$ the cost of unmet demand associated with network state χ^{ks}; $\mathrm{h} \in \mathbb{R}^{N_4}$ is a vector of length N_4; and $\mathrm{B}_2 r^s + \mathrm{B}_3 x^s \geq \mathrm{h} - \mathrm{F}a$ the system of mixed-integer linear constraints on the Stage II decision variables. We hereafter refer to the linear programming relaxation of Problem REC(a,s) as $\overline{\text{REC}}(a,s)$, and the dual of $\overline{\text{REC}}(a,s)$ as D-$\overline{\text{REC}}(a,s)$.

4.1.3 Probabilistic Failure Model

We adapt our modeling approach in Chapter 3 in order to estimate the probabilities $\mathbb{P}(s)$ for each scenario $s \in \mathcal{S}'$. For the purposes of this section, s is defined as a length-$|\mathcal{E}|$ vector, in which $s_e = 1$ if edge e has failed and 0 otherwise. Using the NHPP model detailed in Chapter 3, we estimate the failure probability of each distribution line in the distribution network. This requires partitioning the distribution network area into spatial locations (grids), as discussed in Section 3.1 of Chapter 3, and determining the length of each distribution line in each location. We refer the reader to our work [16] in which we describe our approach for estimating $\mathbb{P}(s)$, which uses an adapted NHPP model to estimate failure probabilities of individual lines.

Note that our examples in this chapter focus on distribution networks with number

of nodes N up to 118. Such networks tend to not be larger than a few km^2 in terms of total area. Thus, the spatial variability in probabilistic damage estimates that we incorporate in the NHPP model of Chapter 3 is less relevant in this chapter. If we consider a collection of distribution networks that form a larger electric power infrastructure, then spatial variability begins to more significantly affect estimated failure probabilities.

4.1.4 Scenario Selection

The set of all possible failure scenarios is of size $|2^{\mathcal{E}}| = 2^{\mathrm{N}}$, i.e., the number of possible scenarios increases exponentially with the network size. This renders enumerating all scenarios infeasible when the network size is sufficiently large. By applying the Sample Average Approximation (SAA) method, one can obtain a random sample $\mathcal{S}$ of scenarios such that $\mathcal{S} \subset \mathcal{S}'$ and the weights $\mathbb{P}(s)$ are considered to be equal to $1/|\mathcal{S}| \quad \forall\, s \in \mathcal{S}$ [2]. The SAA to (DEF) can be written as follows:

$$\begin{aligned} \min_{a} \quad & \mathrm{J}^{\mathrm{I}}(a) + \frac{1}{|\mathcal{S}|} \sum_{s \in \mathcal{S}} \mathrm{J}^{\mathrm{II}}(a, s)\,, \\ \text{s.t.} \quad & \mathrm{A}_1 a \geq b, \\ & a \in \{0,1\}^{N_1} \end{aligned} \tag{SAA}$$

Another way to obtain a subset of scenarios $\mathcal{S} \subset \mathcal{S}'$ is to use a scenario reduction method [29, 46], which involves selecting a representative sample of scenarios.

4.2 Modeling Formulation

In this section, we discuss the formulation of models corresponding to the cost parameters, constraints, and variables in the deterministic equivalent formulation (DEF) of the two-stage stochastic program, as well as the Stage II recourse problems REC(a, s). First, we discuss the associated model of resource allocation, which corresponds to the decisions represented by first-stage variables a (Section 4.2.1). Next, we discuss the multi-period DN restoration model, which corresponds to the second-stage variables

r^s, $\forall s \in \mathcal{S}$ (Section 4.2.2). Finally we discuss the model of multi-master microgrid operation, which corresponds to the second-stage variables x^s, $\forall s \in \mathcal{S}$ (Section 4.2.3).

4.2.1 Resource allocation model

In Stage I, the operator selects a subset of nodes for allocating DERs from set $\mathcal{D}$. Before a DER can be allocated to a DN node, the operator needs to develop the site at that node to ensure a safe and reliable integration with the DN. Developing a DER site entails land or space acquisition (which may be temporary), building enclosures, and/or physically secure platforms [44, 36]. The site location is also determined by access to fuel supplies. After developing the sites, the operator allocates the DERs to the developed sites.

Let $a \coloneqq (u, w)$ denote the joint Stage I strategy – site development (u) and DER allocation (w) – in (DEF). Then, we can define the set of feasible Stage I strategies as $\mathcal{A} \coloneqq \{(u, w) \in \{0,1\}^{\mathcal{U}} \times \{0,1\}^{\mathcal{U}\times\mathcal{D}} \mid 4.1a - 4.1c \text{ hold}\}$. A feasible Stage I strategy satisfies the following constraints:

$$w_{id} \leq u_i \qquad \forall\, d \in \mathcal{D},\ i \in \mathcal{U} \tag{4.1a}$$

$$\textstyle\sum_{i\in\mathcal{U}}\ w_{id} \leq 1 \qquad \forall\, d \in \mathcal{D} \tag{4.1b}$$

$$\textstyle\sum_{i\in\mathcal{U},d\in\mathcal{D}}\ w_{id} \leq \mathbf{G}, \tag{4.1c}$$

where (4.1a) models that a DER can be allocated only to a site that has been developed; (4.1b) states that a DER can be allocated to at most one site; and (4.1c) models the budget constraint; the operator can allocate at most $\mathbf{G} \leq |\mathcal{D}|$ total number of DERs.

For $a \in \mathcal{A}$, we define the operator's Stage I cost as the sum of cost of site development and the cost of DER allocation, i.e.,

$$\mathrm{J}^{\mathrm{I}}(a) = \textstyle\sum_{i\in\mathcal{U}} \left(\mathrm{W}_i^{\mathrm{SD}} u_i + \sum_{d\in\mathcal{D}} \mathrm{W}_{id}^{\mathrm{DA}} w_{id}\right),$$

where $\mathrm{W}_i^{\mathrm{SD}}$ denotes the cost of developing a DER site at node i and $\mathrm{W}_{id}^{\mathrm{DA}}$ denotes

the cost of allocating DER d to site i.

The ratings of DERs (e.g. synchronous generators that run on diesel or natural gas, or photovoltaic generators [44, 36, 1]) vary from 1 kilowatt to several megawatts [24], so placement of DERs by size is a relevant question. For simplicity, we assume in our study that the DERs are homogeneous, i.e. all have the same rating.

4.2.2 A multi-period DN restoration model

After the storm passes, the operator begins the DN restoration, which includes scheduling repair of damaged lines. Additionally, the operator can develop more sites and/or reallocate the mobile DERs. We consider that the post-storm restorative actions are scheduled between periods $k = 1$ and $k = \mathrm{K}$.

Choosing parameter K: The parameter K is an estimate of the maximum of two quantities: (i) number of periods needed to repair all failed lines and the time, and (ii) time to restore the bulk power supply from the transmission network. However, for a straightforward comparison between different scenarios, we assume $\mathrm{K} = |\mathcal{E}| + 2$. This is not a restrictive assumption because if the repairs finish at period $k < \mathrm{K}$, the network state will remain unchanged until period $k = \mathrm{K}$, in which the normal DN operation is fully restored. In general, the bulk power supply can be supplied to the partially restored DN. However, for the sake of simplicity, we assume that the bulk power supply is resumed at period $k = \mathrm{K}$.

As mentioned before, the DN is disconnected from the main grid at period $k = 1$. The subnetworks resulting from component failures can be operated as microgrids. A subnetwork is considered an operational microgrid, if there exists at least one DER allocated to it, and the total capacity of the DERs in the subnetwork is such that at least one load can be operated. As the line repairs are completed in subsequent periods, the operational microgrids gradually increase in size and/or are merged together to form larger microgrids.

Maximum number of lines actually repaired: Let $\overline{\mathbf{Y}}^k$ denote the maximum number of lines that can be repaired in period k. We assume that in each time period,

if there is a failed component and repair capacity is available, then the component must be repaired. We model this by introducing a parameter $\mathbf{Y}^{ks}$ to denote the actual number of lines repaired in period k. The parameter $\mathbf{Y}^{ks}$ depends on the scenario s as follows:

$$\mathbf{Y}^{ks} = \min\left(\max\left(0, \sum_e s_e - \sum_{k'=1}^{k-1} \overline{\mathbf{Y}}^{k'}\right), \overline{\mathbf{Y}}^{k}\right).$$

Thus, $\mathbf{Y}^{ks}$ denotes the minimum value between $\overline{\mathbf{Y}}^{k}$ and the number of lines that are unrepaired in period k for scenario s.

Line repair model: Let $\kappa_e^{ks} = 0$ denote that the line $e \in \mathcal{E}$ is operational in period k and scenario s; $\kappa_e^{ks} = 1$ otherwise. Also, let $\ell_e^{ks} = 1$ denote that line $e \in \mathcal{E}$ is repaired in period k and scenario s; $\kappa_e^{ks} = 1$ otherwise. Then, we can formulate our constraints on the line repair actions as follows ($\forall\ s \in \mathcal{S}$):

$$\ell_e^{ks} = 0 \qquad \forall\ e \in \mathcal{E}_s,\ k = 1 \tag{4.2a}$$

$$\textstyle\sum_{e\in\mathcal{E}_s} \ell_e^{ks} = \mathbf{Y}^{ks} \qquad \forall\ k \in \mathcal{K} \setminus \mathrm{K} \tag{4.2b}$$

$$\ell_e^{ks} = 1 \qquad \forall\ e \in \mathcal{E}_s,\ e^- = 0,\ k = \mathrm{K} \tag{4.2c}$$

$$\textstyle\sum_{k=0}^{\mathrm{K}} \ell_e^{ks} = 1 \qquad \forall\ e \in \mathcal{E}_s \tag{4.2d}$$

$$\kappa_e^{ks} = \kappa_e^{k-1s} - \ell_e^{ks} \qquad \forall\ e \in \mathcal{E}_s,\ k \in \mathcal{K}\backslash\{1\},\ k' = k-1. \tag{4.2e}$$

Here, (4.2a) models that repairs are not carried out in $k = 1$, i.e., repairs begin from $k = 2$; (4.2b) reflects that $\mathbf{Y}^{ks}$ number of lines are repaired in period $k \in \{1, ..., \mathrm{K}-1\}$; (4.2c) means that the bulk power supply is restored and connected to the DN at K, where $e^- = 0$ denotes that line e connects the DN to the substation node 0[2]; (4.2d) ensures a line can be repaired at most once; and (4.2e) states that a line is operational in period k if it was operational in the previous period $k-1$, or if it is repaired in period k.

Post-storm site development and DER reallocation model: For period k

[2]Our model can be extended to allow early reconnection back to the main grid even before DN repairs are completed, as shown in [90].

and scenario s, we define the Stage II restoration actions ρ^{ks} in REC(a, s) as follows:

$$\rho^{ks} := \left([\ell_e^{ks}]_{e\in\mathcal{E}}, [\mu_i^{ks}]_{i\in\mathcal{U}}, [\omega_{id}^{ks}]_{i\in\mathcal{U},d\in\mathcal{D}}, [\varpi_{ijd}^{ks}]_{i,j\in\mathcal{U},d\in\mathcal{D}}\right),$$

where $\mu_i^{ks} = 1$ denotes if node $i \in \mathcal{U}$ is developed in period k and scenario s (otherwise, $\mu_i^{ks} = 0$); $\omega_{id}^{ks} = 1$ if DER d is allocated to node $i \in \mathcal{U}$ in period k and scenario s (otherwise, $\omega_{id}^{ks} = 0$); and $\varpi_{ijd}^{ks} = 1$ if the mobile DER $d \in \mathcal{D}_{\mathrm{m}}$ previously allocated to node $i \in \mathcal{U}$ is reallocated to node $j \in \mathcal{U}$ in period k and scenario s (otherwise, $\varpi_{ijd}^{ks} = 0$).[3] Then, we formulate the constraints on the operator's decisions regarding the development of more sites and reallocation of mobile DERs among the developed sites as follows ($\forall\ s \in \mathcal{S}$):

$$\mu_i^{ks} = u_i \qquad \forall\ i \in \mathcal{U}, k = 1 \tag{4.3a}$$

$$\mu_i^{ks} \leq \mu_i^{k-1s} \qquad \forall\ i \in \mathcal{U}, k \in \mathcal{K}\backslash\{1\} \tag{4.3b}$$

$$\omega_{id}^{ks} = w_{id} \qquad \forall\ d \in \mathcal{D}_{\mathrm{f}},\ i \in \mathcal{U},\ k \in \mathcal{K} \tag{4.3c}$$

$$\omega_{id}^{1s} = w_{id} \qquad \forall\ d \in \mathcal{D}_{\mathrm{m}},\ i \in \mathcal{U} \tag{4.3d}$$

$$\omega_{id}^{ks} = \textstyle\sum_{j\in\mathcal{U}} \varpi_{ijd}^{ks} \qquad \forall\ d \in \mathcal{D}_{\mathrm{m}},\ i \in \mathcal{U},\ k \in \mathcal{K}\backslash\{1\} \tag{4.3e}$$

$$\omega_{id}^{ks} \leq \mu_i^{ks} \qquad \forall\ d \in \mathcal{D},\ i \in \mathcal{U} \tag{4.3f}$$

$$\textstyle\sum_{i\in\mathcal{U}}\ \omega_{id}^{ks} \geq \sum_{i\in\mathcal{U}}\ \omega_{id}^{k-1s} \qquad \forall\ d \in \mathcal{D}_{\mathrm{m}},\ k \in \mathcal{K} \tag{4.3g}$$

$$\textstyle\sum_{i\in\mathcal{U}}\ \omega_{id}^{ks} \leq 1 \qquad \forall\ d \in \mathcal{D},\ k \in \mathcal{K} \tag{4.3h}$$

$$\textstyle\sum_{d\in\mathcal{D}}\ \omega_{id}^{ks}\ \overline{\mathbf{pg}}_d \leq \mathbf{O}_i \qquad \forall\ i \in \mathcal{U},\ k \in \mathcal{K} \tag{4.3i}$$

$$\textstyle\sum_{i\in\mathcal{U},d\in\mathcal{D}}\ \omega_{id}^{ks} \leq \mathbf{G} \qquad \forall\ k \in \mathcal{K}. \tag{4.3j}$$

Here, (4.3a) implies that new sites can be developed from period $k = 1$; (4.3b) states that all developed sites remain operational throughout the restoration process; (4.3c) implies that fixed DERs cannot be reallocated to other sites; (4.3d) states that the mobile DERs can only be reallocated after $k = 0$; (4.3e) implies that a mobile DER is located at site i only if it is either already placed at the site i in a previous period

[3] For simplicity, we do not consider meshed topologies and the network reconfiguration capabilities as in [20, 86]. However, our model may be extended to include these operator response capabilities.

or transferred from an another site; (4.3f) implies that a DER can only be allocated to a developed site; (4.3g) models that a DER allocated at a certain period remains allocated in the DN;[4] (4.3h) models that a DER can only be allocated to exactly one site; (4.3i) implies that the total maximum output of DERs at site i cannot exceed the maximum power output value $\mathbf{O}_i$ for the site i;[5] and (4.3j) implies that at most $\mathbf{G}$ DERs can be used at any point of time.

For convenience, we also define restoration action for $k = 0$ based on the Stage I allocation strategy a as follows:

$$\rho^{\,0s} := ([\mathbf{0}]_{e\in\mathcal{E}}, [u_i]_{i\in\mathcal{U}}, [w_{id}]_{i\in\mathcal{U},d\in\mathcal{D}}, [\mathbf{0}]_{i,j\in\mathcal{U},d\in\mathcal{D}})\,.$$

Here, $\rho^{\,0s}$ is a fixed action which does not depend on the scenario.

Thus, we can define the set $\mathcal{R}^k$ of feasible network restoration action in period k for failure scenario s based on the restoration action in the previous period as follows:

$$\mathcal{R}^k(\rho^{k-1s}) := \{\rho^{ks} \mid (4.2a)-(4.2e),\ (4.3a)-(4.3j) \text{ hold}\} \qquad \forall\ k \in \mathcal{K}.$$

Finally, for a period $k \in \{1, ..., \mathrm{K}\}$, we define the operator cost incurred during network restoration as the sum of cost of post-storm site development and DER reallocation, i.e.,

$$\mathrm{J}_{\mathrm{R}}^{\mathrm{II}}(\rho^{ks}, \rho^{k-1s}) = \sum_{i\in\mathcal{U}} \mathrm{W}_i^{\mathrm{SD}} \left(\mu_i^{ks} - \mu_i^{k-1s}\right) + \sum_{d\in\mathcal{D}_{\mathrm{m}}} \sum_{i\in\mathcal{U}} \sum_{(j\in\mathcal{U}:\ j\neq i)} \mathrm{W}_{ij}^{\mathrm{DT}} \varpi_{ijd}^{ks},$$

where $\mathrm{W}_{ij}^{\mathrm{DT}}$ denotes the cost of transporting a mobile DER from site i to site j. If $\mathrm{W}_{ii}^{\mathrm{DT}} = 0$ denotes that there is no cost if the DER is not reallocated. A positive value for $\mathrm{W}_{ii}^{\mathrm{DT}} > 0$ can be used to model maintenance cost of DER at site i.

[4] In our model, we assume that the DERs can stay connected to the DN even while supplying no output power.

[5] In practice, the maximum power output $\mathbf{O}_i$ parameter for site i may depend upon several factors such as the space available, the line capacity of lines connected at site i, and the actions taken to develop site at node i.

4.2.3 Microgrid model with multi-master DER operation

We now describe our novel model for multi-master operation [66, 72] of microgrids, which includes models for DERs, loads, and power flows within the DN. In multi-master operation, multiple DERs share the responsibility of providing voltage regulation in a single microgrid. On the other hand, in single-master operation, only one of the DERs (typically the one with the largest capacity) provides voltage regulation.[6] Our model is flexible in that it permits both single- and multi-master operation of DERs within the microgrid(s).

DER model: We consider that in each period, the DERs are redispatched to satisfy new operating constraints resulting from line repairs and DER reallocations enabling the energizing of additional loads. The following constraints characterize our DER model ($\forall\ d \in \mathcal{D}, k \in \mathcal{K}, s \in \mathcal{S}$):

$$0 \leq pg_{id}^{ks} \leq \omega_{id}^{ks}\ \overline{\mathbf{pg}}_d \qquad \forall\ i \in \mathcal{U} \tag{4.4a}$$

$$|qg_{id}^{ks}| \leq \overline{\eta}_d pg_{id}^{ks} \qquad \forall\ i \in \mathcal{U} \tag{4.4b}$$

$$pg_{id}^{ks} = qg_{id}^{ks} = 0 \qquad \forall\ i \in \mathcal{N}\backslash\mathcal{U} \tag{4.4c}$$

$$|\mathrm{v}_i^{ks} - (\mathrm{v}_d^{\mathrm{ref}} - \mathbf{mq}_d qg_{id}^{ks})| \leq (1 - \omega_{id}^{ks})\mathrm{L} \quad \forall\ i \in \mathcal{U},\ k \neq \mathrm{K}. \tag{4.4d}$$

Eq. 4.4a implies that if a DER d is allocated to a site i, then the active power contribution of the DER is non-negative and upper bounded by its capacity $\overline{\mathbf{pg}}_d$, otherwise it is 0; (4.4b) models that the magnitude of reactive power output of the DER can be at most $\overline{\eta}_d$ of its active power output, where $\overline{\eta}_d$ is the tan arccos of the minimum power factor[7] [98, 90]; (4.4c) ensures that the active and reactive power contributions of a DER to non-DER site nodes are zero; and (4.4d) models the voltage droop control equation [66], which depends on whether or not a DER is allocated at

[6] In an autonomous microgrid, the master DERs are also responsible for frequency regulation. In our model, we do not consider frequency regulation for simplicity. However, our model can be extended to consider frequency regulation by considering the voltage-source inverter control models [66].

[7] Typically, the DERs are setup such that the minimum power factor $\overline{\eta}_d = 0.95$.

site i (L is a large constant).[8] Note that (4.4d) captures the key feature of the model, which is that multiple DERs can energize a microgrid by providing voltage regulation. We consider that every allocated DER is large enough ($>$ 10 kW active power rating) to contribute to voltage regulation. However, this assumption can be relaxed by dropping (4.4d) for those DERs that do not provide voltage regulation.

Turbine-based DERs such as diesel generators are AC power sources, so they can contribute to voltage regulation via in-built excitation systems that utilize automatic voltage regulators [68]. In contrast, DERs such as batteries or photo-voltaic generators are DC power sources, which are connected to the DN via inverters. Such DERs can contribute to voltage regulation if their inverters are set in the voltage source inverter (VSI) control mode [65].

It is also worth noting that in our model, each DER within an island contributes to the voltage regulation of the microgrid island, simultaneously with other DERs in the same island [6]. A suitable extension of our model can also allow some of the DERs to operate in the PQ control mode, in which both the DERs' active and reactive power supply is fixed. One simple scheme to address this extension is to consider that the largest DG in the island operates in PV mode and the rest in PQ mode. The largest DG would be the substation when the island is in grid-connected mode [91]. Moreover, since the DERs can contribute to frequency regulation of the islanded microgrid, our model can also be extended to consider the frequency droop control equations.

Load model: The constraints governing our load model are as follows ($\forall\ k\ \in \mathcal{K},\ s \in \mathcal{S}$):

$$\alpha_i^{ks} \geq \underline{\mathbf{vc}}_i - \mathrm{v}_i^{ks}, \qquad \alpha_i^{ks} \geq \mathrm{v}_i^{ks} - \overline{\mathbf{vc}}_i \qquad \forall\ i \in \mathcal{N} \tag{4.5a}$$

$$\beta_i^{ks} \geq (1 - \alpha_i^{ks})\underline{\beta}_i, \qquad \beta_i^{ks} \leq (1 - \alpha_i^{ks}) \qquad \forall\ i \in \mathcal{N} \tag{4.5b}$$

Here, (4.5a) ensures that the load remains connected only if the voltage bounds are

[8] At period K, the DN is connected to the bulk power supply and the "stiff" AC system of the bulk power grid determines the terminal voltage of the DERs. Hence, the voltage droop equation does not apply at period K.

satisfied; and (4.5b) implies that if a load i is connected, the fraction of its demand satisfied must lie in the interval $[\underline{\beta}_i, 1]$.

Power flow model: We model the power flows within the DN using the *LinDistFlow* model [90] ($\forall\ s \in \mathcal{S}$):

$$p_i^{ks} = \beta_i^{ks}\ \overline{\mathbf{pc}}_i - \textstyle\sum_{d\in\mathcal{D}} pg_{id}^{ks} \qquad \forall\ i \in \mathcal{N},\ k \in \mathcal{K} \qquad (4.6a)$$

$$q_i^{ks} = \beta_i^{ks}\ \overline{\mathbf{qc}}_i - \textstyle\sum_{d\in\mathcal{D}} qg_{id}^{ks} \qquad \forall\ i \in \mathcal{N},\ k \in \mathcal{K} \qquad (4.6b)$$

$$P_e^{ks} = \textstyle\sum_{l:l^-=e^+} P_l^{ks} + p_{e^+}^{ks} \qquad \forall\ e \in \mathcal{E},\ k \in \mathcal{K} \qquad (4.6c)$$

$$Q_e^{ks} = \textstyle\sum_{l:l^-=e^+} Q_l^{ks} + q_{e^+}^{ks} \qquad \forall\ e \in \mathcal{E},\ k \in \mathcal{K} \qquad (4.6d)$$

$$|P_e^{ks}| \le (1-\kappa_e^{ks})\mathrm{L} \qquad \forall\ e \in \mathcal{E},\ k \in \mathcal{K} \qquad (4.6e)$$

$$|Q_e^{ks}| \le (1-\kappa_e^{ks})\mathrm{L} \qquad \forall\ e \in \mathcal{E},\ k \in \mathcal{K} \qquad (4.6f)$$

$$\mathrm{L}\kappa_e^{ks} \ge |\mathrm{v}_{e^+}^{ks} - (\mathrm{v}_{e^-}^{ks} - 2(\mathrm{r}_e P_e^{ks} + \mathrm{x}_e Q_e^{ks}))| \qquad \forall\ e \in \mathcal{E},\ k \in \mathcal{K} \qquad (4.6g)$$

$$\mathrm{v}_i^{ks} = \mathrm{v}^{\mathbf{nom}} \qquad \forall\ i = 0,\ k = \mathrm{K}. \qquad (4.6h)$$

Eqs. (4.6a)-(4.6b) determine the net active and reactive power consumed at the nodes. Eqs. (4.6c)-(4.6d) determine the resulting active and reactive power flows on the lines. Eqs. (4.6e)-(4.6f) ensure no power flows on the failed lines until they are repaired. Similarly, (4.6g) ensures that the voltage drop constraint along a line e (between 'from' node e^- and 'to' node e^+) is enforced only if e is operational. Finally, (4.6h) ensures that the substation voltage is equal to the nominal voltage when the DN is connected back to the main grid at $k = \mathrm{K}$.

Now, we define the network state variable for scenario s and period k as follows:

$$\chi^{ks} \coloneqq \big((pg_{id}^{ks})_{i\in\mathcal{N},d\in\mathcal{D}},\ (qg_{id}^{ks})_{i\in\mathcal{N},d\in\mathcal{D}},\ (\beta_i^{ks})_{i\in\mathcal{N}},\ (\alpha_i^{ks})_{i\in\mathcal{N}},\ (p_i^{ks})_{i\in\mathcal{N}},\ (q_i^{ks})_{i\in\mathcal{N}},\ (P_e^{ks})_{e\in\mathcal{E}},\ (Q_e^{ks})_{e\in\mathcal{E}},\ (\mathrm{v}_i^{ks})_{i\in\mathcal{N}}\big).$$

Then, under the restoration action ρ^{ks}, the set of feasible network states is defined as $\mathcal{X}^k\left(\rho^{ks}\right) \coloneqq \{\chi^{ks} \mid (4.4\mathrm{a})-(4.4\mathrm{d}),\ (4.5\mathrm{a})-(4.5\mathrm{b}),\ (4.6\mathrm{a})-(4.6\mathrm{h})\ \text{hold}\}$. The sets $\left(\mathcal{X}^k\right)_{k\in\mathcal{K}}$ and $\left(\mathcal{R}^k\right)_{k\in\mathcal{K}}$ collectively define the system of inequalities $\mathrm{B}_2 r^s + \mathrm{B}_3 x^s \ge$

$\mathrm{h} - \mathrm{F}a$ and the binary constraints in $\mathrm{REC}(a, s)$.

For period $k \in \mathcal{K}$, we define the cost of unmet demand as the sum of two costs:

$$\mathrm{J}_{\mathrm{L}}^{\mathrm{II}}(\chi^{ks}) = \sum_{i \in \mathcal{N}} \big((\mathrm{W}_i^{\mathrm{LS}} - \mathrm{W}_i^{\mathrm{LC}}) \alpha_i^{ks} + \mathrm{W}_i^{\mathrm{LC}} (1 - \beta_i^{ks}) \big),$$

where the first term denotes the cost of load shedding and the second term denotes the cost of load control.

Finally, combining the Stage I and Stage II decision variables, we can rewrite the DEF problem (DEF) as follows:

$$\begin{aligned} \min_{a,R,X} \quad & \mathrm{J}^{\mathrm{I}}(a) + \frac{1}{|\mathcal{S}|} \sum_{s \in \mathcal{S}} \sum_{k \in \mathcal{K}} \big(\mathrm{J}_{\mathrm{R}}^{\mathrm{II}}(\rho^{ks}) + \mathrm{J}_{\mathrm{L}}^{\mathrm{II}}(\chi^{ks}) \big) \\ \text{s.t.} \quad & a \in \mathcal{A} \\ & \rho^{ks} \in \mathcal{R}^k(\rho^{k-1s}) && \forall\ k \in \mathcal{K},\ s \in \mathcal{S} \\ & \chi^{ks} \in \mathcal{X}^k\left(\rho^{ks}\right) && \forall\ k \in \mathcal{K},\ s \in \mathcal{S}, \end{aligned} \tag{DEF}$$

where $R \coloneqq [r^s]_{s \in \mathcal{S}}$ denotes the collection of restoration strategies, and $X \coloneqq [x^s]_{s \in \mathcal{S}}$ denotes the collection of microgrid operations combined over all the scenarios in $\mathcal{S}$. Thus, the operator's goal is to minimize the sum of Stage I cost and the expected Stage II cost by choosing both a pre-storm resource allocation, as well as a post-storm strategy for DN restoration and microgrid operations.

4.3 Illustrative Examples

4.3.1 Example No. 1

Figure 4-1 provides an illustration of various aspects of our formulation. In Figure 4-1a, the DN is in nominal operating conditions, i.e., each node is connected to the grid and no load control is exercised.

Suppose that the utility has resources to develop one DER site in Stage I. Further suppose that due to the power flow constraints (4.6c)-(4.6d) and voltage drop con-

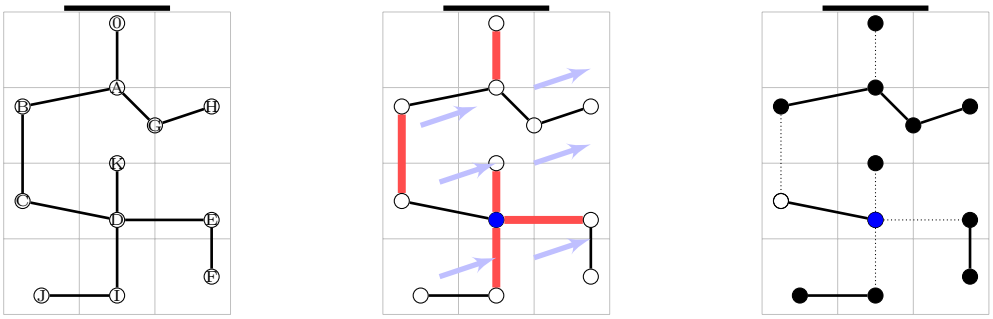

(a) (b) (c) $k = 0$

(d) $k = 1$ (e) $k = 2$ (f) $k = \mathrm{K}$

Figure 4-1: The subfigures show (a) nominal DN (white nodes indicate no load control), (b) pre-storm DER allocation based on storm forecast (blue node denotes DER allocation, red lines illustrate a disruption scenario), (c) microgrid islands (dotted lines indicate failed lines, black nodes denote the loads that are completely unserved), (d) partial line repairs enable partial load restoration (light gray nodes), (e) line repairs completed leading to more load restoration, although with even more load control than before (dark gray nodes), and finally (f) reconnection to main grid and restoration of nominal performance.

straints (4.6g), transmitting power across more than two lines results in voltage bound violations. Hence, from any site location, the DERs will be able to meet the demand of nodes which are at most two hops away from the site. For example, a DER placed at node H can only supply power to nodes A, G, and H, such that {A,B,G,H} form the largest connected island. Hence, placing a site at node A can immediately serve demand of 4 loads. However, if we take into account the line repairs, the maximum number of loads that can be reconnected to the DN (after repairs) is eight if the site is developed at node D. Thus, allocating the DER to node D is optimal because it maximizes number of loads served, though only two loads are served during the first period.

In Figure 4-1c, we see that a failure scenario has been realized for period $k = 0$ where the set of failed lines $\mathcal{E}_s$ include lines (B,C), (D,E), (D,I), and (D,K). The loss of bulk power supply is represented by the DN's disconnection from the substation, i.e. (0,A) $\in$ $\mathcal{E}_s$. Since the demand at just two nodes (C, D) is met in the first period, no load control is necessary (i.e. $\alpha_i^{ks} = 0, \beta_i^{ks} = 1 \ \forall \ i \in$ {C,D}; and $\alpha_i^{ks} = 1, \ \forall \ i \in \mathcal{N} \backslash$ {C,D}).

Next, we schedule line repairs under the constraint Y = 2, i.e. at most two lines can be repaired in each period. Looking at the most number of loads that can be reconnected, the lines (D,E) and (D,I) should be repaired in the period $k = 1$ ($\ell_e^{ks} = 1$ if $e \in$ {(D,E), (D,I)}), and lines (D,K) and (B,C) should be repaired in the period $k = 2$ ($\ell_e^{ks} = 1$ if $e \in$ {(D,K), (B,C)}). Following this schedule, nodes E, F, I, J are connected while $k = 1$ (see Figure 4-1d). The DER power supply is enough to serve only partial demand at these nodes ($\alpha_i^{ks} = 0$ and $\beta_i^{ks} < 1$ for $i \in$ {C,D,E,F,I,J}). The loads at nodes B, C and K are reconnected while $k = 2$ due to further line repairs (see Figure 4-1e), and a greater portion of demand can be met ($\beta_i^{k,s} > \beta_i^{k-1,s}$ for $i \in$ {C,D,E,F,I,J}). Due to power flow constraints, the loads at nodes A, G, and H cannot be reconnected until the complete network is restored. Finally, when the DN is reconnected to main grid ($\ell_e^{ks} = 1$ for $e =$(0,A) and $k =$ K) the nominal operation of the DN is fully restored (see Figure 4-1f).

4.3.2 Example No. 2

In this section, we introduce an illustrative example to discuss how failure uncertainty, repair scheduling and power flow constraints affect the DER allocation (see Figure 4-2).

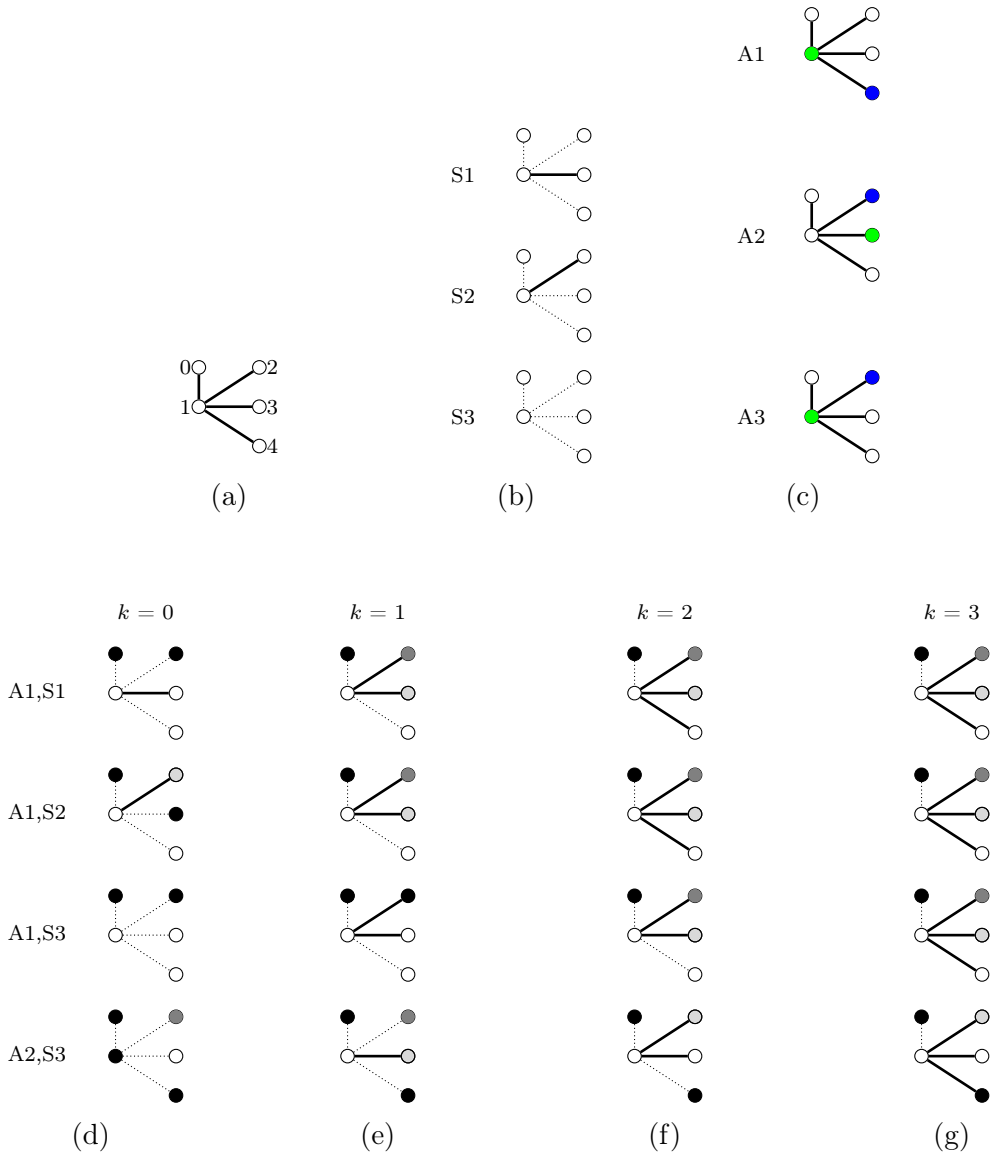

Figure 4-2: The subfigures show (a) nominal DN, (b) considered scenarios with failed lines shown by dotted lines (c) three potential DER allocations, (d) network topology after the storm, and (e)-(g) network restoration. Greater load control is indicated by a darker (grayer) node.

	i	$\mathrm{W}_i^{\mathrm{SD}}$	$\overline{\mathbf{pc}}_i$	$\overline{\mathbf{qc}}_i$	$\underline{\beta}_i$	$\mathrm{W}_i^{\mathrm{LS}}$	$\mathrm{W}_i^{\mathrm{LC}}$	Useful $\mathrm{J}_i^{\mathrm{load}}$ or V^i values for some (α_i, β_i) inputs
Nodes	1	300	0	0	0	0	0	N/A
	2	0	0.9	0.3	1/3	1000	450	$\mathrm{J}_2^{\mathrm{load}}(1,0) = 1000, \mathrm{V}^2(0,2/3) = 850, \mathrm{V}^2(0,1/3) = 700$
	3	0	0.6	0.2	1/2	900	300	$\mathrm{J}_3^{\mathrm{load}}(1,0) = 900, \mathrm{V}^3(0,1/2) = 750$
	4	300	0.3	0.1	1	650	0	$\mathrm{J}_4^{\mathrm{load}}(1,0) = 650$

	e	r_e	x_e	DERs	$\overline{\mathbf{pg}}_d$	$\overline{\mathbf{qg}}_d$	$\mathrm{v}_d^{\mathrm{ref}}$
Edges	$\{0,1\}$	0.1	0.2		0.6	0.2	1.05
	$\{1,2\}$	0.1	0.2				
	$\{1,3\}$	0.1	0.2		0.3	0.1	1.05
	$\{1,4\}$	0.1	0.2				

Scenarios	s	$\mathbb{P}(s)$	$s_{\{0,1\}}$	$s_{\{1,2\}}$	$s_{\{1,3\}}$	$s_{\{1,4\}}$
	S1	1/3	1	0	1	1
	S2	1/3	0	1	1	1
	S3	1/3	1	1	1	1

Table 4.1: Parameters of the example 4-node network.

The voltage bounds for each node i are $\underline{\mathrm{v}}_i = 0.95$ and $\overline{\mathrm{v}}_i = 1.05$ (see parameters in Table 4.1). The considered failure scenarios are shown in Figure 4-2b and three of 16 feasible allocations in Figure 4-2c, where the DER with larger (resp. smaller) capacity is shown in green (resp. blue).

First, we argue that the optimal allocation without considering line repairs, as is the case in [86, 20], is to allocate DERs to nodes 2 and 3 (allocation A2). Based on the costs of load shedding, the operator's load preference is in the order $2 \succ 3 \succ 4$. Even if the power consumed by each load is adjusted to be identical at $0.3 + 0.1\mathbf{j}$ by exercising load control ($\beta_2 = 1/3, \beta_3 = 1/2, \beta_4 = 1$), the value in operating loads 2, 3 and 4 is 700, 750, and 650, respectively; see Table 4.1. If the operator were forced to shed one of three loads, then the operator would be best off shedding load at node 4. Thus without considering repairs, the optimal allocation is to allocate DERs at nodes 2 and 3, and it does not matter which DER is allocated to which node between 2 and 3. However, we show that this allocation is suboptimal.

Second, we show how the power flow constraints influence DER allocation. If for some line e, $P_e = 0.3, Q_e = 0.1$, then $2(\mathrm{r}_e P_e + \mathrm{x}_e Q_e) = 0.1$, i.e., the voltage drop along that line equals 0.1. This constrains the amount of power that can flow along any line. If no DER is allocated to node 1, then the three loads cannot be simultaneously energized even after load control because of voltage bound violations. For e.g., if $u_2 = u_3 = 1$, $w_{21} = 1$, and $w_{32} = 1$ (such an allocation may be considered since there is no cost for developing sites at nodes 2 and 3), then for all three loads

a	$\mathrm{J}^{\mathrm{I}}(a)$	s	Stage II cost in period k				$\mathrm{J}^{\mathrm{II}}(a,s)$	$g(a)$
			$k=0$	$k=1$	$k=2$	$k=3$		
A1	200	S1	1000	450	450	450	2350	3050
		S2	1050	450	450	450	2400	
		S3	1900	1000	450	450	3800	
A3	100	S1	950	450	450	450	2300	3233
		S2	1550	950	450	450	3400	
		S3	1850	950	450	450	3700	

Table 4.2: Costs in different periods for allocations A1 and A3, and scenarios S1, S2, and S3. The costs under A2 is a constant of 950 for each period, and each scenario, thereby resulting in total expected loss of 3800.

to be energized, power from the larger DER at node 2 must travel to node 4. This would result in a voltage drop of 0.2 between nodes 2 and 4, and a voltage bound violation. Thus, the larger of the two DERs, i.e. DER 1, should be allocated at node 1 for all three loads to be energized. Hence, under allocation A2, load 4 cannot be re-energized in any scenario.

Third, we show how the uncertainty in scenarios influence the DER allocation. The summary of the operator costs in various stages under considered allocation strategies and scenarios is shown in Table 4.2. Note that A1 has the lowest total expected cost, i.e. A1 is the optimal strategy. Also, under A1 the smaller DER would be allocated to node 4. This is somewhat counterintuitive in the sense that the DERs are allocated to costly nodes (i.e. larger $\mathrm{W}_i^{\mathrm{SD}}$ values), and in case of node 1, allocated to a node without a load. This can be understood by noting that the line $\{1,4\}$ fails in all scenarios. On the other hand, under allocation A3, the load at node 4 will have to be shed for two time periods in first two scenarios, and for three time periods in the third scenario. Hence, A3 is clearly a suboptimal allocation.

4.4 Computational Studies

To implement the SAA solution approach, we utilize the mixed integer program (MIP) optimization model in JuliaPro. Solutions are obtained using the Gurobi solver.

4.4.1 Computational Setup

For this section, we use a modified IEEE 12-node test feeder, which has number of sites $|\mathcal{U}| = 4$. The distribution test feeders are placed in the Miami-Dade area of Florida, and we assume that the distribution feeders are damaged by a reconstruction of wind velocities for Hurricane Katrina (2005). We assume that the edges connecting nodes are $\sim$1 km apart.

We estimate the probability distribution $\mathbb{P}(s)$ following Section 4.1.3. For the hurricane track forecast, we use the historical track of Hurricane Katrina provided by National Hurricane Centers hurricane databases (HURDAT-2) [56]. For the hurricane wind field forecast, we assume that the wind field is given by the Holland 1980 model [47]. To calibrate the Holland model parameters, we use the wind field data of Hurricane Katrina given by the Hurricane Research Division hurricane surface wind analysis system (H*Wind, now Risk Management Solutions, Inc., (RMS) HWind) radial structure database [82]. Then, the parameters are calibrated following the approach outlined in [15]. Using the calibrated Holland model, we forecast the hurricane wind velocities at one-hour intervals and for each $0.01^\circ \times 0.01^\circ$ spatial grid within the latitude range 25.63°N – 25.92°N and longitude range 80.13°W – 80.37°W. Finally we compute $\mathbb{P}(s)$ by using the NHPP model [117], with the estimated Holland wind velocities as input and model parameter selections from [116]. The computed probability distribution is used to obtain a scenario set $\mathcal{S}$ via Sample Average Approximation (SAA).

To produce wind field forecasts, we consider two different tracks of a Category 1 storm to account for expected uncertainty in the storm trajectory. The storm tracks we used (hereafter referred to as Track 1 and Track 2) differ primarily in that the storm eye wall (region of maximum winds) is farther away from the DN for Track 2, and thus the wind velocities in the DN are lower compared to the case with Track 1. We use synthetic values for the Holland parameters (V_m, R_m, B) to produce predictions of velocities using the Holland 1980 model [47].

Next, we discuss the cost parameters related to DEF. We assume site development

cost $\mathrm{W}_i^{\mathrm{SD}} = 1,000$, $\forall\ i \in \mathcal{U}$; DER allocation cost $\mathrm{W}_{id}^{\mathrm{DA}} = 0$, $\forall\ i \in \mathcal{U},\ d \in \mathcal{D}$; and DER reallocation cost $\mathrm{W}_{ij}^{\mathrm{DT}} = 0, \forall\ i, j \in \mathcal{U}$. The cost of load shedding $\mathrm{W}_i^{\mathrm{LS}} = 1,000$ and cost of load control $\mathrm{W}_i^{\mathrm{LC}} = 100$, for all nodes i with a load. We assume that the 12-node test feeder has 6 nodes with one load each.

Next, we discuss parameters related to formulation of the constraints in DEF. For the constraint parameters related to the DERs, we assume the following parameter values: $\mathbf{mq}_d = 0.1$, $\mathrm{v}_d^{\mathrm{ref}} = 1.0\ \forall\ d \in \mathcal{D}$. The total capacity of available DERs is chosen to be 80% of the total demand in the network. We set voltage bounds $\underline{\mathbf{vc}}_i = 0.9$ and $\overline{\mathbf{vc}}_i = 1.1$, $\forall\ i \in \mathcal{N}$; maximum active and reactive power consumed $\overline{\mathbf{pc}}_i = 1.25/\mathrm{N}$ and $\overline{\mathbf{qc}}_i = \overline{\mathbf{pc}}_i/3$, $\forall\ i \in \mathcal{N}$; resistances $\mathrm{r}_e = 0.01$, $\forall\ e \in \mathcal{E}$; and reactances $\mathrm{x}_e = 2.0$, $\forall\ e \in \mathcal{E}$. We enforce that for each node i with a load, the minimum fraction of demand met must be $\underline{\beta}_i = 0.5$. Finally, we set the nominal voltage $\mathrm{v}^{\mathbf{nom}} = 1.0$.

	Failure probability			Size of islands		
	Mean	Min	Max	Med.	Min	Max
Track 1	0.63	0.56	0.75	1.58	1.08	4.20
Track 2	0.26	0.21	0.34	3.22	2.11	5.61

Table 4.3: Mean, minimum, and maximum failure probabilities of distribution lines (*left side*) and median, minimum, and maximum island size (*right side*) for the two tracks.

We generate a total of S=1,000 failure scenarios to examine distributions in frequency of failures and number/size of islands. The quadratic relationship between Poisson intensity and velocity in the NHPP model (see Section 3.1.3) results in a significant increase in probability of failures and decrease in island size if the test feeder is subject to higher storm velocities (see Table 4.3).[9] An average of 5.96 failures occur per scenario in Track 1, while only 2.88 failures occur per scenario in Track 2 (see Figure 4-3a). The smaller median island size under Track 1 corresponds with a larger number of islands (see Figure 4-3b).

[9]Category 2-5 storms have a larger radial region of high winds, and we can expect much higher failure probabilities in such cases. In contrast, under mild storms with the tropical storm rating, Poisson intensities are uniformly λ_{norm}, and the failure probability is < 0.001.

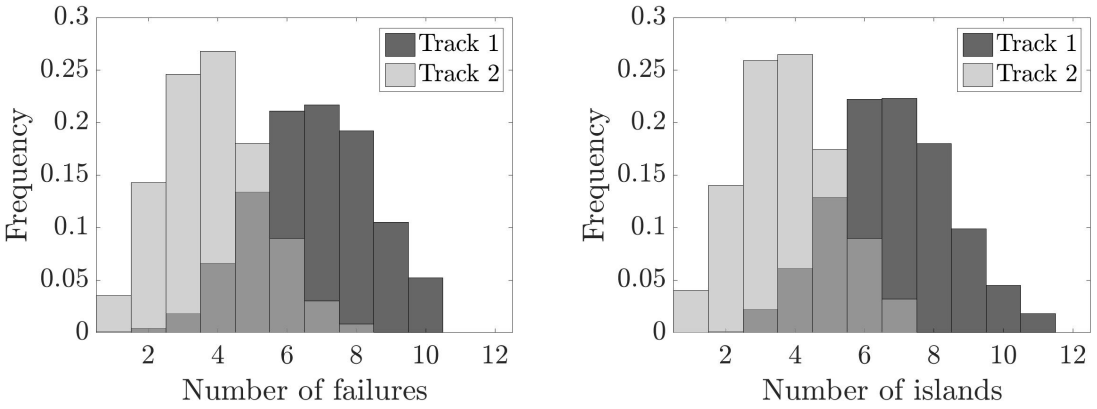

Figure 4-3: (a) – Empirical probability of number of line failures; (b) – Number of islands formed. A total of 1,000 failure scenarios are simulated to produce the histograms.

4.4.2 System Performance

System performance at a period k is defined as the average percentage difference between the cost of unmet demand and the total cost of complete load shedding, averaged over the sampled scenarios s and as a function of the optimal first-stage solution of each scenario. For period $k \in \mathcal{K}$, we define the system performance $\mathcal{P}^k$ as follows:

$$\mathcal{P}^k = \sum_{s \in \mathcal{S}} \mathbb{P}(s) \times 100 \left(1 - \frac{\mathrm{J}_{\mathrm{L}}^{\mathrm{II}}(\chi^{ks\star})}{\sum_{i \in \mathcal{N}} \mathrm{W}_i^{\mathrm{LS}}}\right), \tag{4.7}$$

where $x^{s\star} := [\chi^{ks\star}]_{k \in \mathcal{K}}$ denotes the optimal microgrid operation corresponding to $\mathrm{J}^{\mathrm{II}}(a, s)$. Note that system performance decreases with increasing cost of unmet demand, and is at a maximum of 100% when the demand is fully met.

4.4.3 Effect of Resource Constraints

To evaluate the system performance under different resource constraints, we vary $\mathbf{G}$ (number of available DERs) and Y (maximum number of lines repaired in each period). The system performance as a function of k under different values of $\mathbf{G}$ and Y for two storm tracks is shown in Figure 4-4. Since there are more failures on average in the DN under Track 1, the system performance at $k = 0$ is lower than for Track 2.

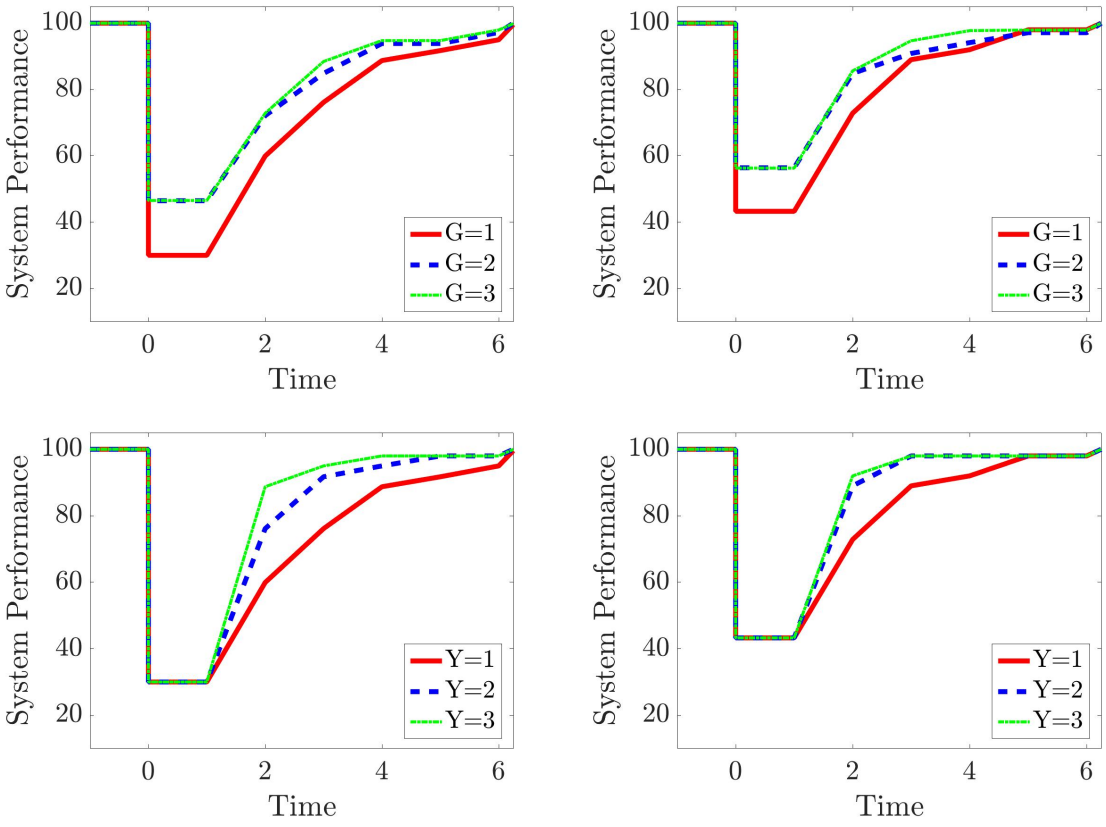

(a) Track 1 (b) Track 2

Figure 4-4: Average system performance of the DN under the two track scenarios, varying **G** while setting Y = 1 (*top row*) and varying Y while setting **G** = 1 (*bottom row*).

If $\mathbf{G} > 0$, even networks with high failure probabilities will be able to meet a portion of demand given a nonzero DER budget – the network repair time will simply be longer. Increasing Y noticeably decreases the average time required to repair the network (return to system performance that is close to 100%) under both track scenarios. Increasing **G** ensures that a larger portion of system demand is met while line repairs are not yet completed.

4.4.4 Effect of Cost Parameters

Next, we evaluate how cost parameters affect the optimal solution to DEF (see Figure 4-5). Recall that the first-stage cost is the sum of the site development cost W^{SD} and resource allocation costs W^{DA} (see Eq. 4.2.1). Recall that the second-stage cost is given by the cost of site development W^{SD}, reallocation W^{DT}, load shedding W^{LS}, and load control W^{LC} (see Eq. 4.2.2-4.2.3). We examine how the allocations $\hat{a}$ and associated cost $g(\hat{a}, \mathcal{S})$ vary with W^{SD} (Stage I), while fixing W^{LC} and W^{LS}. In the analysis, we assume that W^{DA}, W^{DT}, and W^{SD} (Stage II) are zero.

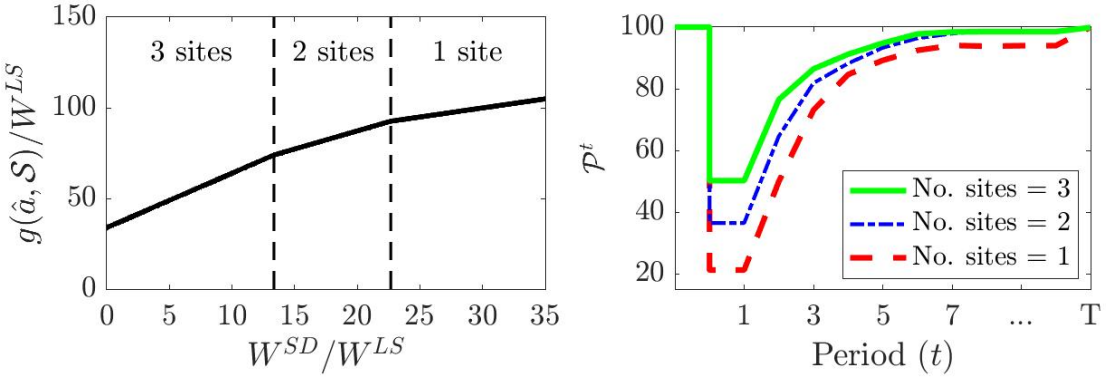

Figure 4-5: (a) – Normalized total cost $g(\hat{a}, \mathcal{S})/\mathrm{W}^{\mathrm{LS}}$ vs. the ratio of site development and load shedding costs $\mathrm{W}^{\mathrm{SD}}/\mathrm{W}^{\mathrm{LS}}$. The plot is divided into three regimes based on $\mathrm{W}^{\mathrm{SD}}/\mathrm{W}^{\mathrm{LS}}$, to indicate that the number of sites developed decreases with increasing W^{LS}. (b) – System performance under the three regimes. We use the following parameters on a 12-node network and using LBD-Greedy: $\mathbf{G} = 3$ (all fixed DERs), $\mathrm{Y} = 2$, $\mathrm{S} = 10$.

When the site development cost W^{SD}, the optimal first-stage solution minimizes

the Stage II cost. In Figure 4-5a, when the site development cost parameter (W^{SD}) is 0, in the optimal allocation three sites are developed. Now, if W^{SD} increases by a small value Δ, then the expected total cost increases by 3Δ (see Section 4.2.1). As W^{SD} further increases, it becomes less costly to two develop just two sites. Now, for a small increase Δ in W^{SD}, the total cost increases by only 2Δ. The number of sites developed will continue to drop as W^{SD} increases further. Eventually, no sites are developed when W^{SD} is sufficiently large. Figure 4-5a highlights the cost regimes corresponding to these differing solutions. Figure 4-5b demonstrates that system performance predictably worsens with decreasing number of sites developed.

4.4.5 Benefits of Mobile DERs

We next investigate the benefits of utilizing a combination of fixed and mobile DERs, as opposed to using only fixed DERs. To measure the benefit, we compare the system performance and total cost of various DER constraints given by $\mathbf{G}$, $|\mathcal{D}_f|$, and $|\mathcal{D}_m|$.

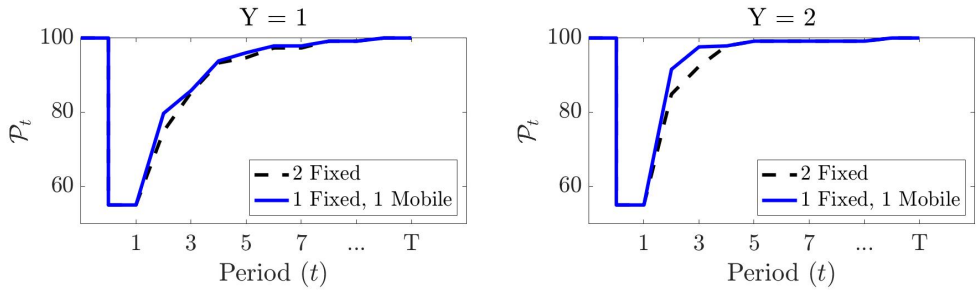

Figure 4-6: Benefit of using mobile DERs for a 12-node network with total number of available DERs $\mathbf{G} = 2$ and number of scenarios S = 5. We consider the case of two fixed DERs ($|\mathcal{D}_f| = 2$, $|\mathcal{D}_m| = 0$) or one fixed DER + one mobile DER ($|\mathcal{D}_f| = 1$, $|\mathcal{D}_m| = 1$), under two values of the repair rate Y.

Figure 4-6 demonstrates the effect of using mobile DERs on the system performance $\mathcal{P}^k$. The benefit of mobile DERs is realized starting at period $k = 2$, when the DERs can begin to move around. This is because microgrid islands expand in size (and eventually merge) with the repairs. Thus at each period, the locations of DERs that would maximize the demand met in the network may change, in which case the movable DER is re-allocated accordingly. Starting around period $k = 5$, the benefit

of re-allocating the mobile DER is limited because connectivity is restored between most loads and the available DERs in the scenarios considered. Therefore the system performance under the cases of two fixed DERs or one fixed + one mobile DER is similar in the later periods.

4.5 Concluding remarks

This work presents a modeling approach to the integrated pre-storm resource allocation and post-storm repair and dispatch problem for improving resilience of electricity distribution networks against storms. The problem is formulated as a two-stage stochastic mixed-integer program (SMIP2). The program considers pre-storm allocation of distributed energy resources (DERs); as well as post-storm network restoration (resource re-allocation and component repairs) and multi-master operation of islanded microgrids over a multi-period timeframe. Furthermore, the model handles uncertainties in the locations of component failures by using a nonhomogeneous Poisson process (NHPP) model (see Chapter 3) to generate the component failure scenarios. Hence, the optimal resource allocations are dependent on damage uncertainties, which in turn are dependent on the physical structure and temporal evolution of the hurricane.

In order to assess network resilience to the hurricane under various resource allocation strategies, we define a period-wise system performance metric. We analyze the effect of resource constraints, cost parameters, and inclusion of mobile DERs on the system performance.

Chapter 5

Solution Approaches for Stochastic Resource Allocation

The two-stage stochastic mixed-integer program (SMIP2) outlined in Chapter 4 is computationally challenging to solve. Typically, linear programs with integer variables are solved using branch-and-bound (B&B) algorithms. B&B algorithms require significant time to solve programs, in comparison to solving linear programs that include only continuous variables, which are typically solved using the simplex method. Furthermore, as noted in Chapter 4, the number of possible damage scenarios increases exponentially with the network size. This necessitates scenario selection approaches to decrease the size of the MILP, and motivated us to use the Sample Average Approximation (SAA) method.

Even solving (SAA) can be computationally expensive. A naive approach to solve (SAA) is to solve the recourse problems $\text{REC}(a, s)$ under every possible resource allocation strategy. This is inefficient because the number of feasible pre-storm resource allocations increases exponentially with the DER resource constraint. Furthermore, the number of binary variables in the recourse problem $\text{REC}(a, s)$ increases quadratically with the network size. In this section, we propose more efficient approaches based on L-shaped Benders decomposition (LBD), which can output a suitable solution to the two-stage program by potentially considering a smaller number of Stage I strategies.

In Section 5.1, we provide a generic overview of the L-shaped Benders decomposition (LBD) solution approach, and discuss the primary ways in which LBD approaches may differ. In Section 5.2, we formulate the LBD with Greedy Approach (LBD-Greedy). In Section 5.3, we formulate the LBD with Dual Integer Cuts (LBD-DIC) approach. Our last approach that we formulate is the Nested Benders Decomposition (NBD) approach, which we discuss in Section 5.4. We compare the solution approaches in terms of convergence and solution accuracy, and make concluding remarks in Section 5.5.

5.1 Overview of L-shaped Benders Decomposition

In this section, we provide a generic overview of the L-shaped Benders Decomposition (LBD) solution approach [12] for solving two-stage stochastic optimization problems. In the LBD approach, we decompose the two-stage problem into a master problem (for the Stage I allocation problem) and the subproblems (S2). Then, we alternately solve the master problem and subproblems (S2) in an iterative manner, until a defined termination criteria is met and/or the number of maximum iterations is exceeded. The motivation for using LBD-based approaches is to solve (DEF) in a manner that is more efficient than simple enumeration of all first-stage strategies $a \in \mathcal{A}$, followed by solving subproblems under each first-stage strategy a.

We denote an iteration of our method by l. Then, the generic master problem in the l^{th} iteration is defined as follows:

$$\begin{aligned} \widehat{a}^l = \arg\min_{a} \quad & \mathrm{J}^{\mathrm{MP}}(a) \\ \text{s.t.} \quad & a \in \mathcal{A}, \\ & \text{Benders cut}(j) \qquad \forall\, j \in \mathcal{J}_l \end{aligned} \tag{5.1}$$

where $\mathcal{J}_l = \{0, \cdots, l-1\}$ denotes the set of completed iterations. For the initial (0^{th}) iteration, the master problem contains only the Stage I feasibility constraints ($a \in \mathcal{A}$), and no Benders cuts or trivial cuts. At each iteration, solving Eq. (5.1)

yields a feasible solution $\widehat{a}^l$, which is then used to parameterize the scenario-wise subproblem (S2) with $a = \widehat{a}^l$ as fixed. These scenario-wise subproblems can be solved independently of each other because no constraint of (S2) involves variables from more than one scenario subproblem. The solution to the Stage II problem is used to generate an optimality cut which is then added to the master problem for the next iteration $l + 1$.

In the classical LBD method, the optimality cut is referred to as the Benders cut. The classical LBD method has been widely used in the context of Stochastic Linear programs. However, its major limitation is that it requires the Stage II problem to be a convex program, in which case the Benders cut is formed using the optimal solutions to the dual subproblems. However, the subproblems given by REC(a, s) are MILPs which are discontinuous and non-convex. The three solution approaches that we devise (LBD-Greedy, LBD-DIC, and NBD) differ in the means by which we generate the optimality cuts.

The optimality cuts are used to constrain the set of feasible first-stage resource allocations $\mathcal{A}$, or to provide updates to lower and upper bounds on the overall two-stage problem objective. The algorithm terminates when a defined convergence criterion (based on the upper and lower bounds) is met, and/or all solutions $a \in \mathcal{A}$ have been eliminated by the Benders cuts.

In summary, the three solution approaches we consider (LBD-Greedy, LBD-DIC, and NBD) differ primarily in terms of: optimality cut formulation, master problem formulation, and algorithm termination criteria. We now proceed to discuss the first approach formulated, LBD with Greedy Approach (LBD-Greedy).

5.2 LBD with Greedy Approach

In this section, we outline an approach that is referred to as "L-shaped Benders Decomposition with Greedy Approach" (LBD-Greedy). The approach is named after the "greedy approach" [17] we employ for solving the Stage II scenario-wise problems given by REC(a, s).

The master problem for the l^{th} iteration in our LBD-Greedy method as follows:

$$\text{(MP1)} \qquad \min_{a \in \mathcal{A}} \quad \mathrm{J}^{\mathrm{I}}(a) \tag{5.2a}$$

$$\text{s.t.} \quad \text{BC-Greedy}(j) \qquad \forall\, j \in \mathcal{J}_l \tag{5.2b}$$

$$\text{TC}(j) \qquad \forall\, j \in \mathcal{J}_l, \tag{5.2c}$$

where the master problem objective $\mathrm{J}^{\mathrm{MP}}(a) = \mathrm{J}^{\mathrm{I}}(a)$, BC-Greedy$(j)$ denotes the Benders (optimality) cut formed at iteration j, and TC(j) denotes the so-called "trivial cut" formed at iteration j. We will subsequently discuss the formulation of the Benders and trivial cuts.

As discussed in Section 5.1, formulation of the Benders cut requires the Stage II problem to be a convex program, but the subproblems given by REC(a, s) are MILPs which are discontinuous and non-convex. Therefore, generating the optimality cut in LBD-Greedy involves two sub-steps. First, we solve the MILP REC(a, s). Then, we use the optimal binary values in the solution of REC(a, s) to fix the binary variables in REC(a, s), and solve the $\overline{\text{REC}}(a, s)$ to generate the Benders cut.

Solving the multi-period subproblem REC(a, s) can be computationally challenging because the number of binary variables in REC(a, s) increases quadratically with the network size. Thus we propose a "greedy approach" as a heuristic to speed up solving of the MILP REC(a, s). This approach entails decomposing REC(a, s) into period-wise subsubproblems; obtaining a greedy, feasible Stage II solution using the subsubproblem solutions; and using the greedy solution as a warm-start solution for solving the complete subproblem REC(a, s).

5.2.1 Formation of Benders and trivial cuts

The generation of Benders cuts at each iteration of the LBD-Greedy method requires two steps. In the first step, we solve REC$(\widehat{a}^l, s)$ to compute the optimal values of (r^s, x^s) in the l^{th} iteration, which we denote as $(\widehat{r}^{sl}, \widehat{x}^{sl})$. Let the variables (r^s, x^s) be partitioned into three types of variables: binary variables δ^s, continuous non-slack

variables ξ^s, and slack variables σ^s. The dimensions of these variables are as follows: $\delta^s \in \{0,1\}^{N_5^s}$ where $N_5^s = \mathrm{K}N_2 + |\mathcal{I}_3|$ Similarly, let the matrix $[\mathrm{B}_2 \ \mathrm{B}_3]$ be partitioned along the columns as $[B_4 \ B_5 \ \mathbf{I}]$, where the columns in B_4 (resp. B_5) correspond to the binary (resp. continuous non-slack) variables, and $\mathbf{I}$ is an identity matrix. Then, we fix the values of binary variables in the optimal solution to $\mathrm{REC}(a,s)$, which results in a linear program stated as follows:

$$\begin{aligned} \underline{\mathrm{LP2}}(l,s): \quad \mathrm{J}_{\mathrm{D}}^{\mathrm{II}}(l,s) + \min_{\xi^s,\sigma^s} \quad & \sum_{k\in\mathcal{K}}\sum_{i\in\mathcal{N}} -\mathrm{W}_i^{\mathrm{LC}}\beta_i^{ks} \\ \text{s.t.} \quad & B_5\xi^s + \sigma^s = \widetilde{\mathrm{h}}(\widehat{a}^l,l,s) \\ & \sigma^s \geq \mathbf{0} \end{aligned}$$

where $\widetilde{\mathrm{h}}(\widehat{a}^l,l,s)$ denotes the coefficient vector of the dual problem, and is defined as:

$$\widetilde{\mathrm{h}}(\widehat{a}^l,l,s) = \mathrm{h} - \mathrm{F}\widehat{a}^l - B_4\widehat{\delta}^{sl},$$

and $\mathrm{J}_{\mathrm{D}}^{\mathrm{II}}(l,s)$ denotes the sum of the cost terms involving only the binary variables, and is defined as:

$$\mathrm{J}_{\mathrm{D}}^{\mathrm{II}}(l,s) = \sum_{k\in\mathcal{K}}\Big(\mathrm{J}_{\mathrm{R}}^{\mathrm{II}}(\rho^{ksl}) + \sum_{i\in\mathcal{N}}\big((\mathrm{W}_i^{\mathrm{LS}} - \mathrm{W}_i^{\mathrm{LC}})\alpha_i^{ksl} + \mathrm{W}_i^{\mathrm{LC}}\big)\Big).$$

In the second step, we solve the dual of $\underline{\mathrm{LP2}}(l,s)$, which we refer to as D-$\overline{\mathrm{LP2}}(l,s)$. Let an optimal solution of D-$\overline{\mathrm{LP2}}(l,s)$ be denoted by $\widehat{\lambda}^{sl} \in \mathbb{R}^{N_4}$. Then, the Benders cut is given as follows:

$$\text{BC-Greedy}(l): \quad \mathrm{J}^{\mathrm{I}}(a^l) + \frac{1}{|\mathcal{S}|}\sum_{s\in\mathcal{S}}\Big(\mathrm{J}_{\mathrm{D}}^{\mathrm{II}}(l,s) + (\widetilde{\mathrm{h}}(a,l,s))^{\top}\widehat{\lambda}^{sl}\Big) \ \leq \ g(\widehat{a}^l,\mathcal{S}) - \epsilon, \tag{5.3}$$

where $\widetilde{\mathrm{h}}(a,l,s)$ is a vector of expressions of Stage I variables given by

$$\widetilde{\mathrm{h}}(a,l,s) = \mathrm{h} - \mathrm{F}a - B_4\widehat{\delta}^{sl},$$

and ϵ is a small positive number (say 10^{-6}). Note that $\widetilde{\mathrm{h}}(\widehat{a}^l,l,s)$ is different from

$\widetilde{\mathrm{h}}(a, l, s)$ because the former is a vector of constants, whereas the latter is a vector of expressions in Stage I variable a.

The cut BC-Greedy(l) renders $\widehat{a}^l$ infeasible. Suppose for contradiction that $\widehat{a}^l$ is not eliminated. Also suppose that we did not add the trivial cut in iteration l. Then, in the next iteration, solving the master problem will again result in the same optimal solution $\widehat{a}^l$. Then, using $\widehat{a}^l$ as a parameter for the Stage II subproblems will result in the same left hand side in Eq. (5.3) as in the previous iteration, which is equivalent to $g(\widehat{a}^l, \mathcal{S})$. This violates the cut given by Eq. (5.3). However, the off-the-shelf solver may sometimes not be able to numerically compute the optimal variables with enough accuracy to guarantee the elimination of $\widehat{a}^l$. This can stall the progress of our algorithm, so we also add the trivial cut to guarantee the elimination of $\widehat{a}^l$. The trivial cut, which is added at each iteration $l+1$ to ensure that the first-stage solution $\widehat{a}^l$ corresponding to iteration l is limited, is given by:

$$\sum_{k=1}^{N_1} \widehat{a}^l_k a_k + (1 - \widehat{a}^l_k)(1 - a_k) \leq N_1 - 1,$$

where index $k \in \{1, ..., N_1\}$ is used to denote the k-th first stage variable.

5.2.2 Greedy Approach for Stage II subproblems

Now we discuss the greedy approach used to solve the scenario-wise subproblems given by REC($\widehat{a}^l, s$). The subproblems each consist of $\mathcal{O}(\mathrm{NK})$ binary variables. Solving each scenario-wise subproblem using a branch-and-bound algorithm can potentially result in $\mathcal{O}(2^{\mathrm{NK}})$ computational time complexity. Our greedy approach finds a feasible solution to REC($\widehat{a}^l, s$) which can be used as a warm-start solution for solving REC($\widehat{a}^l, s$). As a result, the corresponding objective value of the warm-start solution can be used as an upper bound, which prunes the branch-and-bound tree.

The greedy approach involves determining the optimal restoration action and microgrid control that minimizes the operator loss at each period, sequentially from the first to the last period. Given the Stage I allocation $\widehat{a}^l$ and the scenario s, we can obtain the restoration action $\widehat{\rho}^{\,0s}$ for the zeroth period $k = 0$.

At each period k, the solutions ρ^{ks} and χ^{ks} myopically minimize the associated period-wise cost $\mathrm{J}_{\mathrm{R}}^{\mathrm{II}}(\rho^{ks}) + \mathrm{J}_{\mathrm{L}}^{\mathrm{II}}(\chi^{ks})$. The constraints on the restorative actions ρ^{ks} at period k depend on the line operational state κ^{k-1s} and site development state μ^{k-1s} at period $k-1$. Then, for fixed (a, s) and $k = 1, \cdots, \mathrm{K}$, we solve the following MILP:

$$\begin{aligned} \Phi^k(\widehat{\rho}^{\,k-1s}) \quad = \quad & \min_{\rho^{ks}, \chi^{ks}} \quad \mathrm{J}_{\mathrm{R}}^{\mathrm{II}}(\rho^{ks}) + \mathrm{J}_{\mathrm{L}}^{\mathrm{II}}(\chi^{ks}) \\ & \text{s.t.} \quad \rho^{ks} \in \mathcal{R}^k(\widehat{\rho}^{\,k-1s}) \\ & \qquad \chi^{ks} \in \mathcal{X}^k\left(\rho^{ks}\right). \end{aligned} \tag{5.4}$$

Thus, we add the following cut to $\mathrm{REC}(\widehat{a}^l, s)$:

$$\sum_{k=1}^{\mathrm{K}} \left(\mathrm{J}_{\mathrm{R}}^{\mathrm{II}}(\rho^{ks}) + \mathrm{J}_{\mathrm{L}}^{\mathrm{II}}(\chi^{ks}) \right) \leq \sum_{k=1}^{\mathrm{K}} \left(\mathrm{J}_{\mathrm{R}}^{\mathrm{II}}(\widehat{\rho}^{ks}) + \mathrm{J}_{\mathrm{L}}^{\mathrm{II}}(\widehat{\chi}^{ks}) \right). \tag{5.5}$$

Also, the sum of the solutions to the greedy problem, $\Phi(\widehat{a}^l) = \mathrm{J}^{\mathrm{I}}(\widehat{a}^l) + \sum_{s \in \mathcal{S}} \mathbb{P}(s) \sum_{k=1}^{\mathrm{K}} \Phi^k(\widehat{\rho}^{\,k-1s})$ is an upper bound to the optimal objective value $\mathrm{J}^{\mathrm{II}}(\widehat{a}^l, s)$ corresponding to $\mathrm{REC}(\widehat{a}^l, s)$. In summary, the greedy heuristic consists of K smaller MILP problems with $\mathcal{O}(\mathrm{N})$ binary variables each, and a greedy solution can be computed in $\mathcal{O}(\mathrm{K}2^{\mathrm{N}})$ time.

5.2.3 Description of the algorithm

Algorithm 1 provides an in-depth overview of our LBD-Greedy method. At the start of Algorithm 1, an upper bound variable $\bar{Z}$ to (DEF) is initialized to ∞. At the completion of iteration l, we update the current upper bound $\bar{Z}$ if it is greater than the overall loss $g(\widehat{a}^l, \mathcal{S})$ of the strategy $\widehat{a}^l$. The algorithm terminates if one obtains a solution with an associated loss less than or equal to L_{target}, a threshold loss which is acceptable to the operator. Otherwise, the algorithm continues until either the iteration limit is reached or the master problem is rendered infeasible by the Benders cuts and trivial cuts. The objective value associated with the solution to (DEF) is given by the value of $g(\widehat{a}^{\text{best}}, \mathcal{S})$ where $\widehat{a}^{\text{best}}$ is the strategy returned at the termination of Algorithm 1. Since we eliminate at least one Stage I solution in each iteration due

to the trivial cuts and there are finite number of allocation strategies in set $\mathcal{A}$, LBD-Greedy is guaranteed to terminate. However, the Benders cut is considered likely to eliminate more than one Stage I strategy at each iteration. That means the LBD-Greedy method is likely to converge in a smaller number of iterations than the total number of Stage I strategies $|\mathcal{A}|$.

Algorithm 1 Modified LBD method with Greedy Approach

Input: Iteration limit $\bar{l}$
Output: $\widehat{a}^{\text{best}}$ ▷ Optimal resource allocation strategy
Set $\bar{Z} \leftarrow \infty,\ l \leftarrow 0$
For $l = 0$, solve master problem (5.2) to compute $\widehat{a}^0$
while $\widehat{a}^l$ is **not** null **and** $l < \bar{l}$ **do** ▷ Problem (5.2) is feasible
  if $\bar{Z} \leq L_{\text{target}}$ **then return** $\widehat{a}^l$ ▷ Overall loss is acceptable
  Initialize cut $\Psi \leftarrow \mathrm{J}^{\mathrm{I}}(\widehat{a}^l)$
  for $s \in \mathcal{S}$ **do**
    Use greedy approach to compute a greedy solution to REC$(\widehat{a}^l, s)$
    Use greedy solution to add (5.5) to REC$(\widehat{a}^l, s)$; get optimal solution $(\widehat{r}^{sl}, \widehat{x}^{sl})$
    Partition $(\widehat{r}^{sl},\ \widehat{x}^{sl})$ into discrete, continuous, and slack variables $(\widehat{\delta}^{sl},\ \widehat{\xi}^{sl},\ \widehat{\sigma}^{sl})$
    Use $\widehat{a}^l$ and $\widehat{\delta}^{sl}$ to obtain $\underline{\text{LP2}}(l, s)$, compute $\widehat{\lambda}^{sl}$ by solving its dual D-$\overline{\text{LP2}}(l, s)$
    $\Psi \leftarrow \Psi + \frac{1}{|\mathcal{S}|}\left(\mathrm{J}_{\mathrm{D}}^{\mathrm{II}}(l, s) + (\widetilde{\mathrm{h}}(a, l, s))^{\top}\widehat{\lambda}^{sl}\right)$
  end for
  Add Benders cut(l) Ψ and trivial cut(l) to the master problem (5.2)
  if $g(\widehat{a}^l, \mathcal{S}) < \bar{Z}$ **then** $\bar{Z} \leftarrow g(\widehat{a}^l, \mathcal{S}),\quad \widehat{a}^{\text{best}} \leftarrow \widehat{a}^l$
  Update $l \leftarrow l + 1$
  Compute $\widehat{a}^l$ by solving the master problem (5.2)
end while
return $\widehat{a}^{\text{best}}$ ▷ Strategy with lowest overall loss

5.2.4 Computational Experiments

We discuss computational experiments that involve solving (DEF) using the LBD-Greedy solution approach. The experiments are conducted using a modified IEEE 36-node distribution test feeder. In this network, 12 out of 36 randomly-chosen nodes have one load each. We otherwise use the same parameters as in Section 4.4 of Chapter 4.

System Performance Evaluation:

We compare the system performance of solutions obtained using four approaches: (1) Simple enumeration (SE): best solution from the set of feasible allocations obtained by simple enumeration; (2) the solution to LBD with Greedy Approach (LBD-Greedy); (3) 'Best of Random Allocations' (BoRA): the best solution from a set of randomly-sampled allocations; and (4) 'Single Allocation' (SA): one pre-determined allocation such that the DERs have an even spatial distribution across the DN.

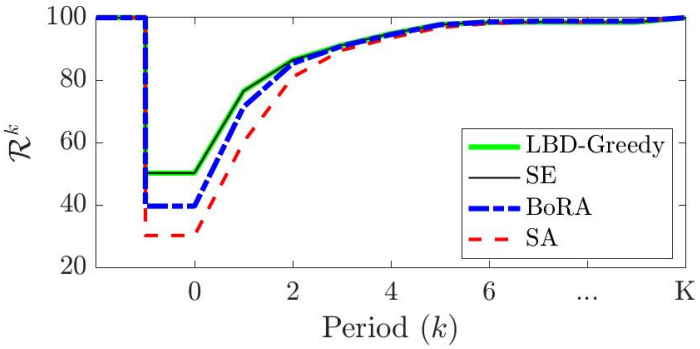

Figure 5-1: Average system performance of the 36-node DN under allocations given by four solution approaches: LBD-Greedy, SE, BoRA, and SA. We use the following parameters: $\mathbf{G} = 3$ (all fixed DERs), $\mathrm{Y} = 2$, and $\mathrm{S} = 10$. The sample is obtained using the scenario reduction method.

Figure 5-1 demonstrates how system performance $\mathcal{P}^k$ (computed using (4.7)) evolves over the set of periods under the four approaches. Before the storm occurs, the network is in nominal operation and $\mathcal{P}^k = 100\%$. After the storm ($k = 0$), $\mathcal{P}^k$ is at a minimum, and improves in subsequent periods with each set of line repairs. Once all the damaged lines are repaired, $\mathcal{P}^k$ is almost (but not fully) restored. Finally, $\mathcal{P}^k$ returns to 100% following reconnection of the DN to the bulk power grid at $k = \mathrm{K}$. As expected, LBD-Greedy and SE have equivalent system performance at all periods and outperform the other methods.

Evaluation of Greedy Approach:

Since the Stage II subproblem REC(a, s) is a minimization problem, the solution computed by the greedy approach will provide an upper bound to the optimal value of REC(a, s). In Figure 5-2, we compare the system performance of the optimal and greedy solutions under two different scenarios and varying values of Y. The results for

Scenario 1 demonstrate that the greedy solution exactly matches the optimal solution. For Scenario 2, the greedy solution is suboptimal, however the difference in system performance from that of optimal solution is small. Although the system performance for a greedy solution is higher than that of the optimal solution (see bottom right plot in Figure 5-2) at $k = 2$, the total expected cost under will be higher in the former case.

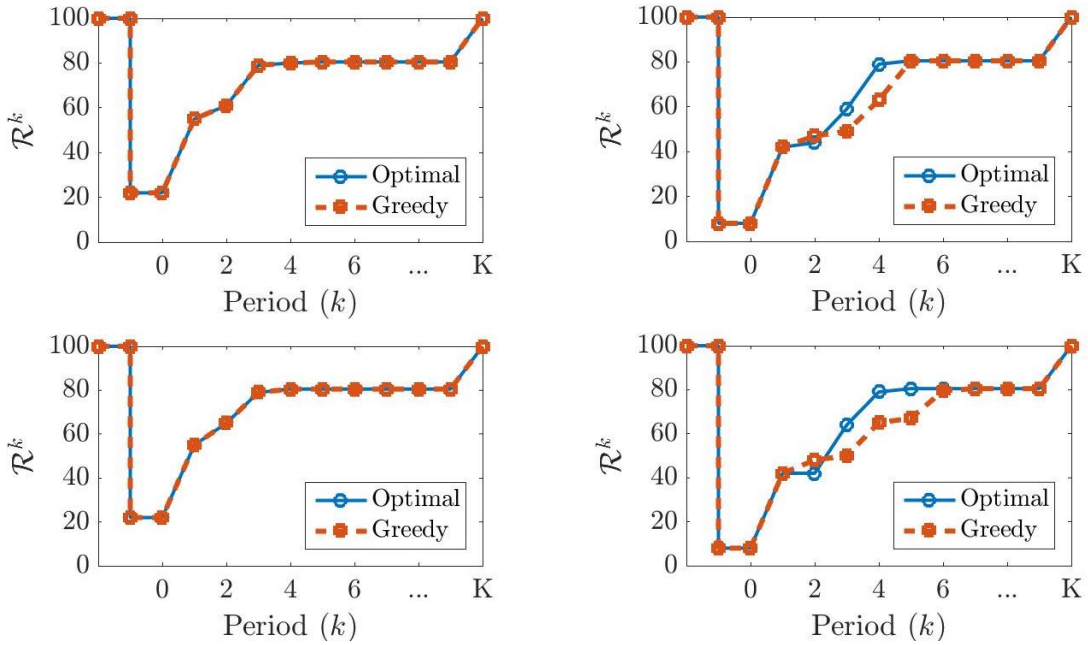

Figure 5-2: System performance under two failure scenarios for two cases. Case 1: $\mathbf{G} = 1, \mathrm{Y} = 2$ (*top row*), and Case 2: $\mathbf{G} = 1, \mathrm{Y} = 3$ (*bottom row*).

A smaller difference between the system performance of the optimal and greedy solutions corresponds to a tighter upper bound. In Scenario 1, the greedy upper bound ensures that the greedy solution is the only feasible solution, because the greedy and optimal solutions are the same. In Scenario 2, the greedy upper bound renders a large number of line repair schedules infeasible, but multiple feasible schedules remain.

5.3 LBD with Dual Integer Cuts

Here, we propose a novel solution approach, which we refer to as "L-shaped Benders Decomposition with Dual Integer Cuts (LBD-DIC)." Our motivation for formulating

the LBD-DIC approach is the computational expense associated with solving the Stage II subproblems REC(a, s). Although the greedy approach in the LBD-Greedy method reduces the computational time required to solve REC(a, s), computing the greedy solution still requires $\mathcal{O}(\mathrm{K2^N})$ computational time.

Similar to the LBD-Greedy approach, the LBD-DIC approach iterates between a master problem and a subproblem for each scenario $s \in \mathcal{S}$. However, the LBD-DIC differs from the LBD-Greedy in two main aspects: 1) In LBD-Greedy, we solve the MILP REC(a, s) using the greedy warm-start solution, fix the binary variable values, and then solve the resulting LP to obtain the Benders cut. In LBD-DIC, we solve the LP relaxation $\overline{\mathrm{REC}}(a, s)$ to obtain the optimality cut. 2) The LBD-DIC generates optimality cuts (referred to as Dual Integer Cuts [110]) by leveraging the product of the reduced costs of the Stage II variables and the optimal values of the Stage II variables. Moreover, the main feature of dual integer cuts is that it leverages the properties of the formulation to lower bound the optimal values of Stage II variables by the Stage I variables. Our main contribution in the LBD-DIC method is that we have derived the dual integer cuts based on the power flow constraints. The resulting dual integer cuts require less computational expense to generate than the optimality cuts in LBD-Greedy because LBD-DIC involves solving D-$\overline{\mathrm{REC}}(a, s)$.

In the LBD-DIC method, we formulate the master problem as follows:

$$\text{(MP2)} \quad \left(\widehat{a}^l, (\widehat{\theta}^{sl})_{s\in\mathcal{S}}\right) \coloneqq \underset{a\in\mathcal{A},(\theta^s)_{s\in\mathcal{S}}}{\arg\min} \quad \mathrm{J}^{\mathrm{MP}}(a) \coloneqq \mathrm{J}^{\mathrm{I}}(a) + \frac{1}{\mathrm{S}}\sum_{s\in\mathcal{S}}\theta^s \tag{5.6a}$$

$$\text{s.t.} \quad \theta^s \geq \underline{g}(a, s) \qquad \forall\, s \in \mathcal{S} \tag{5.6b}$$

$$\theta^s \geq 0 \qquad \forall\, s \in \mathcal{S}, \tag{5.6c}$$

where $\underline{g}(a, s)$ is an expression in Stage I variable such that $\underline{g}(\widehat{a}^l, s)$ is a lower bound to the variable θ^s. In particular, if $\underline{g}(a, s)$ is equal to $g(a, s)$, then the optimal solution of the master problem (MP2) $(a^\star, (\theta^{s\star})_{s\in\mathcal{S}})$ provides an optimal Stage I allocation strategy $a^\star$ for problem (DEF).

LBD-DIC begins with initializing a lower bound $\underline{Z}$ and a "relaxation" upper bound

$\widetilde{Z}$ for the objective value associated with (DEF). In each iteration l, the algorithm first solves the master problem (MP2) with the resource constraints $a \in \mathcal{A}$ and the optimality cuts obtained in the previous iterations. Since, in each iteration, we obtain a stronger relaxation of the master problem, the objective value of (MP2) can only improve or stay the same. An optimal solution $\left(\widehat{a}^l, (\widehat{\theta}^{sl})_{s\in\mathcal{S}}\right)$ to the master problem (MP2) is used to parameterize the sub-problem REC(a, s) for each scenario $s \in \mathcal{S}$. If a sub-problem admits a feasible solution, we add an optimality cut (5.6b) to (MP2); otherwise we add a feasibility cut. However, in our model, there always exist a feasible solution to REC(a, s) for every $(a, s) \in \mathcal{A} \times \mathcal{S}$. Therefore, we do not need to add feasibility cuts. At each iteration, we also update the "relaxation" upper bound $\widetilde{Z}$ as: $\widetilde{Z} \leftarrow \min\{\widetilde{Z}, \underline{g}(\widehat{a}^l, \mathcal{S})\}$. Note that $\widetilde{Z}$ is not necessarily an upper bound to the objective associated with (DEF). However, we still use it to control the algorithm's convergence: the algorithm terminates when the percentage difference between $\underline{Z}$ and $\widetilde{Z}$ is sufficiently small (e.g. 1%).

The main difficulty in solving the master problem (MP2) arises from approximating the Stage II cost $\underline{g}(a, s)$ in (5.6b). In Section 5.3.1, we present our results to lower bound $g(a, s)$, and address how we generate optimality cuts to resolve the difficulty of estimating the Stage II cost $\underline{g}(a, s)$. In Section 5.3.2, we present our results for strengthening the so-called "relaxation" upper bound estimates at each iteration. In Section 5.3.3, we describe the LBD-DIC algorithm in full detail. Finally, Section 5.3.4 discusses the associated computational experiments.

5.3.1 Dual Integer cuts

The main element of the LBD-DIC approach is the *dual integer cut* [110], which is an optimality cut used to approximate the Stage II cost in (5.6b) of (MP2). To derive our the dual integer cut, we first present our theoretical results.

To begin, we restate a result of [110] which states that the optimal value of an REC(a, s) is equal to the sum of (i) a feasible solution of D-$\overline{\text{REC}}(a, s)$ and the dual cost vector, and (ii) the product-sum of optimal solutions of the MILP and the corresponding reduced cost of the primal variables of the LP.

Let $\widehat{a}^l$ be a feasible solution of (MP2), and $\widehat{\lambda}^{sl}$ be a feasible solution of D-$\overline{\text{REC}}(\widehat{a}^l, s)$ in scenario $s \in \mathcal{S}$. Let also $(\delta^{s\star}, \xi^{s\star}, \sigma^{s\star})$ denote the optimal solutions of REC(a, s) in scenario $s \in \mathcal{S}$ with respect to $a \in \mathcal{A}$. For a primal variable v in the Problem REC$(\widehat{a}^l, s)$, let $\Gamma(v)$ denote the reduced cost of v with respect to $\widehat{\lambda}^{sl}$.

Then, the optimal value of REC$(\widehat{a}^l, s)$ in scenario s satisfies:

$$g(\widehat{a}^l, s) = \widehat{\lambda}^{sl}\widetilde{\mathrm{h}}(\widehat{a}^l, l, s) + \delta^{s\star}\Gamma(\delta^s) + \xi^{s\star}\Gamma(\xi^s) + \sigma^{s\star}\Gamma(\sigma^s). \tag{5.7}$$

Recall that the traditional Benders cut valid for 2-stage programs is of the form $\theta^s \geq \widehat{\lambda}^{sl}\widetilde{\mathrm{h}}(a, l, s)$. However, (5.7) cannot be used yet to compute the Stage II cost $g(\widehat{a}^l, s)$ because we do not know the optimal solution $(\delta^{s\star}, \xi^{s\star}, \sigma^{s\star})$ of REC$(\widehat{a}^l, s)$. Hence, we now proceed to devise a strictly positive lower bound for the terms in (5.7) corresponding to $(\delta^{s\star}, \xi^{s\star}, \sigma^{s\star})$, which would give us an optimality cut strictly stronger than the traditional Benders cut. The lower bound for $g(a, s)$ is formulated using the Stage I variables only, such that we do not need to know the optimal solution $(\delta^{s\star}, \xi^{s\star}, \sigma^{s\star})$.

As a first step towards deriving the lower bound, we expand the product terms $\delta^{s\star}\Gamma(\delta^s)$ and $\xi^{s\star}\Gamma(\xi^s)$ in (5.7), and simplify the resulting expression. The final result from these operations is stated in the following proposition. For the sake of simplicity and clarity, we consider the case of $|\mathcal{D}_{\mathrm{m}}| = 0$, i.e. DERs cannot be reallocated in the Stage II.

Proposition 5.3.1. *Let $\widehat{a}^l = (\widehat{u}^l, \widehat{w}^l)$ be a feasible solution of (5.6). Let $\widehat{\lambda}^{sl}$ be the optimal solution of D-$\overline{REC}(\widehat{a}, s)$ in scenario s, and $\widetilde{\mathrm{h}}(\widehat{a}, l, s)$ the corresponding dual cost vector. Let $pg^{ks\star}$, $\ell^{ks\star}$, $\alpha^{ks\star}$, $\mu^{ks\star}$, and $\omega^{ks\star}$ denote the optimal values of the variables pg^{ks}, ℓ^{ks}, α^{ks}, μ^{ks}, and ω^{ks} of REC(a, s) in scenario s and period k with respect to $\widehat{a} \in \mathcal{A}$. Let $\Gamma(pg^{ks})$, $\Gamma(\ell^{ks})$, $\Gamma(\alpha^{ks})$, $\Gamma(\mu^{ks})$, $\Gamma(\omega^{ks}) \geq 0$ be the reduced costs associated with the primal variables of $\overline{REC}(\widehat{a}, s)$, with respect to $\widehat{\lambda}^{sl}$. Finally, let $\Gamma(\mu^{ks})$, $\Gamma(\omega^{ks}) \geq 0$ be the reduced costs with respect to the dual solution $\widehat{\lambda}^{sl}$ for scenario s at period k.*

If $\widehat{\lambda}^{sl}$ is a feasible solution of D-$\overline{REC}(\widehat{a}^l, s)$ in scenario s, then the optimal value

of REC(a, s) in scenario s satisfies:

$$g(\widehat{a}^l, s) \geq \widehat{\lambda}^{sl}\widetilde{\mathrm{h}}(\widehat{a}^l, l, s) + \sum_{k\in\mathcal{K}} \Big(\ell^{ks\star}\Gamma(\ell^{ks}) + \alpha^{ks\star}\Gamma(\alpha^{ks}) + \widehat{u}^l\Gamma(\mu^{ks}) + \widehat{w}^l\Gamma(\omega^{ks}) + pg^{ks\star}\Gamma(pg^{ks}) \Big), \tag{5.8}$$

where

$$\begin{aligned} \ell^{ks\star}\Gamma(\ell^{ks}) &\coloneqq \sum_{e\in\mathcal{E}_s} \ell_e^{ks\star}\Gamma(\ell_e^{ks}), & \widehat{u}^l\Gamma(\mu^{ks}) &\coloneqq \sum_{i\in\mathcal{U}} \widehat{u}_i^l\Gamma(\mu_i^{ks}), \\ \alpha^{ks\star}\Gamma(\alpha^{ks}) &\coloneqq \sum_{i\in\mathcal{N}} \alpha_i^{ks\star}\Gamma(\alpha_i^{ks}), & \widehat{w}^l\Gamma(\omega^{ks}) &\coloneqq \sum_{i\in\mathcal{U}}\sum_{d\in\mathcal{D}} \widehat{w}_{id}^l\Gamma(\omega_{id}^{ks}), \\ pg^{ks\star}\Gamma(pg^{ks}) &\coloneqq \sum_{i\in\mathcal{U}}\sum_{d\in\mathcal{D}} pg_{id}^{ks\star}\Gamma(pg_{id}^{ks}). \end{aligned} \tag{5.9}$$

Proof. We first note that using (5.7), we can write:

$$g(\widehat{a}^l, s) \;\; = \lambda^s\widetilde{\mathrm{h}}(\widehat{a}^l, l, s) + \delta^{s\star}\Gamma(\delta^s) + \xi^{s\star}\Gamma(\xi^s) + \sigma^{s\star}\Gamma(\sigma^s), \tag{5.10}$$

where $\delta^{s\star} = \{\ell^{ks\star}, \mu^{ks\star}, \omega^{ks\star}, \alpha^{ks\star}\}_{k\in\mathcal{K}}$ denote the optimal values for discrete variables, $\xi^{s\star} = \{pg^{ks\star}, qg^{ks\star}, \beta^{ks\star}, p^{ks\star}, q^{ks\star}, P^{ks\star}, Q^{ks\star}, \mathrm{v}^{ks\star}\}_{k\in\mathcal{K}}$ denote the optimal values for continuous variables, and $\sigma^{s\star}$ the optimal values for slack variables.

The product term $\sigma^{s\star}\Gamma(\sigma^s)$ is lower bounded by 0. Thus, we can write:

$$g(\widehat{a}^l, s) \;\; \geq \widehat{\lambda}^{sl}\widetilde{\mathrm{h}}(\widehat{a}^l, l, s) + \delta^{s\star}\Gamma(\delta^s) + \xi^{s\star}\Gamma(\xi^s). \tag{5.11}$$

Second, we consider the term $\xi^{s\star}\Gamma(\xi^s)$. A subset of these Stage II continuous variables namely qg^{ks}, β^{ks}, p^{ks}, q^{ks}, P^{ks}, Q^{ks}, and v^{ks} – are free variables, i.e., they can take both positive and negative values. The reduced costs corresponding to free variables are zero. Therefore, those product terms are also equal to 0. Thus, we can

write:

$$\begin{aligned}\xi^{s\star}\Gamma(\xi^s) &= \sum_{k\in\mathcal{K}}\Big(pg^{ks\star}\Gamma(pg^{ks}) + qg^{ks\star}\Gamma(qg^{ks}) + \beta^{ks\star}\Gamma(\beta^{ks}) + p^{ks\star}\Gamma(p^{ks}) \\ &\qquad + q^{ks\star}\Gamma(q^{ks}) + P^{ks\star}\Gamma(P^{ks}) + Q^{ks\star}\Gamma(Q^{ks}) + \mathrm{v}^{ks\star}\Gamma(\mathrm{v}^{ks})\Big) \quad (5.12)\\ &= \sum_{k\in\mathcal{K}}\Big(pg^{ks\star}\Gamma(pg^{ks})\Big).\end{aligned}$$

Third, we expand the term $\delta^{s\star}\Gamma(\delta^s)$ as follows:

$$\delta^{s\star}\Gamma(\delta^s) = \sum_{k\in\mathcal{K}}\Big(\ell^{ks\star}\Gamma(\ell^{ks}) + \alpha^{ks\star}\Gamma(\alpha^{ks}) + \mu^{ks\star}\Gamma(\mu^{ks}) + \omega^{ks\star}\Gamma(\omega^{ks})\Big). \quad (5.13)$$

Using (5.13), we arrive at the following result regarding $g(\widehat{a}^l, s)$:

$$\begin{aligned}g(\widehat{a}^l, s) \geq \lambda^s\widetilde{\mathrm{h}}(\widehat{a}^l, l, s) + \sum_{k\in\mathcal{K}}\Big(&\ell^{ks\star}\Gamma(\ell^{ks}) + \alpha^{ks\star}\Gamma(\alpha^{ks}) + \mu^{ks\star}\Gamma(\mu^{ks}) \\ &+ \omega^{ks\star}\Gamma(\omega^{ks}) + pg^{ks\star}\Gamma(pg^{ks})\Big).\end{aligned} \quad (5.14)$$

Since DER reallocation is not allowed, then $\mu^{ks\star} = \widehat{u}^l$ and $\omega^{ks\star} = \widehat{w}^l \quad \forall\, k \in \mathcal{K}$. In this case, we obtain:

$$\delta^{s\star}\Gamma(\delta^s) = \sum_{k\in\mathcal{K}}\Big(\ell^{ks\star}\Gamma(\ell^{ks}) + \alpha^{ks\star}\Gamma(\alpha^{ks}) + u\Gamma(\mu^{ks}) + w\Gamma(\omega^{ks})\Big). \quad (5.15)$$

Finally, we can simplify (5.8) by using (5.11)–(5.15). □

Note that if reallocation is allowed, then (5.14) *holds instead of* (5.8).

To compute the right-hand-side of (5.8), we still need the optimal values of the active DER power contribution variables $pg^{ks\star}$, load shedding variables $\alpha^{ks\star}$, and restoration variables $\ell^{ks\star}$. In the following proposition, we describe how to obtain lower bounds for $\alpha^{ks\star}$ without solving REC(a, s). The lower bounds are derived based on the existence of paths which connect loads to DER sources at developed sites.

Proposition 5.3.2. *Consider a fixed Stage I strategy* $\widehat{a}^l = (\widehat{u}^l, \widehat{w}^l)$*, scenario* $s \in \mathcal{S}$*,*

period $k \in \mathcal{K}\backslash\{\mathrm{K}\}$, and a load at node $i \in \mathcal{N}$. For every site $j \in \mathcal{U}$, if either the site j is not developed or at least one DN line along the path connecting node i to site j has failed, then the load at node i cannot be energized, i.e.,

$$\alpha_i^{ks\star} \geq \prod_{j\in\mathcal{U}} \Big[1 - \widehat{u}_j^l \prod_{e\in\mathcal{P}_{ij}} \big(1 - \kappa_e^{ks\star}\big)\Big]. \tag{5.16}$$

Proof. When a load at node i is connected and energized, it consumes a positive amount of active power. Therefore, by the active power conservation equation (4.6c), either the bulk power or some DER must act as a source of power to energize the load at node i. Now for period $k < \mathrm{K}$, the DN is not connected to bulk power supply (4.2c). Thus, the bulk power cannot act as a source for the load.

For a site $j \in \mathcal{U}$, if either the site j is not developed or some line along the path connecting the node i to site j has failed, then the load at node i cannot receive power from the site j. We can mathematically represent this condition as $\Big[1-\widehat{u}_j^l \prod_{e\in\mathcal{P}_{ij}} \big(1-\kappa_e^{ks}\big)\Big] = 1$. If this holds for every site $j \in \mathcal{U}$, then the load at node i cannot receive power from any of the DERs. This concludes the proof for (5.16). □

This is obtained by leveraging the power flow properties, which bound the Stage II variables $\delta^{s\star}$ as a function of the Stage I variables given by a. For the last two terms, we note that they are lower bounded by 0. However, we show that we can obtain a stronger lower bound for the last two terms, by solving an MILP which has lesser number of binary variables than $\mathrm{REC}(a, s)$.

In our next result, we use (5.7) and Propositions 5.3.1-5.3.2 to derive an optimality cut for (5.6b).

Theorem 5.3.3. *Let $\widehat{a}^l = (\widehat{u}^l, \widehat{w}^l)$ be a feasible solution of the master problem (5.6) and $\widehat{\lambda}^{sl}$ be the optimal solution of D-$\overline{REC}(\widehat{a}^l, s)$ in scenario s. Let $\Gamma({\alpha_i}^{1s}) \geq 0$ denote the reduced cost associated with α_i^{ks} with respect to $\widehat{\lambda}^{sl}$, in scenario s for period $k = 1$ and node i. Let $\Gamma(\mu^{ks}), \Gamma(\omega^{ks}) \geq 0$ be the reduced costs of μ^{ks} and ω^{ks} with respect to $\widehat{\lambda}^{sl}$, in scenario s for period k. Then, a valid cut is given by:*

$$\theta^s \geq \widehat{\lambda}^{sl}\widetilde{\mathrm{h}}(a,l,s) + \sum_{k\in\mathcal{K}}\Big(u\Gamma(\mu^{ks}) + w\Gamma(\omega^{ks})\Big) + \sum_{i\in\mathcal{N}}\Gamma(\alpha_i{}^{1s})\prod_{j\in\mathcal{U}}\Big[1-\widehat{u}_j^l\prod_{e\in\mathcal{P}_{ij}}(1-s_e)\Big]. \tag{5.17}$$

Proof. First, we note that the desired optimality cut in the master problem (5.6) is of the form $\theta^s \geq g(a,s)$.

Using Prop. 5.3.1, we get

$$g(\widehat{a}^l,s) \geq \widehat{\lambda}^{sl}\widetilde{\mathrm{h}}(\widehat{a}^l,l,s) + \sum_{k\in\mathcal{K}}\Big(\ell^{ks\star}\Gamma(\ell^{ks}) + \alpha^{ks\star}\Gamma(\alpha^{ks}) + \widehat{u}^l\Gamma(\mu^{ks}) + \widehat{w}^l\Gamma(\omega^{ks}) + pg^{ks\star}\Gamma(pg^{ks})\Big). \tag{5.18}$$

Here, $pg^{ks\star}\Gamma(pg^{ks}) \geq 0$ because of non-negativity of $pg^{ks\star}$ and $\Gamma(pg^{ks})$, and $\ell^{ks\star}\Gamma(\ell^{ks})$ is lower bounded by 0 because of non-negativity of ℓ^{ks} and $\Gamma(\ell^{ks})$. Furthermore,

$$\begin{aligned}\sum_{k\in\mathcal{K}}\alpha^{ks\star}\Gamma(\alpha^{ks}) &= \alpha^{1s\star}\Gamma(\alpha^{\ 1s}) + \sum_{k\in\mathcal{K}\setminus\{1\}}\alpha^{ks\star}\Gamma(\alpha^{ks}) \\ &\geq \alpha^{1s\star}\Gamma(\alpha^{\ 1s}) \\ &\geq \prod_{j\in\mathcal{U}}\Big[1-\widehat{u}_j^l\prod_{e\in\mathcal{P}_{ij}}\big(1-\kappa_e^{1s\star}\big)\Big] \\ &= \prod_{j\in\mathcal{U}}\Big[1-\widehat{u}_j^l\prod_{e\in\mathcal{P}_{ij}}(1-s_e)\Big],\end{aligned} \tag{5.19}$$

where the first inequality holds because of non-negativity of $\alpha^{ks\star}$ and $\Gamma(\alpha^{ks})$, the second inequality holds because of Prop. 5.3.1 and Prop. 5.3.2, and the last equality holds because the operational state of a line $e \in \mathcal{E}$ at the time period $k = 1$ is given by $\kappa_e^{1s\star} = s_e$. □

Note that we do not consider the values of the load shedding variables $\alpha^{ks\star}$ for periods $k > 1$. This is because $\alpha^{ks\star}$ are also dependent on the line restoration variables $\ell^{ks\star}$ in (4.2e), and line repairs start only after $k = 1$. Therefore, we cannot determine a lower-bound on values of $\alpha^{ks\star}$ for $k > 1$ based on Stage I variables alone.

As discussed earlier, the optimality cut (5.17) in Theorem 5.3.3 is a stronger

cut than the traditional Benders cut. Now, solving the large-scale Stage II problem REC(a, s) will yield the strongest optimality cut for (5.6b), i.e., $\theta^s \geq g(a, s)$, since the optimal values of REC(a, s) can be directly used. However, as stated earlier, solving REC(a, s) is computationally challenging due to the presence of a large number of binary variables. Therefore, we next describe an another MILP with fewer number of binary variables than REC(a, s) that can help provide a cut stronger than (5.17) but weaker than $\theta^s \geq g(a, s)$.

5.3.2 Estimating the relaxation upper bound

In [110], the authors use a convergence criterion which involves the percentage difference between a lower bound (denoted by $\underline{Z}$) and a "relaxation upper bound" (denoted as $\widetilde{Z}$) falling below a certain threshold. The lower bound is simply computed as $\underline{Z} = \mathrm{J}^{\mathrm{MP}}(\widehat{a}^l)$. Now, solving the large-scale Stage II problem REC(a, s) will yield an upper bound to REC(a, s). However, as stated earlier, solving REC(a, s) is computationally expensive due to the presence of a large number of binary variables. Therefore, the authors in [110] instead compute a "relaxation upper bound" as $\widetilde{Z} = \mathrm{J}^{\mathrm{I}}(\widehat{a}^l) + \frac{1}{\mathrm{S}} \sum_{s \in \mathcal{S}} \bar{g}(\widehat{a}^l, s)$, where $\bar{g}(\widehat{a}^l, s)$ is the optimal value of $\overline{\mathrm{REC}}(\widehat{a}^l, s)$. This relaxation upper bound is used as a proxy to the actual upper bound. However, having a better proxy for the upper bound will likely help improve the optimality of the solution. Therefore, we next propose a different method for estimating the relaxation upper bound by solving an another MILP with fewer number of binary variables than (S2).

Consider a fixed allocation $\widehat{a}^l = (\widehat{u}^l, \widehat{w}^l)$ and a feasible solution $\widehat{\lambda}^{sl}$ of the problem D-$\overline{\mathrm{REC}}(\widehat{a}^l, s)$. For each node $i \in \mathcal{N}$, site $j \in \mathcal{U}$, period $k \in \mathcal{K}$, and scenario $s \in \mathcal{S}$, we define a continuous variable ϱ_{ij}^{ks}, such that $\varrho_{ij}^{ks} = 1$ indicates that the load at node i cannot be energized by a DER at site j; $\varrho_{ij}^{ks} = 0$ otherwise. We also denote by φ_i^{ks} the continuous variables denoting the relaxation of the binary variables α_i^{ks}. Recall from Prop. 5.3.2 that if $\varrho_{ij}^{ks} = 1 \ \forall \ j \in \mathcal{U}$, then $\alpha_i^{ks} = 1$ because the load is not energized by any DER. We present the following linear constraints ($\forall \ i \in \mathcal{N}, \ k \in \mathcal{K}$):

$$\varrho_{ij}^{ks} \geq 1 - \widehat{u}_j^l \qquad \forall\, j \in \mathcal{U},\ k < \mathrm{K} \tag{5.20a}$$

$$\varrho_{ij}^{ks} \geq \kappa_e^{ks} \qquad \forall\, j \in \mathcal{U},\ e \in \mathcal{P}_{ij} \bigcap \mathcal{E}_s,\ k < \mathrm{K} \tag{5.20b}$$

$$\varphi_i^{ks} \geq 1 - \sum_{j \in \mathcal{U}} \left(1 - \varrho_{ij}^{ks}\right) \qquad \forall\, k < \mathrm{K} \tag{5.20c}$$

Here, (5.20a) and (5.20b) model that a load cannot be energized from a site j if the site j is not developed; and/or there exists one failed (unrepaired) line along the path connecting node i to site j. Lastly, (5.20c) states that load at node i cannot be energized if there is no site that can supply power to the load. By virtue of the constraints (5.20a) and (5.20b) the continuous variable ϱ_{ij}^{ks} can only take values 0 or 1.

Then, given a first-stage solution $\widehat{a}^l$ and scenario s, we formulate the following MILP:

$$\begin{aligned}
\mathrm{J}^{\mathrm{RC}}\left(\widehat{a}^l, s\right) \coloneqq \min \quad & \sum_{k \in \mathcal{K}\setminus\{\mathrm{K}\}} \Big(\sum_{i \in \mathcal{N}} \varphi_i^{ks} \Gamma(\alpha_i^{ks}) \quad + \sum_{e \in \mathcal{E}} \ell_e^{ks} \Gamma(\ell_e^{ks}) \Big) \\
\text{s.t.} \quad & (4.2), (5.20) \\
& \ell_e^{ks} \in \{0,1\} && \forall\, e \in \mathcal{E},\ k \in \mathcal{K} \\
& 0 \leq \varphi_i^{ks} \leq 1 && \forall\, i \in \mathcal{N},\ k \in \mathcal{K}\setminus\{\mathrm{K}\} \\
& 0 \leq \varrho_{ij}^{ks} \leq 1 && \forall\, i \in \mathcal{N},\ j \in \mathcal{U},\ k \in \mathcal{K}\setminus\{\mathrm{K}\}.
\end{aligned} \tag{SMILP}$$

The decision variables of this MILP include the binary restoration variables ℓ_e^{ks}, and relaxed continuous variables ϱ_{ij}^{ks} and φ_i^{ks}. Now, consider an optimal solution of REC(a, s). In this solution, the values of the restoration strategy and load connectivity variables form a feasible solution of (SMILP). Therefore, the optimal value of (SMILP) will provide a non-negative lower bound for the terms $\sum_{k \in \mathcal{K}\setminus\{\mathrm{K}\}} \big(\ell^{ks\star}\Gamma(\ell^{ks}) + \alpha^{ks\star}\Gamma(\alpha^{ks})\big)$ in (5.19), where $(\ell^{ks\star}, \alpha^{ks\star})$ are part of the optimal solution of REC(a, s).

In particular, we can use the following as an estimate for the relaxation upper bound:

$$\widetilde{Z} = \bar{g}(\widehat{a}^l, s) + \sum_{s \in \mathcal{S}} \mathrm{J}^{\mathrm{RC}}\left(\widehat{a}^l, s\right) = \widehat{\lambda}^{sl}\widetilde{\mathrm{h}}(\widehat{a}^l, l, s) + \sum_{s \in \mathcal{S}} \mathrm{J}^{\mathrm{RC}}\left(\widehat{a}^l, s\right). \tag{5.21}$$

The problem (SMILP) does not have binary variables corresponding to the load connectivity variables. Thus, it has lesser number of binary variables than that in (S2). Also, the total number of variables and constraints in (SMILP) are also significantly lesser than (S2). Typically, $\ell^{ks\star}\Gamma(\ell^{ks}) + \alpha^{ks\star}\Gamma(\alpha^{ks}) > \mathrm{J}^{\mathrm{RC}}\left(a^l, s\right)$, because the solution to (SMILP) does not account for load shedding due to voltage bound violations. Thus solving (SMILP) is computationally cheaper but also less accurate, in comparison to solving (S2).

The above formulation assumes no re-allocation of the DERs. If re-allocation is permitted, then (SMILP) can be modified accordingly, which would include: adding cost terms corresponding to μ_i^{ks}, ω_{id}^{ks}, ϖ_{ijd}^{ks}, $\forall\ i \in \mathcal{N}$, $j \in \mathcal{N}$, $k \in \mathcal{K}$, $d \in \mathcal{D}$ to the objective; as well as the constraints given by (4.2).

5.3.3 Description of the algorithm

Algorithm 2 provides an overview of the LBD-DIC method.

Algorithm 2 LBD with Dual Integer Cuts

Set $\widetilde{Z} \leftarrow \infty, \underline{Z} \leftarrow 10^{-6},\ l = 0$
while $\frac{\widetilde{Z}-\underline{Z}}{\underline{Z}} > \bar{\epsilon}$ **do**
    Compute $\widehat{a}^l$ by solving the master problem (MP2)
    Set $\underline{Z} \leftarrow \mathrm{J}^{\mathrm{MP}}(\widehat{a}^l)$
    for $s \in \mathcal{S}$ **do**
        Compute $\widehat{\lambda}^{sl}$ by solving D-$\overline{\mathrm{REC}}(\widehat{a}^l, s)$
        Compute $\underline{g}(\widehat{a}^l, s)$ by solving (SMILP)
        Add optimality cut (5.21) to the master problem (5.6)
    end for
    $\widetilde{Z} \leftarrow \min(\widetilde{Z}, \underline{g}(\widehat{a}^l, \mathcal{S}))$
    Update $l \leftarrow l + 1$
end while

At each iteration, we solve D-$\overline{\text{REC}}(\widehat{a}^l, s)$ for each scenario s to derive the optimality cut for Algorithm 2. After solving D-$\overline{\text{REC}}(\widehat{a}^l, s)$, we use the dual solution $\widehat{\lambda}^{sl} \quad \forall\ s \in \mathcal{S}$ to obtain a dual integer cut. This cut is added to the master problem (MP2). Additionally, in order to obtain an optimality cut stronger than the dual integer cut, we also propose solving an another MILP given by (SMILP). The optimal solutions to D-$\overline{\text{REC}}(\widehat{a}^l, s)$ and (SMILP) help generate a valid optimality cut that is added to the master problem (MP2). The number of binary variables in (SMILP) are relatively lesser than that in REC(a, s). Hence, as we show in Section 5.3.4, this approach significantly decrease the required computation time associated with solving sub-problems.

5.3.4 Computational Experiments

We discuss computational experiments that involve solving (DEF) using the LBD-DIC solution approach. The experiments are conducted using a modified IEEE 12-node distribution test feeder. We use the same parameters as in Section 4.4 of Chapter 4.

We first investigate the convergence of LBD-DIC with the dual integer cut (see Section 5.3.1), and compare it to the traditional Benders cut. Then we examine the effect of using (SMILP) in order to calculate the "relaxation" upper bound $\widetilde{Z}$.

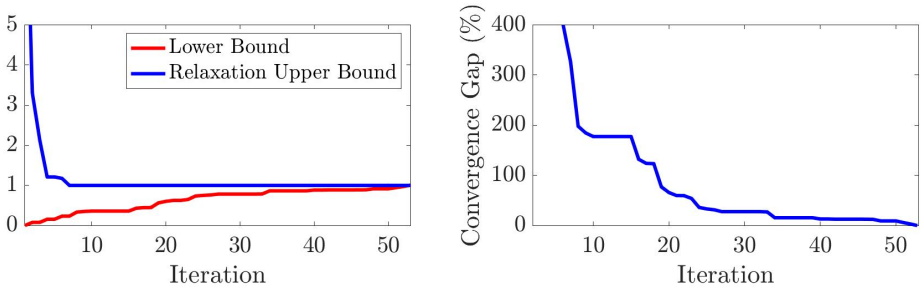

Figure 5-3: Convergence of LBD-DIC. We use the following parameters: $\mathbf{G} = 3$ (all fixed DERs), $\text{Y} = 1$, and $\text{S} = 5$. *Left*: Lower bound $\underline{Z}$ and "relaxation" upper bound $\widetilde{Z}$, normalized by the minimum value of $\widetilde{Z}$ achieved. *Right*: Convergence gap $(\widetilde{Z} - \underline{Z})/\underline{Z}$.

Figure 5-3 shows the lower bound, upper bound, and convergence gap $(\widetilde{Z} - \underline{Z})/\underline{Z}$ for test instance ID I_GF3_GM0_S12. Convergence occurs at iteration $l = 53$. In

comparison, the number of feasible Stage I DER allocation strategies a is $(|\mathcal{U}|+1)^{\mathbf{G}} = 125$. To arrive at this value, we consider that each generator can be placed in any site $i \in \mathcal{U}$, or is not placed at all. Thus for a single DER, the number of possible DER-to-site pairings is $(|\mathcal{U}|+1)$. We take this to the power of $\mathbf{G}$, the total number of DERs that can be allocated. Thus for this test instance, LBD-DIC is able to converge in less iterations than would be required under a simple brute-force enumeration of all possible allocation strategies. We find this to be true in most test instances, with the benefit being more evident as the DER budget $\mathbf{G}$ increases.

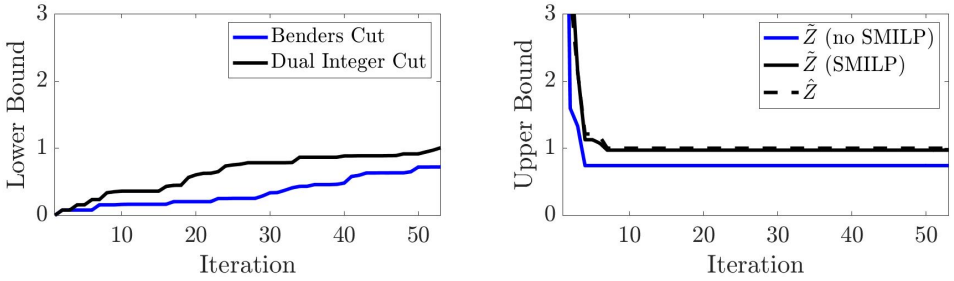

Figure 5-4: Effect of dual integer cut and (SMILP) on convergence of LBD-DIC. We assume the same parameters as in Figure 5-3. *Left*: Lower bound $\underline{Z}$ as a function of iteration l, using the Benders cut or dual integer cut in (5.17). *Right*: Relaxation upper bound $\widetilde{Z}$ using (SMILP) (black) vs. $\widetilde{Z}$ without contribution from (SMILP) (blue) and $\bar{Z}$ (dotted black).

Figure 5-4 shows the lower bound $\underline{Z}$ with dual integer cuts and the traditional Benders cuts. Note that the dual integer cuts noticeably outperform the Benders cuts by improving the lower bound $\underline{Z}$. In addition, the figure shows the "relaxation" upper bound $\widetilde{Z}$ with and without solving (SMILP), and compares the "relaxation" upper bound to the exact upper bound $\bar{Z}$. Solving Eq. SMILP improves estimation of the relaxation upper bound $\widetilde{Z}$, to the extent that the "relaxation" upper bound is nearly equivalent to the exact upper bound at most iterations. Note that we considered the smaller 12-node network for this simulation, which permits us to solve the Stage II MILPs without time-out.

So far, we have described two methods, namely LBD-Greedy and LBD-DIC, in which we generate optimality cut for the master problem using the solution to complete Stage II problem. In the next section, we describe our approach based on

Nested Benders Decomposition method in which we generate optimality cuts for the period-wise subsubproblems.

5.4 Nested Benders Decomposition

In this section, we describe our solution approach based on Nested Benders Decomposition (NBD) method [5, 57]. This method was initially proposed in the context of multi-stage linear stochastic programs [5], which involves stage-wise temporal decomposition. In [57], the NBD method is used in the context of deterministic multi-period MILP models, by performing a temporal decomposition. In our approach, we solve for our 2-stage multi-period mixed-integer program by performing a temporal decomposition across the two stages as well as the multiple periods of Stage II.

In the NBD method, we generate the Benders cuts using a forward-and-backward pass approach that requires a period-wise decomposition of REC(a, s). To facilitate the understanding of the algorithm, we first describe how the multi-period problem REC(a, s) is decomposed by period in Section 5.4.1. Then, we introduce a concise notation to represent the period-wise decomposed MILPs, and use this notation to describe the NBD method in Section 5.4.2.

5.4.1 Decomposition by time period

In our formulation (DEF), the constraints that depend on more than one time period are equations (4.2d), (4.2e), (4.3a), and (4.3g). Therefore, these constraints need to be reformulated in order to be solve the period-wise problems separately. For this purpose, we duplicate the binary linking variables κ_e^{ks}, μ_i^{ks}, and ω_{id}^{ks} with continuous variables $\kappa_e^{ks,\text{prev}}$, $\mu_i^{ks,\text{prev}}$, and $\omega_{id}^{ks,\text{prev}}$ respectively.

Note that (4.2d) and (4.2e) are equivalent to and can be substituted by the following constraints:

$$\kappa_e^{ks} \leq \kappa_e^{k-1,s} \qquad \forall\, k \in \mathcal{K} \setminus \{1\}, e \in \mathcal{E}_s \tag{5.22a}$$

$$\textstyle\sum_{e\in\mathcal{E}_s} \kappa_e^{ks} = \sum_{e\in\mathcal{E}_s} \kappa_e^{k-1,s} - \mathrm{Y}_k \qquad \forall\, k \in \mathcal{K} \setminus \{1\}, e \in \mathcal{E}_s, \tag{5.22b}$$

where (5.22a) models that after a failed line is repaired it remains operational, and (5.22b) models that in each period the number of failed lines reduces by the number of lines repaired, i.e. Y_k. We reformulate (5.22a) and (5.22b) as follows:

$$\kappa_e^{ks} \leq \kappa_e^{ks,\text{prev}} \qquad \forall\, e \in \mathcal{E}_s, k \in \mathcal{K} \quad (5.23a)$$

$$\textstyle\sum_{e\in\mathcal{E}_s} \kappa_e^{ks} = \sum_{e\in\mathcal{E}_s} \kappa_e^{ks,\text{prev}} - \mathrm{Y}_k \qquad \forall\, e \in \mathcal{E}_s, k \in \mathcal{K} \quad (5.23b)$$

$$\kappa_e^{ks,\text{prev}} = \widehat{\kappa}_e^{k-1,s} \quad \leftarrow \lambda_e^{ks,\text{line}} \qquad \forall\, e \in \mathcal{E}_s, k \in \mathcal{K} \setminus \{1\} \quad (5.23c)$$

$$\kappa_e^{ks,\text{prev}} = s_e \quad \leftarrow \lambda_e^{ks,\text{line}} \qquad \forall\, e \in \mathcal{E}_s, k = 1 \quad (5.23d)$$

Here, $\kappa_e^{ks,\text{prev}}$ is a duplicated continuous variable representing $\widehat{\kappa}_e^{k-1,s}$, and $\widehat{\kappa}_e^{k-1,s}$ is the solution of $\kappa_e^{k,s}$ at time period $k-1$ for $k > 1$, which is fixed when solving for time period k. The Lagrange multiplier $\lambda_e^{ks,\text{line}}$ of (5.23c) and (5.23d) is unrestricted in sign.

Similarly, we reformulate (4.3a) as follows:

$$\mu_i^{ks} \geq \mu_i^{ks,\text{prev}} \qquad \forall\, i \in \mathcal{U}, k \in \mathcal{K} \quad (5.24a)$$

$$\mu_i^{ks,\text{prev}} = \widehat{\mu}_i^{k-1,s} \quad \leftarrow \lambda_i^{ks,\text{site}} \qquad \forall\, i \in \mathcal{U}, k \in \mathcal{K} \setminus \{1\} \quad (5.24b)$$

$$\mu_i^{ks,\text{prev}} = \widehat{u}_i \quad \leftarrow \lambda_i^{ks,\text{site}} \qquad \forall\, i \in \mathcal{U}, k = 1. \quad (5.24c)$$

Here, $\mu_i^{ks,\text{prev}}$ is a duplicated continuous variable representing $\mu_i^{k-1,s}$, and $\widehat{\mu}_i^{k-1,s}$ is the solution for variable μ_i^{ks} or u_i in period $k-1$, which are fixed when solving for period k. The Lagrange multiplier $\lambda_e^{ks,\text{site}}$ in (5.24b) and (5.24c) is unrestricted in sign.

Also, constraint (4.3g) can be replaced by following constraints:

$$\textstyle\sum_{i\in\mathcal{U}} \omega_{id}^{ks} \geq \sum_{i\in\mathcal{U}} \omega_{id}^{ks,\text{prev}} \qquad \forall\, i \in \mathcal{U}, d \in \mathcal{D}, k \in \mathcal{K} \setminus \{1\} \quad (5.25a)$$

$$\omega_{id}^{ks,\text{prev}} = \widehat{\omega}_{id}^{k-1,s} \quad \leftarrow \lambda_{id}^{ks,\text{der}} \qquad \forall\, i \in \mathcal{U}, d \in \mathcal{D}, k \in \mathcal{K} \setminus \{1\} \quad (5.25b)$$

$$\omega_{id}^{ks,\text{prev}} = \widehat{w}_{id} \quad \leftarrow \lambda_{id}^{ks,\text{der}} \qquad \forall\, i \in \mathcal{U}, d \in \mathcal{D}, k = 1. \quad (5.25c)$$

Here, $\omega_{id}^{ks,\text{prev}}$ is a duplicated continuous variable representing $\omega_{id}^{k-1,s}$, and $\widehat{\omega}_i^{k-1,s}$ is the

solution for variable ω_{id}^{ks} at period $k-1$ or w_{id} in Stage I, which are fixed when solving for period k. The Lagrange multiplier $\lambda_{id}^{ks,\text{der}}$ in (5.25b) and (5.25c) is unrestricted in sign.

Now, the master problem at iteration l can be succinctly defined as follows:

$$\min_{a\in\mathcal{A}} \ \mathrm{J}^{\mathrm{I}}(a) + \frac{1}{\mathrm{S}}\sum_{s\in\mathcal{S}}\theta^s \tag{5.26a}$$

$$\text{s.t.} \ \ \theta^s \geq \widehat{\Phi}^{ksj} + \sum_{i\in\mathcal{U}}\widehat{\lambda}_{i,j}^{ks,\text{site}}\left(\widehat{u}_i - u_i\right) + \sum_{i\in\mathcal{U}}\sum_{d\in\mathcal{D}}\widehat{\lambda}_{id,j}^{ks,\text{der}}\left(\widehat{w}_{id} - w_{id}\right) \ \ \forall\, j\in\mathcal{J}^l,\ s\in\mathcal{S}, k=1 \tag{5.26b}$$

$$\theta^s \geq 0, \qquad \forall\, s\in\mathcal{S}, \tag{5.26c}$$

where (5.26b) denotes the optimality cut given by scenario s and iteration j, and θ^s denotes an under-approximation to the Stage II cost associated with Stage I strategy a and scenario s.

Furthermore, the objective function for each time period is solved independently, and incorporates the cuts for future cost that are added in following iterations. These cuts project the problem onto the subspace defined by the linking variables. Thus we replace the period-wise objective from $\mathrm{REC}(a,s)$ with the following:

$$\begin{aligned}
\min \quad \Phi^{ks} &= \Phi_{\text{res}}^{ks} + \Phi_{\text{load}}^{ks} + \psi^{ks} \\
\psi^{ks} &\geq \widehat{\Phi}^{k+1,sj} + \sum_{e\in\mathcal{E}_s}\widehat{\lambda}_{e,j}^{k+1,s,\text{line}}\left(\widehat{\kappa}_e^{ks} - \kappa_e^{ks,\text{prev}}\right) \\
&\quad + \sum_{i\in\mathcal{U}}\widehat{\lambda}_{i,j}^{k+1,s,\text{site}}\left(\widehat{\mu}_i^{ks} - \mu_i^{ks,\text{prev}}\right) \\
&\quad + \sum_{i\in\mathcal{U}}\sum_{d\in\mathcal{D}}\widehat{\lambda}_{id,j}^{k+1,s,\text{der}}\left(\widehat{\omega}_{id}^{ks} - \omega_{id}^{ks,\text{prev}}\right) \qquad \forall\, j\in\mathcal{J}_l,
\end{aligned}$$

Master problem for the NBD method: Now, the master problem at iteration l can be restated as follows:

$$\text{(MP3)} \qquad \Phi^{\text{MP},l}(v^l) = \min_{a,u,w} \ \mathrm{J}^{\mathrm{I}}(a) + v^l(\widehat{u}^l, \widehat{w}^l) \tag{5.27a}$$

$$a\in\mathcal{A} \tag{5.27b}$$

where $\mathrm{J}^{\mathrm{I}}(a)$ is the objective function for the master problem, and $\upsilon^l(\widehat{u}^l, \widehat{w}^l)$ is a cost-to-go function that approximates the expected Stage II cost over all the scenarios. The value for cost-to-go function will be calculated in the Backward pass of iteration l, by using the $\widehat{u}^l, \widehat{w}^l$ values obtained in the Forward pass l.

The cost-to-go function for the master problem $\upsilon^l(\cdot)$ is represented as:

$$\begin{aligned}
\upsilon^l(\widehat{u}^l, \widehat{w}^l) = \min_{a,u,w,\theta^s} \quad & \frac{1}{\mathrm{S}} \sum_{s \in \mathcal{S}} \theta^s \\
\text{s.t.} \quad & \theta^s \geq \widehat{\Phi}^{ksj} + \textstyle\sum_{i \in \mathcal{U}} \lambda_{i,j}^{ks,\mathrm{site}} \left(\widehat{u}_i - u_i\right) \\
& \qquad + \textstyle\sum_{i \in \mathcal{U}, d \in \mathcal{D}} \lambda_{id,j}^{ks,\mathrm{der}} \left(\widehat{w}_{id} - w_{id}\right) \qquad \forall\, j \in \mathcal{J}^l, s \in \mathcal{S}, k = 1 \\
& a \in \mathcal{A},
\end{aligned} \tag{5.28}$$

where $\widehat{\Phi}^{ksj}$ is the optimal value for period $k = 1$, $\lambda_{i,j}^{ks,\mathrm{site}}$ and $\lambda_{id,j}^{ks,\mathrm{der}}$ are the Lagrange multipliers for the equality constraints (5.24b) and (5.25b), respectively. The optimal value and the Lagrange multipliers are obtained in the Backward Pass of iteration j. Also, $(\widehat{u}^l, \widehat{w}^l)$ is the solution for (u, w) obtained by solving the master problem (5.27) in the Forward Pass of iteration l, and fixed in the following Backward Pass.

Subproblems after period- and scenario-wise decomposition: For a given period $k \in \mathcal{K}$ and iteration l, we write the MILP concisely as follows:

$$\Phi^{ksl}(\widehat{\zeta}^{k-1,sl}, \phi^{ksl}) = \min_{\zeta^{ks}, \tau^{ks}, \nu^{ks}} \quad f^{ks}(\zeta^{ks}, \tau^{ks}) + \phi^{ksl}(\widehat{\zeta}^{ksl}) \tag{5.29a}$$

$$\textbf{s.t.} \quad \nu^{ks} = \widehat{\zeta}^{k-1,sl} \qquad : \qquad (\lambda^{ks}) \tag{5.29b}$$

$$(\zeta^{ks}, \tau^{ks}, \nu^{ks}) \in \mathcal{Z}^{ks}, \tag{5.29c}$$

where $\nu^{ks} = (\mu^{ks,\mathrm{prev}}, \omega^{ks,\mathrm{prev}}, \kappa^{ks,\mathrm{prev}})$,

$$\widehat{\zeta}^{k-1,sl} = \begin{cases} (\widehat{\mu}^{k-1,sl}, \widehat{\omega}^{k-1,sl}, \widehat{\kappa}^{k-1,sl}) & \text{if } k > 1 \\ (\widehat{u}^l, \widehat{w}^l, s) & \text{otherwise.} \end{cases}$$

The feasible region $\mathcal{Z}^{ks}$ is a mixed-integer set given by

$$\mathcal{Z}^{ks} = \Big\{(\zeta^{ks}, \tau^{ks}, \nu^{ks}) \quad | \quad (4.3c) - (4.3j), (4.4a) - (4.6h), (5.23), (5.24), (5.25)\Big\}. \tag{5.30}$$

The components of the problem (5.29) are as follows: Let ζ^{ks} represent the linking variables, which are binary variables linking two time periods; ν^{ks} the duplicated state variables, which are continuous variables; τ^{ks} the local variables, i.e. all the other variables which are not listed above. These are mixed-integer variables. $\widehat{\zeta}^{k-1,sl}$ is the system state at the start of period k in scenario s of iteration l, i.e. the solution for ζ^{ksl} obtained in the previous period of the Forward Pass. $f^{ks}(\zeta^{ks}, \tau^{ks})$ is the objective function in terms of the state and local variables, ζ^{ks}, τ^{ks}, respectively.

The cost-to-go function $\phi^{ksl}(\cdot)$ is represented as:

$$\begin{aligned} \phi^{ksl}(\widehat{\zeta}^{ksl}) = \min_{\zeta^{ks}, \psi^{ks}} \quad & \psi^{ks} \\ \text{s.t.} \quad & \psi^{ks} \geq \widehat{\Phi}^{k+1,j} + \widehat{\lambda}^{k+1,sj}(\widehat{\zeta}^{ksj} - \zeta^{ks}) \qquad \forall\, j \in \mathcal{J}^l \end{aligned} \tag{5.31}$$

where $\widehat{\Phi}^{k+1,j}$ is the optimal value for period $k+1$, $\widehat{\lambda}^{k+1,sj}$ is the Lagrange multiplier for the equality constraint, both obtained in the Backward Pass of iteration j, such that $\lambda^{ksj} = (\lambda^{ksj,\text{line}}, \lambda^{ksj,\text{site}}, \lambda^{ksj,\text{der}})$. Also, $\widehat{\zeta}^{ksj}$ is the solution for ζ^{ks} obtained in the Forward Pass of iteration j, and fixed in the following Backward Pass.

5.4.2 Description of the algorithm

The Nested Benders Decomposition algorithm involves decomposing the two-stage problem as master problem and subproblem, then further decomposing the subproblem per time period, and finally solving these problems iteratively in a forward-and-backward fashion. The Forward Pass yields a feasible upper bound $\bar{Z}$, while the Backward Pass generates cuts from the LP relaxations of the subproblems and provides a lower bound $\underline{Z}$. New cuts are added in the Backward Pass of each iteration l and kept in the following Forward Pass. Similar to LBD-II, the lower bound $\underline{Z}$

(upper bound $\bar{Z}$) to the optimal solution of NBD is initialized to 10^{-6} (resp. ∞). The algorithm terminates when the normalized difference $(\bar{Z} - \underline{Z})/\underline{Z}$ is less than a threshold $\bar{\epsilon}$.

Algorithm 3 Nested Benders Decomposition

Set $\bar{Z} \leftarrow \infty, \underline{Z} \leftarrow 10^{-6},\ l = 0$
while $(\bar{Z} - \underline{Z})/\underline{Z} > \bar{\epsilon}$ **do**
  Compute $\widehat{a}^l$ by solving master problem (5.27)
  for $s \in \mathcal{S}$ **do**
    for $k = 1, \cdots, \mathrm{K}$ **do** ▷ Forward pass
      Solve for subproblem (5.29) to compute $(\widehat{\zeta}^{ksl}, \widehat{\tau}^{ksl}, \widehat{\nu}^{ksl})$
    end for ▷ Update upper bound
    for $k = \mathrm{K}-1, \mathrm{K}-2, \cdots, 0$ **do** ▷ Backward pass
      Use $\widehat{\Phi}^{k+1,sl}$, $\widehat{\lambda}^{k+1,sl}$ to solve (5.31) and compute cost-to-go values
    end for
  end for
  Use $\widehat{\Phi}^{0,sl}$, $\widehat{\lambda}^{0,sl}$ to solve (5.28) and compute cost-to-go values for (5.27)
  Update upper bound $\bar{Z}$ using (5.32)
  Update $l \leftarrow l + 1$
  Set $\underline{Z} \leftarrow \mathrm{J}^{\mathrm{MP}}(\widehat{a}^l) + \frac{1}{\mathrm{S}} \sum_{s \in \mathcal{S}} \sum_{k=0}^{\mathrm{K}} \Phi^{ks} - \widehat{\psi}^{ks}$ ▷ Update lower bound
end while

Forward Pass:

The purpose of the Forward Pass is to generate a feasible solution to the full problem. First, we obtain a feasible solution for the master problem. Then, we implement that solution for the subproblem with period $k = 0$ for each scenario s. Then, for each scenario s, we obtain optimal solutions, which are then considered as fixed parameters for the subsequent period. Therefore, the forward pass involves solving a relaxed master problem and then the period-wise problems sequentially, using the solution from previous subproblem.

Since the problem is assumed to have complete continuous recourse, which means that for any value of linking variable and local binary variables, there are values for the local continuous variables such that the solution is feasible.

The upper bound $\bar{Z}_l$ in the iteration l is calculated in the Forward Pass as follows:

$$\bar{Z}_l = \left(\mathrm{J}^{\mathrm{I}}(\widehat{a}^l) - \frac{1}{\mathrm{K}} \sum_{s \in \mathcal{S}} \widehat{\theta}^s \right) + \frac{1}{\mathrm{S}} \sum_{s \in \mathcal{S}} \sum_{k=1}^{\mathrm{K}} \left(\widehat{\Phi}^{ksl} - \widehat{\psi}^{ksl} \right) \qquad \forall\ l. \tag{5.32}$$

Note that the weighted sum of the optimal values of the problems solved in the forward pass, $\mathrm{J}^{\mathrm{I}}(\widehat{a}^l))$ and $\widehat{\Phi}^{ksl}$, $\widehat{\Phi}^{ksl}$, minus the cost-to-go functions, $\widehat{\theta}^s$ and $\widehat{\psi}^{ksl}$, yields a valid upper bound, because when the master problem and the Stage II subproblems are solved in a myopic fashion, without relaxing any constraint or integrality, we obtain a full solution that is feasible for the entire MILP problem.

Backward Pass:

After the completion of the Forward Pass by solving the master problem and the subproblems for all the time periods, the next step is the Backward Pass used to generate cuts. This step consists of solving the period-wise subproblems from the last to the first period followed so that the solutions of future periods can be used to generate cuts to provide approximations of the cost-to-go functions. These are cumulative cuts which are specific for each period, i.e., they are added at each iteration l whenever a Backward Pass subproblem for period k is solved. These cuts are also retained in the formulation of the Forward Pass. Note that the fixed variables stored in the Forward Pass, $\widehat{\zeta}$, are also used in the Backward Pass.

The lower bound $\underline{Z}_l$ is calculated in the Backward Pass as follows:

$$\underline{Z}_l = \widehat{\Phi}^{\mathrm{MP},l}. \tag{5.33}$$

We argue that the optimal value, $\Phi^{\mathrm{MP},}$, for the Stage I master problem is a lower bound to the total cost since it only has a subset of the original constraints of the complete MILP problem.

Below, we provide a discussion for the cuts corresponding to the period-wise subproblem, as the cut for the master problem can be obtained in a similar fashion.

If the recourse problem were convex and solved by Nested Benders Decomposition, the objective value and the Lagrange Multiplier of equality constraint (5.29b) would be enough to generate the Benders cut:

$$\theta^{ks} \;\geq\; \widehat{\Phi}^{k+1,j} + \widehat{\lambda}^{ks}(\widehat{\zeta}^{ks} - \zeta^{ks}) \tag{5.34}$$

However, the subproblems have binary variables due to which the Benders cut cannot be generated directly. To provide a valid cut, the subproblems first need to be convexified using linear or Lagrangian relaxations. The cuts generated by the relaxed problems are Benders and Lagrangean cuts, respectively. An another type of cut is the strengthened Benders cut [119] is also valid for the Backward Pass problems.

The choice of cuts impact the computational performance of the algorithm. Some cuts may be tighter and more/less computationally expensive to generate. We describe the cuts as below:

Benders Cut. The Benders cut is exactly like (5.34), but the optimal value and the multipliers for the complicating equalities are obtained from the solution of linear relaxation. Thus, the cut generated is as follows:

$$\theta^{ks} \;\geq\; \widehat{\Phi}_{\mathrm{LP}}^{k+1,j} + \widehat{\lambda}^{ks}(\widehat{\zeta}^{ks} - \zeta^{ks}) \tag{5.35}$$

This is the weakest of the possible cuts. However, it can be quickly computed. It is expected to perform well, if the LP relaxation of the subproblem is tight, and the optimal value of the LP relaxation is closer to the optimal value of the MILP. However, this is not true in our problem. Therefore, the algorithm does not have guaranteed finite convergence since there can be a duality gap.

Lagrangean cut. The MILP subproblem P^{ksl} can also be convexified using the Lagrangean relaxation, which yields the convex hull of the noncomplicating constraints. The Lagrangean relaxation L^{ksl} of the MILP P^{ksl} is given as follows:

$$\begin{aligned} L^{ksl}: \quad \Phi_{\mathrm{LR}}^{ks}(\widehat{\lambda}^{ksl}, \widehat{\zeta}^{k-1,sl}, \phi^{ksl}) = \min_{\zeta^{ks},\tau^{ks},\nu^{ks}} \quad & f^{ks}(\zeta^{ks}, \tau^{ks}) + \phi^{ksl}(\widehat{\zeta}^{ksl}) + \widehat{\lambda}^{ks\top}(\widehat{\zeta}^{k-1,sl} - \nu^{ks}) \\ \textbf{s.t.} \quad & (\zeta^{ks}, \tau^{ks}, \nu^{ks}) \in \mathcal{Z}^{ks} \end{aligned} \tag{5.36}$$

The closer the Lagrange multipliers are to their optimal value, the tighter approximation is, and the stronger the cuts generated by these multipliers. The optimal

Lagrange multipliers, $\bar{\lambda}^{ksl}$, are obtained by the maximization problem:

$$\Phi_{\text{LD}}^{ks}(\widehat{\zeta}^{k-1,sl}, \phi^{ksl}) = \max_{\lambda^{ksl}} \quad \widehat{\Phi}_{\text{LR}}^{ks}(\widehat{\lambda}^{ksl}, \widehat{\zeta}^{k-1,sl}, \phi^{ksl}) \tag{5.37}$$

The Lagrangean cut uses the coefficients obtained by solving the Lagrangian dual (5.37), as follows:

$$\theta^{ks} \;\geq\; \Phi_{\text{LR}}^{k+1,j} + \bar{\lambda}^{ks}(\widehat{\zeta}^{ks} - \zeta^{ks}) \tag{5.38}$$

However, the maximization problem (5.38) can be computationally expensive. One way to solve (5.38) would be to use the Lagrange multiplier optimization algorithm using the subgradient method [39].

Strengthened Benders cut: Depending on the structure of the problem, the Benders cuts can be weak and the Lagrangean cuts can take a long time to compute. As proposed in [119], the Strengthened Benders cut is a compromise between the Benders and Lagrangean cuts. The method to generate Strengthened Benders cut is similar to that of the Lagrangean cut, but does not use the subgradient method to improve the multipliers. Instead, it uses the coefficients from the first Lagrangian relaxation solved after the initialization of the multipliers using LP relaxation as follows:

$$\theta^{ks} \;\geq\; \Phi_{\text{LR}}^{k+1,j} + \widehat{\lambda}^{ks}(\widehat{\zeta}^{ks} - \zeta^{ks}). \tag{5.39}$$

These cuts are at least as tight as the Benders cut, but usually less computationally expensive than the Lagrangean cuts. We refer the reader to [57] for the definitions and the proofs of the validity of the Benders cut, Lagrangean cut, and the Stengthened Benders cut.

5.4.3 Comparison of LBD-DIC and NBD

Finally, we analyze differences in the convergence of the LBD-DIC and NBD approaches. The experiments are conducted using a modified IEEE 12-node distribution test feeder. We use the same parameters as in Section 4.4 of Chapter 4.

Figure 5-5 shows the lower bound and upper bound under the LBD-DIC and NBD

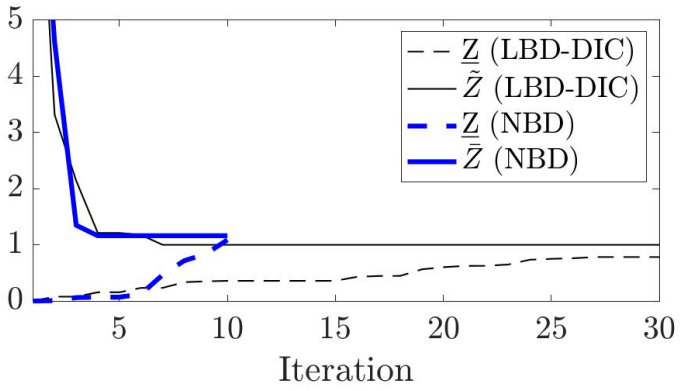

Figure 5-5: Convergence of LBD-DIC and NBD: evolution of lower bound $\underline{Z}$ and "relaxation" upper bound $\widetilde{Z}$ for LBD-DIC, compared with evolution of lower bound $\underline{Z}$ and upper bound $\bar{Z}$ for NBD. Lower and upper bounds are normalized by the minimum value of $\widetilde{Z}$ achieved under LBD-DIC. We use the following parameter values: $\mathbf{G} = 3$ (all fixed DERs), $\mathrm{Y} = 1$, and $\mathrm{S} = 5$.

approaches. Convergence requires only $l = 11$ iterations under NBD, in comparison to $l = 53$ iterations under LBD-DIC. This is because the NBD lower bound estimates are strengthened by the inclusion of the cost-to-go under-approximation in the Benders cut. In comparison, there is no cost-to-go term in the dual integer cut of LBD-DIC. Regarding the upper bound, it is evident that the NBD upper bound estimates $\bar{Z}$ are greater in value than the LBD-DIC "relaxation" upper bound estimates $\widetilde{Z}$ at most iterations. This is because the "relaxation" upper bound estimate $\widetilde{Z}$ is an under-approximation, as updates to $\widetilde{Z}$ are obtained from solutions to D-$\overline{\mathrm{REC}}(a, s)$ and (SMILP). In comparison, the updates to $\bar{Z}$ in the case of NBD are obtained using upper bounds to the optimal objectives of the Stage II recourse problems.

5.5 Summary and Discussion

In this section, we discussed solution approaches based on L-shaped Benders Decomposition (LBD), in order to efficiently solve (DEF) to the two-stage stochastic mixed-integer program (SMIP2) proposed in Section 4. In particular, we formulate the following approaches: LBD with Greedy Approach (LBD-Greedy), LBD with Dual Integer Cuts (LBD-DIC), and Nested Benders Decomposition (NBD). These

approaches differ in terms of master problem formulation, optimality (Benders) cut formulation, and termination criteria. While discussing the approaches, we compare the solution accuracy and computational time associated with these approaches.

5.5.1 Summary of Solution Approaches

The LBD-Greedy method is named after the greedy approach used to solve the Stage II recourse problems, which are mixed-integer linear programs and thus computationally expensive to solve. LBD-Greedy involves a two-step process to obtain the Benders cut at each iteration, by first solving the full Stage II recourse MILPs and then solving linear programs formed by fixing the integer variables in the Stage II MILPs. LBD-Greedy is an improvement over the brute-force "simple enumeration" approach that involves exhaustively considering every feasible Stage I resource allocation strategies, but the algorithm termination relies on iteration-wise elimination of the Stage I strategies and is thus slow. Solving the Stage II recourse problems, even while using the greedy approach, becomes expensive when the network size becomes sufficiently large.

The limitations of the LBD-Greedy method motivate us to develop LBD with Dual Integer Cuts (LBD-DIC). The LBD-DIC method involves forming Benders cut(s) at each iteration by solving LP relaxations to the Stage II recourse problems. The algorithm terminates when the convergence gap, or difference between defined lower and upper bounds, is sufficiently small. We derive "dual integer cuts" which result in strengthened lower bound estimates, as compared to traditional Benders cuts. LBD-DIC typically has faster termination (by convergence) in comparison to LBD-Greedy, and obtaining solutions to the Stage II problems using the LP relaxations is less expensive. However, this comes at a slight sacrifice in terms of optimality of the solutions to (DEF).

We formulate our final solution approach, Nested Benders Decomposition (NBD), with the motivation of further speedening the process of obtaining solutions to the Stage II recourse problems. In order to solve the Stage II recourse problems, we employ a period-wise decomposition of the problem and use a forward-and-backward

pass approach. Using this approach, we are able to solve the recourse problems in much less time than if we solve LP relaxations (as in LBD-DIC), when networks are sufficiently large. Furthermore, the cost-to-go approximations in NBD typically assure faster algorithm termination by convergence, in comparison to LBD-DIC.

5.5.2 Discussion on Scalability

Overall, NBD is the most computationally efficient strategy, whereas LBD-Greedy is the least efficient. On the other hand, LBD-Greedy performs best in terms of solution accuracy. However, we consider problem scalability to be a key priority (i.e., ability of the solution approach to handle networks with >100 nodes). Utilities or system operators need to make operational decisions within the span of several hours, such that they can prepare accordingly for network damage in advance of an incoming hurricane. From this point-of-view, NBD is the most desirable solution approach, in that it is readily able to solve (SMIP2) for 118-node network instances in comparison to the other approaches . Furthermore, NBD is most easily able to accommodate extensions to the two-stage stochastic program. For example, one may be interested in incorporating multi-stage pre-storm resource allocation decisions, or damage localization decisions prior to infrastructural component repairs.

The 118-node network instance can be considered a realistic distribution network of a smaller size. Consequently, additional computational innovations would be desirable to e nsure that NBD (or a similar solution approach) may be feasibly applied to networks that have several hundred or >1,000 nodes. A significant computational expense associated with solving (DEF) comes from the power flow and voltage bound constraints detailed in Chapter 4. If these constraints are relaxed, then the solution approaches proposed here could be feasibly applied to larger networks.

In an electric power infrastructure, there are typically multiple distribution networks connected along a single transmission backbone. Thus, a realistic resource allocation problem would require solving (DEF) separately for each distribution network. The solutions to these problems would provide implications regarding resource allocation and network response for the broader transmission network. Furthermore,

when the broader power infrastructure is considered, the effect of spatial variability in hurricane wind velocities on damages and resource allocations is more evident. This would naturally integrate the results presented in Chapter 3 with Chapters 4-5.

Consideration of realistic-scale networks also permits analysis of how microgrid islands evolve due to repairs. For instance, the microgrid islands could form multiple decentralized clusters that grow and eventually merge after a sufficient number of repairs. On the other hand, it might also be possible that the repairs form a large "backbone" that eventually grows to encompass the remaining nodes. The microgrid evolution process was illustrated in Figures 4-1 – 4-2, but only simple networks were considered here and thus the insights are limited.

Chapter 6

Conclusions and Ongoing Work

6.1 Thesis Summary

In this thesis, we have addressed the challenge of resource allocation and response strategies for infrastructural network resilience to extreme weather events. Specifically, we formulated a modeling and decisions approach for operationally-based strategies that enhance electric power infrastructure resilience to hurricane winds.

In Chapter 1, we defined risk and infrastructural resilience within the context of our problem, and stated that our objective is to minimize risk (maximize resilience). Then, we presented a generalized modeling and decisions framework to address this objective. The framework incorporates a hurricane model; probabilistic model of infrastructural damage; and decisions concerning pre-storm resource allocation as well as post-storm restoration and response. We identify key gaps in the literature that addresses our objective: the necessity of incorporating physically-based hurricane models in probabilistic damage etsimation, of incorporating uncertainties in infrastructural damage when making operational decisions for infrastructural systems, and of models for joint pre- and post-disruption decision-making. We summarize our contributions, which aim to address the gaps in satisfying our research objective.

In Chapter 2, we formulate a parametric model of the asymmetric hurricane wind field. This model can be suitably coupled with existing hurricane track models for the purposes of nowcasting, forecasting, and large-scale ensemble simulation. Most

namely, the model incorporates low-wavenumber asymmetries into the maximum intensity parameter of an axisymmetric wind field model. Model parameters are estimated by solving a constrained, nonlinear least squares (CNLS) problem that minimizes the sum of squared residuals between wind field intensities of historical storms and model-estimated winds. The CNLS method can handle the inherently nonlinear wind field model in a flexible manner; thus, it is well suited to capture the radial variability in the hurricane wind field's asymmetry. We demonstrate that our model outperforms a typical benchmark model of the asymmetric wind field.

In Chapter 3, we introduce a modeling approach for probabilistic estimation of hurricane wind-induced damage to infrastructural assets. In the approach, we employ a Nonhomogeneous Poisson Process (NHPP) model for estimating spatially-varying probability distributions of damage as a function of hurricane wind field velocities. Specifically, we consider a physically-based, quadratic NHPP model for failures of overhead assets in electricity distribution systems. The wind field velocities are provided by Forecasts of Hurricanes using Large-Ensemble Outputs (FHLO), a framework for generating probabilistic hurricane forecasts. We use FHLO in conjunction with the NHPP model, such that the hurricane forecast uncertainties represented by FHLO are accounted for in estimating the probability distributions. Furthermore, we evaluate the spatial variability and extent of hurricane damage under key wind field parameters (intensity, size, and asymmetries). By applying our approach to prediction of power outages (loss-of-service) in northwestern Florida due to Hurricane Michael (2018), we demonstrate a statistically significant relationship between outage rate and failure rate. We conclude with the formulation of parametric models that relate total damage and financial losses to the hurricane parameters of intensity and size.

In Chapter 4, we develop an integrated approach for strategic, operational decision-making in electricity distribution networks (DNs). This approach considers a pre-storm Distributed Energy Resources (DER) allocation problem under the uncertainty of failure scenarios as well as a post-storm dispatch problem in islanded microgrids during the multi-period restoration of the network. Network restoration includes

repair of failed infrastructural assets and re-allocation of DERs within the DN to optimally meet demand due to the growth and eventually reconnection of islands as a result of asset repairs. We formulate a two-stage stochastic mixed-integer linear program (SMIP2), whose objective is to minimize cost by selecting optimal pre- and post-storm decisions. The chapter concludes with discussions of how the system performance is dependent on resource constraints, cost parameters, and the inclusion of mobile DERs.

In Chapter 5, we formulate solution approaches based on L-shaped Benders Decomposition (LBD) to solve (SMIP2), in order to address the scalability challenge introduced by uncertainties in infrastructural asset failures. Our formulated approaches – LBD-Greedy, LBD-DIC, and Nested BD – differ in terms of the formulation of the master problem, optimality (Benders) cuts, and algorithm termination. We demonstrate that our solution approaches outperform the brute-force approach based on simple enumeration of possible resource allocations. Furthermore, although the optimality (Benders) cuts formulated for typical LBD-based approaches require convex and continuous recourse problems, our solution approaches include appropriate formulations of Benders cuts that handle the discontinuous and non-convex recourse problems in (SMIP2). In particular, we derive strengthened "dual integer cuts" for the LBD-DIC approach, which outperform classical Benders cuts in terms of algorithm convergence. We compare the scalability of the three approaches, and demonstrate that Nested BD is most suitable to solving (SMIP2) under distribution networks of realistic sizes.

6.2 Ongoing and Future Work

The work in this thesis can be potentially extended in several directions. With regards to solution approaches for the two-stage stochastic mixed integer linear program (SMIP2) posed in Chapter 4, we consider scenario reduction for problem scalability (Section 6.2.1) and optimality gap estimates for solution evaluation (Section 6.2.2). Then, we discuss briefly how distributed monitoring and control as well as analysis

of spatial scales would affect (SMIP2) in Section 6.2.3. In Section 6.2.4, we discuss integration of decision-making for dual-layer networks consist of electricity (service) networks and transportation networks. In Section 6.2.5, we apply network science approaches by examining how the stability of networks would affect loss-of-function arising from natural disturbances.

6.2.1 Scenario Reduction

The accuracy of solutions to approximations of the two-stage problem (SMIP2) depends on the selected sample $\mathcal{S} \subset \mathcal{S}'$. We can use scenario reduction to strategically select a more representative subset in place of a randomly-sampled subset. Thus, scenario reduction permits us to obtain a more accurate solution to (SMIP2) under fixed $\mathrm{S} = |\mathcal{S}|$.

The scenario reduction approach takes the distribution $\mathcal{P}$ and set $\mathcal{S}'$ as input, then outputs a distribution $\mathcal{P}_{\mathrm{sr}}$ over a selected subset $\mathcal{S}$. The objective of scenario reduction is to minimize the Kantorovich distance between $\mathcal{P}$ and $\mathcal{P}_{\mathrm{sr}}$. In this sense, the subset $\mathcal{S}$ with probabilities defined by $\mathcal{P}_{\mathrm{sr}}$ is the most accurate approximation of the damage uncertainty. We define the Kantorovich distance $D(\mathcal{P}, \mathcal{P}_{\mathrm{sr}})$ as the weighted sum of the distances from all scenarios in $\mathcal{S}'$ to their closest scenario within the selected subset $\mathcal{S}$:

$$D(\mathcal{P}, \mathcal{P}_{\mathrm{sr}}) \;=\; \sum_{s' \in \mathcal{S}'} \mathbb{P}(s') \min_{s \in \mathcal{S}} \Delta_1(s, s'), \tag{6.1}$$

where $\Delta_1(s, s') = \sum_{e \in \mathcal{E}} |s_e - s'_e|$ denotes a symmetric distance between s and s' using the L1-norm. As a notational clarification, $\mathcal{P}$ and $\mathcal{P}_{\mathrm{sr}}$ refer to probability distributions, whereas $\mathbb{P}(s)$ and $\mathbb{P}_{\mathrm{sr}}(s)$ refer to the probabilities of a given scenario s under these distributions.

To solve the scenario reduction problem, we cast it as an integer program known as the uncapacitated p-location problem [110]. Even for moderately-sized networks ($\mathrm{N} = 36$), the number of scenarios is huge $|\mathcal{S}'| > 10^9$. Hence, we first randomly sample a subset $\mathcal{S}^{(R)} \subset \mathcal{S}'$ using $\mathcal{P}$, and then use $\mathcal{S}^{(R)}$ as an input to the uncapacitated

p-location problem.

Scenario reduction modifies the solutions to (SMIP2) in two ways. First, the approximate objective of (SMIP2) is re-defined such that the expected Stage II cost is the sum of the costs $\mathrm{J}^{\mathrm{II}}(a,s)$ weighted by the probabilities $\mathbb{P}_{\mathrm{sr}}(s)$:

$$g(a) \approx \mathrm{J}^{\mathrm{I}}(a) + \sum_{s\in\mathcal{S}} \mathbb{P}_{\mathrm{sr}}(s)\ \mathrm{J}^{\mathrm{II}}(a,s)\,. \tag{6.2}$$

Second, the set of failure scenarios used as input to the LBD-based solution approaches is obtained from scenario reduction after the initial random sampling.

6.2.2 Optimality Gap Estimation

When one reduces the number of scenarios considered using either Sample Average Approximation (SAA) or scenario reduction, the resultant two-stage program provides an approximate solution to (SMIP2). Consequently, the optimal value and solution of the approximate problem may differ from the optimal value and solution of the original (SMIP2) problem. To evaluate the accuracy of approximate solutions, one needs to compute optimality gap estimates. If $v^\star$ is the optimal value of (SMIP2), then for a solution $a^\star$ to the approximate problem, the optimality gap is simply $g(a^\star) - v^\star$. If $a^\star$ is the optimal solution of (SMIP2), then the optimality gap is zero.

Let us consider optimality gap estimation under the SAA method. Our estimation of the optimality gap is based on [52]. To estimate $v^\star$, we obtain M samples each with S scenarios. For each $m = 1, \cdots, \mathrm{M}$, we solve an SAA problem with sample $\mathcal{S}_m$. Let a_m be the optimal solution and v_{S}^m be the corresponding objective. An estimator of $v^\star$ is given by $\bar{v}_{\mathrm{S}}^{\mathrm{M}} = \sum_{m=1}^{\mathrm{M}} v_{\mathrm{S}}^m$. Let $\mathcal{A}_{\mathrm{S}}^{\mathrm{M}} \coloneqq \{a_1, \cdots, a_{\mathrm{M}}\}$ be the set of solutions.

To estimate $g(a^\star)$, we choose $\mathrm{S}^{\mathrm{b}} >> \mathrm{S}$, and then obtain a sample $\mathcal{S}^{\mathrm{b}} \subset \mathcal{S}'$ such that $\mathrm{S}^{\mathrm{b}} \coloneqq |\mathcal{S}^{\mathrm{b}}|$. The estimated value of the objective for a first stage decision a is:

$$g_{\mathrm{S}^{\mathrm{b}}}(a) \coloneqq \mathrm{J}^{\mathrm{I}}(a) + \frac{1}{\mathrm{S}^{\mathrm{b}}} \sum_{s\in\mathcal{S}} \mathrm{J}^{\mathrm{II}}(a,s)\,. \tag{6.3}$$

Then, the optimal first-stage solution is chosen from the set of solutions to be the one with the lowest objective value, i.e, $a^\star = \mathrm{argmin}_{a\in\mathcal{A}_{\mathrm{S}}^{\mathrm{M}}}\ g_{\mathrm{S}^{\mathrm{b}}}(a)$. An unbiased

estimator of $g(a^\star)$ is given by $g_{\mathrm{S}^\mathrm{b}}(a^\star)$.

Since $g(a^\star)$ and $v^\star$ are estimated using random samples, the estimated optimality gap is a random variable which would have some variance. Therefore, an optimality gap estimator which takes accuracy into account is chosen as:

$$g_{\mathrm{S}^\mathrm{b}}(a^\star) - \bar{v}_{\mathrm{S}}^{\mathrm{M}} + z_\alpha \sqrt{\frac{\mathrm{Var}(g_{\mathrm{S}^\mathrm{b}}(a^\star))}{\mathrm{S}^\mathrm{b}} + \frac{\mathrm{Var}(\bar{v}_{\mathrm{S}}^{\mathrm{M}})}{\mathrm{M}}}, \tag{6.4}$$

where $\mathrm{Var}(g_{\mathrm{S}^\mathrm{b}}(a^\star))$ denotes the sample variance of the Stage II cost, $\mathrm{Var}(\bar{v}_{\mathrm{S}}^{\mathrm{M}})$ the sample variance of the objectives v_{S}^m, and z_α the cumulative distribution function of the standard normal distribution. We set $z_\alpha = 1.96$ to obtain a 95% confidence interval.

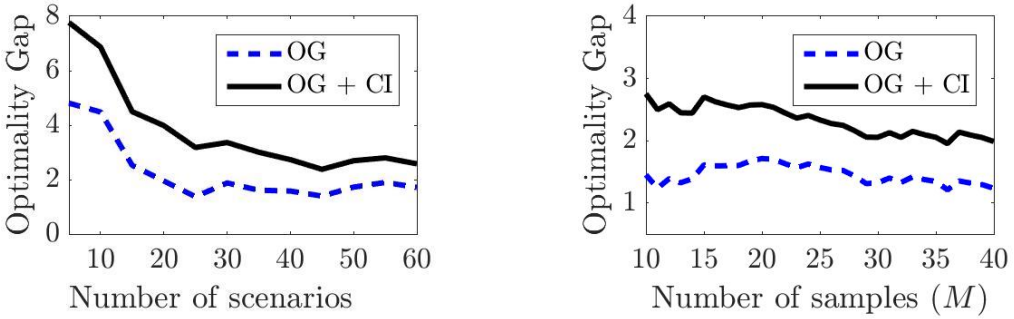

(a) (b)

Figure 6-1: (a) – Optimality gap estimates for the 36-node DN as a function of S, under fixed M = 20 and $\mathrm{S}^\mathrm{b} = 10,000$. (b) – Estimates varying M under fixed S = 60 and $\mathrm{S}^\mathrm{b} = 10,000$. "OG" is the optimality gap estimate and "OG+CI" is the estimate with the 95% confidence interval.

In Figure 6-1a, we plot the optimality gap as a function of sample size S. The optimality gap is normalized by the estimator $\bar{v}_{\mathrm{S}}^{\mathrm{M}}$, and is thus interpreted as a percentage deviation from the estimate of the true objective. We also plot the 95% confidence interval corresponding to the estimate. The optimality gap predictably tends to decrease with increasing S. In Figure 6-1b, we plot the optimality gap as a function of number of samples M. Both the confidence interval and optimality gap tend to decrease with increasing M. This implies that solving more instances of SAA will produce greater confidence in the optimality of DER allocation.

In order to explain the trends in Figure 6-1, we separate the optimality gap estimator into its components:

$$\left(g_{\mathrm{S^b}}(a^\star) - g(a^\star)\right) + \left(g(a^\star) - v^\star\right) + \left(v^\star - \bar{v}_{\mathrm{S}}^{\mathrm{M}}\right) + z_\alpha \sqrt{\frac{\mathrm{Var}(g_{\mathrm{S^b}}(a^\star))}{\mathrm{S^b}} + \frac{\mathrm{Var}(\bar{v}_{\mathrm{S}}^{\mathrm{M}})}{\mathrm{M}}}. \quad (6.5)$$

The first term has an expected value of 0, because $\mathbb{E}[g_{\mathrm{S^b}}(a^\star)] = g(a^\star)$. The variance of this term decreases with increasing $\mathrm{S^b}$. The second term is the true optimality gap. The third term has a positive bias because $\mathbb{E}[\bar{v}_{\mathrm{S}}^{\mathrm{M}}] \leq v^\star$. The variance of this term decreases with increasing M, and the bias decreases with increasing S. These properties are evident in the decreasing width of the confidence interval with increasing M and the decreasing optimality gap with increasing S, respectively. The fourth term is the confidence interval.

6.2.3 Extensions to Resource Allocation and Response for Electricity Networks

One can readily incorporate distributed monitoring and control systems into the models discussed in Chapter 4. This specifically entails utilization of analytics derived from sensor and Internet of Things (IoT) data, in order to inform real-time state estimation and network repair. Distributed monitoring and control – as opposed to centralized network control – increases the efficiency of response and repair decisions in the face of disruptions. I will also integrate models of distributed generators that produce power from renewable energy sources. To do so, I consider literature on optimal renewable energy dispatch that addresses the intermittency and stochasticity of renewables. Integration of renewable energy sources will lead to a power grid that is both environmentally sustainable and more resilient to disruptions.

In addition, I am interested in more closely integrating my work on resource allocation and repair with my models for infrastructural damage, to consider the impact of spatial scales on resource allocation. Hurricanes typically have a radius greater than 400 km, which necessitates decision-making for power systems that can span counties or districts. Such systems include bulk generators; high-voltage transmis-

sion networks that deliver power from bulk generators; and distribution networks that connect transmission networks to end users. My current stochastic optimization approach is tailored to decision-making at the level of distribution networks, but the approach is readily extendable to consider larger spatial scales and transmission network topologies. Consideration of damage estimation and decision-making at the spatial scale of hurricanes maximizes the impact of my models, such as when federal agencies must decide how to optimally allocate resources across states in advance of an incoming disaster.

6.2.4 Response of Service Networks Following Hurricanes

I will continue to research post-hurricane response and recovery strategies in infrastructure networks, which improve the ability of crisis managers to make operationally-informed decisions. Effective response is conducive to more rapid recovery, thus minimizing network service disruptions following natural disasters. I focus on strategies for damage localization and repair, by considering optimal crew routing schedules. Consequently, this work necessitates modeling of storm-induced transportation network disruptions, which affect the connectivity between resource depots, crews, and damage sites. To this end, I will model the electricity and transportation network as a dual-layer network [101], and integrate my models of electricity network damage with models of storm-induced disruptions on transportation paths. I will focus on how network recovery rates and optimal response strategies are affected by hurricane forecast accuracy, as estimated using our approach detailed in Chapter 3. In addition, I will integrate work on the application of small unmanned aerial systems (sUAS) to network exploration and damage isolation [58].

6.2.5 Stability of Critical Infrastructure Networks

The network topology, which determines connectivity between nodes (i.e., supply and demand locations in a power network), has an impact on the network's loss-of-function following a disturbance. This suggests that networks can be designed or configured to

be more resilient to natural disasters. For instance, if a path between an energy supply node and demand node is disrupted, the demand is more likely to be met if alternative paths exist and remain functional. More formally, the proportion of nodes that remain connected to the network despite disruptions is defined as the network's stability. In my postdoctoral position, I will study how resilience of electricity networks and dual-layer service-transport networks (see Sec. 6.2.4) depends on network topology, in addition to the damage forecasts as discussed in Chapter 3. To do so, I will apply fundamental work on the stability of single- and dual-layer networks [51]. This provides insights on optimal network topologies, which inform strategies for network design and/or re-configuration to improve resilience.

Bibliography

[1] Chad Abbey, David Cornforth, Nikos Hatziargyriou, Keiichi Hirose, Alexis Kwasinski, Elias Kyriakides, Glenn Platt, Lorenzo Reyes, and Siddharth Suryanarayanan. Powering Through the Storm: Microgrids Operation for More Efficient Disaster Recovery. *IEEE Power and Energy Magazine*, 12(3):67–76, 2014.

[2] Shabbir Ahmed and Alexander Shapiro. The Sample Average Approximation Method for Stochastic Programs with Integer Recourse. *Submitted for publication*, pages 1–24, 2002.

[3] Karin Alvehag and Lennart Söder. A Reliability Model for Distribution Systems Incorporating Seasonal Variations in Severe Weather. *IEEE Transactions on Power Delivery*, 26(2):910–919, 2011.

[4] Daniel Bienstock and Abhinav Verma. The N-k problem in power grids: New models, formulations, and numerical experiments. *SIAM Journal on Optimization*, 20(5):2352–2380, 2010.

[5] John Birge. Decomposition and Partitioning Methods for Multistage Stochastic Linear Programs. *Operations Research*, 33, 10 1985.

[6] K. De Brabandere, B. Bolsens, J. Van den Keybus, A. Woyte, J. Driesen, and R. Belmans. A Voltage and Frequency Droop Control Method for Parallel Inverters. *IEEE Transactions on Power Electronics*, 22(4):1107–1115, July 2007.

[7] Daniel C. Brown. Selecting a Vehicle-Mounted Generator. `https://www.concreteconstruction.net/products/selecting-a-vehicle-mounted-generator_o`. Accessed: 2021-02-24.

[8] R.E. Brown, S. Gupta, R.D. Christie, S.S Venkata, and R. Fletcher. Distribution System Reliability Assessment: Momentary Interruptions and Storms. *IEEE Transactions on Power Delivery*, 12(4):1569–1575, 1997.

[9] U.S. Census Bureau. Florida Census Data: Population & Housing Density. `https://www.census-charts.com/Density/Florida.html`. Accessed: 2021-02-09.

[10] Kenneth P. Burnham and David R. Anderson. Multimodel Inference. *Sociological Methods and Research*, 33(2):261–304, 2004.

[11] Richard J. Campbell. Weather-Related Power Outages and Electric System Resiliency. Congressional Research Service, Library of Congress Washington, DC, 2012.

[12] Claus C. Carøe and Jørgen Tind. L-shaped decomposition of two-stage stochastic programs with integer recourse. *Mathematical Programming*, 83:451–464, 1998.

[13] E. Casson and S. Coles. Simulation and extremal analysis of hurricane events. *Journal of the Royal Statistical Society: Series C (Applied Statistics)*, 49(3):227–245, 2000.

[14] National Hurricane Center. Definition of the NHC Track Forecast Cone. `https://www.nhc.noaa.gov/aboutcone.shtml`.

[15] Derek Chang, Saurabh Amin, and Kerry Emanuel. Modeling and Parameter Estimation of Hurricane Wind Fields with Asymmetry. *Journal of Applied Meteorology and Climatology*, 59(4):687–705, 2020.

[16] Derek Chang, Devendra Shelar, and Saurabh Amin. DER Allocation and Line Repair Scheduling for Storm-induced Failures in Distribution Networks. In *2018 IEEE SmartGridComm*, pages 1–7. IEEE, 2018.

[17] Derek Chang, Devendra Shelar, and Saurabh Amin. Stochastic Resource Allocation for Electricity Distribution Network Resilience. In *2020 American Control Conference*, pages 1–6, 2020.

[18] Daniel R. Chavas, Ning Lin, and Kerry Emanuel. A Model for the Complete Radial Structure of the Tropical Cyclone Wind Field. Part I: Comparison with Observed Structure. *Journal of the Atmospheric Sciences*, 72(9):3647–3662, 2015.

[19] L. Che, M. Khodayar, and M. Shahidehpour. Only Connect: Microgrids for Distribution System Restoration. *IEEE Power Energy Magazine*, Jan 2014.

[20] C. Chen, J. Wang, F. Qiu, and D. Zhao. Resilient Distribution System by Microgrids Formation After Natural Disasters. *IEEE Transactions on Smart Grid*, 7(2):958–966, March 2016.

[21] Jan Wesner Childs. Why Winter Storm Uri Caused Millions of Power Outages in Texas. `https://weather.com/news/news/2021-02-16-why-so-many-power-outages-in-texas-winter-storm`. Accessed: 2021-02-24.

[22] Smart Energy Consumer Collaborative. How the smart grid helps during the hurricane season. `https://www.whatissmartenergy.org/featured-article/how-the-smart-grid-helps-during-hurricane-season#:~:text=Smart\%20grid\%20technology\%20can\%20also,and\%20cost\%20for\%20restoring\%20power`.

[23] James Conca. Puerto Rico Needs 50,000 Utility Poles. https://www.forbes.com/sites/jamesconca/2017/10/13/puerto-rico-needs-50000-utility-poles/?sh=5071784d3d84. Accessed: 2021-02-24.

[24] Applied Technology Council. Emergency Power Systems for Critical Facilities: A Best Practices Approach to Improving Reliability. https://www.wbdg.org/FFC/DHS/femap1019.pdf.

[25] L. Dean, K. A. Emanuel, and D. R. Chavas. On the size distribution of Atlantic tropical cyclones. *Geophysical Research Letters*, 36(14), 2009.

[26] Mark DeMaria, Michelle Mainelli, Lynn K. Shay, John A. Knaff, and John Kaplan. Further Improvements to the Statistical Hurricane Intensity Prediction Scheme (SHIPS). *Weather and Forecasting*, 20(4):531–543, 2005.

[27] Steven M. DiNapoli, Mark A. Bourassa, and Mark D. Powell. Uncertainty and Intercalibration Analysis of H*Wind. *Journal of Atmospheric and Oceanic Technology*, 29(6):822–833, 2012.

[28] Erin Douglas, Kate McGee, and Jolie McCullough. Texas leaders failed to heed warnings that left the state's power grid vulnerable to winter extremes, experts say. https://www.texastribune.org/2021/02/17/texas-power-grid-failures. Accessed: 2021-02-24.

[29] J. Dupačová, N. Gröwe-Kuska, and W. Römisch. Scenario Reduction in Stochastic Programming. *Math Program.*, 95(3), Mar 2003.

[30] Kerry Emanuel. Tropical cyclone energetics and structure. *Atmospheric Turbulence and Mesoscale Meteorology*, page 165–192, 2004.

[31] Kerry Emanuel. Increasing destructiveness of tropical cyclones over the past 30 years. *Nature*, 436(7051):686–688, 2005.

[32] Kerry Emanuel. A fast intensity simulator for tropical cyclone risk analysis. *Natural Hazards*, 88(2):779–796, Jun 2017.

[33] Kerry Emanuel, Christopher Desautels, Christopher Holloway, and Robert Korty. Environmental Control of Tropical Cyclone Intensity. *Journal of the Atmospheric Sciences*, 61(7):843–858, 2004.

[34] Kerry Emanuel, Sai Ravela, Emmanuel Vivant, and Camille Risi. A Statistical Deterministic Approach to Hurricane Risk Assessment. *Bulletin of the American Meteorological Society*, 87(3):299–314, 2006.

[35] Kerry A. Emanuel. The Finite-Amplitude Nature of Tropical Cyclogenesis. *Journal of the Atmospheric Sciences*, 46(22):3431–3456, 1989.

[36] David Eoff. Diesel generator failures: Lessons taught by hurricanes. https://go.gale.com/ps/anonymous?id=GALE\%7CA168813994&sid=googleScholar&v=2.1&it=r&linkaccess=abs&issn=00325961&p=AONE&sw=w.

[37] Sean Ericson and Dan Olis. A Comparison of Fuel Choice for Backup Generators. https://www.nrel.gov/docs/fy19osti/72509.pdf.

[38] Robert Fares. Hurricane Maria Dealt a Devastating Blow to Puerto Rico's Electric Grid. https://blogs.scientificamerican.com/plugged-in/hurricane-maria-dealt-a-devastating-blow-to-puerto-ricos-electric-grid. Accessed: 2021-02-24.

[39] Marshall L. Fisher. The Lagrangian Relaxation Method for Solving Integer Programming Problems. *Management Science*, 27(1):1–18, 1981.

[40] Thomas J. Galarneau and Christopher A. Davis. Diagnosing Forecast Errors in Tropical Cyclone Motion. *Monthly Weather Review*, 141(2):405–430, 2013.

[41] Haixiang Gao, Ying Chen, Shengwei Mei, Shaowei Huang, and Yin Xu. Resilience-Oriented Pre-Hurricane Resource Allocation in Distribution Systems Considering Electric Buses. *Proceedings of the IEEE*, 105(7):1214–1233, 2017.

[42] Benjamin W. Green and Fuqing Zhang. Impacts of Air-Sea Flux Parameterizations on the Intensity and Structure of Tropical Cyclones. *Monthly Weather Review*, 141(7):2308–2324, 2013.

[43] Thomas M Hamill, Jeffrey S Whitaker, Michael Fiorino, and Stanley G Benjamin. Global ensemble predictions of 2009's tropical cyclones initialized with an ensemble kalman filter. *Monthly Weather Review*, 139(2):668–688, 2011.

[44] Robert Hamilton. Lessons in Emergency Power Preparedness: Planning in the Wake of Katrina. https://goo.gl/8TjK5K.

[45] Seung-Ryong Han, Seth D Guikema, Steven M Quiring, Kyung-Ho Lee, David Rosowsky, and Rachel A Davidson. Estimating the spatial distribution of power outages during hurricanes in the gulf coast region. *Reliability Engineering & System Safety*, 94(2):199–210, 2009.

[46] Holger Heitsch and Werner Römisch. Scenario Reduction Algorithms in Stochastic Programming. *Computational Optimization and Applications*, 24(2):187–206, Feb 2003.

[47] Greg J. Holland. An Analytic Model of the Wind and Pressure Profiles in Hurricanes. *Monthly Weather Review*, 108(8):1212–1218, 1980.

[48] Greg J. Holland, James I. Belanger, and Angela Fritz. A Revised Model for Radial Profiles of Hurricane Winds. *Monthly Weather Review*, 138(12):4393–4401, 2010.

[49] CBS Interactive Inc. Texas power outages stretch into third day as millions face freezing conditions. https://www.cbsnews.com/news/texas-power-outage-ercot-grid-investigation. Accessed: 2021-02-24.

[50] Jip Kim and Yury Dvorkin. Enhancing Distribution System Resilience With Mobile Energy Storage and Microgrids. *IEEE Transactions on Smart Grid*, 10(5):4996–5006, 2018.

[51] Maksim Kitsak, Alexander A. Ganin, Daniel A. Eisenberg, Pavel L. Krapivsky, Dmitri Krioukov, David L. Alderson, and Igor Linkov. Stability of a Giant Connected Component in a Complex Network. *Physical Review E*, 97(1):012309, 2018.

[52] Anton J. Kleywegt, Alexander Shapiro, and Tito Homem-de Mello. The Sample Average Approximation Method for Stochastic Discrete Optimization. *SIAM Journal on Optimization*, 12(2):479–502, February 2002.

[53] Bradley W. Klotz and Haiyan Jiang. Examination of Surface Wind Asymmetries in Tropical Cyclones. Part I: General Structure and Wind Shear Impacts. *Monthly Weather Review*, 145(10):3989–4009, 2017.

[54] Bradley W. Klotz and David S. Nolan. SFMR Surface Wind Undersampling over the Tropical Cyclone Life Cycle. *Monthly Weather Review*, 147(1):247–268, 2019.

[55] Christophe Lallemand. Methodology for a risk based asset management. *Royal Institute of Technology*, 2008.

[56] Christopher W. Landsea and James L. Franklin. Atlantic Hurricane Database Uncertainty and Presentation of a New Database Format. *Monthly Weather Review*, 141(10):3576–3592, 2013.

[57] Cristiana L. Lara, Dharik S. Mallapragada, Dimitri J. Papageorgiou, Aranya Venkatesh, and Ignacio E. Grossmann. Deterministic electric power infrastructure planning: Mixed-integer programming model and nested decomposition algorithm. *European Journal of Operational Research*, 271(3):1037 – 1054, 2018.

[58] Andrew C. Lee, Mathieu Dahan, Andrew J. Weinert, and Saurabh Amin. Leveraging sUAS for Infrastructure Network Exploration and Failure Isolation. *Journal of Intelligent & Robotic Systems*, 93(1-2):385–413, 2019.

[59] S. Lei, J. Wang, C. Chen, and Y. Hou. Mobile Emergency Generator Pre-Positioning and Real-Time Allocation for Resilient Response to Natural Disasters. *IEEE Transactions on Smart Grid*, 9(3):2030–2041, May 2018.

[60] Shunbo Lei, Chen Chen, Hui Zhou, and Yunhe Hou. Routing and Scheduling of Mobile Power Sources for Distribution System Resilience Enhancement. *IEEE Transactions on Smart Grid*, 10(5):5650–5662, 2018.

[61] Jonathan Lin, Kerry Emanuel, and Jonathan L Vigh. Forecasts of Hurricanes using Large-Ensemble Outputs. *Weather and Forecasting*, 35(5):1713–1731, 2020.

[62] Ning Lin, Kerry Emanuel, Michael Oppenheimer, and Erik Vanmarcke. Physically based assessment of hurricane surge threat under climate change. *Nature Climate Change*, 2(6):462–467, 2012.

[63] H. Liu, R. A. Davidson, and T. V. Apanasovich. Statistical Forecasting of Electric Power Restoration Times in Hurricanes and Ice Storms. *IEEE Transactions on Power Systems*, 22(4):2270–2279, Nov 2007.

[64] Haibin Liu, Rachel A. Davidson, David V. Rosowsky, and Jerry R. Stedinger. Negative Binomial Regression of Electric Power Outages in Hurricanes. *Journal of Infrastructure Systems*, 11(4):258–267, 2005.

[65] J. A. P. Lopes, C. L. Moreira, and A. G. Madureira. Defining control strategies for MicroGrids islanded operation. *IEEE Transactions on Power Systems*, 21(2):916–924, May 2006.

[66] J. A. P. Lopes, C. L. Moreira, A. G. Madureira, F. O. Resende, X. Wu, N. Jayawarna, Y. Zhang, N. Jenkins, F. Kanellos, and N. Hatziargyriou. Control strategies for microgrids emergency operation. In *2005 International Conference on Future Power Systems*, pages 6 pp.–6, 2005.

[67] Sharanya J. Majumdar and Peter M. Finocchio. On the Ability of Global Ensemble Prediction Systems to Predict Tropical Cyclone Track Probabilities. *Weather and Forecasting*, 25(2):659–680, 2010.

[68] Z. Miao, A. Domijan, and L. Fan. Investigation of Microgrids With Both Inverter Interfaced and Direct AC-Connected Distributed Energy Resources. *IEEE Transactions on Power Delivery*, 26(3):1634–1642, July 2011.

[69] Oliver Milman. Climate change is making hurricanes even more destructive, research finds. `https://www.theguardian.com/environment/2018/nov/14/climate-change-hurricanes-study-global-warming`, Nov 2018.

[70] Mitigation Division, Federal Emergency Management Agency, Department of Homeland Security. *Multi-hazard Loss Estimation Methodology: Hurricane Model*.

[71] Franco Molteni, Roberto Buizza, Tim N. Palmer, and Thomas Petroliagis. The ECMWF ensemble prediction system: Methodology and validation. *Quarterly Journal of the Royal Meteorological Society*, 122(529):73–119, 1996.

[72] C. L. Moreira and J. A. Peças Lopes. *MicroGrids Operation and Control under Emergency Conditions*, pages 351–399. Springer Berlin Heidelberg, Berlin, Heidelberg, 2012.

[73] Erin B. Munsell and Fuqing Zhang. Prediction and uncertainty of Hurricane Sandy (2012) explored through a real-time cloud-permitting ensemble analysis and forecast system assimilating airborne Doppler radar observations. *Journal of Advances in Modeling Earth Systems*, 6(1):38–58, 2014.

[74] Susan Myers and Victoria Yang. Email Communication, July 15, 2020.

[75] Jorge Nocedal and Stephen J. Wright. *Numerical Optimization*. Springer, 2006.

[76] William D Nordhaus. The Economics of Hurricanes in the United States. Technical report, National Bureau of Economic Research, 2006.

[77] Min Ouyang. Review on modeling and simulation of interdependent critical infrastructure systems. *Reliability Engineering & System Safety*, 121:43–60, 2014.

[78] Mathaios Panteli and Pierluigi Mancarella. Modeling and Evaluating the Resilience of Critical Electrical Power Infrastructure to Extreme Weather Events. *IEEE Systems Journal*, 11(3):1733–1742, 2015.

[79] Christina M Patricola and Michael F Wehner. Anthropogenic influences on major tropical cyclone events. *Nature*, 563(7731):339–346, 2018.

[80] Veronica Penney. No, Wind Farms Aren't the Main Cause of the Texas Blackouts. `https://en.wikipedia.org/wiki/2021_Texas_power_crisis#cite_note-NYT-20210219-13`. Accessed: 2021-02-24.

[81] Brad Plumer. Why Getting the Power Back On in Florida Could Take Weeks, Sep 2017.

[82] Mark D. Powell, Sam H. Houston, Luis R. Amat, and Nirva Morisseau-Leroy. The HRD real-time hurricane wind analysis system. *Journal of Wind Engineering and Industrial Aerodynamics*, 77-78:53–64, 1998.

[83] Jason Ray and Victoria Yang. Email Communication, July 23, 2020.

[84] Raphaël Rousseau-Rizzi and Kerry Emanuel. An Evaluation of Hurricane Superintensity in Axisymmetric Numerical Models. *Journal of the Atmospheric Sciences*, 76(6):1697–1708, 2019.

[85] Richard W Schwerdt, Francis P Ho, and Roger R Watkins. Meteorological Criteria for Standard Project Hurricane and Probable Maximum Hurricane Windfields, Gulf and East Coasts of the United States. 1979.

[86] K. S. A. Sedzro, A. J. Lamadrid, and L. F. Zuluaga. Allocation of Resources Using a Microgrid Formation Approach for Resilient Electric Grids. *IEEE Transactions on Power Systems*, 33(3):2633–2643, May 2018.

[87] GM Shafiullah, Amanullah MT Oo, ABM Shawkat Ali, and Peter Wolfs. Smart Grid for a Sustainable Future. *Smart Grid and Renewable Energy*, 4(1):23–34, 2013.

[88] Alexander Shapiro and Tito Homem-de Mello. A simulation-based approach to two-stage stochastic programming with recourse. *Mathematical Programming*, 81(3):301–325, 1998.

[89] Lloyd J. Shapiro. The Asymmetric Boundary Layer Flow Under a Translating Hurricane. *Journal of the Atmospheric Sciences*, 40(8):1984–1998, 1983.

[90] Devendra Shelar, Saurabh Amin, and Ian Hiskens. Resilience of Electricity Distribution Networks - Part II: Leveraging Microgrids, Dec 2018.

[91] Manish Kumar Singh, Vassilis Kekatos, and Chen-Ching Liu. Optimal Distribution System Restoration with Microgrids and Distributed Generators. *arXiv preprint arXiv:1811.04147*, 2018.

[92] Ken Stocks and Victoria Yang. Email Communication, July 29, 2020.

[93] Yushi Tan, Feng Qiu, Arindam K Das, Daniel S Kirschen, Payman Arabshahi, and Jianhui Wang. Scheduling Post-Disaster Repairs in Electricity Distribution Networks. *arXiv preprint arXiv:1702.08382*, 2017.

[94] Energy Innovation: Policy and Technology. Hurricanes Harvey And Irma Show U.S. Must Boost Grid Resiliency. Energy Storage Is Doing Just That. `https://www.forbes.com/sites/energyinnovation/2017/09/08/hurricanes-harvey-and-irma-show-u-s-must-boost-grid-resiliency-energy-storage-is-doing-just-that/26aa75e224c9`, Sep 2017.

[95] Frances Fragos Townsend. *The Federal Response to Hurricane Katrina: Lessons Learned*. Government Printing Office, 2006.

[96] M. Steven Tracton and Eugenia Kalnay. Operational ensemble prediction at the National Meteorological Center: Practical aspects. *Weather and Forecasting*, 8(3):379–398, 1993.

[97] Jenna Tsui. How Smart Microgrids Will Change the Way We Consume Energy. `https://www.altenergymag.com/article/2020/06/how-smart-microgrids-will-change-the-way-we-consume-energy/33212`. Accessed: 2021-02-24.

[98] K. Turitsyn, P. Sulc, S. Backhaus, and M. Chertkov. Options for Control of Reactive Power by Distributed Photovoltaic Generators. *Proceedings of the IEEE*, 99(6):1063–1073, 2011.

[99] Katherine Tweed. Here Come the Apps: Florida Power & Lfight Finishes $800M Smart Grid, May 2013.

[100] Eric W. Uhlhorn, Bradley W. Klotz, Tomislava Vukicevic, Paul D. Reasor, and Robert F. Rogers. Observed Hurricane Wind Speed Asymmetries and Relationships to Motion and Environmental Shear. *Monthly Weather Review*, 142(3):1290–1311, 2014.

[101] Aybike Ulusan and Ozlem Ergun. Restoration of services in disrupted infrastructure systems: A network science approach. *PloS one*, 13(2):e0192272, 2018.

[102] National Infrastructure Advisory Council (US). *Critical Infrastructure Resilience: Final Report and Recommendations*. National Infrastructure Advisory Council, 2009.

[103] Pascal Van Hentenryck, Russell Bent, and Carleton Coffrin. Strategic Planning for Disaster Recovery with Stochastic Last Mile Distribution. In *International Conference on Integration of Artificial Intelligence (AI) and Operations Research (OR) Techniques in Constraint Programming*, pages 318–333. Springer, 2010.

[104] Tine L. Vandoorn, Juan C. Vasquez, Jeroen De Kooning, Josep M. Guerrero, and Lieven Vandevelde. Microgrids: Hierarchical Control and an Overview of the Control and Reserve Management Strategies. *IEEE Industrial Electronics Magazine*, 7(4):42–55, 2013.

[105] P. J. Vickery, P. F. Skerlj, A. C. Steckley, and L. A. Twisdale. Hurricane Wind Field Model for Use in Hurricane Simulations. *Journal of Structural Engineering*, 126(10):1203–1221, 2000.

[106] P. J. Vickery, P. F. Skerlj, and L. A. Twisdale. Simulation of Hurricane Risk in the U.S. Using Empirical Track Model. *Journal of Structural Engineering*, 126(10):1222–1237, 2000.

[107] Peter J. Vickery, Dhiraj Wadhera, Mark D. Powell, and Yingzhao Chen. A Hurricane Boundary Layer and Wind Field Model for Use in Engineering Applications. *Journal of Applied Meteorology and Climatology*, 48(2):381–405, 2009.

[108] Tomislava Vukicevic, Eric Uhlhorn, Paul Reasor, and Bradley Klotz. A Novel Multiscale Intensity Metric for Evaluation of Tropical Cyclone Intensity Forecasts. *Journal of the Atmospheric Sciences*, 71(4):1292–1304, 2014.

[109] Meg Wagner, Melissa Macaya, Judson Jones, and Mike Hayes. Millions are still without power as winter storms continue. `https://www.cnn.com/us/live-news/snow-ice-storm-power-outages-updates-02-17-21/index.html`. Accessed: 2021-02-24.

[110] Kai Wang and Alexandre Jacquillat. A Stochastic Integer Programming Approach to Air Traffic Scheduling and Operations. *Operations Research*, 68:1375–1402, 2020.

[111] Charles C. Watson and Mark E. Johnson. Hurricane Loss Estimation Models: Opportunities for Improving the State of the Art. *Bulletin of the American Meteorological Society*, 85(11):1713–1726, 2004.

[112] Yonghui Weng and Fuqing Zhang. Assimilating Airborne Doppler Radar Observations with an Ensemble Kalman Filter for Convection-Permitting Hurricane Initialization and Prediction: Katrina (2005). *Monthly Weather Review*, 140(3):841–859, 2012.

[113] H. E. Willoughby, R. W. R. Darling, and M. E. Rahn. Parametric Representation of the Primary Hurricane Vortex. Part II: A New Family of Sectionally Continuous Profiles. *Monthly Weather Review*, 134(4):1102–1120, 2006.

[114] H. E. Willoughby and M. E. Rahn. Parametric Representation of the Primary Hurricane Vortex. Part I: Observations and Evaluation of the Holland (1980) Model. *Monthly Weather Review*, 132(12):3033–3048, 2004.

[115] Lian Xie, Shaowu Bao, Leonard J. Pietrafesa, Kristen Foley, and Montserrat Fuentes. A Real-Time Hurricane Surface Wind Forecasting Model: Formulation and Verification. *Monthly Weather Review*, 134(5):1355–1370, 2006.

[116] Peng Zhang, Gengfeng Li, Peter B. Luh, Wenyuan Li, Zhaohong Bie, and Camilo Serna. Risk Analysis for Distribution Systems in the Northeast U.S. Under Wind Storms. *2014 IEEE PES General Meeting | Conference & Exposition*, 2014.

[117] Junhui Zhao, Caisheng Wang, Bo Zhao, Feng Lin, Quan Zhou, and Yang Wang. A Review of Active Management for Distribution Networks: Current Status and Future Development Trends. *Electric Power Components and Systems*, 42, 02 2014.

[118] Y. Zhou, A. Pahwa, and S.-S. Yang. Modeling Weather-Related Failures of Overhead Distribution Lines. *IEEE Transactions on Power Systems*, 21(4):1683–1690, 2006.

[119] Jikai Zou, Shabbir Ahmed, and Xu Andy Sun. Stochastic dual dynamic integer programming. *Mathematical Programming*, 175(1):461–502, 2019.